UCL Université catholique de Louvain

École polytechnique de Louvain (EPL)

epl

Biocorrosion of iron based alloys for bioresorbable coronary stent applications

Dissertation presented by
Sarah REUTER

for obtaining the Master's degree in
Chemical and Materials Engineering

Supervisors
Pascal JACQUES , Aude THOMAS

Readers
Dominique LISON, Quentin VAN OVERMEERE

Academic year 2015-2016

Abstract

Cardiovascular diseases, such as blood vessels obstructions are common. They are the main cause of death in Belgium and worldwide [1]. Bad diets can cause these atherosclerosis plaques to build up. In such cases, percutaneous coronary intervention (PCI) needs to be performed, during which a stent is implanted. Different stent families exist. Permanent bare-metal stents, drug-eluting and bioresorbable stents are differentiated. Complication due to stenting include restenosis and thrombosis. The foreign body can induce an unwanted cell proliferation, resulting in a re-narrowing of the blood vessels. By making stents bioresorbable, late-thrombosis can be avoided, as the foreign body will degrade and not alter the blood environment anymore. The mechanical support should be present for about 6 month-1 year, after which the stent is obsolete and should degrade. Investigated bioresorbable stents are polymer based, or metal based. The former category does not present good mechanical properties and the latter category can be distinguished between magnesium based and iron based stents. The magnesium based stents degrade too fast, whereas iron stents degrade too slowly. The aim of this Master's thesis is to investigate the corrosion behaviour of iron based alloys. The two materials that will be tested are Armco iron for comparison reasons and Fe-22Mn-0.6C. Armco iron is used as a reference material, which corrosion properties are widely investigated in the literature. Therefore, the experimental protocol is validated on this material. Fe-22Mn-0.6C is a twinning induced plasticity (TWIP) alloy, presenting excellent work-hardening properties. This is a critical feature for the mechanical support of the injured vessel. Its corrosion properties have not been studied a lot and will be investigated and compared to the ones of iron. The impact of deformation on these samples has also been investigated. Indeed, the stent undergoes compression to be placed onto the balloon and expansion to be put in place in the injured vessel. Locally the deformation is supposed less than 30%. The different deformations tested were 0%, 10%, 20%, 30%, and 40%.

Corrosion properties will be studied by the use of electrochemical tests and quasi static immersion tests. Electrochemical tests were performed on iron and TWIP samples using simulated body fluid (SBF) with or without Hepes buffer. Once the experimental protocol was put in place, the tests were performed on TWIP samples (in SBF containing 50mM buffer). Quasi static immersion were also performed on these TWIP samples (SBF containing 50mM buffer).

The electrochemical results highlighted a higher corrosion rate for the non TWIP samples compared to Armco iron. Inside the TWIP samples, the differences in corrosion rates are minimal. The non deformed samples exhibit the highest corrosion rate. The 40% samples seem to corrode slightly faster than 30% and 20% families and the 10% family seems to have the slowest corrosion rate. SEM and EDX analysis showed the presence of a cracked layer on top of iron samples containing Ca, P, Na, and Mg. The TWIP samples showed the presence of agglomerates on a surface layer composed mainly of the metal constituents and some SBF elements (Ca, and Mg especially). The corrosion products contain P, Ca, Na, Mg, and also Cl.

The immersion tests (in SBF containing 50mM Hepes buffer) on Fe-22Mn-0.6C showed that the corrosion rate was highest after one day immersion and decreased significantly between day 1 and day 7, followed by a slighter decrease from day 7 to day 21. The samples tested were non deformed samples and 40% deformed ones. The differences between the different deformation families for one week immersions (non-deformed, 10%, 20%, 30%, and 40%) were slight and the standard deviations too high to conclude any dependence. The higher buffer concentration (100mM), however showed an increased corrosion rate. The corrosion mechanism is similar to ones already explained in the literature [2, 3, 4]: the metal gets attacked by oxygen reduction, forming a rust layer. Chlorine then attacks the matrix creating metal chlorides. A final layer is made of Ca/P deposits (and some Na, Mg, and and K). A qualitative idea of the sublayer compositions was found by ToF-SIMS to correspond to this mechanism (expect Cl that was present on the top layer aswell). XPS showed the presence of hydroxides (corrosion

products), phosphorous, calcium, and sodium (all three are SBF deposits).
Keywords: Corrosion rate, Corrosion mechanism, electrochemistry, stent, SBF, TWIP alloys, iron, Ca/P layer.

Acknowledgements

This thesis could not have been achieved without the precious help of many people.

First, I would like to thank Pascal Jacques, who supervised this thesis. I am grateful for guidance and advice, ensuring that I remained on the right path throughout this project.

I would also like to thank my PhD supervisor Aude Thomas, who was there for me throughout the year. She found the way to lift my spirits in moments of challenges. Her constant energy was motivating. Additionally, the numerous discussions we had, enlighten several aspects that had to be dealt with. Finally, I am very grateful for the time she put into reading my thesis before submission.

I would like to thank my assessors: Dominique Lison and Quentin Van Overmeere for taking the time to read and assess my thesis. Additionally, I would like to thank Dominique Lison and his PhD student Eleonora Scarcello for letting me perform immersion tests in their premises. An additional thank goes to Eleonora for always being present when the immersion tests started and ended in order to measure the dissolved oxygen concentration in the premises of St. Luc in Brussels. Finally, an important thank goes to Quentin Van Overmeere, without whom I would not have acquired the level of understanding of the electrochemical aspects that I do now. He always took the time to respond to my numerous emails and was always available to Skype to help me clarify some aspects. I could never be thankful enough for all his help.

I am also thanking the whole IMAP team, who made me feel part of the team. Their constant enthusiasm and passion was contagious and made the working environment more enjoyable. A special thank goes to Ronny Santoro for all the ICP analyses he performed on my behalf as well as the numerous SBF solutions prepared by him as well as by Nadine Deprez. I would also like to express my gratitude to Quentin de Radiguès, Adeline Delvaux, and Raphaël Poulain, who were always ready to help and enlighten me. Their various advices were always helpful. I would also like to thank Frédéric Van Wonterghem for his precious advice throughout the year. An additional thank goes to Laurence Ryelandt for all her helpful expertise concerning the SEM and EDX analysis. Finally, I would like to thank Jonathan Lorfèvre for his precious help throughout the year but especially for building the handmade setup used for some immersion tests and Marc Sinnaeve for performing the tensile tests.

A special thanks goes to Joris Proost, who took the time to understand the difficulties encountered and offering advice on how to tackle these challenges.

I would also like to thank Claude Poleunis for the ToF-SIMS analysis and Pierre Eloy for the XPS analysis, whose result interpretation was of great help.

I am grateful for my friends support in the most challenging periods of my thesis but also throughout my five years of university. My time here would not have been the same without them. Special thanks go to Lena Peschke, and Sophie Neven for their continuous support in this difficult period. Another special thanks goes to my dear friends Thérèse Plissart and Anaïs Powell for their support while proofreading parts of my thesis.

I am also grateful for the proof reading of Adam Jordan, who took the time to go over each section of this thesis.

Last but not least, I could never have been here without the love, understanding and support of my loving family. My parents (Khadija Ben Lahbib and Guido Reuter) as well as my sister (Nadia Reuter)

were always present for me, and made sure that I would not be missing anything.

CONTENTS

LIST OF FIGURES

LIST OF TABLES

LIST OF ABBREVIATIONS

CV	**C**yclic **V**oltametry
CE	**C**ounter **E**lectrode
FCC	**F**ace **C**entered **C**ubic
LSV	**L**inear **S**weep **V**oltametry
MIC	**M**icrobiologically **I**nduced **C**orrosion
OCP	**O**pen **C**ircuit **P**otential
PCI	**P**ercutaneous **C**oronary **I**ntervention
RE	**R**eference **E**lectrode
SBF	**S**imulated **B**ody **F**luid
SHE	**S**tandard **H**ydrogen **E**lectrode
SCC	**S**tress **C**orrosion **C**racking
SCE	**S**aturated **C**alomel **E**lectrode
SEM	**S**canning **E**electron **M**icroscope
SFE	**S**tacking **F**ault **E**nergy
ToF-SIMS	**T**ime **o**f **F**light **S**econdar **I**on **S**pectometry
TWIP	**TW**inning **I**nduced **P**lasticity
WE	**W**orking **E**lectrode
XRD	**X R**ay **Diffraction**
XPS	**X**-ray **P**hotoelectron **S**pectroscopy
ICP	**I**nductively **C**oupled **P**lasma

LIST OF SYMBOLS

a_i	activity of specie	-
C_{dl}	double electric layer capacitance	farad
c	concentration	mol/m^3
CR, v_{corr}	corrosion rates	mm/year and $g/(m^2.d)$
d	tip diameter of the Luggin capillary	distance
D	diffusion coefficient	m^2/s
ΔG	GIbb's free energy	kJ/mol
ΔG°	standard GIbb's free energy	kJ/mol
E	potential	V
E_{eq}	equilibrium potential	V
E°	standard potential (at 1 atm)	V
EW	equivalent weight	grams/equivalent
I	current	A
i	current density	$A\,m^{-2}$, A/cm^2
i_a	anodic current density	$A\,m^{-2}$, A/cm^2
i_c	cathodic current density	$A\,m^{-2}$, A/cm^2
i_L	limiting current density	$A\,m^{-2}$, A/cm^2
i_{ox}	oxydation current density	$A\,m^{-2}$, A/cm^2
i_{red}	reduction current density	$A\,m^{-2}$, A/cm^2
iR drop	uncompensated solution resistance	Ω
J	flux of substance	$mol/(m^2.s)$
m_i	molality of specie	mol/kg
m	mass	kg
M	number of moles	mol
Q, K	equilibrium constants	-
Q	can also mean electric charge	C
R	gas constant	J/(K.mol)
R_p	polarisation resistance	$V.cm^2/A$
S	surface	cm^2, m^2
T	temperature	K
t	time	s
T	temperature	K
x	position	m
z	number of electrons exchanged	-
α	symmetry factor [0 1] that defines the position across the double layer	-
β_a	anodic Tafel slope	mV/dec

β_b	cathodic Tafel slope	mV/dec
η	overpotential	V
ρ	density	g/cm^3

CHAPTER 1

INTRODUCTION

The rate of heart disease is increasing year on year, with many cases due to the obstruction of blood vessels. In most cases, these obstructions can be healed by implanting stents inside the injured vessel. However, adding foreign bodies inside the human body can have adverse effects. As a matter of fact, once the stent is implanted, restenosis[1] and late-thrombosis[2] can occur. Restenosis is due to a proliferation of tissue caused by the presence of the foreign body. This excessive proliferation of tissue can lead to a re-narrowing of the vessel. The presence of a foreign body can also induce some sort of inflammation. All these issues are a clear sign that better technologies need to be developed in order to avoid these complications as much as possible. That is where bioresorbable stents are of interest. They are thought to start degrading once the body does not need the extra mechanical support anymore. This is typically the case after 6-12 months. The biodegradable stent should thus provide the mechanical support and resorb as soon as possible once its task has been fulfilled. Bioresorbable stents made of polymers have been developed. The negative aspect of these stents is their mechanical weakness: they sometimes break before fulfilling their task. Besides, they resorbed totally after 2 years, which is still too long and thus the stent could still be responsible for late-thrombosis. Metallic resorbable stents have then been introduced to increase the mechanical properties. Magnesium stents were resorbing after only 4 months of implantation, which is not enough to support the injured vessel and could lead to even earlier mechanical failure. Iron stents have then been developed but these present a too low corrosion rate.

The subject of bioresorbable stents is the focus of this Master's thesis. Twinning induced plasticity (TWIP) alloys will be investigated on a corrosion behaviour basis. Indeed, these alloys have extremely interesting mechanical properties. They possess significant work-hardening properties, which are of interest in the needed radial support of the injured vessel. Besides radial support, they also provide good ductility (for the deployment) and mechanical strength. Moreover, the addition of manganese to iron has been found to be beneficial for increasing the corrosion rate [5, 3, 6, 7]. The TWIP alloy that will be investigated in this study is the Fe-22Mn-0.6C alloy.

The stents also undergo plastic deformation before implantation. As a matter of fact, the stent is first shrunk around a balloon and once it reaches the injured vessel, it is expanded to the vessel diameter. The impact of deformation on the corrosion behaviour will also be investigated for the TWIP samples.

[1] Restenosis is defined as being an abnormal re-narrowing of arteries or valves after a corrective surgery has been performed.

[2] Thrombosis occurs because stents are foreign bodies and activate coagulation.

In order to investigate the corrosion behaviour, electrochemical tests as well as quasi static immersion tests will be undergone in simulated body fluid (SBF) with or without addition of Hepes buffer. The former are able to give some good approximation on the actual corrosion rate while performing tests lasting around 2.5 hours, whereas the quasi static immersion tests are performed over longer time ranges and allow the study of the effect on corrosion rate, when elements deposit on the metal, which is more realistic compared to *in vivo* situations.

This document will be divided in following sections:

- Background information on stents, their fabrication process, the mechanical behaviour of twinning induced plasticity alloys. Further, the theory behind electrochemistry will be detailed, as well as the corrosion mechanisms for metals. Finally, this section will deal with previous findings in the literature on bioresorption of iron and iron-based alloys.
- The second part will present the materials and methodology used for the polarisation tests, immersion tests, morphological studies (SEM, EDX, XPS, ToF-SIMS, XRD) and composition analysis (ICP).
- The third part will present the different results of the present study. For the electrochemical tests, a preliminary study on Armco iron will be performed. Indeed, the corrosion rate of iron has already been studied throughout the literature, which is why it is interesting to study the corrosion rate of iron to see if it can be compared to values found in the literature. Also, a reproducible protocol needs to be put in place and this will be investigated on iron. Once the best method has been chosen, it will be used to compare the TWIP samples deformed to different levels (10%, 20%, 30%, and 40%). The immersion tests results will then be related. These tests lasted 1, 7 or 21 days.
- Finally, the results will be discussed regarding two main aspects: the kinetics of corrosion and the morphology changes due to corrosion. Recommendations for future investigations will be given as well as a conclusion on all the results, their impacts and their corrosion behaviour.

CHAPTER 2
BACKGROUND INFORMATION AND THEORY

In this chapter, the fundamentals on stents will be explained as well as the advantages and disadvantages of different modern stent implantations materials, with a particular focus on TWIP steel stents[1]. Furthermore, the theory behind electrochemistry and the different corrosion types will be explained in detail. Finally, previous papers on biocorrosion found in the literature will be related in this chapter as well as their outcomes.

2.1 Fundamentals on stents

First, it is to be stated why stents are used in the medical industry: Coronary artery diseases are one of the primary causes of death [8] and stents are one way to overcome these diseases along with previously used balloon angioplasty and by-passes.

Stents are mesh tubes that are used when blood vessels are narrowed, obstructed or weakened. They are placed into the human body during an angioplasty [2], also known as a percutaneous coronary intervention (PCI) [9].

Blood vessels can get obstructed when the patient suffers of atherosclerosis which is a disease where artery walls are covered by plaques made of lipids, cholesterol crystals, necrotic debris, proteins, degenerating blood elements and cells such as macrophages, smooth muscle cells and foam cells [10]. An angioplasty is undertaken if the occlusion is not too big; otherwise a bypass has to be performed. The aortic wall can also be weakened and can threaten to rupture following an aneurysm. An angioplasty can be performed with or without the insertion of stents. Inserting stents reduce the risk of restenosis from 30% up to 7-10% depending on which kind of stent is used. Restenosis occurs when too much tissue is growing inside the treated area, see Figure 2.1a [9].

2.1.1 How is a stent placed?

The example of a balloon expandable stent inserted in a coronary artery will be taken. The procedure consists of a number of steps. First, the surgeon inserts a needle in the femoral artery for example. A catheter is then carefully passed upwards near the obstructed area by means of a guidewire. Once the wire is near the obstructed area, the catheter releases a contrast dye, so that the surgeon can spot the exact area where the obstruction is. A wire is then inserted into the catheter and guided just beyond

[1] This part will mainly be taken from a previous work of mine that I did in December 2014 for the 4B19 Biomechanics class in Trinity College Dublin.

[2] Angioplasty is a surgical repair of blocked blood vessels, especially of the coronary artery.

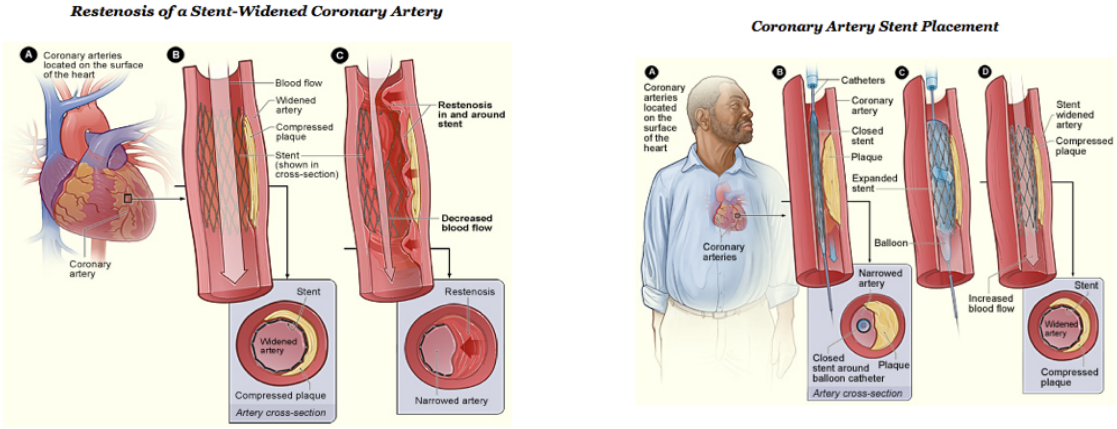

(A) Restenosis

(B) Stent placement

FIGURE 2.1: Restenosis and placement of a stent: a catheter is passed upwards to the obstructed area and deploys the stent once the the injured area has been reached [9].

the obstructed area. Then a balloon is released; this balloon will inflate and deflate until the blood flow is normal again. Then another balloon, carrying the stent, is placed in the obstructed area and is briefly inflated which expands the stent, which will remain permanently or temporarily to provide support to the artery and to resist the build-up of plaque [9, 11] .

On Figure 2.1b, a summary of how the procedure is done and how the artery is widened and will remain so can be seen.

2.1.2 The different stent types and their biocompatibility issues

The most common biocompatibility issues due to stenting are thrombosis[3] and restenosis. These issues will be assessed in detail later in this section. For the tissue to heal re-endothelialization should be taking place as early as possible in order to avoid late-thrombosis.

2.1.2.1 Balloon expandable and self-expanding stents

Balloon expandable stents and self-expanding stents can be distinguished. The first stents used on the market were balloon-expandable stents. Balloon-expandable stents were mainly made of stainless steel. Most of the self-expanding stents are made of nitinol which is a metal alloy made of nickel and titanium. Nitinol is known for its superelasticity and shape memory properties, which are very interesting for self-expanding stents. The two families differ in different properties such as radial strength, acute recoil, chronic recoil and hyperplasia, fatigue and long-term mechanical integrity [12]. The ability to withstand radial pressure is very important for stents and is fulfilled by nitinol, however not always by stainless steel stents. The recoil due to the vessel spring-back force is a negative feature and is less present for balloon-expandable stents in calcified environments. Hyperplasia is defined as an organ or tissue enlargement due to an increased cell proliferation. Intimal hyperplasia happens when blood vessels have been reconstructed and it is the endothelial cells[4] that proliferate [13]. The self-expanding stents continue to increase in size and remodel the vessel. In this case hyperplasia is a positive effect. As a matter of fact, the lumen may increase in size due to the presence of stents and as for the self-expanding stents cell proliferation encompassed the sample, this stent will not be exposed to

[3]Thrombosis occurs because stents are foreign bodies and activate coagulation.

[4]Endothelial cells are one of the three major cells of which blood vessels are made, along smooth muscle cells, and fibroblasts

blood flow, compared to balloon-expandable stents. Finally, nitinol stents can withstand vessel diameter changes due to their super-elasticity, but stainless still is rigid enough to prevent diameter pulsation.

New stents are being developed, mixing balloon-expandable and self-expanding features. One example is a stent made of nitinol that contains two stable states: open and closed. The balloon is able to change the state of the stent from closed to open during implantation [12].

Thrombogenicity is also to be considered. In order to reduce the risk of thrombosis and restenosis the deployment must be optimal. This implies a high-pressure dilatation for balloon-expandable stents which can lead to vessel injuries. Also balloon-expandable stents are less elastic and are subject to longitudinal shortening. These negative effects do not occur while using nitinol self-expanding stents. *Thierry et al.* [14] tested the blood compatibility of nitinol stents against stainless steel stents using an ex-vivo, AV-shunt porcine model. The results highlighted a lower thrombogenicity for nitinol as the amount of labeled fibrinogen adsorption and platelet deposition after 15 minutes of perfusion were of 36% for nitinol stents against 63% for stainless steel stents. This lower thrombogenicity can be explained by the fact that electropolished nitinol is covered by a Titanium-rich oxide layer (TiO_2) that is known for its good haemocompatibility. Electropolished stainless steel, on the other hand is covered by a chromium- and iron-rich oxide layer. These results are also independent of the material geometry effects on blood interaction as the stainless steel stent and the nitinol stent had both the same shape in the study [14].

2.1.2.2 Bare-metal stents

For big arteries such as the aorta (aortic aneurysm) stent grafts, which are composed of a metallic frame covered by a fabric tube that is usually polyester or ePTFE (Polytetrafluoroethylene), are used [9, 10]. For coronary stents (among others), the type used may also be differentiated between bare-metal, drug-eluting and resorbable stents.

Bare-metal stents include stainless steels (first generation), cobalt chromium (second generation) and platinum chromium (third generation). These metal alloys are incompatible with the vasculature and promote thrombosis due to their surface properties. Dual anit-platelet therapy is a treatment using aspirin and anticlotting medicine, usually clopidogrel. If this treatment is not administered, failure due to thrombosis can achieve 24%. Dual anti-platelet therapy cannot be administrated to everyone such as patients with high bleeding risk or patients requiring surgery. Thrombosis can lead to an abrupt vessel closure, to large non-fatal myocardial infarction or death. The other major cause (beside thrombosis) of bare-metal failure is restenosis (neointimal hyperplasia). As a reminder, in-stent restenosis occurs due to an uncontrolled immune response. This response is caused by damage to the vessel and the disruption of the native endothelium. Improvements made between the different bare-metal stents generations have reduced the thrombosis rate but not the restenosis rate. The material is not the only cause of biocompatibility issues, the design of the stent also has major influence. Figure 2.2 relates the different generations of bare-metal stents. [15]

2.1.2.3 Drug-eluting stents

Drug-eluting stents were introduced to lower the restenosis rate. Drug-eluting stents are bare-metal stents covered by a special material that releases an antiproliferative drug. These drug-eluting stents reduce the risk of restenosis at a higher degree than simple bare-metal stents; 25% of restenosis (within the first six months) for bare-metal stents against less than 10% for drug-eluting stents (as a remainder, there were 30% of restenosis cases for angioplasties without stent implantation) [17]. While these

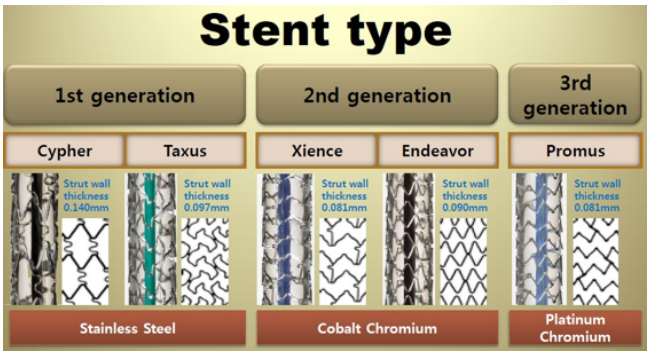

FIGURE 2.2: Different generations of bare metal stents on the market covered by different types of drugs elutedt [16]

drugs (paclitaxel for first generation stents) reduce the in-stent restenosis risk, they also deregulate the cell-cycle, which means that they dramatically delay the tissue healing end re-endothelialization by blocking the cell-cycle specific kinase and this can lead to late thrombosis; as a result the drug-eluting stents struts only have 50% or less endothelial coverage after three years. Re-endothelialization can be improved by changing the metal alloy, the polymer coating and the eluted drug. For example, the change could be following: cobalt chromium metal alloy, fluoropolymer coating and everolimus elution drug. Here the biocompatibility issues are also due to the polymer coating and the drug eluted. Just like bare-metal stents, the polymer coating can lead to inflammations and while the design and material improvements have been able to reduce the biocompatibility issues throughout the time, the polymer coating and the drug effects are still problematic in such a way that the risk of inflammations and late re-endothelialization are still present. Drug-eluting stents can also lead to late stent thrombosis. For this issue, dual anti-platelet therapy should be administrated in a longer term [15].

2.1.2.4 Bioresorbable stents

Bioresorbable stents were implemented to reduce the long-term biocompatibility issues that the drug-eluting stents imply. This is done by them degrading over time. As a matter of fact, the human body does not need the mechanical support of stents indefinitely. The intended use of stents is to scaffold intimal flaps that have been separated from deeper layers, prevent early constrictive remodelling and sometimes deliver anti-proliferative drugs to limit excessive healing. Once that is done, they are of no use and can even be harmful for the human body. If all the mechanical supports needed are analysed, after 6-12 months a stent is not needed anymore.

Polymer based bioresorbable stents

The first generation of bioresorbable stents were balloon-expandable and made of poly-L-lactic acid. The degradation process involved the hydrolysis of the stent in lactic acid, which is then metabolized in H_2O and CO_2. This stent is not drug-eluting. Due to the fact that this process is done by bulk erosion (and takes 2 years), the stent is able to keep its shape a long time. But these stents had the same restenosis rate as bare-metal stents. A new generation of stents was later created by coupling these resorbable stents with drug-elution, such as everolimus elution. One of the developed stents had a polymer coating made of poly-D,L-lactide. In this type of stent, the absorption is done by bulk erosion and the absorption time is of almost two years. This stent resisted to the negative remodeling; main cause of restenosis. Another stent is the bioresorbable therapeutics stent, which is a sirolimus-eluting stent and releases additionally salicylic acid. The salicylic acid is added to reduce the inflammations

implied by stent placement. The absorption is done by surface erosion and finishes after six months approximately. The surface erosion still led to a high restenosis rate. Hence, they revisited it by reducing the struts thickness and increasing the drug concentration. [15, 18]

If stents completely disappear there might be no inflammation leading to late thrombosis. The main problem of polymer-based bioresorbable stents is that they have noticeably inferior mechanical properties (flexibility, deliverability, device profile and radial strength) so that they cannot be used for different coronary lesions such as bifurcation lesions, calcified lesions, etc [15, 18].

This is why metal-based biodegradable stents are starting to be investigated. Figure 2.3 illustrates typical stress/strain curves for polymers and metals on which it can clearly be seen that metals have better mechanical properties. Magnesium-based stents have already been quite investigated but iron-based alloys are also starting to get investigated. These biodegradable stents need to start corroding with a slow rate until about 6-12 months, in order to fulfill their task and from there on a higher corrosion rate is wanted so that degradation products do not stay in the human body for any longer than possible. A degradation time of 12-24 months is acceptable [7].

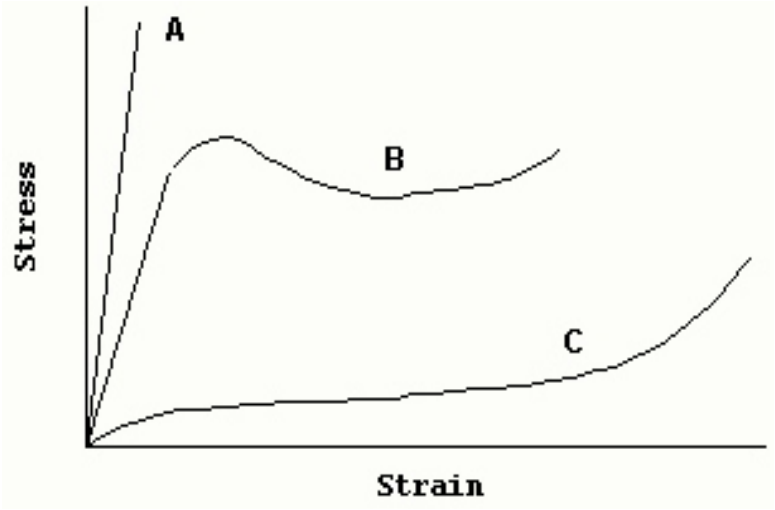

FIGURE 2.3: Stress-Strain curves for (A) a typical elastomer, (B) a metal, and (C) a ceramic [19].

The mechanical properties of materials used for stent applications should be close to the properties of 316L SS which is, so far, the material with the best mechanical properties for these applications. A few materials studied in the goal to be used as biodegradable materials for stent applications are outlined on Figure 2.4 [7].

Up to now, following metals have been investigated for biodegradable application [7]: magnesium based alloys, iron based alloys and metallic glasses from magnesium- or iron-based alloys.

Iron-based bioresorbable stents

It has been confirmed that iron-based stents were not responsible for degradation product accumulation, metal overload or any signs of metal-related organ toxicity, in heart, lung, spleen, liver, kidney and para-aortic lymphatic node [20, 21]. Mechanically speaking, iron is very ductile which is of great advantage during stent deployment in the artery [22]. Additionally, its high radial strength allows

Metal, metallurgy and its composition (wt%)	Density (g/cm^3)	Yield strength (MPa)	Tensile strength (MPa)	Young's modulus (GPa)	Ductility (%)
SS316L, annealed plate Fe, 16–18.5 Cr, 10–14 Ni, 2–3 Mo, <2 Mn, <1 Si, <0.03 C (ASTM 2003)[a]	8.00	190	490	193	40
Fe, annealed plate 99.8 Fe (Goodfellow 2010)	7.87	150	210	200	40
Fe-Mn-Pd alloy, cast + heat treatment Fe, 10.2 Mn, 0.92 Pd, 0.12 C (Schinhammer et al. 2010)	N/A	850	1450	N/A	11
Mg, annealed sheet 99.98 Mg (ASM 2005)	1.74	90	160	45	3
WE43 Mg alloy, temper T6 Mg, 3.7–4.3 Y, 2.4–4.4 Nd, 0.4–1 Zr (ASTM 2001)	1.84	170	220	44	2
Mg-Ca alloy, extruded Mg, 1 Ca (Li et al. 2008)	N/A	140	240	N/A	11

[a] Non-degradable, taken for comparison purpose. The values shown here are the minimum requirements by ASTM

FIGURE 2.4: Mechanical properties of biodegradable metals compared to SS316L [7]

iron-based stents struts to be made thinner, resulting in a quicker degradation [22]. However, Armco iron is not degrading fast enough and thus composition and design (larger surface and strut thickness reduction) need to be modified in order to overcome this problem [22]. On Figure 2.5, a table compares different iron-based alloys in terms of mechanical properties, average grain size, and in vitro degradation rate. By adding manganese, the standard electrode potential of the alloy is decreased and by adding palladium, nobler intermetallic phases are created, adding cathodic sites in the alloy, which then increases the overall corrosion rate. Mechanical properties are not only altered from the alloy composition but also by the heat treatment that the alloy experienced. [22]

Liu et al [5] recently developed a shape memory stent with composition Fe-30Mn-6Si. It was produced by casting in a vacuum induction furnace followed by a solution treatment at 850°C during one hour. The alloy was then water quenched in order to increase the shape memory effect. The findings of the mechanical properties testing was that this alloy is made of ϵ martensite and γ austenite phases at room temperature with better mechanical properties than pure iron and Fe-30Mn alloy. Regarding the corrosion rate, this alloy corroded more rapidly than Fe-30Mn but less rapidly than pure iron. At first sight, this alloy inhibits the metabolic activity of human endothelial cells more than pure iron. Nevertheless the human endothelial cells viability started to increase from day 2 to day 4, which is a good sign. In comparison to 316L SS, this alloy had slightly higher hemolysis [5] value but could still be considered non-hemolytic according to the ASTM-F756-08 standard. [22]

Another attempt in increasing the corrosion rate was to change the microstructure. Electroformed iron, with notably smaller grain size than Armco iron (6μm vs 40μm) were found to have higher

[5] Hemolysis is the rupturing of red blood cells and the release of the contents of these celles into the surrounding fluid [23].

tensile and yield strength than the latter. Due to its smaller grains, electroformed iron exhibited a higher degradation rate as a larger grain boundaries area was available for uniform corrosion (this type of corrosion will be explained in section 2.4). Compared to 316L SS and Armco iron, electroformed iron did not exhibit any cell metabolic activity inhibition of primary rat smooth muscle cells and the proliferation of these cells decreased in contact with electroformed iron which could result in a decreased stent restenosis [22]. This fabrication process will be explained in detail in the next section.

Nie et al. [24] investigated nanocrystalline materials and they found a slower corrosion rate as outcome. Despite this smaller corrosion rate, they also found that the cell response and hemocompatibility were improved as there is a certain size-dependent behaviour between the cells and the grains of the corresponding material. [22]

Material	Yield Strength (MPa)	Tensile Strength (MPa)	Elongation (%)	*In vitro* Degradation Rate (mm y^{-1}) *	Average Grain Size (μm)
316L SS: annealed (ASTM F138) [17]	190	490	40	-	12–30
Armco® Fe: annealed [13,18]	150	200	40	0.19	40
Fe-35Mn alloy: annealed [19–21]	230	430	30	0.44	<100
Fe-10Mn-1Pd alloy: heat treated [22]	850–950	1450–1550	2–8	-	-
Electroformed Fe: annealed at 550 °C [23,24]	270	290	18	0.46–1.22	2–8
Fe alloyed by different elements (Mn, Co, Al, W, Sn, B, C and S): as cast [25]	100–220	190–360	12–23	0.10–0.17	100–400
Fe-30Mn-6Si alloy: solution treated [26]	180	450	16	0.30	<100
Nanocrystalline Fe: ECAP, 8 passes [27]	-	250–450	-	0.09–0.2	0.08–0.20

* The degradation rate is calculated from potentiodynamic polarization test.

FIGURE 2.5: Mechanical properties, in vitro degradation rate and average grain size of biodegradable iron-based metals studied for stent applications [22].

Magnesium-based bioresorbable stents

Magnesium has also been investigated for bioresorbable stent applications as it has low thrombogenicity and is known to be biocompatible and non-carcinogenic. Magnesium is a structural element of tissue and essential to be present in the body: it is involved in more than 300 biological cell reactions. However, magnesium degrades very rapidly in chloride solution, as is the case in SBF. This high degradation rate (absorbed within the four first months) results in an overload of corrosion products on the tissue and this could lead to neointimal hyperplasia. This increased degradation rate also leads to a decrease in mechanical strength, which could result in early mechanical failure. This is why magnesium needs to be alloyed (with elements such as manganese or aluminium for example) in order to be used as bioresorbable implant. A list of different magnesium-based alloys are compared to 316LSS in a table that can be found on Figure 2.6. It has been found that Mg-Al alloy lost 15-20% of its mechanical properties in modified-simulated body fluid (SBF) compared to its mechanical properties in atmospheric conditions. [22, 15, 18]

2.1.3 Conclusion

In conclusion, stents have improved the biological response to angioplasty by reducing the risk of restenosis. Self-expanding stents should be distinguished from balloon-expandable stents since the self-expanding stents become part of the body anatomy and act in harmony with native vessels whereas

Material	Yield Strength (MPa)	Tensile Strength (MPa)	Elongation (%)	*In vitro* Degradation Rate (mm y^{-1}) *	Average Grain Size (μm)
316L SS: annealed (ASTM F138) [17]	190	490	40	-	12–30
Pure Mg: as cast [18,41]	20	86	13	407	-
WE43 alloy: extruded T5 [41]	195	280	2	1.35	10
AM60B-F: die cast [18,41,42]	-	220	6–8	8.97	25
ZW21: extruded [43–45]	200	270	17	-	4
WZ21: extruded [43–45]	140	250	20	-	7

* The degradation rate is calculated from potentiodynamic polarization test.

FIGURE 2.6: Mechanical properties, in vitro degradation rate and average grain size of biodegradable magnesium-based metals studied for stent applications [22].

balloon-expandable stents change the geometry and properties of the anatomy.

Progresses in research have been made about combining the advantages of these two stent types by creating balloon-expandable, superelastic stents.

Bare-metal stents, drug-eluting stents and bioresorbable stents can also be distinguished. What a stent is supposed to do, in regard to biocompatibility, is perform haemocompatibility, promote rapid re-endothelialization and suppress restenosis. Bare-metal stents are still thrombogenic and predisposed to restenosis. Drug-eluting stents, on the other hand, are delaying healing and do not fulfil the second task, which was to promote rapid re-endothalialization; they also induce inflammations and therefore increase the risk of late thrombosis. Bioresorbable stents have been introduced to reduce these biocompatibility issues as the mechanical support is not needed anymore after six months implantation. In these stents, the resorption should be by bulk erosion to avoid losing the mechanical properties too early. Another approach was to just make the coating of drug-eluting stents resorbable so that the late thrombosis risk is lowered to the one of bare-metal stents. The main issue with these resorbable stents is that their mechanical properties are inferior to the other stents so that they cannot be used in all cardiovascular lesions. Concretely, the challenges are to produce biodegradable stents with a controllable corrosion rate, longer mechanical stability and reduction of neointimal hyperplasia [22].

Therefore, research is still needed in order to find the most suitable stent type that will be able to fulfill the tasks needed, and resorb in the body afterwards. For now, different stents are used for different issues depending on the most critical property needed. But what if, one stent could fulfill all the tasks for all the different issues? This is where this thesis subject is of interest. A mechanically strong and quick resorbing stent is needed. That is why we will focus on TWIP steels as they have very strong mechanical properties and questions are arising on how fast and with which mechanism these alloys degrade. Once shaped into a stent, this stent will undergo different deformations. First, it will be compressed and once it is inside the body, it will undergo a radial tensile deformation. Therefore, an important question is to see how these deformations will influence the corrosion behaviour of the stent.

2.2 Stent fabrication process

Stents are made from metallic ingots that are produced by casting. They could be shaped directly while being cast as this would be less expensive but the structure resulting from as-cast materials is much coarser than that of a material undergoing subsequent heat-treatment or annealing. This coarser structure is due to the fact that the growth rate of crystalline phases is higher in liquid state compared to the solid state. This is why, casting will only be used in order to produce the metal but shaping as

well as obtaining the desired mechanical properties will be done through the use of thermo-mechanical processes. [22]

Melting is undergone under vacuum conditions in order to reduce the amount of porosity formed and inhibit the material oxidation. Other factors affecting porosity are the purity and nature of the elemental components that are mixed before melting and the melt practice. These factors are also ruling the homogeneity and microcleanliness of the cast alloy. After casting, different hot working processes are used in order to improve the mechanical properties by plastic deformation and work-hardening. These processes include forging, rolling and extrusion. The temperatures at which these processes are undergone is dependent of the material. It will be chosen such to be in the temperature range in which the material is easily workable and where oxidation is not too severe. After these hot working processes, the metal is cold worked and heat treated. This step is the one in which the material desired final dimensions and physical and mechanical properties are obtained. Once this is done, the stent needs to be shaped correctly. Welding should be avoided as it is impossible to get a defect-free weld and seamless tubing should be used. Then, lasers are generally used to get the stent design. As lasers are computer-controlled, the design can be easily changed. The stents are then annealed to relieve the stresses caused during laser-cutting and tube-drawing as well as to improve the mechanical properties. They are then acid pickled to remove the unwanted parts and debris and finally electropolished to achieve a smoother metal surface and remove burrs and mechanical defects. [22]

This fabrication process is the one used for most biodegradable stents made of metals used nowadays, but new fabrication processes are being investigated: powder metallurgy and electroforming. [22]

Powder metallurgy

This technique compacts powdered metal followed by heat-treatment in order to get a denser material. The final density is variable from one process to the other, with a maximum density achieved being 95%. This technique has been used for the fabrication of nitinol implants and one challenge is the oxygen content. When the oxygen concentration exceeds 3000 ppm, ductility and fatigue resistance can be weakened. Another challenge in powder metallurgy (especially in sintering) is to obtain a high density without having grains that are out of range. Indeed, higher sintering temperatures will result in higher densities but also in grain growth and a compromise needs to be made. *Hermawan et al.* [25] investigated powder metallurgy on biodegradable Fe-Mn alloys for stent applications. Their process was following: powder mixing, compacting, sintering, cold-rolling, re-sintering, cold rolling and finally another re-sintering. The purity, size and morphology of the powders as well as the mixing time, the pressing load and the atmosphere under which sintering is performed are crucial parameters influencing the final properties of the material. As an example, Fe-35Mn produced by powder metallurgy resulted in an exclusively austenitic phase with high ductility and yield strength. Cold rolling and re-sintering were performed in order to improve the density. After these cold rolling and re-sintering processes, there still was about 0.3% of porosity and 2% MnO inclusions but these features were found to be beneficial to an increase in corrosion rate. The corrosion rate of this Fe-35Mn prepared by powder metallurgy can be compared to Fe-30Mn produced by casting and thermo-mechanical treatment by *Liu et al.* [5]. The casted and thermo-mechanically treated alloy had a higher density and ductility. On the other hand, the powder metallurgy fabricated alloy had a higher degradation rate (0.44 mm year^{-1} versus 0.12 mm year^{-1}) [6].

Electroforming

Electroforming [7] is generally used in microfabrication. Electrodeposition has already been used in the stent industry, in order to alter the surface morphology, to release drugs, to enhance radio-opacity

[6] These degradation rate were calculated from potentiodynamic polarization tests.

[7] "*Electroforming is the production of a thin metallic layer on a conductive substrate by electrolysis*" [22].

and also to prevent corrosion but never in biodegradable applications. This technique could lead to a more economic and energy saving way of producing thin layers, instead of ingots which thickness get progressively reduced. Typical stents strut thicknesses range between 75 to 200 μm. Investigation was thus made on electroformed iron foils of thickness of about 100-200 μm. The effect of different deposition parameters on mechanical properties, microstructure and degradation rate were studied. The electrolyte used was ferrous chloride-calcium chloride, a Ti6Al4V alloy [8] for the substrate (cathode) and Armco iron sheet as anode. The process parameters were such that the surface was not too rough and the foils were annealed at 550°C for 1h in order to decrease the internal stresses arising from electrodeposition. Grains of 6 μm average size were observed even after annealing. This can be seen on Figure 2.7 compared to Armco iron (40 μm on average). [22]

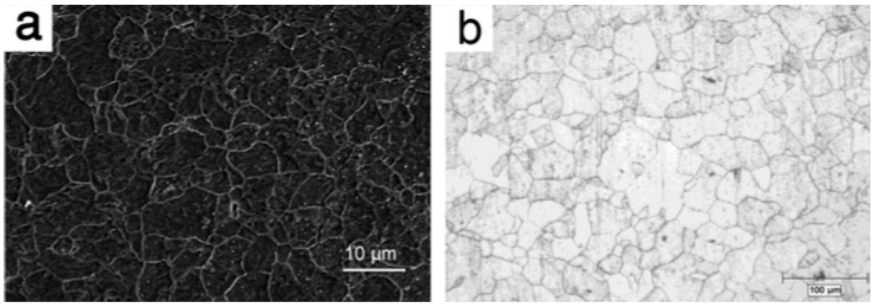

FIGURE 2.7: Microstructure of a) annealed electroformed iron and b) Armco iron [22].

Moravej et al. [22] investigated the feasibility of using this fabrication process for biodegradable stents. The substrate used was made of tin [9]. Once the tubes were electroformed, they were heated to 300°C in order to melt and remove the substrate. Surface roughness optimisation was done by grounding the samples. This also suppressed the residual tin traces. Laser cutting was subsequently performed followed by an annealing step at 550°C for 1h to relieve the residual stresses caused by electroforming and laser-cutting. Figure 2.8 shows the stent microstructure after the different fabrication stages. It can be seen that before annealing, the grains are columnar and become fine and equiaxed with average size of 5 μm. Mechanical properties could potentially be increased due to this finer grain size and the risk of strut breaking would be reduced. 10-12 grains is the minimal amount of grains that should be present in the wall thickness to prevent failure of the stent. The investigated electroformed iron sample with an average grain size of 5 μm and 100 μm wall thickness responds positively to the criteria. However, other studies on 316L SS showed that the requirement was not always achieved and thus stent failure could sometimes happen. [22]

2.3 Mechanical behaviour of twinning induced plasticity (TWIP) alloys

This section is mainly inspired from the article *High manganese austenitic twinning induced plasticity steels: A review of the microstructure properties relationships* [27].

Fe-22Mn-0.6C will be investigated, regarding its corrosion behaviour. This alloy belongs to the TWIP family, which presents excellent work-hardening properties resulting from mechanical twins induced by plasticity. These twins result in high strain-hardening due to their contribution as planar obstacles to

[8] This titanium alloy is the most common used titanium alloy and is also referred to as Grade 5. Its composition is as follows: 6% aluminium, 4% vanadium, maximum 0.25% iron and 0.2% oxygen [26].

[9] The melting temperature of tin is of 232 °C.

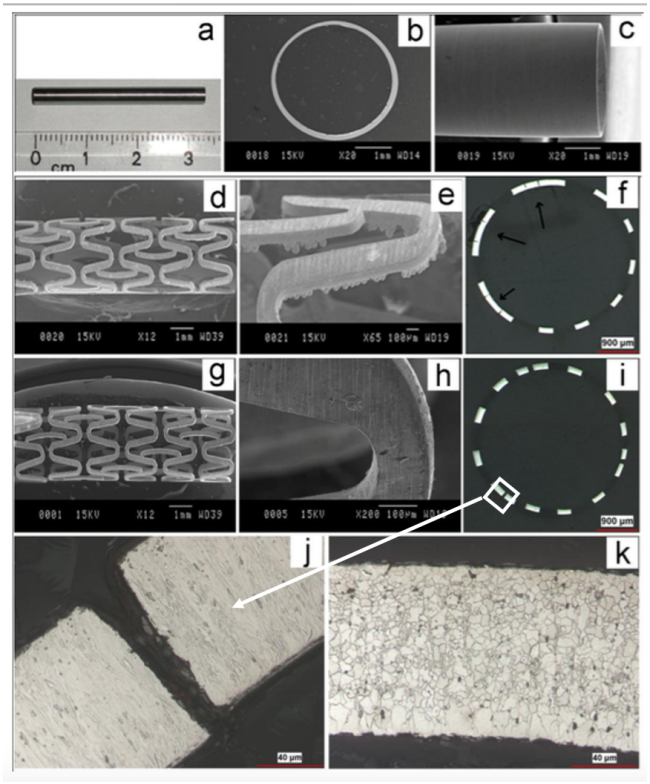

FIGURE 2.8: Microstructure of electroformed iron stents at different processing steps: (a-c) as ground minitube (d-f) as laser cut minitub (g-i) final stent (j) cross section of a laser cut minitube and (k) cross section of the stent after final annealing [22]

the dislocation glide. [28]

TWIP steels have been investigated frequently in the past few years due to the combination of their very good ductility (elongation) and strength as can be seen on Figure 2.9 which is a result of high strain-hardening capacities [29, 27]. They are austenitic (FCC) steels with above 20 wt.% manganese and small additions of carbon, silicon or aluminium, respectively less than 1 wt.%, 3 wt.% and 3 wt.% [30]. Hadfield steels are TWIP steels with manganese contents of 12-14%Mn and 1.2-1.5 % C [31]. In 1936, Tofaute and Linden shed the light on a necessary condition for such a steel to stabilize its austenitic structure:

$$wt.\%Mn + 13wt.\%C \geq 17 \tag{2.1}$$

In low stacking fault energy (SFE) FCC steels, twins are formed by collaborative glide of a/6 <112> partial Schockley dislocations on successive {111} planes and this results in high strain-hardening as twins are obstacles to dislocation glide. [29, 27].

Two main families (Fe-Mn-C and Fe-Mn-Si-Al) exist. The Fe-Mn-C family exhibit TWIP effect by presenting mechanical twins. The Fe-Mn-Si-Al family show either martensitic transformation (TRIP) or mechanical twins (TWIP). [28]

TRIP (Transformation Induced Plasticity) steels are steels where strain-hardening leads to ϵ-martensite transformation. The mechanism is the same as for TWIP steels: collaborative glide of partial dislocations on {111} planes. The austenite can also transform into α'-martensite but this transformation is not ruled by the stacking fault energy. Nevertheless, when the TWIP effect is more stable than

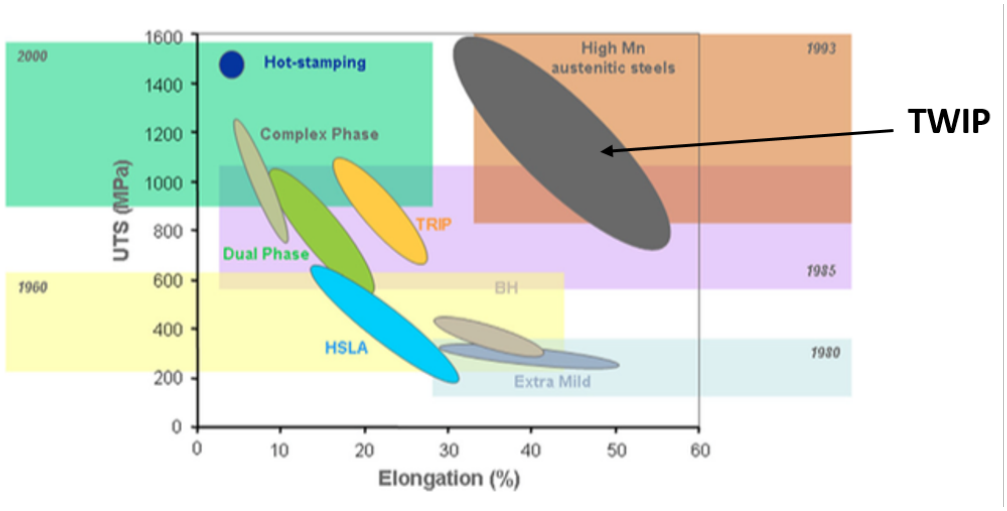

FIGURE 2.9: Fracture elongation in tension as a function of ultimate strength in tension for steels in automotive applications, where the years indicate the beginning of real development of these steels by steelmakers [27]

ϵ-martensite TRIP effect it is also more stable than the α'-martensite TRIP effect.

TWIP effect is observed when the SFE is situated between 20 and 40 mJ m^{-2}. The TRIP effect is observed when the SFE is lower than 20 mJ m^{-2}. And when the SFE is greater than 40 mJ m^{-2}, simple dislocation glide takes place [30, 32, 27, 33]. SFE increases with temperature and thus, depending on the transformation temperature, simple dislocation slip, TRIP or TWIP effect will be triggered. In the beginning of the 70's, Schumann attempted to correlate the chemical composition and the occurrence of strain-induced martensitic transformation. The following equation represents the austenite phase stability domain at 20°C with the limit corresponding to the apparition of the transformation induced martensite:

$$wt.\%Mn = -20wt.\%C + 32 \tag{2.2}$$

The difference in microstructures between mechanical twins and martensitic platelets in Fe-22Mn-0.6C can be seen on Figure 2.10. This steel is of importance in the current work as it will be studied in detail.

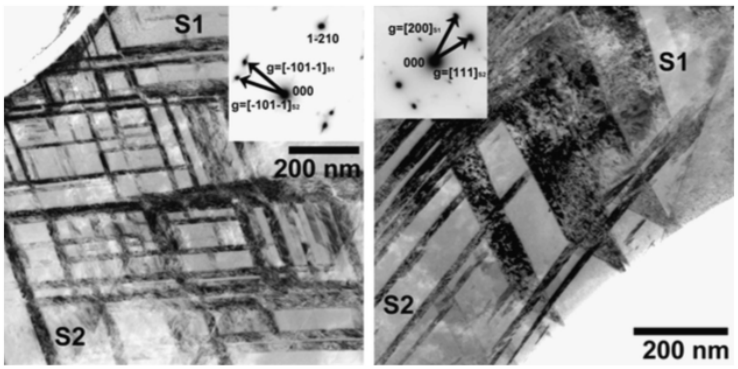

FIGURE 2.10: TEM images of the deformation microstructure of Fe-22Mn-0.6C at 77K (ϵ martensite) and room temperature (mechanical twins) [27].

It can be seen on Figure 2.11, that Fe-30Mn has a different response to deformation at room temperature: it does not form any mechanical twins but deforms only by dislocation glide. All the other compositions shown on that figure did present mechanical twinning as a response to deformation and this can be seen on Figure 2.12 for a Fe-22Mn-0.6C alloy.

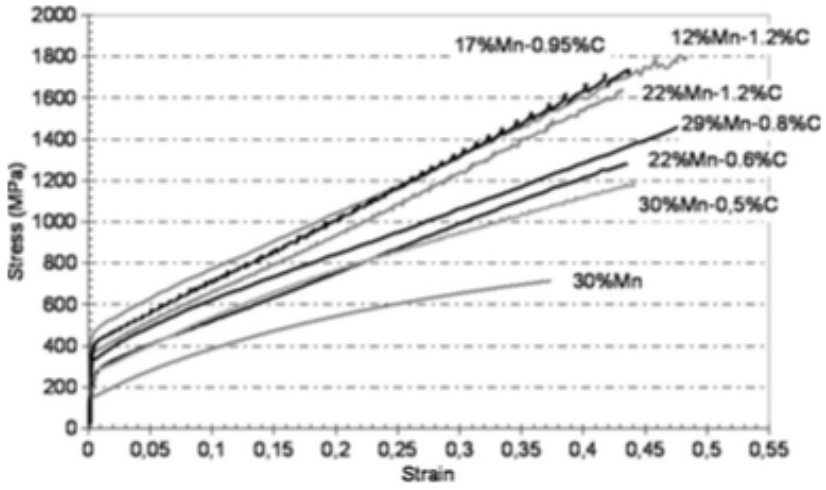

FIGURE 2.11: Tensile behaviour of TWIP steels with 20-40 μm coarse grains for different chemical compositions [27].

In conclusion, in order for the twinning mechanism to be activated, a fully austenitic phase and a stacking fault energy ranging between 20 and 40 mJ m^{-2} needs to be present and this is done by the addition of high amounts of manganese (between 18 and 30 wt.%) and smaller amounts of further alloying elements such as C, Si, Al, and N [33].

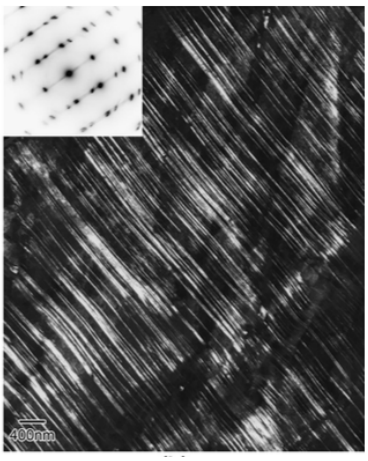

FIGURE 2.12: Dark field image of Fe-22Mn-0.6C after 50% strain showing mechanical twins [27].

2.4 Corrosion behaviour of metals

The subject of this Master's thesis is to determine the corrosion rates and corrosion mechanisms of Fe-22Mn-0.6C TWIP samples that underwent different deformations as well as Armco iron for comparison reasons. Therefore a detailed knowledge on corrosion mechanisms in iron and steel is needed.

This section is mainly inspired from the book *Corrosion for Science and Engineering* [34].

When iron corrodes in the presence of water it produces rust [35]:

$$2Fe + 2H_2O + O_2 \longrightarrow 2Fe(OH)_2$$

This outcome is the result of an anodic reaction, a cathodic reaction and a chemical reaction:

anodic reaction: $Fe \longrightarrow Fe^{2+} + 2e^-$
cathodic reaction: $2H_2O + O_2 + 4e^- \longrightarrow 4OH^-$
chemical reaction: $Fe^{2+} + 2OH^- \longrightarrow Fe(OH)_2$

And if there are Cl^- ions present, the anodic regions are further activated following this reaction:

$$FeCl_2 + 2H_2O \longrightarrow Fe(OH)_2 + 2HCl$$

The corrosion can take place following different manners:

2.4.1 Uniform corrosion

The most common corrosion is uniform corrosion. In this case, the whole surface (or a large part of it) is evenly attacked. During such corrosion, the material undergoes losses until it fails [35].

2.4.2 Galvanic corrosion

This corrosion type arises when two different metals are coupled under water (or other electrolyte) and connected by electrical contact. One of the metals will act as an anode and corrode faster than predicted if alone and the opposite is occurring for the other metal playing the role of the cathode [35].

Following factors affect galvanic corrosion [34]:

- Alloy composition: main constituents and impurities
- Electrode potential
- Reaction kinetics: metal dissolution, oxygen reduction polarisation curve and hydrogen evolution polarisation curve
- Protective film characteristics: pH, potential and solution dependence
- Mass transport: migration, diffusion, convection
- Bulk solution environment: temperature, flow rate, volume
- Bulk solution properties: conductivity, corrosivity, pH, oxygen content
- Geometry: area ratio, surface shape, distances involved, surface condition, number of galvanic cells

2.4.3 Selective corrosion

2.4.3.1 Grain boundary corrosion

At grain boundaries, atoms are thermodynamically less stable making them more subject to corrosion. Thus, investigating the grain size of a certain material is an important tool for corrosion understanding [34].

2.4.3.2 Intergranular corrosion

When precipitates are formed at grain boundaries, and cause these boundaries to be exposed to corrosive attack, one talks about intergranular corrosion. These precipitates can either act cathodic or anodic to the rest of the metal and their presence causes the formation of small localized galvanic cells when the metal is put in presence of an electrolyte. If the precipitates are acting anodic to the rest of the material, the precipitates will dissolve and create porosity in the material. If now they act cathodic to the rest of the material, they will enhance the corrosion of that material. Either way, precipitates weaken the material. Such corrosion is mostly found in austenitic stainless steels, aluminum alloys but also in ferritic stainless steels and nickel-based corrosion-resistant alloys [34].

2.4.3.3 Selective leaching

Similar to intergranular corrosion, selective leaching occurs when an element of an alloy corrodes and dissolves. This type of corrosion is referred as **desalloying**. The principle is the same as previously, one compound is playing the role of the anode and the material is left porous, losing all its mechanical strength. When localized, it can perfore the material. In such corrosion cases, temperature and differential aeration are very important. Brass and copper alloys are the most subject to such corrosion [34].

2.4.3.4 Microbiologically Induced Corrosion (MIC)

In cases where MIC is governing the corrosion process, microbes or biological organisms are responsible for it. The microbes are categorized regarding the by-products they form or the compounds that they affect, e.g. sulfur oxidizing bacteria. They can be aerobic or anaerobic. [35]

Biofouling on ship hulls is quite common where macrospecies such as weed, barnacles and mussels deposit and become a micro-habitat for bacterial species. Fungi and algae can cause localized corrosion such as pitting due to catalyze of differential aeration and concentration cells. For example, microbes can excrete organic acids, which will lower the pH and enhance corrosion. Due to the small size of microbes, it is rare hat these are responsible for uniform corrosion. The best way to control MIC is by the use of biocides. [34]

When interested in iron and steel corrosion, the most affecting bacteria is the sulphate-reducing bacteria (anaerobic). They reduce sulphate ions into sulfide ions, which are very corrosive. These bacteria can be present in any industrial system. Additionally, they are very resistant to biocides and are favoured under a pH range of 5-10. [34]

2.4.3.5 Pitting and crevice corrosion

Up to now, electrolytes of homogeneous composition were considered. But when the electrolyte is of heterogeneous composition (changes in oxygen or electrolyte concentration), the corrosion behaviour can be affected. What is meant by a heterogeneous composition is that, for example, oxygen can get concentrated at specific spots and not be present around other areas, resulting in heterogeneous oxygen

concentration throughout the electrolyte. Two examples of corrosion where this is the case are pitting and crevice corrosion.

Crevice corrosion

This kind of corrosion is also localized, occurring when the sample is in presence of a stagnant solution under a small crevice. In close proximity to the stagnant volume, the corrosive effect can be much more pronounced than in contact with the bulk solution. Stainless steel, usually very corrosion resistant, can undergo severe damage due to crevice corrosion [34]. Examples of systems where crevice corrosion can arise are for examples samples where crevices under disbonded coatings, insulation materials or surface deposits are present [35]. This type of corrosion very much depends on the geometry of the sample, giving rise to a heterogeneous distribution of the species dissolved in the electrolyte setting the local attacks in motion.

Pitting corrosion

In such cases, the corrosion is localized and renders the design and prediction of corrosion much more difficult. It is taking place when the passive film (oxide layer) that has been formed on the metal breaks. Failure of a whole material can occur when a narrow pit of corrosion is formed even when the overall mass loss is very small and as pits get covered by the corrosion products it gets difficult to determine such a corrosion process and thus to take account of these early failures [35]. It is quite similar to crevice corrosion except for the initiation step. Indeed, as mentioned in previous paragraph, crevice corrosion arises from a heterogeneous oxygen concentration repartition. Pitting corrosion, on the other hand, arise from metallurgical factors and is initiated on plane surfaces. Different structures of pits can be observed on Figure 2.13.

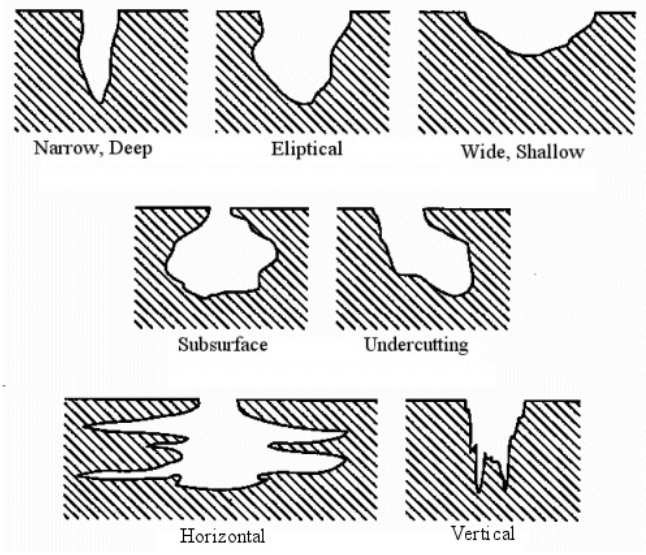

FIGURE 2.13: Different structures of pits [36].

Pits can be repassivated if the material contains alloying elements such as Cr and especially Mo. Once repassivated, the pit is healed and no further pitting occurs. On the other hand, inclusions such as MnS trigger pitting. When differential aeration conditions are present, pits can occur at the anodic area and this is explained in the following paragraph. [36, 34]

Pitting corrosion due to differential aeration under a water droplet

When steel is in presence of rain, pits occur due to differential-aeration corrosion. First, general corrosion occurs underneath the wetted area; probably due to grain boundary effect. The cathodes are consuming oxygen and thus an oxygen gradient takes place within the electrolyte. And the areas near the electrolyte/air interface are more easily replenished by air than the areas far away from this interface. This oxygen concentration gradient will trigger the anodic reaction to take place in the central area and the hydroxyl ions generated at the cathode area (thus at the electrolyte/air interface) will diffuse inwards to react with the iron ions that diffuse outwards producing rust around the pit. This mechanism can be seen in Figure 2.14. [34]

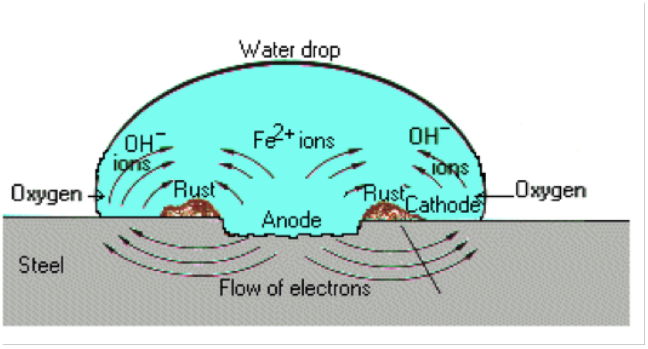

FIGURE 2.14: Corrosion mechanism in a differential-aeration cell [37].

2.4.4 Flow induced corrosion

For blood in arteries and for a lot of other electrolytes, the material is surrounded by a constantly flowing electrolyte, giving rise to flow-induced corrosion. Under laminar flow, the flow layer closest to the sample has the slowest velocity as the friction forces are the most present, while the upper flow layer has the maximum velocity. [34]

As will be seen in section 2.5, under stagnant electrolyte conditions, an equilibrium is reached at which the anodic and cathodic processes are occurring at the same rate, giving rise to the double electric layer at the metal vicinity. This is not the case when the electrolyte is flowing around the sample, as it removes the metal ions and no equilibrium can be established, leading to an increased rate of corrosion. When under neutral pH (as is the case in the human body), oxygen is constantly replenished and thus the corrosion rate is also increased. On the other hand, the oxygen replenishment can decrease the presence of differential-aeration cells leading to a more uniform corrosion. In materials where an oxide film is protecting them from corrosion attacks, the oxygen replenishment also helps maintaining this oxide layer and reducing the risk of local corrosion pitting. However, aggressive ions (such as chloride and sulphide ions) can also be replenished leading to more severe corrosion attacks. Finally, if solid particles are present in the electrolyte, they can also scour away protective layers and at the same time prevent dirt to deposit on the material protecting it from crevice corrosion. [34]

2.4.5 Stress-corrosion cracking (SCC)

Stress-corrosion cracking occurs when static tensile stresses and specific environments lead to intergranular or transgranular cracking. It has, for example, occurred that materials, known for their good corrosion resistance, have failed at stress levels below their normal fracture stress due to SCC [34].

Nevertheless, there is no such thing as a single mechanism of SCC but Parkins [38] proposed a stress-corrosion spectrum, listing the important alloy/environment combinations and the involved mechanism features which can be seen on Figure 2.15. Following, is a summary of the main features of SCC [34]:

- Stress and corrosion must both be present in order for SCC to take place. The stress can be applied throughout the material lifetime or during the fabrication process.
- Generally, alloys are more keen to SCC than pure metals.
- The cracking will occur due to only a few chemicals in the environment and these need to be present in significant quantities.
- Under the same environmental conditions as the previous point, an alloy exempt of stresses would not fail due to cracking.
- Even the most ductile material would suffer a brittle fracture under SCC.
- A threshold under which a material cannot suffer SCC can be determined.

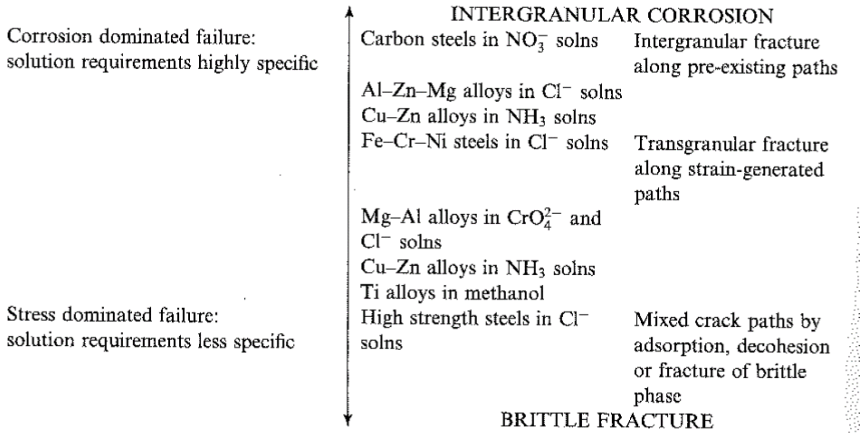

FIGURE 2.15: Stress-corrosion spectrum after Parkins [34].

2.4.6 Temperature effect on corrosion

In oxygen diffusion controlled corrosion, the corrosion rate doubles when the temperature increases of 30°C up to 80°C where the corrosion rates falls due to the smaller oxygen solubility at higher temperatures, which overshadows the accelerating effect of temperature. This is only valid in open systems. If the system is closed, no oxygen can escape and the corrosion rate keeps increasing until the entire oxygen is consumed [39].

2.4.7 Controlling corrosion by changing the environment

In aqueous environments, the electrolyte can be modified in order to accelerate the corrosion rate by either increasing the ionic conductivity, decreasing the pH, uniformly increasing the oxygen content or changing the temperature. When trying to protect materials in such environments, which is not sought in this work, by adding calcium or magnesium a thin scale can grow on the material protecting it from further corrosion. But this thin layer can be worn out due to the flow, exposing the material to a potential corrosive environment again. In order for such a scale to form, a minimum amount of carbon dioxide needs to be present in order to form bicarbonate ions which will react with the calcium present in the solution. If the carbon dioxide amount is too low, the scale will dissolve in acidic solutions, leaving the material unprotected. [34]

2.4.8 Summary of corrosion factors in aqueous environments

Following elements have to be taken into consideration when trying to understand corrosion mechanisms and behaviours of steels [34] in an environment such as an artery:

- **Chloride ions**: Chloride ions are excessively corrosive to most steels.
- **Electrical conductivity**: By increasing conductivity, corrosion possibilities are increased as it allows anodes and cathodes to operate over longer distances.
- **Oxygen concentration**: As corrosion for most steels is cathodically controlled, increasing the oxygen content of the electrolyte also increases the corrosion rate.
- **Temperature**: Corrosion is normally increased when the temperature is raised. However, an increase in temperature can also lead to protective scale to deposit when in presence of salts which reduces the corrosion rate. An increase in temperature can also lead to a decrease in oxygen content, decreasing the corrosion rate.
- **Biofouling**: Bacteria can play a role in corrosion as has been explained in the MIC section.
- **Stress**: Stresses can accelerate corrosion in certain cases.
- **Sulfides**: Sulfides are not normally present in blood but the experiments undertaken in the laboratory for this present work will mostly use HEPES buffer containing sulfur. Sulfides highly accelerate corrosion, which is why this needs to be kept in mind. Indeed, *Deyab et al.* showed that sulfide increased pitting due to the auto-catalytic effect of SH^- [40].
- **Film formation**: Calcium and magnesium salts can form thin scales, altering the amount of oxygen that can diffuse to the metal and this lowers the corrosion rate.
- **Alloying elements**: Up to 0.3%, copper decreases pitting corrosion of steels leading to a lighter uniform corrosion. Large additions of chromium increase the corrosion resistance. Vanadium as well as molybdenum are beneficial for SCC resistance.

2.5 Theory behind electrochemistry

In order to study the corrosion mechanisms and corrosion rates, a detailed knowledge of the electrochemical aspect of corrosion reactions is needed, where the thermodynamics as well as kinetics aspect will be detailed in this section. The three-electrode cell, which is typically the cell used to measure electrochemical behaviours, will be presented and its working principles explained.

This section is mainly inspired from the book *Corrosion for Science and Engineering* [34].

2.5.1 Thermodynamical aspect

In order for corrosion to take place, four components need to be present, namely the anode, the cathode, the electrolyte and the connections. Indeed during a corrosion process, electrons are flowing from the anode to the cathode as can be seen on Figure 2.16 and corrosion occurs when there is a net release of Gibb's free energy across the metal/electrolyte interface. The anodic half-reaction taking place is expressed as following:

$$M \longrightarrow M^{z+} + ze^-$$

And the cathodic half-reaction could either be involving the reduction of another metal from its ions:

$$M^{z+} + ze^- \longrightarrow M$$

or it could also be involving the reduction of hydrogen or oxygen:

$$2H^+ + 2e^- \longrightarrow H_2$$
$$2H_2O + O_2 + 4e^- \longrightarrow 4OH^-$$

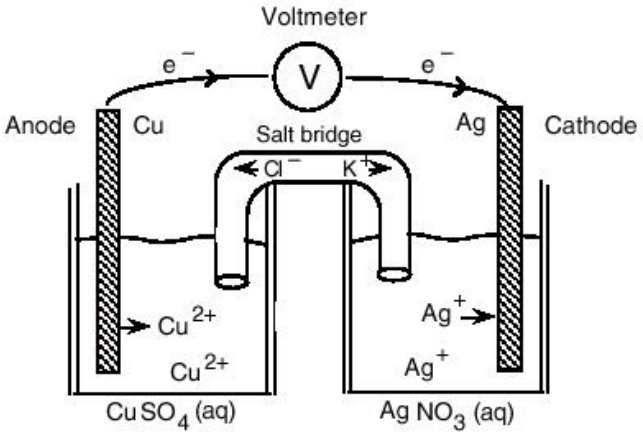

FIGURE 2.16: Illustration of an electrochemical cell [41].

Upon inspection of the thermodynamical aspect of metals, it is found that they are formed from oxides found in nature. These oxides are thermodynamically more stable than the metal, which needs a high energy supply in order to be produced. By looking at Gibb's free energy profiles of most metals and their oxides, it can be seen that the free energies of most metals are higher than the free energies of the corresponding oxides. Additionally, once a metal is formed, it will, in most cases, thermodynamically change towards corrosion products that have a lower Gibb's free energy than the metal. These corrosion products are different from the ore and the transition from the metal to its corrosion products, i.e. the rate of corrosion, strongly depends on the size of the energy barrier: the Gibb's free energy of activation. These transformations can be seen on Figure 2.17. The rate of a reaction can be formulated as:

$$v = k_{corr}[reactants] \tag{2.3}$$

with

$$k_{corr} = A \exp\left(\frac{-\Delta G^*}{RT}\right) \tag{2.4}$$

k_{corr} is the rate constant, ΔG^* is the Gibb's free energy of activation, R is the universal gas constant, T is the temperature and A is a constant. [34].

By examining first the thermodynamics of corrosion, it can be found that most metals already possess a corroded thin layer on their surface. Metals have on their surface an invisible oxide layer that protects it from the environment and thus from further corrosion. This layer can either be protecting the whole metal, like it is the case for aluminum, or it could only protect the metal surface at some places allowing the metal to corrode at other places. This oxide layer could also be attacked, making it lose its protective character. [34].

Precious metals don't corrode. This can be due to the fact that the Gibb's free energy of the reaction involving the transformation of the metal into the corresponding oxide is positive as it is the case for gold [34]:

$$Au + \frac{3}{2}H_2O + \frac{3}{4}O_2 \longrightarrow Au(OH)_3 \quad ; \quad \Delta G^\circ = 66kJ/mol$$

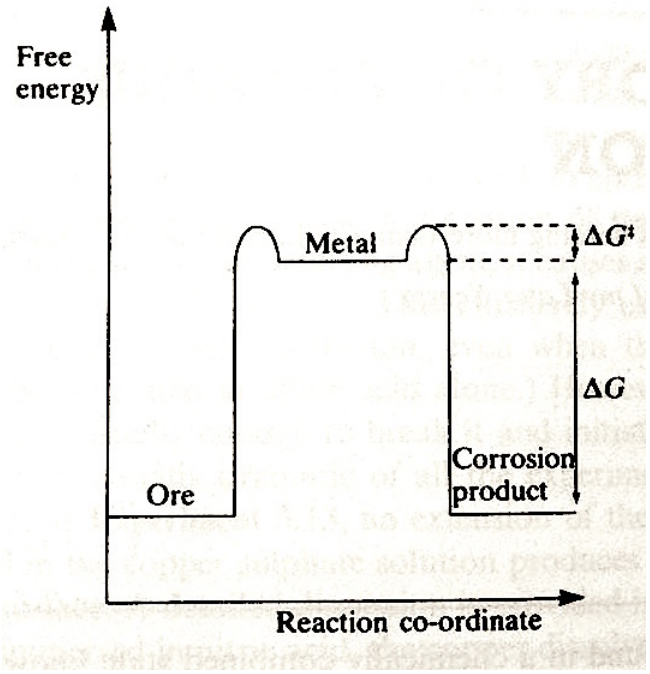

FIGURE 2.17: Gibb's free energy of a metal and its ore and corrosion products [34]. ΔG is the difference in Gibbs's free energy between the corrosion products and the metal. ΔG^+ is the activation energy that needs to be overcome before the metal can dissolve into its corrosion products.

Another explanation could be that the Gibb's free energy of activation is too high for it to be overcome [34].
Corrosion is dependent on the temperature and the Gibb's free energy of a corrosion reaction can be calculated using the following fundamental thermodynamic equation [34]:

$$\Delta G = \Delta G^\circ + RTlnQ \tag{2.5}$$

where Q is equal to the equilibrium constant when the system is in equilibrium, i.e. $\Delta G = 0$. In other words, for a standard half-reaction:

$$Ox + ze^- \longrightarrow Red$$

with Ox the oxidizing agent and Red the reducing agent.

$$Q = \frac{a_{Red}}{a_{Ox}a_{e^-}} \tag{2.6}$$

with a_i the activity of specie i and equal to [42]:

$$a_i = \gamma_i \frac{m_i}{m^\circ} \tag{2.7}$$

where γ_i is the activity coefficient, m_i is the molality and m° is the standard concentration 1 $\mathrm{mol\,kg^{-1}}$ (very close to 1 $\mathrm{mol\,dm^{-3}}$ in aqueous solution).

These Gibb's free energy changes can be measured as electrical potentials and flow of current and they can be related by Faraday's Law [34]:

$$\Delta G = -zFE \tag{2.8}$$

where z is the number of electrons exchanged during the process, E is the potential in volts and F is Faraday's constant and is equal to 96,500 coulombs per mole [34, 3].

For the reaction to be spontaneous, the Gibb's free energy needs to be negative and hence the potential measured needs to be positive. By substituting equation 2.8 into equation 2.5, the following relation is obtained [34]:

$$-zFE = -zFE^{\circ} + RTlnQ \tag{2.9}$$

Dividing each term by zF, the equation becomes the **Nernst equation**:

$$E = E^{\circ} - \frac{RT}{zF}lnQ \tag{2.10}$$

By converting the logarithms to the base 10 and by using the standard temperature, 298K, the equation simplifies to:

$$E = E^{\circ} - \frac{0.059}{z}logQ \tag{2.11}$$

This is a very important equation, allowing to find the theoretical potential that can be obtained from the cell.

In order to compare the different potentials between them, they are all measured against a standard electrode, which potential is set to zero: the standard hydrogen electrode (SHE). From there, a table is obtained (Figure 2.18). This table contains the standard reduction potentials that are independent of the used electrolyte [34]. However, the use of the standard hydrogen electrode in practical experiments is quite difficult. This is why other reference electrodes might be used such as the saturated calomel electrode (SCE), which has a standard electrode potential of +0.242V at 25°C. This electrode insures a constant and well-defined potential and is made of mercury(I)chloride: Hg_2Cl_2 in combination with a solution saturated in chloride ion. As can be seen on Figure 2.19, the saturated calomel electrode consists of two glass tubes [34]:

- A smaller glass tube contains a platinum wire connected to a sample of mercury and mercury(I)chloride.
- A larger glass is filed with a saturated KCl solution and KCl crystals.

Porous plugs holds this setup together and allow the ions to flow while avoiding cross-contamination with the test electrolyte [34].

2.5.1.1 Pourbaix diagram

A further step is to study the stability of a certain specie as a function of the potential and the pH. Depending on these two factors, it can be shown if a specie will be corroding under certain conditions or be granted immunity: if the metal ions concentration in solution exceed 10^{-6} M, the metal will corrode but not if the concentration is less than this threshold.

Also, up to now it has been assumed that when a metal corrodes it releases ions in solution. But some corrosion products do not dissolve in solution (such as oxides) and most frequently form films on the metal surface, hindering an electrolyte/metal contact and granting the metal passivity. Nevertheless, if the film formed is not uniform or is conducting and permeable to ions or even if it is damaged then corrosion can still take place, probably following a pitting mechanism (which will be explained later) as the exposed anode area is made smaller than before formation of that film. Pourbaix found a way to correlate the behaviour of a metal depending on the potential and pH. E/pH charts, also known as Pourbaix diagrams came alive. They are based on Nernst equation and solubility data. By analyzing the Pourbaix diagram of iron, it can be seen that the possible phases are: Fe, Fe^{2+}, Fe^{3+} and Fe_2O_3,

Metal and Reaction	Potential E^0 (V)
$Al \rightarrow Al^{3+} + 3e^-$	−1.706
$Zn \rightarrow Zn^{2+} + 2e$	−0.763
$Cr \rightarrow Cr^{3+} + 3e^-$	0.744
$Fe \rightarrow Fe^{2+} + 2e^-$	−0.409
$Cd \rightarrow Cd^{2+} + 2e^-$	−0.401
$Ni \rightarrow Ni^{2+} + 2e$	−0.230
$Pb \rightarrow Pb^{2+} + 2e$	−0.126
$H_2 \rightarrow 2H^+ + 2e^-$	0.000 by definition
$Ag + Cl^- \rightarrow AgCl + e$	+0.223
$2Hg + 2Cl^- \rightarrow Hg_2Cl_2 + 2e^-$	+0.268
$Cu \rightarrow Cu^{2+} + 2e$	+0.340
$Cu \rightarrow Cu^+ + e$	+0.522
$Ag \rightarrow Ag^+ + e$	+0.799
$Au \rightarrow Au^{3+} + 3e^-$	+1.420
$Au \rightarrow Au^+ + e^-$	+1.680

FIGURE 2.18: Nernst table of some half-reactions with the most anodic components on top of the table and most cathodic components on bottom of the table [43]. The standard electrode potential of the Mn^{2+}/Mn system is -1.185 V.

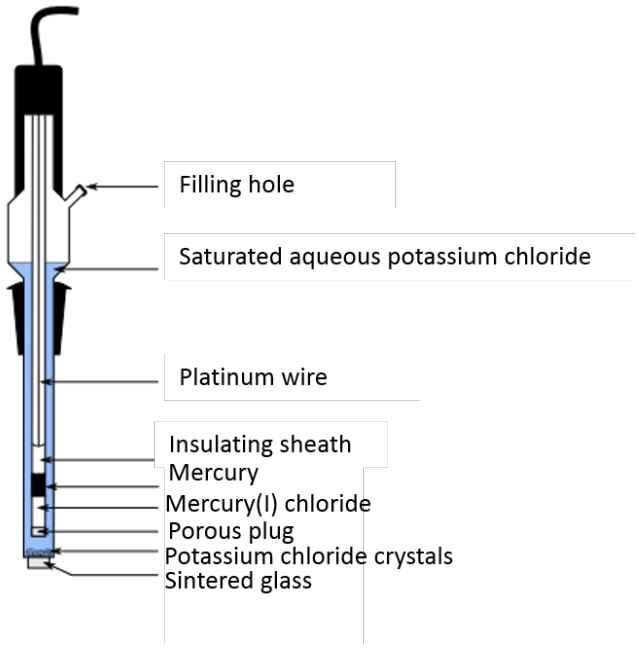

FIGURE 2.19: A saturated calomel electrode inspired from [44].

Fe_3O_4 in a dry cell or $Fe(OH)_3$ and $Fe(OH)_2$ in a wet cell (these hydroxydes are in metastable equilibrium with the oxides). In a Pourbaix diagram such as the ones illustrated in Figure 2.20, a horizontal line represents a reaction that is pH independent but potential dependent and thus an electron transfer is taking place. On the other hand, a vertical line represents a pH dependent reaction but potential independent with no electron transfer.

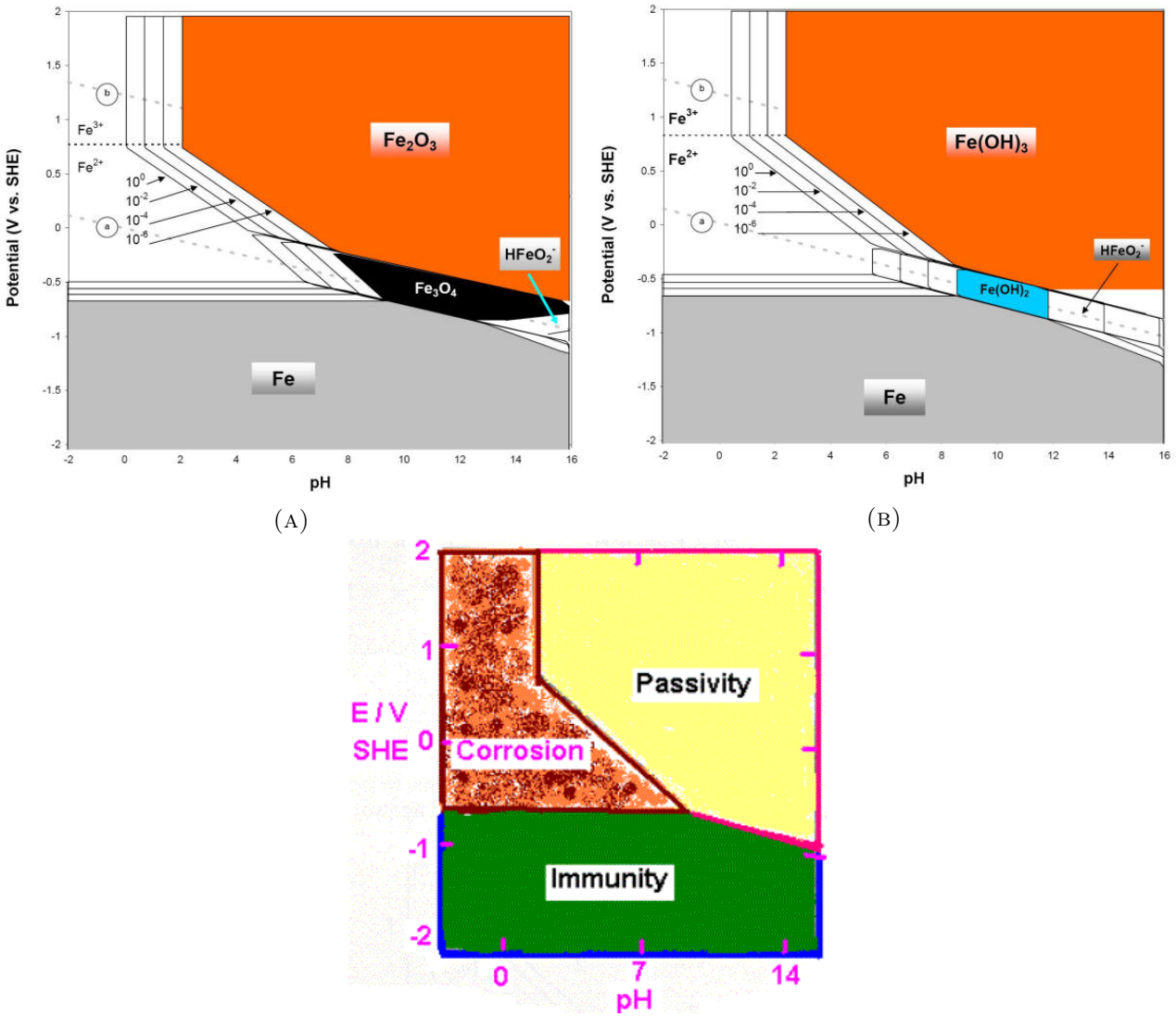

FIGURE 2.20: Pourbaix diagram of iron or steel at 25°C illustrating (A) wet corrosion products, (B) dry corrosion products, and (C) the passivation/immunity/corrosion regions [45, 46].

The different equilibria shown on Figure 2.20 can be calculated. As an example, the Fe^{3+}/Fe_2O_3 and Fe^{2+}/Fe_2O_3 equilibria will be presented [47]:

Fe^{3+}/Fe_2O_3 equilibrium: $2Fe^{3+} + 3H_2O = Fe_2O_3 + 6H^+$

The oxidation stage of all reactant components are unchanged in the products. Therefore, no electron transfer is taking place and the reaction will be represented by a vertical line in the Pourbaix diagram. The reaction constant is given by:

$$K = \frac{a_{H^+}^6}{a_{Fe^{3+}}^2} \tag{2.12}$$

This reaction constant can be calculated by using $\Delta G^\circ = -RTlnK$ and as $\Delta G^\circ = -8240\,\mathrm{J\,mol^{-1}}$ and by assuming an ion concentration of 10^{-6}M, the vertical line equation is:

$$pH = 1.76 \tag{2.13}$$

On the left of that vertical line, it is the stability domain of Fe^{3+} ions and on the right of Fe_2O_3.

Fe^{2+}/Fe_2O_3 equilibrium: $Fe_2O_3 + 6H^+ + 2e^- = 2Fe^{2+} + 3H_2O$

Nernst equation for this reaction is as following:

$$E = E^\circ - 2.303\frac{RT}{zF}log\left(\frac{a^2_{Fe^{2+}}}{a^6_{H^+}}\right) \tag{2.14}$$

where $E^\circ = 0.728V$ and, again, if an ion concentration of 10^{-6}M is assumed, the line equation is as follows:

$$E = 1.082 - 0.178pH \tag{2.15}$$

It has to be kept in mind that these E-pH diagrams are only giving thermodynamical information and it will be seen that the kinetics of the reactions are greatly important as well. Environmental factors also influence corrosion, such as changes of flow rates, oxygen concentration, pressure, temperature and many other factors. Finally, the presence of counter-ions in the electrolyte that could interfere with water also change the shape of the corresponding E-pH diagram. Therefore, these diagrams need to be used very carefully while always keeping in mind that the situation on paper will not necessarily be representative of what will happen on the field.

2.5.2 Kinetics of corrosion

When looking at corrosion reactions that are not in equilibrium, current is flowing and when current flows through the electrochemical cell, the potential is reduced. This is due to the "Le Chatelier's Principle": the anodic potential becomes less negative while the cathodic potential becomes less positive when current flows through the cell [34]. The thermodynamical aspect of corrosion only gives information on the tendency of a certain system to undergo corrosion or not but in order to have an understanding of the **rate of corrosion**, the relationship between current and potential must be fully understood [34].

When examining the corrosion kinetics, current densities (i) instead of currents (I) need to be taken into account. As a matter of fact, a smaller sample will corrode faster than a bigger one.

By examining a metal sample placed in an electrolyte, corrosion will take place if there is enough energy in the environment to overcome the barrier potential. Once the barrier is overcome, the dissolution of metal into M^{z+} ions will start. The Gibb's free energy profile resembles then the one on Figure 2.21a. It has also been seen that a metal can act as an anode, a cathode and electrical connection all in once. Indeed, due to micro-variations in the solid, some parts can act anodic to others. [34]

The ions formed can "*pass back over the energy barrier*" [34] and transform back into a metal. Here the rate of reaction is not only governed by the energy barrier but also by the free energy that was released during the oxidation of the metal. These two reaction rates (of the forward and backward reactions) will become equal as the difference in Gibb's free energy between the metal and its corrosion products decreases and eventually becomes zero, establishing an equilibrium. The Gibb's free energy profile is now similar to the one in Figure 2.21b. When equilibrium is reached, the anodic current density (i_a) is equal to the cathodic current density (i_c) and no net current is flowing through the system. This equal current density is called the exchange current density (i_0). This equilibrium can be represented as followed:

$$M \rightleftharpoons M^{z+} + ze^-$$

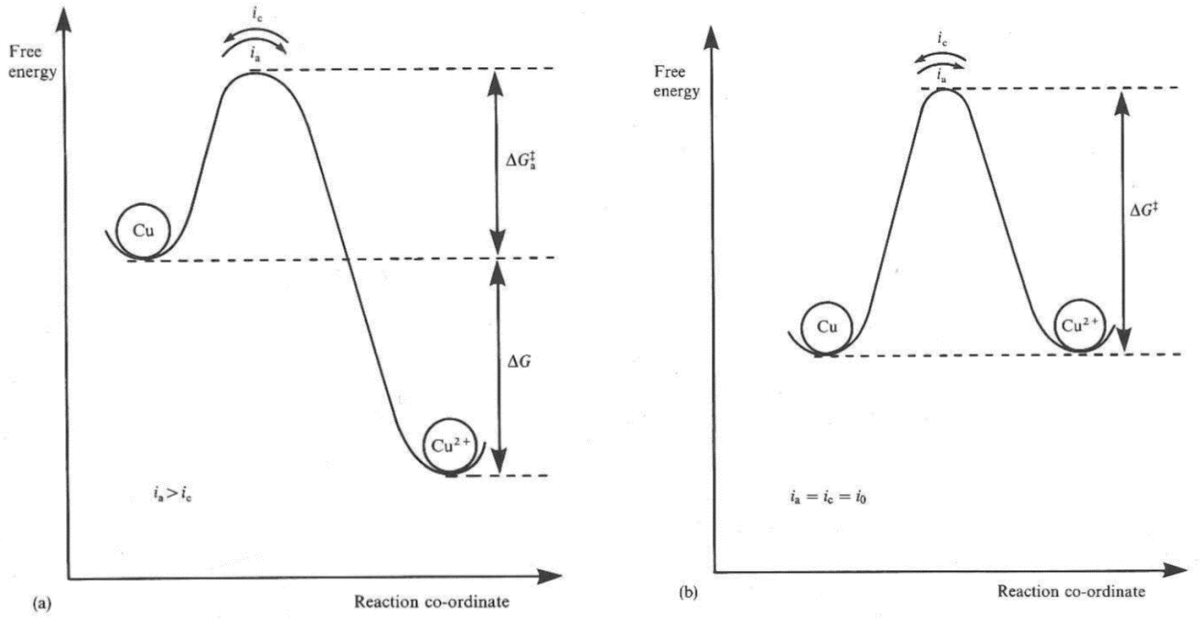

FIGURE 2.21: Energy profile of copper in pure water (A) when oxidation takes over reduction (i.e. $i_a > i_c$) and (B) when equilibrium is reached (i.e. $i_a = i_c$) [34]

When a piece of metal is immersed in an electrolyte, the ions are not distributed homogeneously throughout the electrolyte. This gives rise to the double layer which is composed of a compact layer (the Helmholtz layer) where the potential varies linearly with the distance from the electrode and a diffuse layer (the Gouy-Chapman layer) where the potential varies exponentially. This can be seen on Figure 2.22.

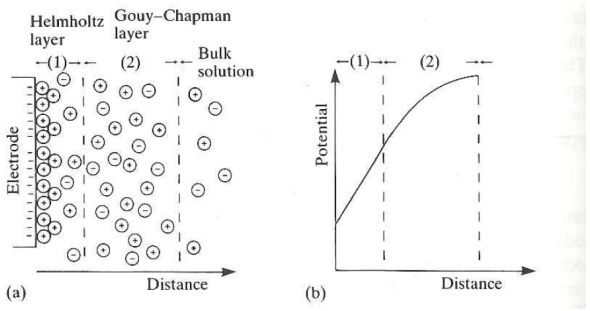

FIGURE 2.22: (a) the distribution of ions as a function of distance away from an anode and (b) variations of potential with distance for the model illustrated in (a) [34].

By using **Faraday's Law of Electrolysis**, the total amount of charge passing through the circuit can be found:

$$Q = zFM \tag{2.16}$$

where M is the number of moles of material that have been ionized.

When differentiating equation 2.16 with respect to time, following expression is deduced:

$$\frac{dQ}{dt} = zF\frac{dM}{dt} \tag{2.17}$$

By further dividing each term by the cross-section, one gets:

$$i = zFJ \tag{2.18}$$

where J is the flux of substance, also known as the corrosion rate per unit area. Thus, the corrosion rate of a metal can be calculated thanks to the current density measured through the circuit. The unit mostly used in order to define the corrosion rate is mmpy (millimeters per year) and the conversion from $\mathrm{A\,m^{-2}}$ into mmpy can be made using following equation [48]:

$$v_{corr} = \frac{3272 \cdot i_{corr} \cdot EW}{\rho} \tag{2.19}$$

where v_{corr} is the corrosion rate, EW is the equivalent weight in grams per equivalent [10], the corrosion current density units are A $\mathrm{cm^{-2}}$, and the density is given in g $\mathrm{cm^{-3}}$.

Nevertheless, these corrosion rate calculations cannot be used when localized corrosion, such as pitting and crevices, takes place. In these cases, corrosion can be very rapid and pronounced over small areas of the material and the corrosion rate can also vary over long periods. Localized corrosion can be studied using the *ASTM G61: Standard Test Method for Conducting Cyclic Potentiodynamic Polarization Measurements for Localized Corrosion Susceptibility of Iron-, Nickel-, or Cobalt-Based Alloys*. The susceptibility of a metal to undergo localized corrosion will be illustrated by a rapid increase of anodic current for a small potential change. Localized corrosion is often taking place in chloride solutions and in the scope of this work, Simulated Body Fluid (SBF) will be used to carry out the experiments and chlorine is contained in this electrolyte. However, no tests using this standard were carried out for this thesis but should be made for further experiments regarding the corrosion of iron based alloys for bioresorbable stent applications.

2.5.2.1 Overpotential and Butler-Volmer relation

When a metal immersed in an electrolyte is not in equilibrium with its ions, the difference between its potential and its equilibrium potential is known as the overpotential η, which is an interesting factor for determining the rate of corrosion. Under equilibrium conditions, the rate of corrosion is equal to the exchange current density $i_0 = i_a = i_c$.

In order to study the corrosion rates, equations 2.3 and 2.4 need to be employed again. The rate of the oxidation reaction is thus:

$$v_{ox} = A_0 \exp\left(\frac{-\Delta G^*}{RT}\right) \tag{2.20}$$

where $A_0 = A \cdot [reactant]$. In fact, most of the time, the reactants concentration can be considered constant.

On the other hand, the rate of the reduction is here:

$$v_{red} = A_1 \exp\left(\frac{-(\Delta G^* + \Delta G)}{RT}\right) \tag{2.21}$$

[10] The equivalent weight of pure elements is calculated as the atomic weight of the element divided by the number of electrons required to oxidize an atom of the element, i.e. the element valence.

where $A_1 = A \cdot [products]$

It has already been said that when the M/M^{z+} system is in equilibrium, the free energies of the metal and its ions are equal but as soon as the equilibrium is broken, the free energies differ. The free energy of the metal will increase whereas the free energy of the environment will decrease resulting from an anodic polarization of the metal and a cathodic polarization of the environment. The equilibrium and non-equilibrium situations are illustrated, again, on Figure 2.23.

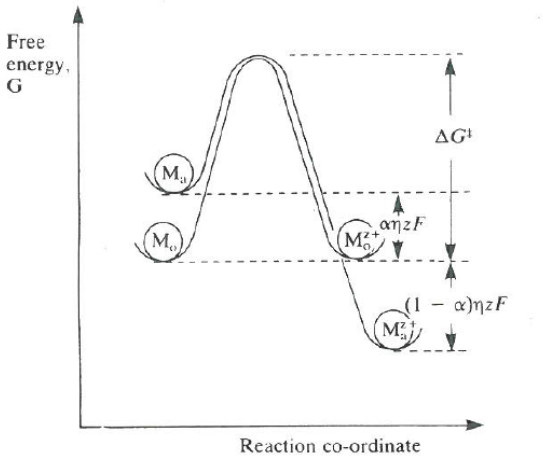

FIGURE 2.23: Energy profile of an anode at equilibrium (M_0/M_0^{z+}) and undergoing an anodic activation polarisation of E (M_a/M_a^{z+}) [34].

Under an applied potential "E", the free energy between the environment and the metal will be changed by an amount -zFE. But this potential will not only change the free energy ΔG but also the activation energy and the position of the maximum of energy with respect to the surface [49]. It is assumed that this applied potential acts over a finite distance, known as the electric double layer, and the transition can lie anywhere across that layer [49]. This is why a symmetry factor α will be used in order to define where the maximum energy state lies across the double layer [49]. As a simplified fact, we will consider a favoured reduction reaction as illustrated on Figure 2.24.

From there, the rate constants of the reduction and oxydation when an applied potential is present can be found using equations 2.20 and 2.21 but this time, reduction and oxidation are reversed:

Reduction rate constant:

$$k_{red} = A \exp\left(\frac{-(\Delta G^* + \alpha zFE)}{RT}\right) \tag{2.22}$$

Oxidation rate constant:

$$k_{ox} = A \exp\left(\frac{-(\Delta G^* + \alpha zFE + \Delta G - zFE)}{RT}\right) \tag{2.23}$$

When only the chemical energies were taken into account (**without the applied potential**), equations 2.20 and 2.21 were obtained. As a reminder:

Reduction rate constant:

$$k_{red,ch} = A \exp\left(\frac{-\Delta G^*}{RT}\right) \tag{2.24}$$

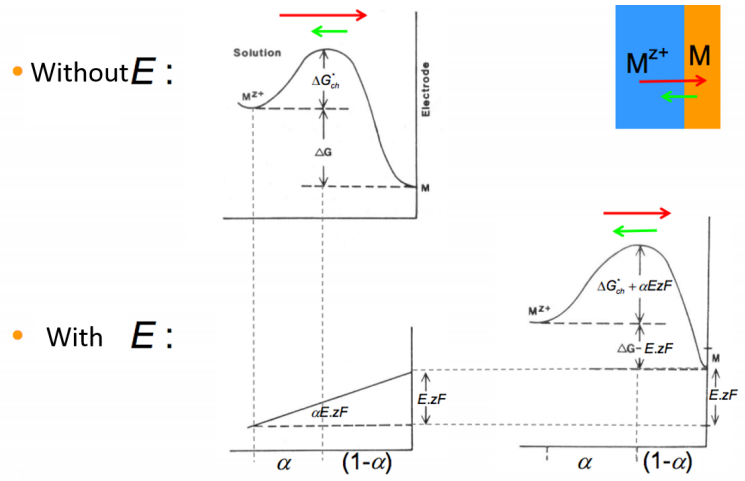

FIGURE 2.24: Energy-distance curves for reactions taking place at an electrode surface without addition of an applied potential (top left figure) or in the presence of an applied potential (bottom right figure). The bottom left figure represents the potential gradient over the system. Inspired from [49].

Oxidation rate constant:

$$k_{ox,ch} = A \exp\left(\frac{-(\Delta G^* + \Delta G)}{RT}\right) \tag{2.25}$$

And thus, **under an applied potential**, equations 2.22 and 2.23 can be simplified to:

Reduction rate constant:

$$k_{red} = k_{red,ch} \exp\left(\frac{-\alpha z F E}{RT}\right) \tag{2.26}$$

Oxidation rate constant:

$$k_{ox} = k_{ox,ch} \exp\left(\frac{-(\alpha z F E - z F E)}{RT}\right) = k_{ox,ch} \exp\left(\frac{(1-\alpha) z F E}{RT}\right) \tag{2.27}$$

The reduction and oxydation current densities can now be calculated [49]:

$$i_{red} = k_{red} \cdot zF \cdot [M^{z+}] \tag{2.28}$$

$$i_{ox} = k_{ox} \cdot zF \cdot [M] \tag{2.29}$$

As said previously, when the system is under equilibrium, the cathodic and anodic current densities are equal and the net flowing current is equal to zero. The equilibrium potential will be denoted as "E_{eq}".

Thus,

$$i_{tot,eq} = 0 \tag{2.30}$$

And,

$$i_{red,eq} = i_{ox,eq} = i_0 \tag{2.31}$$

In other words,

$$zF \cdot [M^{z+}] \cdot k_{red,ch} \cdot \exp\left(\frac{-\alpha z F E_{eq}}{RT}\right) = zF \cdot [M] \cdot k_{ox,ch} \cdot \exp\left(\frac{(1-\alpha) z F E_{eq}}{RT}\right) \tag{2.32}$$

By simplifying, one gets:

$$\exp\left(\frac{zFE_{eq}}{RT}\right) = \frac{k_{red,ch}}{k_{ox,ch}} \cdot \frac{[M^{z+}]}{[M]} \tag{2.33}$$

Which gives:

$$E_{eq} = \frac{RT}{zF} \ln\left(\frac{k_{red,ch}}{k_{ox,ch}}\right) + \frac{RT}{zF} \ln\left(\frac{[M^{z+}]}{[M]}\right) \tag{2.34}$$

One can see that Nernst equation is hidden behind equation 2.34:

$$E_{eq} = E^{\circ}_{eq} - \frac{RT}{zF} \ln\left(\frac{[M]}{[M^{z+}]}\right) \tag{2.35}$$

Finally, by denoting that the deviation of the actual potential difference from the equilibrium potential is $\eta = E - E_{eq}$, all the parts needed in order to describe the net flowing current under non-equilibrium conditions are known and following equation, also known as **Butler-Volmer equation**, can be derived:

$$i_{tot} = i_{ox} - i_{red} = i_0 \left(\underbrace{\exp\left(\frac{(1-\alpha) z F \eta}{RT}\right)}_{\text{cathodic contribution}} - \underbrace{\exp\left(\frac{-\alpha z F \eta}{RT}\right)}_{\text{anodic contribution}} \right) \tag{2.36}$$

This equation is fundamental in order to deal with the kinetics of electrochemical reactions. From this equation, it can be seen that when the overpotential η is positive the oxidation reaction will take place, whereas the reduction reaction takes place for negative overpotentials.

To illustrate this equation graphically, a semi-logarithmic graph is most often used as can be seen on Figure 2.25. This graph is also called Tafel plot. When the overpotential is high, i.e. $|\eta| \geq 100mV$, the graph behaves linearly and the slopes are equal to [49]:

$$\underline{\text{cathodic slope}}\text{: } \beta_c = \tfrac{RT}{-\alpha z F} \ln 10$$
$$\underline{\text{anodic slope}}\text{: } \beta_a = \tfrac{RT}{(1-\alpha) z F} \ln 10$$

Indeed, when $\eta \gg 0$, equation 2.36 leads to:

$$\eta \cong \frac{RT}{(1-\alpha) z F} \ln\left(\frac{i_{tot}}{i_0}\right) \tag{2.37}$$

And when $\eta \ll 0$, equation 2.36 leads to:

$$\eta \cong \frac{RT}{-\alpha z F} \ln\left(\frac{i_{tot}}{i_0}\right) \tag{2.38}$$

When the overpotential is very small, $\eta \cong 0$, another linear approximation can be done (valid for $|\eta| \geq 20mV$):

$$i_{tot} \cong i_0 \frac{zF}{RT} \eta \tag{2.39}$$

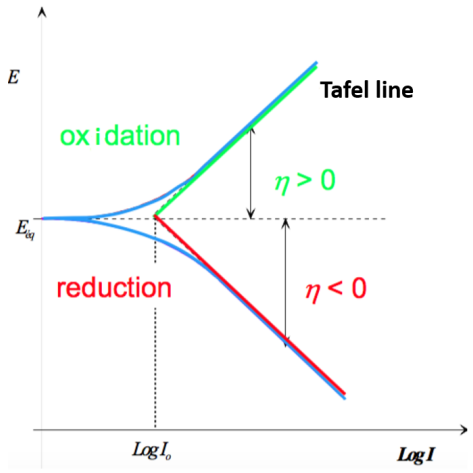

FIGURE 2.25: Generalized Tafel plot. Inspired from [49]

2.5.2.2 Diffusion processes

In the previous section, the kinetics of the reactions taking place at the electrode/electrolyte interface have been analyzed. All the theory related in these sections are only **valid if electron transfer is dominant**. However, other factors are of equal importance in an electrochemical system and can render the previous theory invalid. Indeed, the species transport through the solution is a very important factor due to the amount of time needed for this process. As a matter of fact, the current transport by electrons takes a negligible amount of time whereas in the solution, the current is carried by ions and this process is time-consuming [34].

When the rate of reaction is being analyzed, it is always the slowest step that is determining it. Therefore, if the diffusion is slow, the system's rate will be transport determined. As illustrated in the "*Corrosion for Science and Engineering*" book [34], the situation taking place in an electrochemical system can be compared to the traffic on a highway when there is the presence of roadworks: when a few cars are travelling on the highway, the roadworks do not hinder the traffic and the rate of cars along the highway equals the rate at which they joined it. However, when a lot of cars use the highway, the roadworks do obstruct the traffic and become rate-determining. It is similar in an electrochemical cell. When a small current has to pass through the electrolyte, the dissolved oxygen (when considered cathode reactant) can be transported easily. Whereas, when the current flow is important, the electrolyte cannot accommodate the charge transfer needed by the cell. In the latter case the passage of the dissolved oxygen occurs at a rate-determining speed giving rise to a diffusion-controlled system.

On Figure 2.26, one can see how the cathode reactant concentration varies with distance from the cathode. When no current flows through the system, the concentration is identical throughout the electrolyte. On the other hand, as soon as current flows through the cell, the concentration near the cathode drops. The situation can be illustrated using Fick's First Law of Diffusion [34]:

$$J = -D\frac{dc}{dx} \tag{2.40}$$

where J is the flux of substance, D the diffusion constant and $\frac{dc}{dx}$ the concentration gradient.

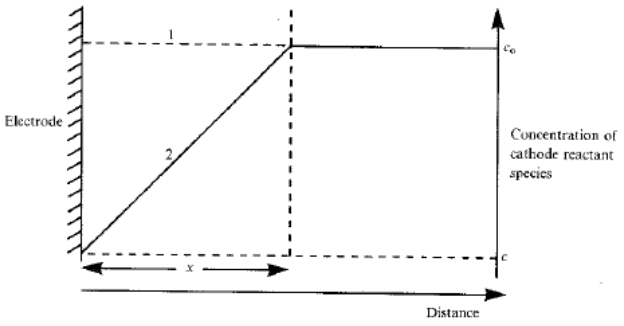

FIGURE 2.26: Variation of cathode reactant concentration with distance from the cathode when no current is flowing through the cell (situation 1) and when current is flowing through the cell (situation 2) [34].

The flux of substance can be substituted by the relation found on equation 2.18 and following equation arises:

$$i = -zFD\frac{dc}{dx} \tag{2.41}$$

If a linear gradient is considered, $\frac{(c_0-c)}{x}$, previous equation becomes:

$$i = -zFD\frac{(c_0 - c)}{x} \tag{2.42}$$

The negative signs implies that the current is carried away from the electrode in form of hydroxyl ions. Concentrations are always positive, thus the maximum current density magnitude will be maximal when $c = 0$. Thus, the **limiting current density** is obtained as followed:

$$i_L = -zFD\frac{c_0}{x} \tag{2.43}$$

It can be noted that when the concentration near the electrode is increasing (i.e. $c > c_0$), the current density is reversed.

Nernst equation at the electrode surface can be written in the case where no current flows through the cell and when current flows through the system:

System at equilibrium:

$$E_1 = E^\circ - \frac{0.059}{z}log(c_0) \tag{2.44}$$

System subject to a current flow:

$$E_2 = E^\circ - \frac{0.059}{z}log(c) \tag{2.45}$$

Recall that the overpotential was defined as the difference between the actual potential and the equilibrium potential. In this situation: $\eta = E_2 - E_1$. Therefore,

$$\eta = \frac{0.059}{z}log\left(\frac{c_0}{c}\right) \tag{2.46}$$

By dividing equation 2.42 by equation 2.43, an expression for $\frac{c}{c_0}$ can be obtained and substituted in equation 2.47, giving:

$$\eta = \frac{0.059}{z}log\left(1 - \frac{i}{i_L}\right) \tag{2.47}$$

It has already been discussed previously that for very small currents, the Tafel equation behaves in a non-linear way. When the current is intermediate, linearity is observed and now it has been proven that for high currents, the Tafel plot is non-linear again and reaches the limiting current density asymptotically [11]. These regions can be seen on Figure 2.27.

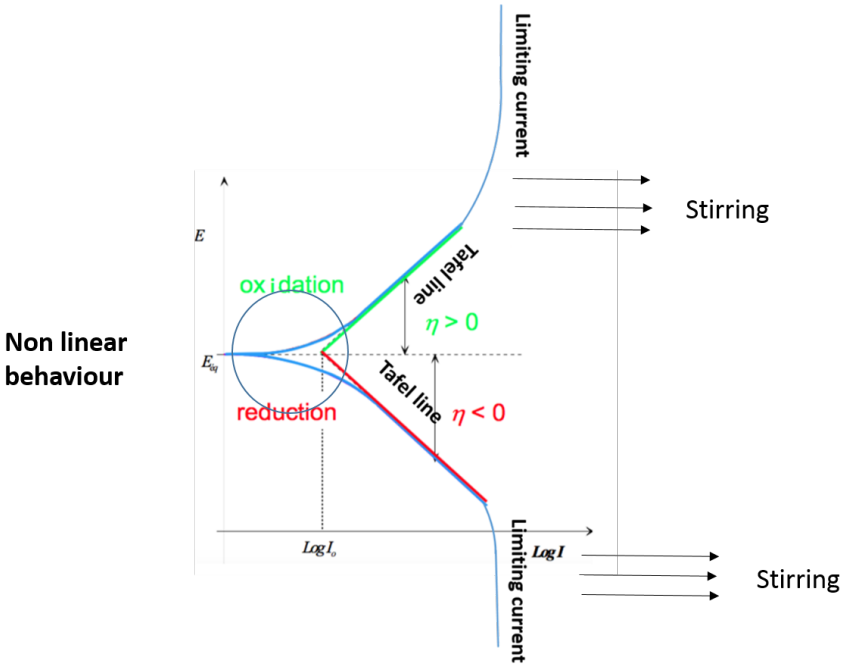

FIGURE 2.27: Tafel plot showing the three different regimes: non-linearity around very small current, linear behaviour at intermediate currents and asymptotic behaviour for high currents. Inspired from [49].

A Tafel plot illustrates the oxidation and reduction of the same component, the metal. In order to investigate the whole corrosion mechanism, i.e. the metal oxidation as well as hydrogen evolution or dissolved oxygen reduction, Evans diagrams are used. They relate the thermodynamical aspect (potential) to kinetics (current densities). Figure 2.28 illustrates two corrosion cells in hydrochloric acid: the corrosion of iron and of zinc. The cathodic (hydrogen evolution) and anodic (metal dissolution) lines of the two systems intercept at a certain point. At this point the current density is called the free corrosion density and the potential is called the free corrosion potential. When looking at Figure 2.28, it can be noted that the exchange current density of hydrogen evolution, $i_{0(H_2)}$ (always occurring at 0V vs SHE), is different in the iron corrosion cell than the for the zinc corrosion cell. By taking a look at the galvanic series of different metals, it can be seen that zinc is more active than iron. This can also be seen on Figure 2.28. However, because of the fact that the hydrogen evolution exchange current density is higher in an iron corrosion cell (in HCl), iron will corrode much faster than zinc in HCl. On the other hand, if one analyses a noble metal such as platinum, it will be seen that the hydrogen evolution exchange current is quite high but because it has an excessively high positive electrode reduction potential, it is protected from corrosion.

[11] Stirring can help against this current limitation.

In the presence of a neutral or alkaline environment, it is the oxygen reduction that takes place at the cathode and this reaction depends greatly on the rate of diffusion of oxygen to the metal surface and on stirring.

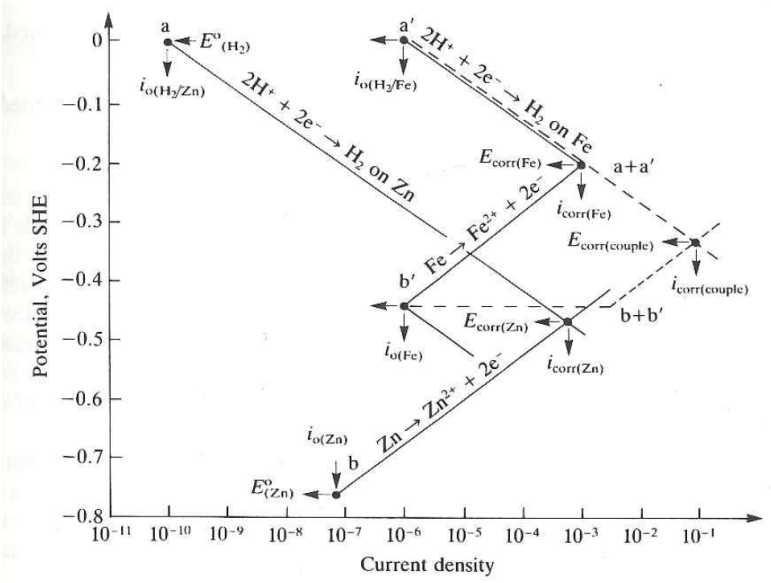

FIGURE 2.28: Mixed potential plot for the iron/zinc couple explaining why iron corrodes faster than zinc despite a more positive reduction potential in HCl (pH=3) [34].

2.5.2.3 Three-electrode cell

In order to investigate a corrosion cell, a three-electrode cell is common standard and is constituted of:

1. **A working electrode (WE)**, which is the metal that has to be inspected. Electrodes as large as possible should be used in order to work under the best conditions. There are different ways to prepare such samples: they can be mounted in cold-settling resin, in which case electrical contact must be made or more sophisticated systems for more accurate work can be used such as rotating disk electrodes. In the case of mounted samples, these are usually ground and polished, in which case the passive films on the original sample break down and the surface becomes active. It has thus to be kept in mind that the results found when performing tests under polished conditions differ from a field reality.

2. **A reference electrode (RE)**. As explained previously in this section, the SCE is usually used for potentiodynamic polarisation measurements as it provides a very stable behaviour. The working electrode cannot carry any current (in order to keep a constant potential) and this is where the third electrode comes into play.

3. **The counter (auxiliary) electrode (CE)** carries the current created in the cell and should be made of inert materials such as a carbon rod or platinum.

In a potentiostat, predetermined potentials are applied to the working electrode allowing the measurement of the cell current by alternating the curent at the counter electrode such that the determined potential value at the working electrode is maintained.

2.5.2.4 iR drop and capacitive current

Another important factor in this system is the electrolyte conductivity as the electrolyte is responsible for the ionic transport. Therefore, the reference electrode should be placed as close to the working electrode as possible as the electrolyte portion that will be carrying the ions taking place in the electrochemical reactions will be the one between the working and reference electrodes (position RE1 on Figure 2.29 with 0 IR drop) [34, 50]. If direct currents are involved, Ohm's law ($V = IR$) can be used to determine the potential difference across the electrolyte. It is known as the IR drop and depends on the distance between the WE and RE, the magnitude of current and the electrolyte conductivity. This IR drop should be as small as possible, otherwise its contribution to the overall cell potential would be too difficult to evaluate as the actual potential is as follows [34, 50]:

$$E_{actual} = E_{applied} - E_{IRdrop} = E_{applied} - IR \tag{2.48}$$

Hence, the electrolyte should be of very small resistance. In other words, its conductivity should be as large as possible. If this is not the case, a Luggin capillary can be used but some contaminations between the electrolyte and the saturated potassium chloride solution connected by salt bridge is possible.

When cyclic voltammetries, for example, with fast scan rates are used to investigate the system, a transient current exists due to the charge and discharge of the double electric layer (acting like a capacitance) and the actual potential differs from the applied potential by [50]:

$$E_{actual} = E_{applied}\left(1 - \exp\left(\frac{-t}{RC_{dl}}\right)\right) \tag{2.49}$$

where R is the ohmic resistance, C_{dl} the double layer capacitance and t the measurement time. Thus, for fast scan rates (i.e. short times), the exponential term tends to 1 and the errors become significant whereas for slow scan rates (i.e. long times), the exponential term tends to 0 and the error is negligible [50]. This explains why current densities are higher when the test is performed with a faster scan rate.

When current is flowing through the circuit, there always is some kind of IR drop and the true cathodic potential of the working electrode will be less negative than the one measured by the value of the IR drop and the true anodic potential will be more negative by that amount [50]. The IR drop can be minimized by increasing the electrolyte conductivity, by decreasing the size of the WE the double layer capacitance decreases correspondingly, and by minimizing the distance between the WE and RE by the use of a Luggin capillary for example [50]. The problem with such capillaries is that it can cause shielding errors when the RE is so close to the WE blocking it. A common standard is to use a minimum distance of 2d between the WE and the Luggin capillary (d being the tip diameter of the capillary) [50]. Also, when analyzing Figure 2.29, it is seen that closer to the WE, the equipotential lines are compacted and thus small changes of distances can cause a large variation of ohmic drop. This is why, sometimes, it is desirable to put the RE far away from the WE instead of using a Luggin capillary and measure the ohmic drop and compensate accordingly.

2.5.2.5 Polarisation resistance

As has already been mentioned, most common way to analyse corrosion measurements are the use of Evans plots such as the one on Figure 2.28. And during a corrosion process, more than just one reaction takes place. For example, when iron corrodes, Fe^{2+} ions are formed as well as surface corrosion products: iron oxides and hydroxides.

The potential at which current changes sign is called the free corrosion potential and is denoted as E_{corr}. The corrosion rate under freely corroding conditions is obtained by the means of the theoretical

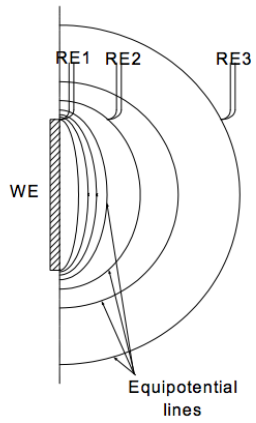

FIGURE 2.29: Equipotential lines where the reference electrode can be placed away from the working electrode [50].

anode current density at the free corrosion potential (then labelled corrosion current density, i_{corr}). When more than one redox reaction is taking place, this corrosion current density cannot be equated to the cathodic current density but is still equal to the metal dissolution current density, i_a.

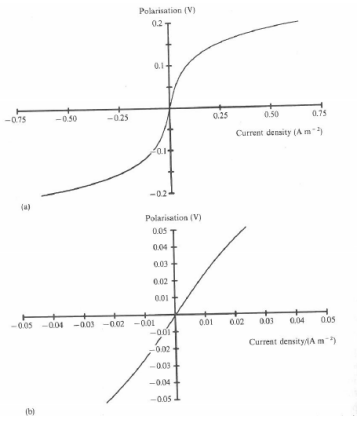

FIGURE 2.30: (a) Data of Tafel plot redrawn on a linear scale with positive anodic current density and negative cathodic current density and (b) expanded graph of (a) exhibiting linear behaviour over ±30mV and which slope is called polarisation resistance R_p [34].

Corrosion rates can also be found by using linear graphs of potential versus current density, as shown on Figure 2.30. On such graphs, anodic current densities are plotted positive and cathodic current densities are plotted negative. At the near proximity of the corrosion potential (about 20-30mV [34, 49]), there is a certain linear behaviour. And in this region,

$$\frac{\Delta\eta}{\Delta i} = \frac{\beta_a \beta_c}{2.3 i_{corr}(\beta_a + \beta_c)} \tag{2.50}$$

This slope is called the polarisation resistance R_p. From there,

$$i_{corr} = \frac{\beta_a \beta_c}{2.3 R_p(\beta_a + \beta_c)} \tag{2.51}$$

This **linear polarisation technique** is quite approximate and highly depends on the system. It is also common that around the free corrosion potential, the corrosion kinetics are not obeying Tafel equation and thus the Tafel constants cannot be determined. Thus, a full analysis of the polarisation curve is necessary in order to determine the kinetics parameters and make sure that Tafel equation is being used correctly. Sometimes, Evans diagram do not contain a linear part. Different reasons could be:

- If more than one reaction takes place on the electrode: the corrosion products that are deposited on the electrode surface are reducing the anode conductivity and thus the measured current densities are lower than the ones predicted by the Tafel equation.
- If the scan rate is too fast, the sample is not given the time to react to each potential step.
- If there are any diffusion limitations.
- If the Tafel relationship is not obeyed because either the anodic or the cathodic reaction is determined by mass transport. The most common example is when the cathodic polarisation is determined by oxygen diffusion, in which case no Tafel slope can be determined, the free corrosion current density is only the value of the anodic current density at the intersection with the oxygen consumption lines.

2.5.2.6 Summary of the different factors influencing polarisation curves

Polarisation curves can be predicted by taking good care of including **all** the reactions taking place. From the E-pH diagram of the studied material, the different species that could be involved during the process (under specific pH and potential) can be estimated. Indeed, just an estimation can be made as these data are only considering the thermodynamical aspect of corrosion but not the kinetics and thus, some species shown on the E-pH diagram could not be involved in the process or some species not supposed to take place in the process could be present. Then, by using Nernst equation, the equilibrium potentials of the different species can be calculated. Afterwards, the polarisation/current density relationship can be calculated. First, the total polarisation needs to be taken into account, i.e. the polarisation due to charge transport, mass transport and ohmic drop:

$$\eta_{total} = \eta_{activation} + \eta_{diffusion} + \eta_{resistance} = \frac{2.3RT}{\alpha z F} \ln\left(\frac{i}{I_0}\right) - \frac{2.3RT}{zF} \ln\left(1 - \frac{i}{I_L}\right) + i(R_s + R_f) \quad (2.52)$$

where R_s is the resistance of the solution and R_f is the resistance of potential films that deposit on the metal.

The last step can now be undertaken: the current density can be determined by adding all the anodic and cathodic current densities, at each potential step:

$$i_{total} = \sum_{1}^{N} i_a - \sum_{1}^{N} i_c \quad (2.53)$$

2.6 Previous studies on corrosion behaviours

This section will present the results found by different authors concerning the biocorrosion of iron based alloys. First the materials and methods used by different studies. Polarisation and static immersion tests are described in more detail as these will be used in this work. Dynamic immersion will also be described as these kind of tests should be performed in future investigations. In fact,

dynamic immersion mimics the behaviour in human blood more realistically than polarisation and immersion tests. Finally, biocompatibility responses will also be detailed as they are of importance in order to decide if a stent should be further investigated or not. If a stent is found not to be biocompatible, it cannot be used in vivo even if its corrosion behaviour is as perfect as possible for its task.

The potentiodynamic polarisation and immersion tests were performed in electrolytes that are called simulated body fluids (SBFs). There exists different types of SBFs, such as Hank's solution or Ringer solution. A typical concentration of SBF is given in Table 3.2 in section 3.2.3 (this SBF is the one used for the present investigations).

At the end of this section, possible effect of twins and surface roughness on the corrosion behaviour will be highlighted.

2.6.1 Materials and Methods

2.6.1.1 Potentiodynamic polarisation tests

Liu et al. [51] investigated the effect of adding different alloying elements to iron. Since Cr, Ni, Mo, Cu, Ti, V and Si are known for their corrosion resistant properties when added to stainless steels, these were not investigated. Other elements, such as Mn, B, Al, Co, W, Sn, C, and S are not yet categorized as corrosion resistant or corrosion accelerating, which is why *Liu et al.* decided to investigate these alloying elements. Alloys of 97 at.% iron and 3 at.% alloying element [12] were prepared in a vacuum induction furnace with Ar as atmosphere. The ingots were then cut into plates of 10 mm thickness and hot-rolled to achieve a thickness of 4 mm at 1000°C for 30 minutes. They were then cold-rolled to obtain a thickness of 1.5 mm. To investigate the corrosion response of C and S elements, high carbon steel 1070 (Finkl, USA with nearly 3 at.% C content) and free cutting steel 1119 (Finkl, USA with nearly 0.5 at.% S content) were used. The authors differentiate two classes: as-cast and as-rolled. Previous examples belong to the latter class and were compared to 316L SS. 10x10x1.5 mm samples were prepared and mechanically polished up to 2000 grit.

They performed their electrochemical tests with the following method: they measured the open circuit potential (OCP) up to 7200s. The actual potentiodynamic polarization test was carried out anodically from -1000mV to -400mV vs SCE with 0.33 mV s^{-1} as scan rate. **Hank's** solution was the simulated body fluid electrolyte chosen for the tests with a physiological pH of 7.4. The degradation rates were measured following the ASTM-G102-89 standard:

$$v_{corr} = K_1 \frac{I_{corr}}{\rho} EW \quad CR = K_2 I_{corr} EW \tag{2.54}$$

where v_{corr} is the degradation rate in terms of penetration rate given in mm $year^{-1}$ and CR is the degradation rate in terms of mass loss rate given in g m^{-2} day^{-1}. K_1 is equal to 3.27 10^{-3} mm g μA^{-1} cm^{-1} year−1 and K_2 to 8.954 10^{-3} g cm^2 μA^{-1} m^{-2} day^{-1}.

Cheng et al. [52] used the same method as Liu et al. [51] to study the electrochemical response of Fe, Mn, Mg, Zn, and W pure metals.

Harjanto et al. [6] investigated the corrosion behaviour of powder metallurgy fabricated Fe-25Mn-1C and Fe-35Mn-1C by performing potentiodynamic polarization tests and immersion tests in **Ringer** solution [13]. The electrochemical tests were performed using the ASTM G5 standard with a scanning

[12] more precisely: 3.31 at.% Mn, 3.48 at.% Co, 3.07 at.% Al, 3.28 at.% W, 3.05 at.% Sn, and 3.34 at.% B [51].

[13] This solution is composed of 1.55 g/l sodium lactate, 3 g/l sodium chloride, 0.15 g/l potassium chloride, and 0.1 g/l calcium chloride.

area of ± 250mV.

Zhang et al. [4] studied the corrosion behaviour of pure iron. For all the different tests, the samples were mounted in epoxy resin with an exposed surface area of 1 cm^2. The samples were polished up to 1 μm. For the electrochemical tests, OCP determination was made up to 3600s. Then samples were immersed for 20 minutes in 350 ml of **Hank's** solution at 37±1°C and the potentiodynamic test was then performed with a 0.5 mV s^{-1} scan rate. The electrode was cleaned by 5000 grit SiC paper to avoid electrode fouling.

Schinhammer et al. [3] investigated the corrosion behaviour of Fe-21Mn-0.7C-(1Pd) alloys. Indeed, Mn lowers the standard electrode potential of the matrix and the formation of noble Pd-rich precipitates would be expected to induce microgalvanic corrosion which would increase the corrosion rate. It was shown for Mg-based alloys that the solution composition and especially the buffering agent greatly influence the corrosion rate [14]. Thus, the use of gaseous CO_2 was suggested in order to keep a constant pH. Active regulation of pH could also be used. By using one or the other, it could be shown that the degradation behaviour correlated quite well with in vivo studies on well-vascularized tissues. This is why *Schinhammer et al.* decided to use this approach and undertook immersion and electrochemical impedance spectroscopy (EIS) tests. The electrochemical tests let the OCP stabilize for one hour. The measurements were made using a rotating disc electrode (RDE) setup with a sample rotation rate of 500 min^1. The samples were cylinders of 4 mm long and had a 5 mm diameter. The sample holder was made of PTFE and the outer edge of the sample was sealed with silicone to prevent crevice corrosion. The effective surface was determined individually for each sample but was about 0.13 cm^2. 250ml **SBF** at 37±1°C was used and the effect of 100 mM Hepes buffer was investigated for some samples. The exact setup can be seen on Figure 2.31.

Table 2.1 summarizes the different methods used by the different studies for polarisation tests.

2.6.1.2 Immersion tests

Liu et al. performed their static immersion tests according to the ASTM-G31-72 standard in **Hank's** solution: the specimens were immersed in 50ml solutions and the temperature was kept at 37°C thanks to the use of a water bath. The specimens were immersed for different periods: 3, 10, 30, 90 and 180 days. 10x10x1.5 mm samples were prepared and mechanically polished up to 2000 grit. The changes in surface morphology were characterized by scanning electron microscope (SEM) and Energy-dispersive X-ray spectroscopy (EDX) data. The corrosion products released in the solution were investigated using and Inductively coupled plasma atomic emission spectroscopy (ICP-AES) instrument. The degradation rate was calculated in terms of mass loss rate:

$$CR = \frac{cV}{ST} \tag{2.55}$$

where c is the released ion concentration in g ml^{-1}, V is the volume in ml, S is the specimen surface area in m^2 and T is the immersion time in days. Thus CR has g/(m^2d) as units.

Harjanto et al. [6] investigated the corrosion behaviour of powder metallurgy fabricated Fe-25Mn-1C and Fe-35Mn-1C by performing potentiodynamic polarization tests and immersion tests in **Ringer** solutions. They performed the immersion tests using ASTM G31 standard for 2 days.

Zhang et al. [4] studied the corrosion behaviour of pure iron. For all the different tests, the samples were mounted in epoxy resin with an exposed surface area of 1 cm^2. The immersion tests were carried

[14] During magnesium corrosion, H_2 reduction is taking place, where pH is of great importance.

TABLE 2.1: Methodology of polarization tests undertaken in different studies (different kinds of SBF solutions).

Authors	Polishing	Volume (ml)	OCP time	Scan rate (mV/s)
Liu et al. [51]	2000 grit	/	up to 7200s	0.33
Harjanto et al. [6]	/	/	/	/
Cheng et al. [52]	2000 grit	/	up to 7200s	0.33
Zhang et al. [4]	1 μm	350	up to 3600s	0.5

Authors	Scan range (mV vs SCE)	T (°C)	pH
Liu et al. [51]	-1000 to -400	/	7.4
Harjanto et al. [6]	$\pm$250	/	/
Cheng et al. [52]	-1000 to -400	37	7.4
Zhang et al. [4]	$\approx$-900 to -500	37	/

out according to ASTM-G31-72 standard and the samples were immersed in 150 ml **Hank's** solution at 37°C for 7, 14, 21, and 28 days. Before weighing after immersion, they were cleaned using a 595 g/l HCl solution with 3.5 g/l hexamethylenetetramine to remove surface corrosion products and weight loss rate was calculated as following: (weight before immersion - weight after clean)/(surface area x immersion time).

The immersion samples of the *Schinhammer et al.* [3] study were 3.5 mm thick and 7 mm (pure iron, TWIP-1Pd cold-worked and annealed) or 8 mm (TWIP and TWIP-1Pd recrystallized) in diameter and ground up to P1200 grit SiC paper. Immersion took place in two different media: **SBF** at 37$\pm$1° and 0.5M H_2SO_4 at room temperature. The immersions taking place in SBF were kept under 7.35 to 7.45 pH values by the means of gaseous CO_2. The SBF volume was taken in such a way to obtain a volume to surface ratio of 160 ml cm^{-2}. Immersions in H_2SO_4 were performed to investigate the influence of the size of the precipitates on the corrosion rate. In acidic environment, any kind of degradation products formed on the sample surface can limit the diffusion of the reacting species. In addition, the degradation rate can be measured by the amount of evolved hydrogen as this is the dominant cathodic reaction in acidic environment. The electrochemical tests let the OCP stabilize for one hour. The measurements were made using a rotating disc electrode (RDE) setup with a sample rotation rate of 500 min^{-1}. The samples were cylinders of 4 mm long and had a 5 mm diameter. The sample holder was made of PTFE and the outer edge of the sample was sealed with silicone to prevent crevice corrosion. The effective surface was determined individually for each sample but was about 0.13 cm^2. 250ml SBF at 37$\pm$1°C was used and the effect of 100 mM Hepes buffer was investigated for some samples. The exact setup can be seen on Figure 2.31.

Table 2.2 summarizes the methods used by the different studies for immersion tests.

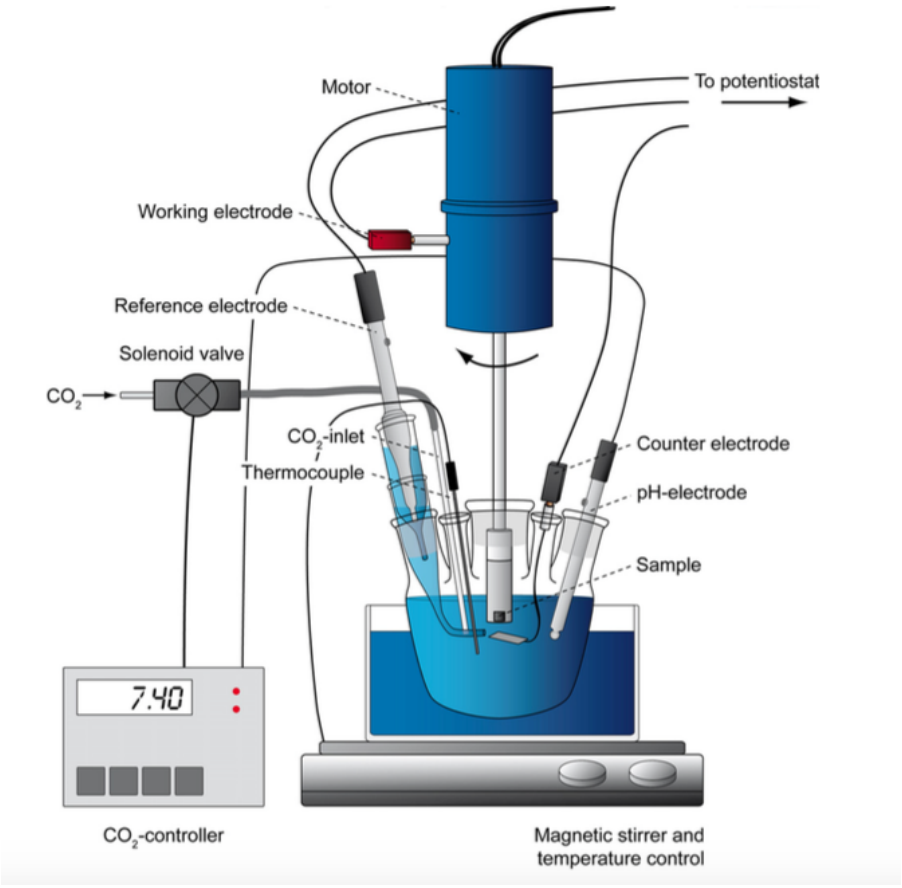

FIGURE 2.31: Schematic of the electrochemical measurements setup of Schinhammer et al. with CO_2 pH regulation and sample rotation as well as temperature control [3].

2.6.2 Potentiodynamic polarisation tests: results and discussion

On Figure 2.32, a table comparing the corrosion rates resulting from *Liu et al.* [51] tests [15] can be found for the different alloys when investigated in as-cast or as-rolled form. It is shown, that Fe-Mn, Fe-Al, Fe-W, Fe-B, and Fe-S alloys have a lower corrosion rate for as-rolled alloy compared to as-cast alloy (as-rolled Fe-Mn even has a smaller corrosion rate than pure iron). The only alloy that increases its corrosion rate by undergoing rolling, is the Fe-Co alloy. The table also shows, that the corrosion rates between the different alloys and pure iron are not significantly different. This is due to the fact that during electrochemical tests, the corrosion products do not interfere, whereas these play a very important role in immersion tests.

Liu et al. [5] also investigated the corrosion behaviour of Fe-30Mn-6Si compared to pure iron and Fe-30Mn. The potentiodynamic polarization tests resulted in the following corrosion rate order: pure iron<Fe-30Mn<Fe-30Mn-6Si. X-ray Diffraction (XRD) showed that the pure iron was made of α ferrite as single phase, whereas Fe-30Mn and Fe-30Mn-6Si were constituted of ϵ-martensite and γ-austenite. This shows that the crystalline structure might have an impact on the corrosion rate and thus explaining the higher corrosion rate compared to pure iron. *Harjanto et al.* [6] showed that the higher the

[15] No specification on how they determine the corrosion current is given in their article but it seems that they are taking the potential at which the current density is minimal as the corrosion potential and take the average between the "anodic current density" and the "cathodic current density" at this potential.

TABLE 2.2: Methodology of immersion tests undertaken in different studies (different kinds of SBF solutions).

Authors	Polishing	Volume (ml)	Sruface (cm^2)
Liu et al. [51]	2000 grit	150	1
Harjanto et al. [6]	/	/	/
Zhang et al. [4]	1 μm	150	1
Schinhammer et al. [3]	1200 grit	160 ml/cm^2	/

Authors	T (°C)	pH	Immersion times (days)
Liu et al. [51]	37	/	3,10,30,90,180
Harjanto et al. [6]	/	/	2
Zhang et al. [4]	37	/	7,14,21,28
Schinhammer et al. [3]	37	7.35-7.45	3,7,14,28

	V_{corr} (V)	I_{corr} (μA cm^{-2})	v_{corr} (mm $year^{-1}$)	Corrosion rate (g m^{-2} d)		
				Electrochemical	Static	Dynamic
Pure iron						
As-cast	−0.748	8.961	0.105	2.240	0.256	4.033
As-rolled	−0.702	8.768	0.103	2.192	0.166	3.133
Fe–Mn						
As-cast	−0.711	9.003	0.105	2.251	0.038	0.956
As-rolled	−0.68	7.454	0.087	1.863	0.028	0.678
Fe–Co						
As-cast	−0.713	10.966	0.128	2.741	0.250	1.367
As-rolled	−0.693	12.099	0.142	3.025	0.220	1.956
Fe–Al						
As-cast	−0.704	9.538	0.112	2.385	0.140	1.544
As-rolled	−0.721	9.485	0.111	2.372	0.116	1.056
Fe–W						
As-cast	−0.717	12.89	0.151	3.223	0.350	1.122
As-rolled	−0.709	12.663	0.148	3.166	0.361	0.822
Fe–B						
As-cast	−0.698	14.962	0.175	3.741	0.142	1.033
As-rolled	−0.728	10.309	0.121	2.577	0.070	1.111
Fe–C						
As-rolled	−0.68	15.964	0.187	3.991	0.231	3.456
Fe–S						
As-rolled	−0.703	12.351	0.145	3.088	0.230	2.58

V_{corr}, corrosion potential; I_{corr}, corrosion current density; and v_{corr}, corrosion rate in terms of penetration rate.

FIGURE 2.32: Corrosion rates and electrochemical data calculated for Fe-X binary alloys with pure iron as a control in Hank's solution [51].

Mn content of the alloy, the higher the electrochemical corrosion rate.

Cheng et al. [52] found following corrosion rate order: Mg>Fe>Mn>Zn>W. Generally, a higher corrosion current density is also associated to a lower corrosion potential, however this was not the case between iron and manganese and zinc (-0.748V, -1.285V, and -1.049 V respectively). They also showed, that the reverse polarization plot of W coincided with the forward curve, evidencing that the surface of the sample did not significantly changed.

Zhang et al. [4] did not find a plateau in the anodic region, meaning no passivation film was formed. The corrosion current was found to be smaller for pure iron compared to Mg-Mn-Zn alloy but higher than stainless steel and the corrosion potential of stainless steel is indeed higher than the corrosion potential of pure iron and Mg-Mn-Zn alloy. Previous studies highlighted that the OCP value of magnesium increased with time resulting in lower corrosion rates with time due to the increase in pH value and accumulation of corrosion products on the surface. For iron, *Zhang et al.* showed that the OCP value decreased with time until reaching a steady value, therefore the corrosion rate should first increase up to a certain value where it will stay steady due to accumulation of corrosion products on the surface. This is consistent with the immersion findings illustrated below.

EIS measurements undergone by *Schinhammer et al.* [3] showed that TWIP-1Pd alloy had a higher corrosion current density than TWIP alloy and that the latter had a higher degradation rate than pure iron. The differences were more pronounced than in the immersion tests. It was shown that increased flow favoured the occurrence of localized attacks. These localized attacks were not seen in immersion tests even after the removal of corrosion products. These differences can be explained by the enhanced oxygen transport in the EIS measurements setup and also by the fact that the degradation products were partially transported away from the metal surface, exposing the metal surface to increased corrosion. The localized attacks seemed to start after 7 hours.

2.6.3 Static immersion tests: results and discussion

The different corrosion rates of *Liu et al.* [51] alloys that underwent static immersion can be seen on Figure 2.32. After 3 days immersion, the corrosion products were found on the specimen corners. After 30 days, some specimens were totally covered by corrosion products and after 180 days more than half of the specimens were totally covered by corrosion products with still a few bright areas found. All this can be seen on Figure 2.33 for the as-rolled Fe-W alloy after 180 days immersion. The pH varied between 7.25 and 8.48 depending on the immersion time. They saw that on the brown areas where the alloy had already been corroded, white CaP compounds were apparent on the cracked corrosion product layer and so these compounds would more rapidly form on already existing corroded surfaces. EDX analyses showed that the corroded surface composition included iron, oxygen, calcium and phosphorus. This corroded surface layer is not compact and adherent to the alloy surface and it easily falls apart, especially after dehydration. When investigating the released ion concentrations, *Liu et al.* observed that the released concentrations were comparable between the different alloys and pure iron. Only Fe-Mn showed a decreased long-term corrosion rate. The concentrations for the different alloys can be seen on Figure 2.34 and the large error-bars shown on this figure are the result of localized corrosion and also due to the fact that the actual corroded surface differs from sample to sample.

Cheng et al. [52] showed that the order of ion concentrations released in Hank's solution by the pure metals investigated was following after 30 days: W > Mn > Mg > Zn > Fe with Fe and Zn ion concentration being way smaller than the other metals [16]. This is due to the fact that $Fe(OH)_3$ and $Zn(OH)_2$ are insoluble in Hank's solution and were not dissolved in HNO_3 before ICP-AES, meaning that precipitates are not taken into account. Between day 10 and day 30, magnesium's released ion concentration became static, making it go from most releasing material to third place, even with the

[16] The ranking of immersion tests is different from the one obtained by means of electrochemical tests, which was: Mg > Fe > Mn > Zn > W

highest electrochemical corrosion rate. This is due to the fact that Mg ions have reached saturation after 10 days. Iron and zinc corrosion products greatly increased between day 10 and day 30. These are insoluble, which means that the human body needs to have a mechanism present that can transport these insoluble corrosion products out of the body. After 30 days, magnesium specimens were totally degraded, zinc and iron samples showed localized corrosion, and tungsten samples showed uniformed corrosion.

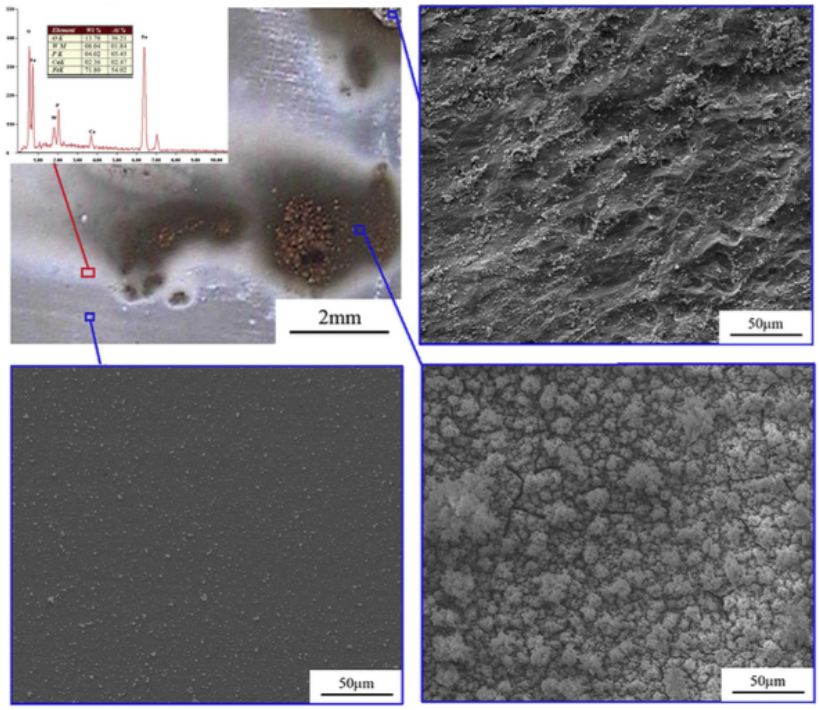

FIGURE 2.33: SEM images of the surface morphology of as-rolled Fe-W alloy after 180 days immersion at three different positions showing localized corrosion [51].

Liu et al. [5] found a different order in corrosion rate for the static immersion tests than for the potentiodynamic polarization tests. Indeed, static immersion tests gave following order: pure iron > Fe-30Mn-6Si > Fe-30Mn. The difference with the electrochemical tests can be explained by the fact that the corrosion products are not playing a role in electrochemical testing. Surface morphologies investigation showed that pure iron was completely covered by brown corrosion products after 6 months immersion whereas bright metal parts were still present in the two other alloys. *Harjanto et al.* [6] showed a degradation rate of 0.82 mm year^{-1} and 1.11 mm year^{-1} for Fe-25Mn-1C and Fe-35Mn-1C respectively.

Zhang et al. [4] showed that the pH of a Hank's solution with or without iron sample did not increase equally but that Hank's solution with iron sample increased the pH even more. The weight loss rate of pure iron was quite high up to 21 days, when it started decreasing. XRD spectra showed the evidence that the corrosion products were mainly phosphates ($Mg_3(PO4)_2$, $Ca_3(PO4)_2$ and $Fe_3(PO4)_2.8H_2O$). As has already been shown in previous studies, phosphate layers protect the metal from corrosion which explains the decrease of degradation rate from a certain moment on. The expected reactions taking place during corrosion are following:

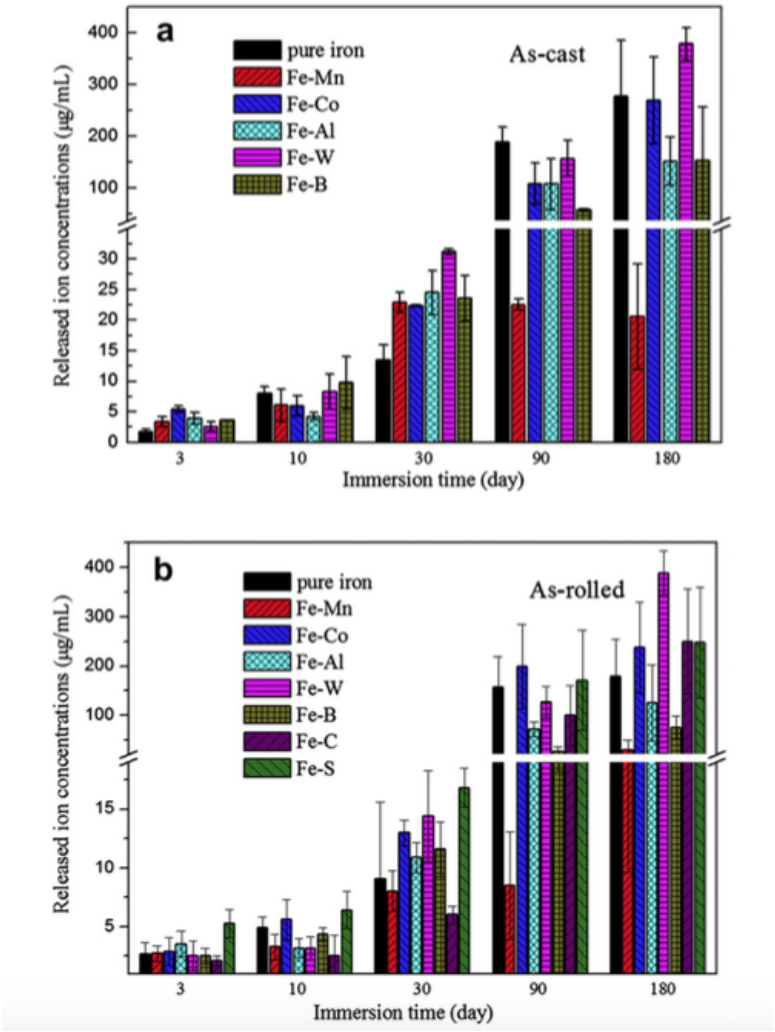

FIGURE 2.34: Released iron concentrations after static immersion tests for 3, 10, 30, 90, and 180 days for different a) as-cast and b) as-rolled Fe-X binary alloys [51].

Cathode reaction: $O_2 + 2H_2O + 4e^- = 4OH^-$
Anode reaction: $Fe + 2OH^- = 2e^- + Fe(OH)_2$

However, beside the phosphates, no iron hydroxyde was detected by XRD. This can be due to the fact that an increase in pH due to iron corrosion promotes the precipitation and deposition of phosphates. Therefore, they proposed a mechanism taking place in Hank's solution that is illustrated on Figure 2.35. The increase in pH is a bad thing for the physiological mechanisms and could even lead to an alkaline poisoning effect. However, for pure iron, the pH increase due to iron corrosion was only of 0.26, which would not lead to such poisoning, as the human body regulation processes can counter these changes. The immersion tests also revealed a uniform corrosion which suggests that the stent would not fail due to mechanical failure.

Schinhammer et al. [3] showed that after 14 days the degradation rate became steady. This can be seen on Figure 2.36. Even after just one day of immersion, the sample surface was partially covered by brownish-white corrosion products. The edges are first attacked and then the corrosion spreads over the whole sample. Surface characterization of the immersion samples showed a layered degradation

$$Fe(OH)_2 + Cl^- = FeClOH + OH^-$$
$$FeClOH + H^+ = Fe^{2+} + Cl^- + H_2O$$
$$Fe^{2+} + O_2 + 3OH^- = Fe(OH)_3\downarrow + O_2^-$$
$$Fe(OH)_3 + 2Cl^- = FeCl_2OH + 2OH^-$$
$$FeCl_2OH + H^+ = Fe^{3+} + 2Cl^- + H_2O$$
$$2PO_4^{3-} + 3Ca^{2+} = Ca_3(PO_4)_2\downarrow$$
$$2PO_4^{3-} + 3Mg^{2+} = Mg_3(PO_4)_2\downarrow$$
$$2PO_4^{3-} + 3Fe^{2+} + 8H_2O = Fe_3(PO_4)_2{\cdot}8H_2O$$
$$PO_4^{3-} + Fe^{3+} = FePO_4\downarrow$$

FIGURE 2.35: Proposed corrosion mechanism in Hank's solution by Zhang et al. [4].

products structure in backscattered electron (BSE) contrast. EDX spectra showed that the compositions were different in these layers. Indeed, for TWIP samples, the first layer[17] (appearing porous) was found to be mainly composed of iron and some manganese and some regions contained high concentrations of chlorine. The second layer appears denser and is composed of iron and manganese oxides with minor amounts of calcium and phosphor. The third layer was again porous and composed of significant amounts of calcium and phosphor, which are thought to be precipitates from the SBF. The third layer also contains some iron and manganese. The TWIP-1Pd samples showed similar layers but the first layer also contained significant Pd concentrations, even higher than in the bulk. Some minor amounts of Pd were still found on the second layer. The third layer however, had a quite different morphology than the two other layers: It was formed by deposition of precipitates from SBF and contains significant concentrations of Ca, P, and Na besides Fe, Mn, and O. Finally, the corrosion attack appears homogeneous, except in TWIP-1Pd were the twin boundaries seem to be more favourable to corrosion. Immersions in H_2SO_4 showed a much higher mass loss rate for TWIP-1Pd samples than for TWIP or pure iron samples (see Figure 2.37) and the pH increased from 1.4 to 1.5 during the immersion period for TWIP-1Pd, whereas it stayed steady for TWIP alloy and pure iron. The degradation rate in SBF between day 14 and day 28 was calculated to be about 0.10 mm year^{-1} for pure iron which is slightly lower than what is found in most literature (0.14 mm year^{-1} to 0.23 mm year^{-1}). These differences can be explained by the use of buffering agents such as Tris or Hepes. The TWIP samples degradation rate was calculated to be about 0.13 mm year^{-1}. TWIP-1Pd showed the highest degradation rates of about 0.20 mm year^{-1} for cold worked samples. The increase from the TWIP degradation rate is of a factor 1.6 showing that just 1% Pd addition already greatly increased the degradation rate. The size of the precipitates did not seem to be of importance in the corrosion rate, thus mechanical properties which greatly depend on the microstructure and size and distribution of precipitates can be optimized without having any effect on the degradation rate. The degradation products also seem to increase the volume and forces arising from such volume increase can lead to corrosion-induced failure.

[17]The first layer is the one directly on top of the metal surface.

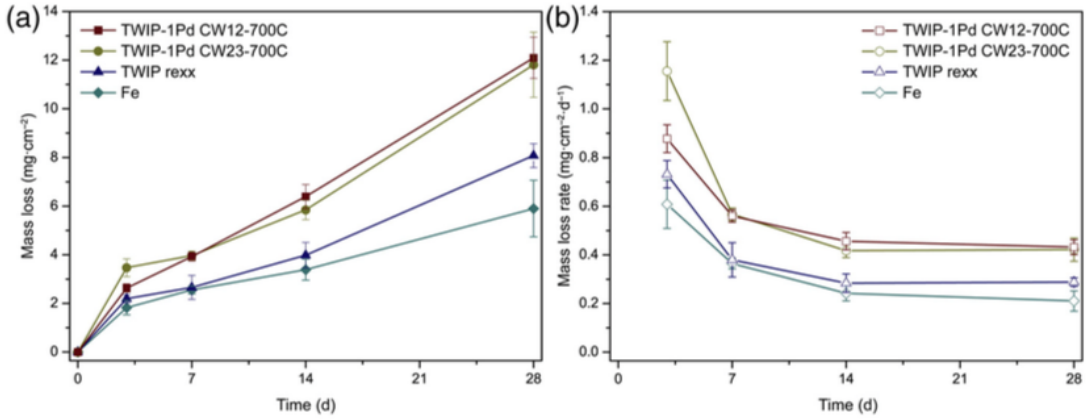

FIGURE 2.36: Mass loss and mass loss rate of pure iron, TWIP and TWIP-1Pd alloys investigated by Schinhammer et al. in SBF [3].

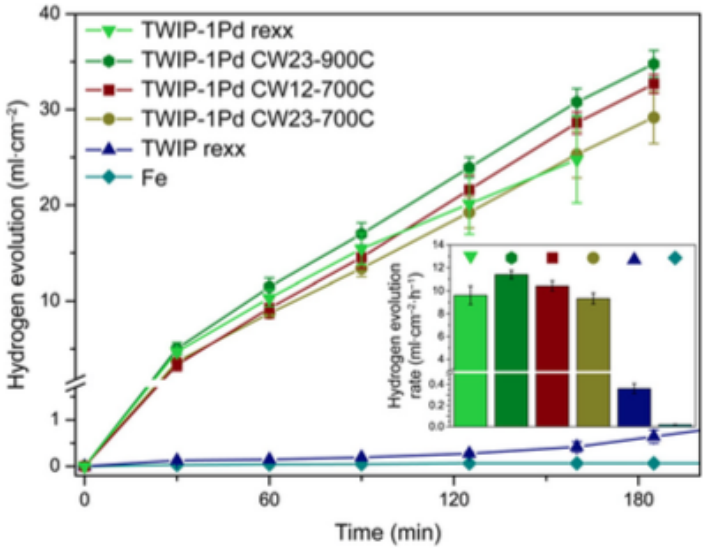

FIGURE 2.37: Hydrogen evolution from immersion tests in H_2SO_4 comparing pure iron, TWIP, and TWIP-1Pd samples. The corrosion rate of TWIP-1Pd is excessively higher than pure iron and TWIP samples. However, no correlation could be made between the microstructures tested (i.e. precipitate size) and the corrosion rate [3].

2.6.4 Summary of polarisation and static immersion findings

Liu et al. [5] found a corrosion ranking of Fe<Fe-30Mn<Fe-30Mn-6Si for the polarisation tests whereas they found a ranking of Fe>Fe-30Mn-6S>Fe-30Mn for the immersion tests, showing a different impact of corrosion products on the different samples. *Liu et al.* [51] observed a CaP layer on top of the samples and more concentrated on already corroded surfaces. All alloying elements tested exhibited similar released ion concentration except for Fe-Mn that exhibited a decreased long term corrosion rate.

Cheng et al. [52] also showed a change in ranking from polarisation tests and static immersion tests, with Fe and Zn resulting in the smallest corrosion rates for static immersion tests due to the fact that the solutions of corroded products were not attacked before ICP, thus $Fe(OH)_3$ and $Zn(OH)_2$ were not taken into account.

Zhang et al. [4] showed that phosphates precipitated on static immersion sample, possibly due to the local increase in pH of the iron surface.

Schinhammer et al. [3] showed during EIS that TWIP-1Pd corroded faster than TWIP which corroded faster than iron. The immersion tests give the same result with an overall decrease over time. The corners of the samples were attacked first but the corrosion seemed homogeneous except for TWIP-1Pd where the corrosion was concentrated around the twin boundaries.

As is evident from these studies, uncertainties are still present in this field of work.

2.6.5 Dynamic immersion tests: results and discussion

This aspect will not be studied in this present work. Nevertheless, it is very important in the understanding of flow-induced features.

Liu et al. [5] followed *Levesque et al.* [53] work and designed a dynamic immersion testing instrument to better simulate the blood flow. This can be seen on Figure 2.38. As previously highlighted, oxygen concentration plays an important role in the corrosion of metals in neutral media. This is why the system regulates the oxygen concentration to better mimic the blood environment (2.8-3.2 mg l^{-1}). The wall shear stress was controlled by the velocity of flow to be equal to 0.68 Pa, the temperature ranged between 36.9 and 37.1°C, and the pH was kept between 7.35 and 7.45 by adding NaOH or HCl. The specimens were mounted in paraffin and placed in a sample holder. The dynamic immersion test lasted 30 days as coronary stents are thought to be covered by endothelial cells after 30 days and would not be exposed to blood flow from there on. Surface morphology changes were inspected using a SEM instrument and the corrosion product layer was removed by peeling and dissolving in NaOH solution. After final cleaning, the specimen were weighed and the corrosion rate was calculated according to the following formula:

$$CR = \frac{m}{St} \tag{2.56}$$

where m is the mass loss in g, S the specimen surface area in m^2 and t the time in days.

The surface morphology changes seen on Figure 2.39 showed that local corrosion took place that initiated at the edges and the corrosion products grew in the flow direction. Some of the corrosion products got washed-out by the fluid flow. Except for pure iron, as-rolled Fe-Co, Fe-C, and Fe-S a localized bright metal surface was still present. There is also the presence of black corrosion products, which is a sign of the presence of FeO. The black corrosion products become brown when longer exposed to air due to the higher oxygen concentration in the air. In the dynamic immersion test, Fe-Mn still was the alloy exhibiting the slowest corrosion rate, which is consistent with the static immersion tests. These values can be found on Figure 2.32. It can be seen that the corrosion rates in dynamic immersion are higher than in static immersion as the corrosion products are washing out and the flow inhibits the accumulation of iron ions in localized regions.

2.6.6 Biocompatibility of the different specimens tested

Three different cell types play an important role when considering stenting: endothelial cells, vascular smooth muscle cells, and fibroblast cells. Indeed, blood vessels contain mainly endothelial cells, vascular smooth muscle and connective tissue (fibroblasts are the most present cells in this tissue, and they also play a critical role in wound healing) [54, 55]. A simplified illustration of the cell structure in an

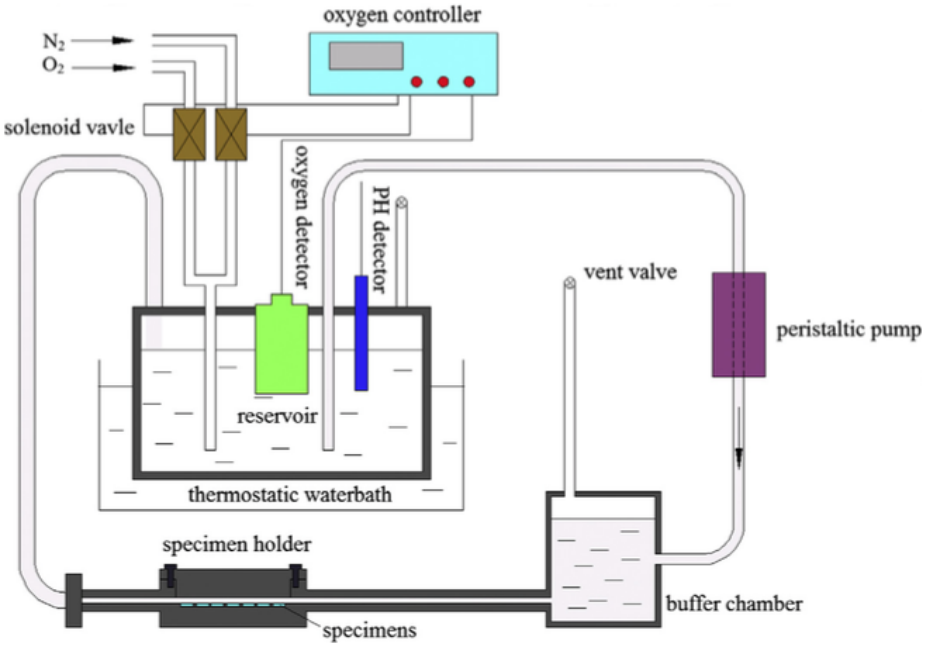

FIGURE 2.38: Schematic of the dynamic immersion testing instrument used by *Liu et al.* with Hank's solution circulating with a velocity such that the wall shear stress equals 0.68 Pa. The temperature was controlled by a thermostatic waterbath, the pH value regulated by the addition of NaOH or HCl, and the dissolved oxygen concentration was controlled by supplying oxygen and nitrogen [51].

artery can be found in Figure 2.40.

Liu et al. [51] found that Fe-Mn was cytotoxic to human umbilical vein endothelial cells (ECV304) but no other of the investigated alloys. On the other hand, all alloys and pure iron decreased the cell viabilities of Murine fibroblast cells (L929), and rodent vascular smooth muscle cells (VSMC) compared to 316L SS. The hemolysis percentage of all the alloys and pure iron were found to be less than 5% and the platelets adherent on the surface were round and not showing any thrombogenicity. For the Fe-30Mn and Fe-30Mn-6Si alloys [5], the cell viabilitiy of ECV304 and VSMC cells after 1, 2, and 4 days incubation in extraction media compared to stainless steel showed following order in cell viability: 316L SS>pure iron>Fe-30Mn>Fe-30Mn-6Si. The ion concentration released in these extraction media was the highest for Fe-30Mn-6Si alloy. This lower cell viability (lower biocompatibility) is thus explained by the higher corrosion rate. But from day 2 to day 4, the ECV304 cell viability increased and the fact that these cells viability is higher than for VSMC cells could be advantageous in the prevention of restenosis due to excessive neointimal smooth muscle cell proliferation. The hemolysis percentage being less than 2 % for these samples, they can be considered non hemolytic according to the ASTM-F756-08 standard.

Cheng et al. [52] showed that pure Fe, Mg, and W had no cytotoxic behaviour on L929 and ECV304 cells, whereas Mn induces high cytotoxicity to both cell types. Except for Mg (37% hemolysis percentage), the hemolysis percentage is lower than 5% and Fe, Mn, Zn, and W can thus be considered as non-hemolytic.

Zhang et al. [4] found that pure iron was non hemolytic. Platelet adhesion can lead to thrombus, which is why it has to be investigated. It was shown that the platelet were round-shaped and of low number showing good anti-platelet adhesion properties compared to Mg-Mn-Z alloy and stainless steel.

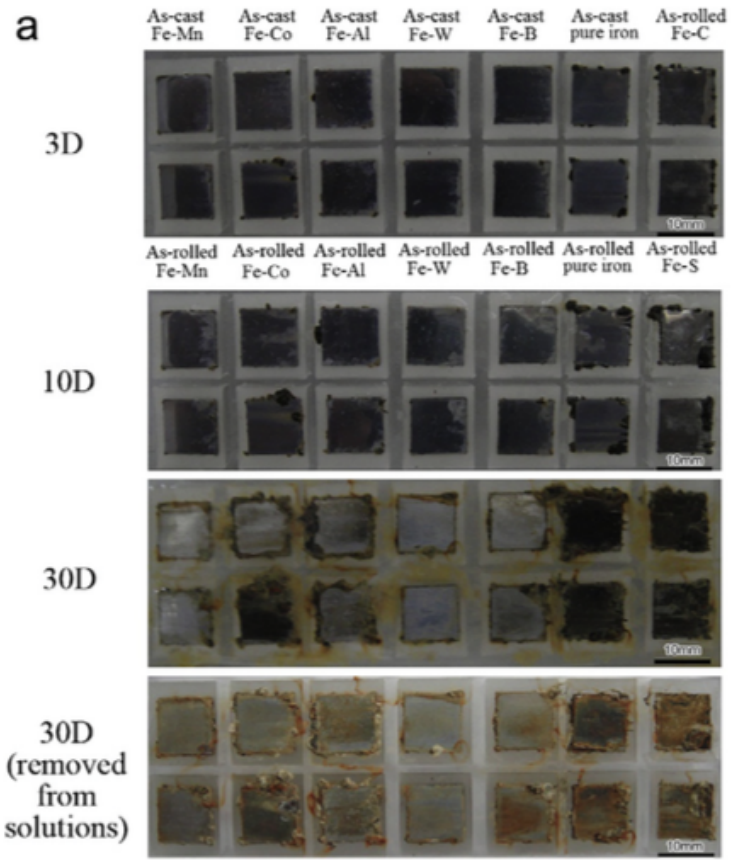

FIGURE 2.39: Surface morphologies of Fe-X alloys compared to pure iron after 3, 10, and 30 days dynamic immersion [51].

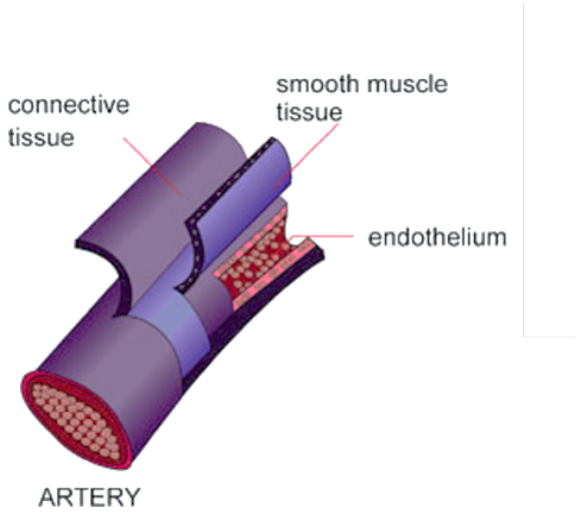

FIGURE 2.40: Simplified illustration of the cell structure of an artery [56].

The pure iron was also shown to have excellent anti-coagulant properties.
Iron can be cytotoxic to cells because it can generate reactive oxygen species via Fenton reactions:

$$Fe^{3+} +^{\bullet} O_2^- \longrightarrow Fe^{2+} + O_2 \tag{2.57}$$

$$Fe^{2+} + H_2O_2 \longrightarrow Fe^{3+} +^{\bullet} OH + OH^- \tag{2.58}$$

Highly reactive oxygen species (ROS) such as hydroxyl anions and superoxide radicals (O_2^-) are highly toxic as they can rapidly react with almost every molecule in the living cells. But these ROS are also generated during normal metabolism and so as long as the iron concentration is lower than a critical value, the body will be able to defend itself against excessive ROS accumulation and their effects. *Zhang et al.* found that the critical value was of 0.075 mg/ml and previous studies reported that this critical value should be 0.05 mg/ml close to the one calculated in Zhang's study.

2.6.7 Effect of twins and surface roughness on corrosion behaviour

2.6.7.1 Twinning effect

Aung et al. [57] investigated the effect of twins on the corrosion behaviour. It was shown that the presence of twins accelerated intergranular corrosion. In twinned microstructures, the grain size was less affecting the corrosion rate than in untwinned microstructures.

Grajcar [58] also investigated the effect of twins on corrosion as well as the deformation effect of TWIP steels on corrosion. In cases where two phases were present (ferrite and austenite), which is the case in Fe-0.2C-25Mn-8Al, corrosion preferentially occurs in the ferrite phase. *Ghayad et al.* [59] investigated the effect of deformation of Fe-0.5C-29Mn-3.5Al-0.5Si steel on corrosion. Deformed specimens corroded faster due to annealing twins which induced faster steel dissolution. Strain-aged samples had the highest corrosion rate due to the presence of ferrite which created a corrosive galvanic cell within the austenite matrix. *Mazancova et al.* [60] also observed higher corrosion attack at deformation twin boundaries in Fe-22Mn-0.5C. By increasing the steel strength, the hydrogen embrittlement susceptibility is also increased. Hydrogen has a low diffusion rate in austenite and is thus less susceptible to cause hydrogen embrittlement. However, *Lovicu et al.* showed that the hydrogen content in high-Mn steels is much higher at the surfaces than in the centre and this can cause intergranular fracture because of strain-induced or hydrogen-induced martensitic transformation and thus to a decrease in strength and ductility. *Grajcar* [58] showed that the percentage of mass loss of plastically deformed samples was slightly higher than non-deformed samples in acidic solutions but slightly lower in chloride solutions and that the mass percentage loss in steels with single austenitic phase was slightly lower than in steels with ϵ-martensitic lamellas. The steels containing these ϵ-martensite plates (in initial structure, strain-induced or hydrogen induced) are especially susceptible to corrosion cracking in chloride solution. *Khalissi et al.* [61] also showed that TWIP samples tested in chloride solution suggested that twin bands played a profound role in environment-assisted crack propagation, whereas samples tested in air revealed a ductile failure.

2.6.7.2 Surface roughness effect

It has been shown that the surface roughness plays a very important role in corrosion [62, 63]. When passive films can form as the surface roughness decreases, these passive films protect the metal from corrosion and thus corrosion is faster for rougher surfaces where more available active sites are present able to form pits. Thus, stainless steel for example exhibits lower corrosion rates for smoother surfaces [62]. However, when these passive films do not form, as is the case in mild steel, the inverse effect has been observed [63]. This was explained by the fact that the passive film of mild steels is weaker

for smooth surfaces (the breaskdown potential is more noble for higher surface roughness) and can easily break down and as the electrolyte contained chloride ions, which are aggressive and responsible for pits formation. These pits propagate at such a fast rate, that the corrosion rate would increase [63]. *Landolt* [64] showed that rougher surfaces increased the friction coefficients and thus the mass transport rate, leading to higher corrosion rates. This has also been illustrated in the "*Flow-induced corrosion*" section. Thus, no typical theory has been found in order to investigate the surface roughness effect on corrosion.

2.6.8 Proposed corrosion mechanisms

Regarding the different findings, *Liu et al.* [51] proposed a possible corrosion mechanism taking place:

1. **Initiation**: When the Fe-X alloys are immersed, there is anodic dissolution of iron that takes place. The Fe^{2+} ions combine to OH^- ion in solution to form iron(II) hydroxide, which will further be oxidized by the oxygen present in the solution.

2. **Formation and growth**: Due to chloride ions accumulating at the metal-solution interface, the passive film could break down, which would lead to pits formation covered by a loose corrosion layer. Changes inside the pits are due to localized acidification and chloride ions accumulation. And the corrosion potential of iron continues to decrease resulting in a self-catalytic corrosion. At some point, CaP compounds will form on the specimen surface.

3. **Development after 6 months**: There are two different possible outcomes:

   (a) One outcome was that the pits just grew bigger and deeper while shiny metal parts were still visible (protected by passivation).

   (b) The other outcome is that the whole surface was covered by a thick layer of corrosion products. This layer increased the anodic dissolution of iron. Thus, a larger specimen surface covered by corrosion products meant more activated reaction positions which lead to a higher corrosion rate.

Such a localized corrosion is unwanted as it could cause local failure as well as an unpredictable corrosion rate. Unfortunately, the high chloride concentration in blood plasma is not helping towards a uniform corrosion. Also, crevices can be formed between the stent and the inner wall of the blood vessel. The stress distribution being not uniform at different points along the stent, this can also lead to localized corrosion. Thus, different improvements could be done:

- Pits should be formed during the formation and growth stages on the whole surface in such a way that after a while, the different pits will get connected forming a generalized corrosion surface. Adding a secondary phase of intermetallics could be a way to achieve this.

- The pits should grow horizontally. Due to the self-catalytic iron corrosion mechanism, this is hard to achieve. Decreasing the localized acidification, this could be helpful in order to achieve this corrosion mechanism.

The two present corrosion mechanisms and the two ideal corrosion mechanism just highlighted can be seen on Figure 2.41.

Schinhammer et al. [3] also proposed a degradation mechanism in SBF for TWIP alloys:

The anodic reactions are iron and manganese dissolution into Fe^{2+} and Mn^{2+} ions.

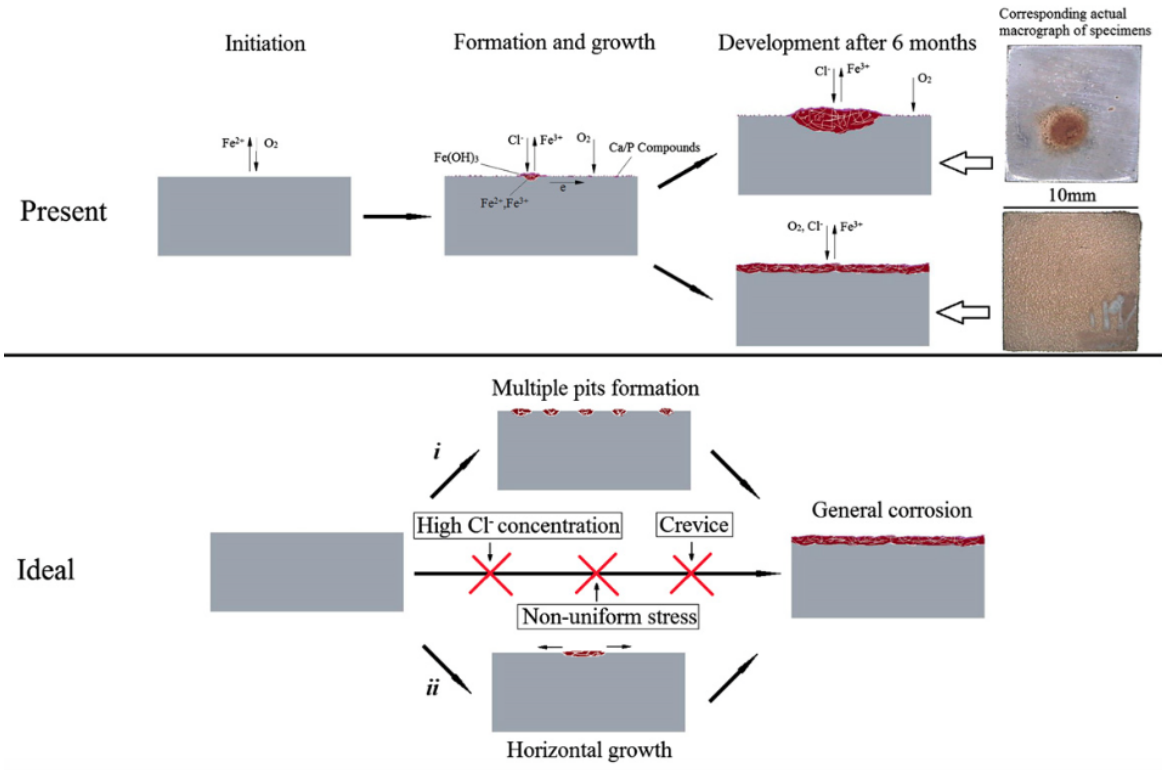

FIGURE 2.41: Present and ideal corrosion mechanisms in Hank's solution [51].

The cathodic reaction, generally rate determining and diffusion-controlled is the reduction of oxygen:

$$H_2O + \frac{1}{2}O_2 + 2e^- \longrightarrow 2OH^- \tag{2.59}$$

As iron is the main component of the alloys, the following mechanisms will only consider what is happening to iron. Figure 2.42 shows schematically the corrosion mechanism where anode and cathode are at different places. The iron ions will react with the hydroxyl ions to form hydrous ferrous oxide $FeO.nH_2O$ or $Fe(OH)_2$. At the outer layer, this hydroxide can further react with dissolved oxygen to form hydrous ferric hydroxide $Fe(OH)_3$. Hydrous ferric oxide (Fe_2O_3) has an orange or brownish aspect and degradation products usually have a layered structure with $FeO.nH_2O$ on the first layer (next to the metal), a black intermediate layer made of $Fe_3O_4.NH_2O$ and a top layer made of hydrous $Fe_2O_3.nH_2O$. Orange-white degradation products were also found on the samples and correspond to calcium rich layers. Iron and manganese ions are also able to react with CO_3^{2-} ions that are present in SBF. The hydroxyl ions generated by the cathodic reaction generate a local increase in pH, which promotes the precipitation of carbonates and phosphates. Because of these compounds, the degradation rate will decrease after a while due to mass transport limitations through the precipitates. Iron was found to be more present in a close vicinity to the metal, whereas manganese was found to be more present in the intermediate and top layers, showing that manganese diffuses away from the metal interface to react with dissolved oxygen. A high Cl^- concentration was found in the bottom layer, showing that these ions play an important role in the degradation mechanism. Some iron ions will thus react with chloride ions:

$$Fe^{2+} + 2Cl^- \longrightarrow FeCl_2 \tag{2.60}$$

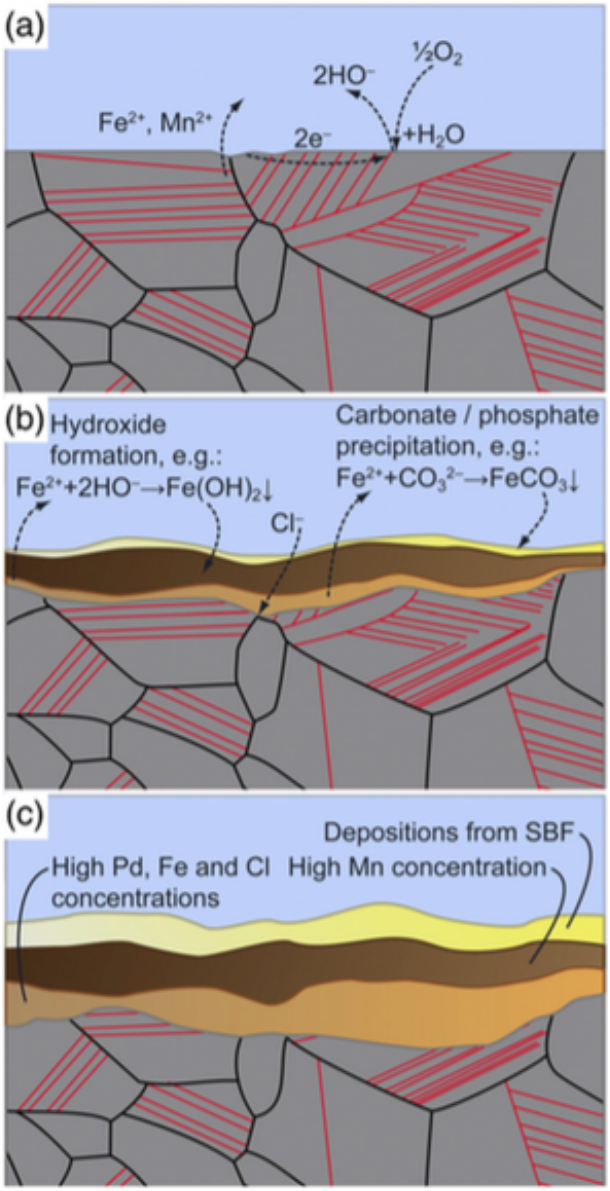

FIGURE 2.42: Schematic of the corrosion mechanism of TWIP-1Pd proposed by Schinhammer et al. [3].

The same thing takes place with manganese ions. These chlorides are then hydrolyzed by water and generate acid which will cause localized corrosion.

$$FeCl_2 + H_2O \longrightarrow Fe(OH)_2 + HCl \tag{2.61}$$

If no diffusion barrier is present due to the corrosion products, the theoretical current density is calculated following:

$$i_s = \frac{DnF}{d} c_{O_2} \tag{2.62}$$

where D is the diffusion coefficient for dissolved oxygen in water, n = 4 eq mole^{-1} is the number of electrons transferred, F is the Faraday constant, d is the thickness of the stagnant layer, and c_{O_2} is the

dissolved oxygen concentration.

This would mean that under limited mass-transport conditions, the composition of an alloy would not have any impact on the degradation rate. However, this was not observed. But, these conditions are only valid at the beginning of the experiment when the whole metal surface is accessible for corrosion reactions. However, degradation products start forming after a certain time and this hinders the oxygen diffusion and therefore decreases the degradation rate. And it can be assumed that the corrosion product layers differ from alloy to alloy and so the accessible surfaces for the cathodic reaction are different. However, the EIS measurements pointed out that the oxygen reduction was not totally mass-transport limited but also partially involving charge-transfer. The authors also explained the increased degradation rate due to the addition of Pd by its high H_2 affinity and its accelerating effect on oxygen reduction. Therefore, additional H_2 evolution and oxygen reduction that are catalyzed by Pd-rich precipitates could explain the greater degradation rates.

2.7 State of the art conclusion

Different kind of stents have been detailed: balloon-expandable, self-expanding, bare metal stents, drug-eluting stents, and bioresorbable stents. The latter category is the one of interest in the present work. Indeed, once the mechanical support needed by the artery has been obtained, the stent is of no use and can have adverse effects on the human body. Polymer-based bioresorbale stents have been investigated but these present weak mechanical properties. Metal-based bioresorbable stents encompass magnesium-based stents and iron-based stents. The former degrades during the four first months of implantation, which corresponds to a corrosion rate too high in order to fulfil its task. It could even mechanically fail under four months. Iron-based alloys degrade too slowly. This is why, TWIP alloy is going to be investigated. These alloys present exceptional work-hardening properties making them great candidates from a mechanical point of view. In addition, it has been proven that by adding manganese, the corrosion rate is increased compared to pure iron [5, 6, 3, 7].

The corrosion behaviour of the Fe-22Mn-0.6C TWIP alloy will be studied by performing electrochemical and immersion tests and by undertaking a morphological study of the corroded surface. The corrosion mechanisms have thus been introduced. Metals can either corrode uniformly or present localized corrosion such as pitting. The theory hidden behind electrochemistry was described in the next section. The important aspects to remember are that the kinetics relations, such as Butler-Volmer, are only valid when charge transfer is limiting. The corrosion current density is found as being the current density value when the anodic and cathodic current densities are equal, in which case the total measured current is zero. The corrosion potential is thus the potential where the measured current density is zero. In a Tafel plot, there is a region (low currents) where non-linear behaviour is observed. In this region, the polarisation resistance can be measured and the corrosion current density can be deduced from it. However, this method can only be used if the charge transfer is limiting but not the mass transport. At intermediate currents, a linear behaviour is observed, giving rise to anodic and cathodic Tafel lines, and the intersection between these two lines at the corrosion potential gives the value of the corrosion current density. When mass transport is limiting, the values obtained for the Tafel slopes (in mV/dec) are more important than the theoretical values. At higher currents, an asymptotic behaviour takes place, where the limiting current range is reached. When potentiodynamic polarisation tests are performed, capacitive currents should be taken into account as well as iR drops. In fact, a certain capacity arises from the double electric layer and the importance of this effect increases with higher scan rates. iR drops are due to the electrolyte conductivity. Ions need to diffuse through the electrolytes and if a solution is more or less conductive, a certain resistance will arise. This resistance also depends on the distance between the working electrode and reference electrode (being

higher for longer distances). The films that deposit on the sample also present a certain iR drop but this resistance is variable throughout the polarisation test.

A final point was made by highlighting the findings from different authors on the corrosion of iron-based alloys. The studies concentrated on polarisation tests and static immersion tests with sometimes dynamic immersion tests, which mimic the in-vivo behaviours in a more realistic way. Biocompatibility studies have also been described.

CHAPTER 3

MATERIALS AND METHODOLOGY

3.1 Investigated samples

Two different materials will be investigated:

1. Armco iron which composition has been determined by ICP [1] (see Table 3.1).
2. Fe-22Mn-0.6C TWIP steel which composition has also been determined by ICP (see Table 3.1).

Table 3.1: Composition of Armco iron and Fe-22Mn-0.6C steel determined by ICP.

Sample	%wt										
	Fe	Al	Cr	Cu	Mn	Ni	P	Si	Ti	Mo	V
Armco iron 1.5 mm thickness	98.8	0.04	0.02	0.02	0.67	0.03	0.02	0.32	0.06		
Fe-22Mn-0.6C	76.8		0.18	0.04	22.2	0.07	0.03	0.21		0.01	0.2

The carbon content of the TWIP samples was analyzed by oxygen combustion and found to be 0.55 wt.%.

Stents will undergo different deformations before final placement: compressions and extensions. Thus, the Fe-22Mn-0.6C TWIP steel samples were deformed at different rates. However, as compressing test samples would cause buckling, only tensile deformations will be studied. Following deformations were performed: 10%, 20%, 30% and 40% by the means of a Zwick 1474 instrument with a maximum capacity of 50kN [2]. The tests were performed with the following characteristics:

- A 100N pre-charge is performed
- A deformation rate of 2mm/min is imposed
- A data point is obtained every 2 μm or 5N
- The test is terminated once the wanted deformation is achieved [3].

[1] with 3% relative error accepted

[2] The deformed samples used by Olivier Declerck last year were first used and two new tensile tests were performed to achieve 40% and 10% deformation.

[3] During the test, the force is imposed and the deformation measured.

FIGURE 3.1: Electrical contact made by a copper sheet if front of the sample.

3.2 Potentiodynamic polarisation tests

3.2.1 Sample preparation

Armo iron samples

The first purpose of this work was to establish a reliable experimental protocol on Armco iron. In order to achieve this, different samples were tested. A first batch of 1cm x 1 cm square samples were tested (designated as Fe 1 to 7). The reproducibility of these samples was not conclusive. The biggest issue of these samples was their size. Indeed, the circular cell opening is of 0.894 cm^2 and as copper sheets were used to make the electrical contact between the sample and the working electrode (see Figure 3.1) the remaining corners were too small to allow a perfectly established electrical contact between the copper sheet and the sample. The next samples (Fe 9 to 21) had surface areas of 1.5cm x 1.5cm allowing the contact to be more reliable.

These samples were first mounted in a conducting Polyfast resin. The compression mounting was made using a 20kN force and by first heating the resin to 180°C for 6 minutes followed by 3 minutes cooling.

Once the specimens are mounted, they were polished. First, the samples are pre-polished using P320 grit SiC paper, P800 grit SiC paper and P1200 grit SiC paper. Then, 6 μm and 1 μm polishing steps using diamond paste are undertaken. Both steps last 10 minutes. The final step consists of suppressing the strain-hardened layer by chemically polishing the samples. This was done by using a non-drying colloidal silica suspension (OP-S NonDry) [65]. In order to define which timing would be most suitable in order to suppress the deformation layer but without chemically attack the sample, different iron samples with different OP-S times were observed at the scanning electron microscope (SEM). Figure 3.2 shows the effect on the microstructure for the different OP-S times used: 1, 2, 5, 15, and 30 minutes. 15, and 30 minutes result in a too attacked samples; 5 minutes still shows some traces of a chemical attack whereas samples with 1 and 2 minutes OP-S do not show significant attack. The scratches are as present for 1 minute OP-S than for 2 minutes. This is why, it has been decided to polish all following samples up to 1 minute OP-S. It can be noted that the samples were rinsed and cleaned with use of distilled water and ethanol between each step.

A final third batch of Armco iron was made. These samples underwent the same polishing steps but were either removed from the mounted resin (specified as Fe X - SR, with surface area 1.5 cm x 1.5cm) or polished directly without being mounted (one sample; specified as Fe-Rod) in order to allow the electrical contact to be made either with a copper sheet from behind the sample or directly from the sample respectively. The electrical contact must be optimal in order to allow accurate measurements.

It has to be noted that some samples are re-polished once a potentiodynamic polarization test is performed. These samples are then re-polished from the step P1200 grit SiC paper.

Note also that from th 24^{th} of March on the sample/copper sheet ensemble was covered by a porthole, allowing a better waterproofness (see Figure 3.3d).

Fe-22Mn-0.6C TWIP samples

These samples were prepared following the same procedure as the mounted Armco iron samples, i.e. mounted in a Polyfast resin, polished using SiC papers (320, 800, 1200), 10 minutes 6 μm step and 10 minutes 1 μm step and finally 1 minute OP-S. Again, when samples are re-polished, the polishing will start from the step P1200 grit paper.

However, some samples will be polished up to 3 minutes OP-S for SEM microstructure images but it will be specified when this is the case. Also, when samples are re-polished, they will be named Fe X-Y (e.g. Fe 19-3 means Fe 19 sample polished for a third time) or TWIP X-Y (e.g. TWIP 1-2).

3.2.2 Experimental setup

The first analysis made in this study is to evaluate the corrosion rate of the materials tested by using quick methods such as polarisation tests. With these tests, a certain corrosion behaviour can be deduced. However, it has to be kept in mind that during these tests, electrochemical reactions are forced to take place by injecting current into the system, which is not what is going to happen with the stents placed inside an artery. Section 2.5.2.3 details the aspects of the polarisation investigation.

The three-electrode cell as well as a sample ready for testing can be seen on Figure 3.3. The counter electrode is a platinum electrode and the reference electrode a saturated calomel electrode. The potentiostat used is an Autolab PGSTAT302N and the software is Nova 1.10. The principle behind a three electrode cell has already been explained in the previous chapter (section 2.5.2.3). Note that, in such a cell electrochemical reactions are studied by imposing a certain potential and requiring the Autolab to compensate the needed current at that certain potential. Thus by scanning towards specific potential ranges, different electrochemical reactions can be studied. A simplified illustration of an electrochemical cell can be seen on Figure 3.4. The experimental parameters are as follow: room temperature, 315ml cell, 7.4 starting pH [4], and the electrolyte is simulated body fluid (SBF). Hepes buffer is sometimes added to the electrolyte for better pH regulation.

[4]The pH value was regulated by adding HCl to the solution to reach that pH. Throughout the test, the pH increased to values up to 7.42 if 50mM Hepes buffer was used, 7.46 if 25mM Hepes buffer was used, 7.56 if no buffer was added.

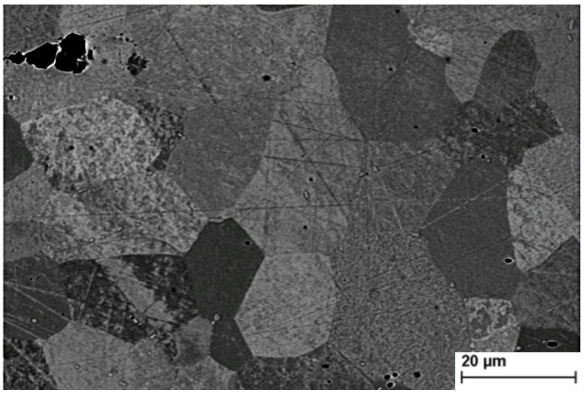

(A) SEM BSD image for 1 minute OP-S.

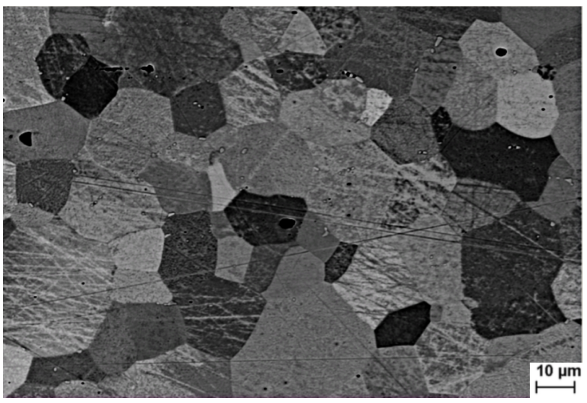

(B) SEM BSD image for 2 minutes OP-S.

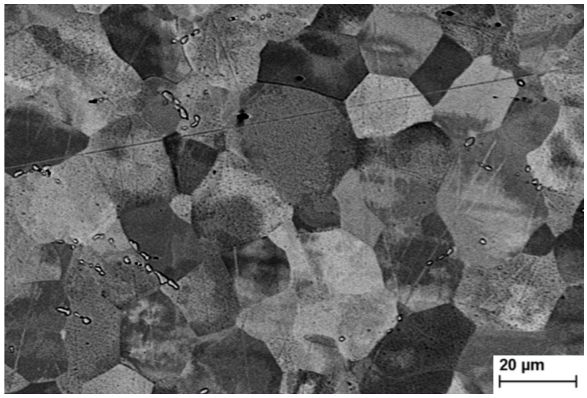

(C) SEM BSD image for 5 minutes OP-S.

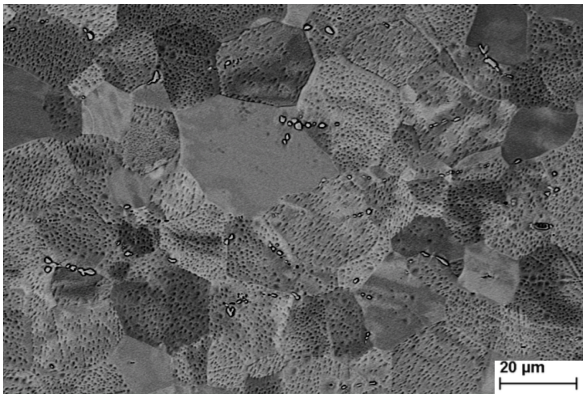

(D) SEM BSD image for 15 minutes OP-S.

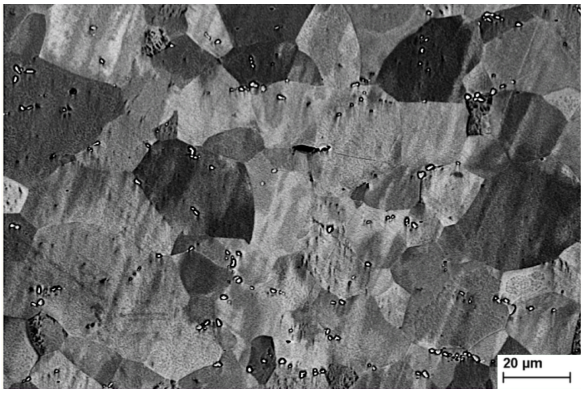

(E) SEM BSD image for 30 minutes OP-S.

FIGURE 3.2: SEM AsB images for OP-S time determination: 1, 2, 5, 15, and 30 minutes.

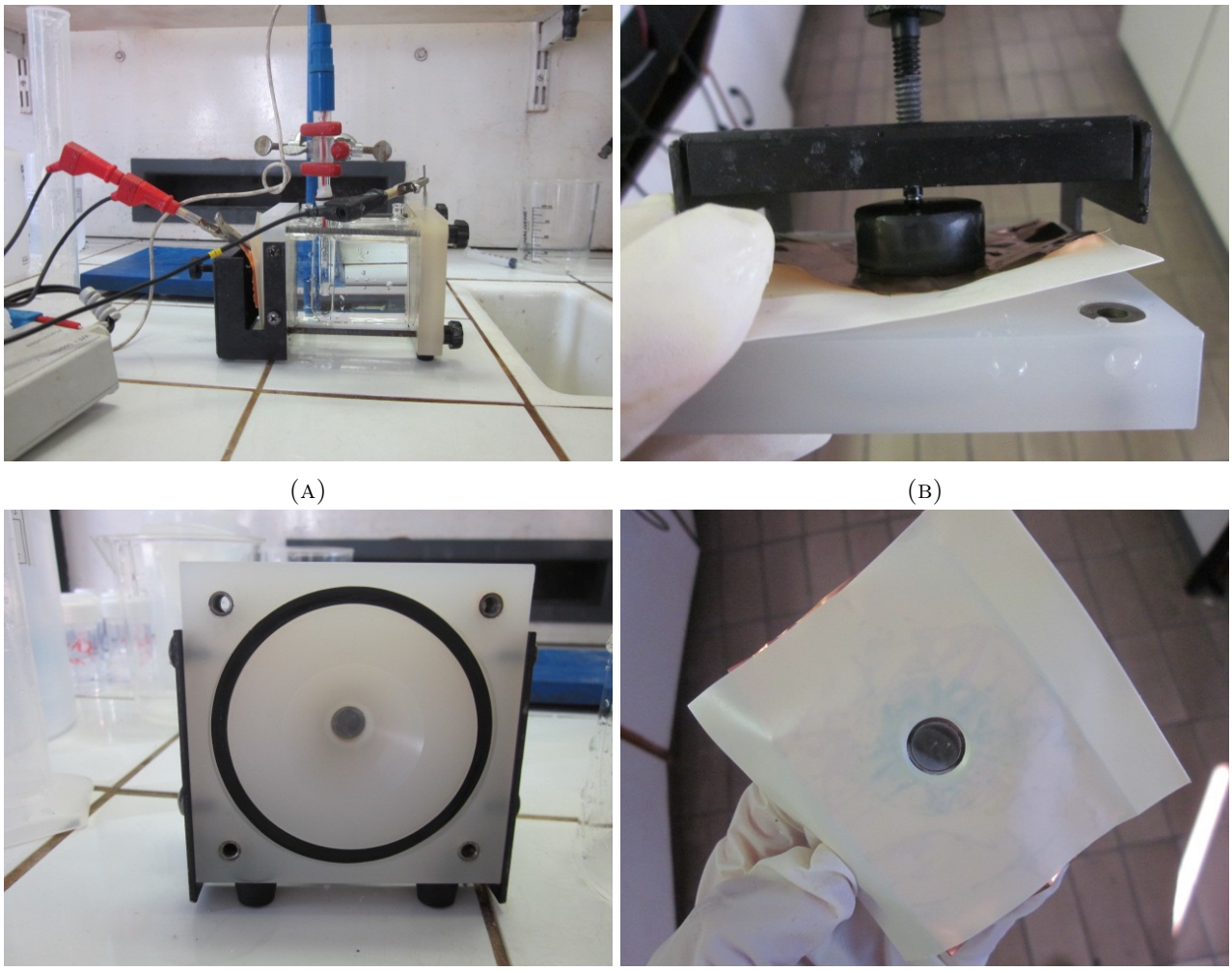

(A) (B)

(C) (D)

FIGURE 3.3: (A) illustrates the experimental setup used for the electrochemical tests, where the working electrode is seen on the left with the electric contact between the working electrode and the potentiostat is made possible by the copper sheet and the crocodile clip. On the right, the platinum counter electrode is connected to another crocodile clip. In the middle, the calomel reference electrode is seen. (B) shows a sample ready for testing from behind and (C) from the front, (D) shows that same sample outside of the cell, where the porthole is clearly seen and the copper sheet can be seen underneath that porthole.

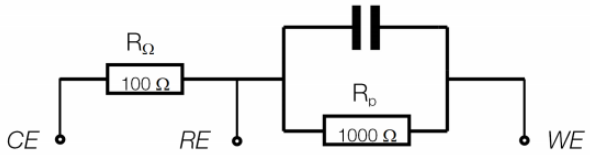

FIGURE 3.4: Simplified electrochemical cell illustration with the capacitance and resistances typical of such an electrochemical cell [66].

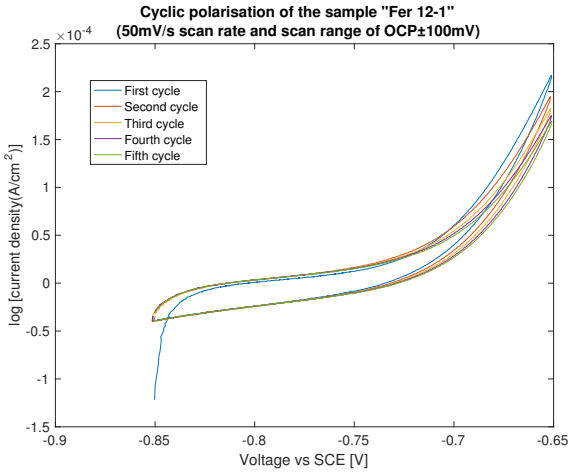

FIGURE 3.5: Representation of the five cycles undergone for CV scans with 50mV/s scan rate and OCP±100mV scan range.

3.2.3 SBF composition

Simulated body fluid is used as electrolyte in the present work and it composition can be en on Table 3.2.

TABLE 3.2: Composition of the SBF used for this study.

Compound	**g/l ultrapure water**
Mg chloride hexahydrate	0.2033
Na chloride	6.0193
K chloride	0.2982
dibasic Na phosphate	0.1420
Na sulfate	0.0710
Ca chloride dihydrate	0.3676
Na acetate trihydrate	0.9526
Na bicarbonate	2.6043
Na citrate dihydrate	0.0970

3.2.4 Categories tested

The first purpose was to define a reproducible method for corrosion measurements. It was already proven in different articles that the iron reproductibility is not an easy task. A previous study was

already performed on the subject by Olivier Declerck [67]. First, it was decided to follow the experimental setup of *Olivier Declerck*. In this study the bad reproducibility of iron was already highlighted and a possible track to overcome these reproducibility issues was to perform rapid scans to avoid surface changes during the scan, i.e. preform cyclic voltammetries (CV) at high scan rate. In such cyclic voltammetry, the scan is first performed anodically from OCP-100mV to OCP+100mV. Then the scan is reversed cathodically from OCP+100mV to OCP-100mV. Five cycles in a row are undertaken. Such a plot can be seen on Figure 3.5 [5]. The OCP value is found by letting the open circuit potential stabilize between 2500s and 7200s, depending on each sample. The first cycle should not be used for data analysis as during the first cycle, the surface is not the same as during the next cycles. Thus, the other cycles could be used, such as the 3^{rd} or 5^{th} cycle (here the 5^{th} cycle is chosen). It has to be noted that when a high scan rate (50mV/s in this case) is used, a certain capacitive current is influencing the scan. This current is proportional to the scan rate:

$$I_{cap} = C_{dl}\frac{dE}{dt} \tag{3.1}$$

Thus, it can be assumed that this capacitive current[6] is suppressed during a return cycle and the faraday current is thus equal to half a return cycle:

$$i_{one-way} = i_{farad,one-way} \pm C_{dl}\frac{dE}{dt} \tag{3.2}$$

And so for a forward and reverse scan combined,

$$i_{return} = i_{farad,forward} + i_{farad,return} + C_{dl}\frac{dE}{dt} - C_{dl}\frac{dE}{dt} = 2i_{farad} \tag{3.3}$$

A graph showing a resulted plot in logarithmic scale can be seen on Figure 3.6 along with the corresponding cycle and mean "cycle". The vertical line corresponds to the observed corrosion potential and the linear lines are the extrapolated Tafel lines and their intersections with the observed corrosion potential will be denoted as anodic and cathodic corrosion current densities. The anodic Tafel line is the one on the right side of the graph, which is the part of the scan where the anodic reaction takes place. The cathodic line is the one on the left side of the graph, where the cathodic reaction takes place.

Another study was to see the effect of previously letting the sample stabilize in the SBF solution or not. Up until now, all samples were left the time to stabilize [7]. Stabilization could last less than an hour or more than two hours and was varying from sample to sample [8]. It was then tested to see if by letting the system immerse in the SBF solution for three minutes as soon as in contact with the solution, the reproducibility of the tests would be more pronounced than for the samples undergoing total stabilization. The method used to compare these categories is CV 50mV/s with OCP±100mV scan range.

Other tests, with cyclic voltammetries 100mV from each side of OCP as scan range and 50mV/s scan rate were tested but with different ways of making the electrical contact. In the sample preparation section, it was already talked about iron rods tall enough to be used as their own electrical contact. Samples that were taken out of their mounted resin and where the electrical contact was still made by the use of a copper sheet, but this time from behind the sample where also detailed in the sample preparation part. Other tests involved the use of carbon lacquer and carbon tape in order to make

[5] It can be seen the cycles have very similar cathodic behaviour but the anodic parts differ from cycle to cycle.

[6] This statement should be used with precaution as the capacitance could change during the scan.

[7] Sometimes, the samples were not sealed impermeably which resulted in a voltage rise over time and such results will not be analyzed

[8] As said in the previous paragraph stabilization is obtained by leaving the system reach a steady state equilibrium.

sure that the contact between the copper sheet and the sample was optimal.

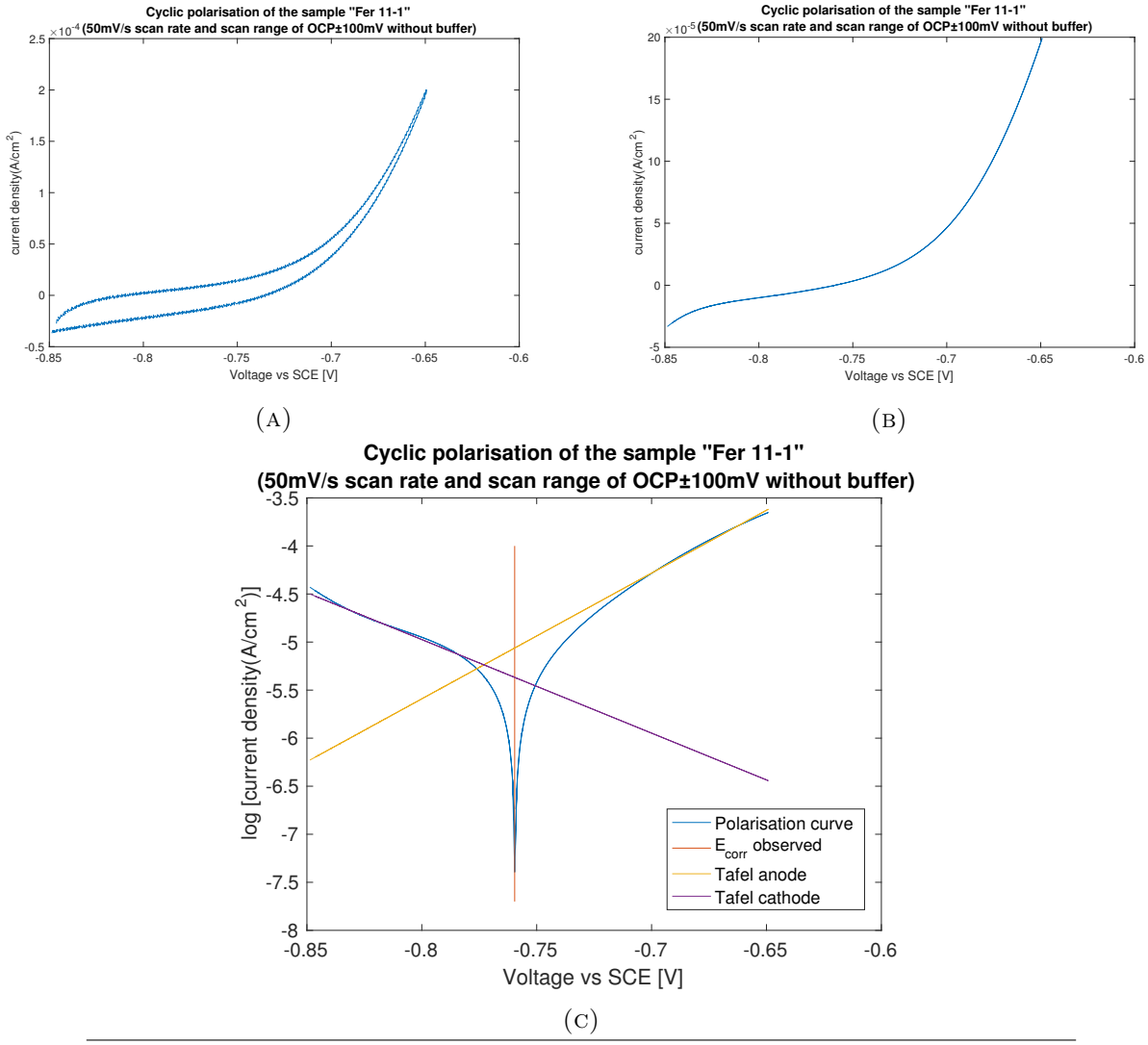

FIGURE 3.6: Example of a cyclic voltammetry analysis, with (A) a raw fifth cycle, (B) an average of such cycle and finally (C) a Tafel analysis, with the observed corrosion potential, the anodic and cathodic Tafel lines also illustrating the cathodic and anodic corrosion current densities. The anodic corrosion current density is found by the intersection of the anodic extrapolated Tafel line and the observed corrosion potential and the cathodic corrosion current density by the intersection of that observed corrosion potential and the cathodic extrapolated value.

The next step was to study the effect of the method on the corrosion behaviour and system reproducibility. CV 50mV/s scans were compared to linear sweep voltammetries (LSV). LSV were tested with scan ranges 0.33mV/s and 1mV/s. Indeed, most articles use this method and in most corrosion references, scan rates below 1mV/s are favoured. In such a technique a one-way anodic scan is performed from OCP-100mV to OCP+100mV and by avoiding a cathodic scan [9], it is made sure that the starting surface is not heavily corroded before forcing the scan. For these LSV tests, the OCP was left to stabilize. It can also be noted that the capacitive current is negligible with such small scan rates as

[9]Performing a cathodic scan means that the potential is imposed from more positive values to more negative ones. An anodic scan is the opposite: the potential is scanned from more negative to more positive values.

the capacitive current is proportional to the scan rate (see equation 3.1)

The next step was to study the effect of scan range (100, 150, 200, and 300 mV) on the free corrosion potential and free corrosion current density. This is of importance as 100 mV from each side of the OCP is not enough in order to define Tafel lines. Indeed, it has been shown in the previous chapter, that for the high field approximation to be valid, the range involved for the determination of thee lines should be at least 100 mV away from the OCP [49]. Some other references agree that 50 mV away from the OCP is enough [68] or 80mV [69] But still, having plots with only 100 mV away from the OCP is not optimal for such an analysis. The effect of scan range was studied on CV 50mV/s (100mV and 300mV) and LSV 1mV/s (100mV, 200mV, and 300mV) and LSV 0.33mV/s (100mV and 150mV). Other studies also pointed out that the current must be observed through at least one decade in order to have a good Tafel aproximation [70, 71].

The impact of buffer has also been investigated. All the above categories were tested without any buffer. It was investigated if adding Hepes buffer alters the corrosion rate depending on the buffer concentration (25mM and 50mM). The buffer effect was investigated because the static immersion tests underwent too important pH changes over the tested times for iron [10]. The first tested concentration was 25mM followed by 50mM Hepes buffer. The effect of pH induced by this buffer was also investigated. These effects were tested using the LSV 0.33mV/s and OCP±150mV scan range method.

The last studied parameter was the effect of repolishing. The method used was LSV 0.33mV/s.
Once the best method had been chosen, tests on the different samples of interest (TWIP samples with different deformations) could be undertaken using this method. The method that was decided on was a linear sweep voltammetry with 0.33mV/s scan rate and 150mV scan range to allow a better Tafel fit and the electrolyte chosen will be SBF with addition of 50mM Hepes buffer. The scan ranges as well as the scan rates and methods used will always be clearly stated for each sample.

3.2.5 Corrosion current density determination

The corrosion current density calculation as well as the corrosion rate calculation were undergone using different methods. Indeed, there is more than just one way to tackle the problem of corrosion rate determination. Theoretically, the cathodic current and anodic current should be equal at the free corrosion potential but that is rarely the case in practice. One example is a disturbance due to charging current can result in a difference between the anodic and cathodic extrapolated values at E_{corr}, (from the Tafel lines), where the measured current is zero [69].

First it needs to be said that the corrosion rate measurement by the help of resistance polarisation will not be undertaken as the Tafel slopes values are needed and if the oxygen reduction is diffusion limited it would be faulty to define such a slope (see equation 2.51). See section 2.5.2.5 for details on this technique and Figure 3.7 for an illustration of a system where oxygen reduction is diffusion limited.

Schweinsberg et al [70] studied different methods to obtain the best possible reproducibility of corrosion parameters for acidic iron dissolution and these methods determined the corrosion current density either by the **extrapolation of anodic and cathodic Tafel lines on a mean corrosion potential** value **or only** by extrapolating the **cathodic** current Tafel line on the corrosion potential.

Princeton Applied Research application note on *"Basics of Corrosion Measurements"* [72] states that **the corrosion process is usually resulting from anodic currents**. Further in that same application note they highlight the fact that the corrosion mechanisms are quite difficult to interpret as

[10] The tests were performed by Aude Thomas and Eleonora Scarcello.

more than one element can be present in the corrosion mechanism. Additionally, surface effects are also present (such as passive film formations etc). They also state that it can happen that in experimental tests, the anodic and cathodic extrapolated values do not intersect at E_{corr}, in which case the corrosion current density value is to be found by interpretation. It is stated, that most of the time, the error comes from the anodic part as the Tafel plot could be reflecting a combination of different Tafel slopes either than a simple metal oxidation reaction or also because non metallic parts in the solution that could take part in the oxidation process). Additionally, the **surface changes** which can possibly affect the corrosion mechanism. In this case it is best to consider the corrosion current density as the **intersection between the cathodic extrapolated value and the corrosion potential**. In another application note of Princeton Applied Research *"Electrochemistry and Corrosion: Overview and Techniques"* [73], it is stated that **when both cathodic and anodic extrapolated values do not intersect at the corrosion potential, the most linear Tafel line needs to be taken into accounts** as the other one could be affected by more complex mechanisms.

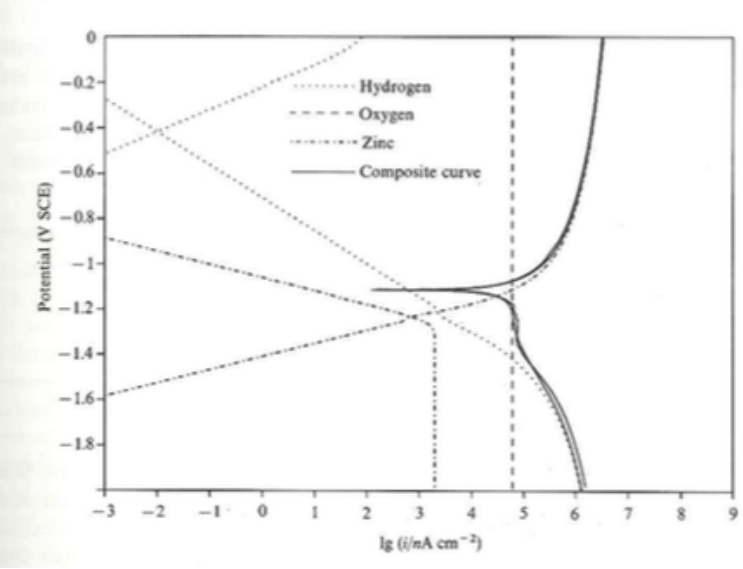

FIGURE 3.7: Experimental and model curves for zinc in 3% NaCl solution acidified solution. The oxygen plateau is seen at the beginning of the cathodic region (bottom of image) [34].

Sato [74] considers that **the corrosion current density is determined at the point where both cathodic and anodic extrapolated values are equal**. However, in his document, it is also shown that this intersection corresponds to the potential where the actualmeasured current is zero, i.e. the oberved corrosion potential [11]. *Badea et al* [68] agree with the corrosion current density being the one when the cathodic and anodic extrapolated values intersect. However they also agree on the fact that such graphical estimation can lead to quite high errors. Indeed, poor selection of slopes can change the current density by a factor of 5 to 10. Thus, at least one branch should exhibit a linear behaviour for at least one decade and should start at least 50 to 100mV away from the OCP. A lot of factors can erroneously change the Tafel lines such as ohmic losses leading to a curvature (and thus leading to higher corrosion current densities) or diffusion controlled processes. Also, for more accurate interpretation, before starting the polarisation scan, the potential should be left to stabilize to a value that does not change more than 5mV over 10 minutes.

[11] The measured current density is zero when the anodic and cathodic current densities are equal, which is the point that defines the corrosion potential and current density in theory (see section 2.5.2.1 for more detail).

Finally *Chamberlain at al.* [34] states that when one reaction is diffusion controlled, as might be the case for the oxygen reduction reaction, the Tafel extrapolation being prohibited, only the anodic extrapolated value at the corrosion potential should be considered as the corrosion current density. The ASTM G102-89 is also agreeing with this saying, that metal corrosion can always be determined by the anodic behaviour but not always by cathodic reaction, especially when more than just one cathodic reactions take place.

However, it should be noted that most articles stay very unclear on how they determine their corrosion current densities. As said in Princeton Applied Research application note [73] *"Unfortunately, most of the literature either skips over the basic electrochemical theory (referring the reader to original literature) or presents the theory in complex mathematical terms."*.

Due to this very unclear procedure, a statistical study on four different methods will be undergone to determine which one seems the most reproducible. However, it has to be kept in mind that method the fourth method stated underneath seems to be the least used in the literature.

In summary, the four methods used to calculate the corrosion rate in the present work are the following:

1. **First method**: In this method, the corrosion current density is defined as the intersection between the extrapolated anode Tafel line and the observed free corrosion potential (denoted as E_{corr} on Figure 3.8).
2. **Second method**: In this method, the corrosion current density is defined as the intersection between the extrapolated cathode Tafel line and the observed free corrosion potential.
3. **Third method**: In this method, the corrosion current density is defined as the average value between the two previous methods.
4. **Fourth method**: In this method, the corrosion current density is defined as the intersection between the extrapolated anodic and cathodic Tafel lines to be consistent with the theory that states that he corrosion current density is found at the point where anodic and cathodic current densities are of same magnitude.

Methods 1, 2, and 4 are summarized on two given examples on Figure 3.8. Note that E_{corr} is represented as in Figure 3.6c, i.e. the potential at which the measured current is zero (the y-axis being a logarithm of the current density absolute value).

The corrosion rates will be calculated in mm/year using equation 2.54 reminded here:

$$v_{corr} = K_1 \frac{i_{corr}}{\rho} EW \tag{3.4}$$

with K_1 equal to 3272 and the corrosion current density is in A/cm^2 As a reminder EW Is the equivalent weight of the reactive species in the dissolution reaction. For the Armco Iron, it is straightforward and the EW of iron will be considered (27,925) and the density of iron is 7,86. For the Fe-22Mn-0.6C it is more difficult to define which species should be taken into account. It will be assumed that only the manganese and iron participate in the corrosion reaction with valence 2 in both cases. This leads to an equivalent weight of 27.8 [12]. From the samples prepared for the static immersion tests, it could be found that the average density is of 7.7 g/cm^3 [13].

[12] The equivalent weight is calculated as follow: $EW = \frac{1}{\sum \frac{n_i f_i}{W_i}}$ with n_i being the valence of the i^{th}element, f_i the mass fraction of the i^{th} element and W_i the atomic weight of th i^{th} element.

[13] This density was calculated from the mass of the different samples and their geometry.

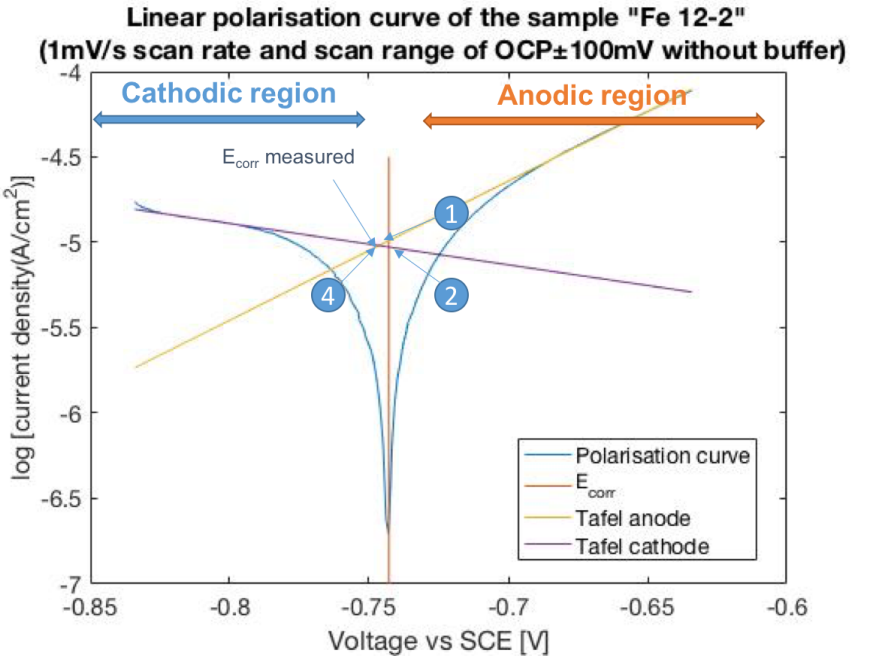

(A)

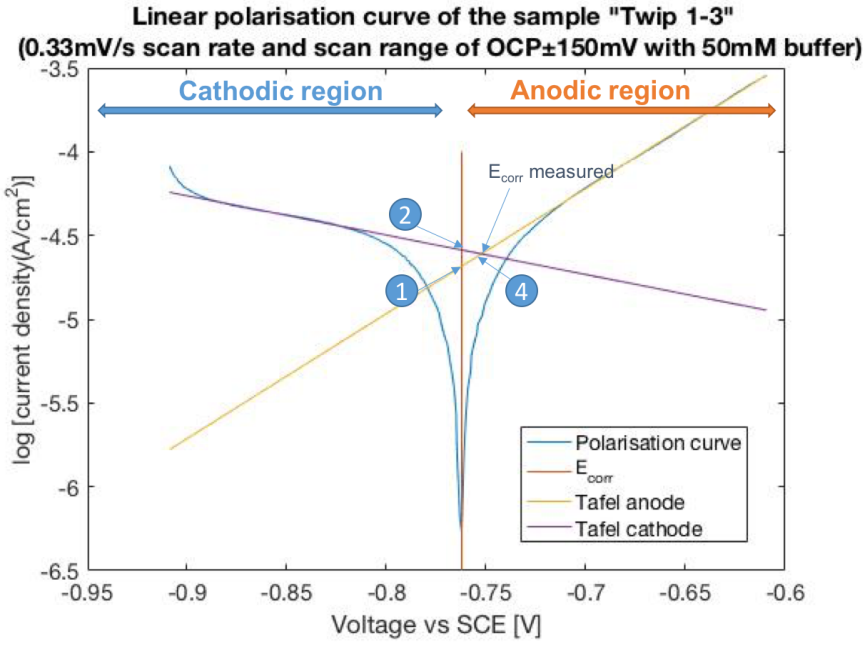

(B)

FIGURE 3.8: Evans diagram illustrating the different corrosion current densities determination methods on (A) an Armco iron sample immersed in a solution without buffer and on (B) a TWIP 0% deformed sample immersed in a 50mM buffer solution. The E_{corr} vertical line presenting the observed corrosion potential.

3.2.6 Tafel lines determination

The Tafel lines were determined separately for each sample. On Figure 3.8, two example of Tafel determinations are shown. The data points included were never situated within OCP±50mV but the extrapolation could use data points starting later than OCP±50mV and ending before the end of the data range. When two distinct lines were present in the same branch (anodic or cathodic), the first one was considered. A standard matlab code for this determination as well as the matlab code for the OCP determination can be found in Appendix A. The polarisation code is different when a CV scan was performed or an LSV. For the CV scan, the mean between the forward and reverse scan need to be made (the fifth cycle was used) and this average was fitted by the best polynomial for each sample.

3.3 Static immersion tests

3.3.1 Samples for static immersion experiments

In addition to potentiodynamic polarisation tests, static immersion tests[14] were undertaken. *Aude Thomas and Eleonora Scarcello* put in place an experimental setup on Armco iron samples. In order to compare this work results to *Aude Thomas and Eleonora Scarcello* results, their setup will be followed. Thus, samples of about 2.5 cm^2 were polished using a TechPrep polishing system from *Allied High Tech Products Inc.* for 8" polishing discs. The samples were glued to a sample holder and polished on both sides using MD-Piano 220, 600, and 1200 discs. These are resin bonded diamond grinding discs that are comparable to P220. 600, and 1200 grit SiC papers respectively. The samples thicknesses were polished with P320, 800, and 1200 grit SiC papers. After polishing, the samples were cleaned by the use of an ultrasonic bath with ethanol for 10 minutes. The samples were then weighed and measured. Table 3.3 relates the different samples studied with their immersion time, solution composition, and rotor.

After the polarisation tests were performed, analyzing the corrosion behaviour of the alloys over longer periods was interesting. Indeed, over longer periods, scales can be formed on the metal, pitting can occur and many other corrosion mechanism that are difficult to analyze using only the potentiodynamic polarisation tests. The immersion tests were carried out according to the ASTM G 31-72 standard.

Once the specimen are polished, they are immersed in about 50ml SBF solution with 50mM Hepes buffer [15] and under 37°C The volume was chosen according to the ASTM G 31-72 standard, stating that the recommended minimum "volume-to-specimen area" ratio are either $20ml/cm^2$ or $40ml/cm^2$. The former was chosen for this study. Two rotors were used: the VWR Tube Rotator (10136-084) and an IKA Loopster rotor that can contain up to 12 tubes of 50ml with 28mm diameter. [16]. These rotors rotated with 20rpm rotation speeds. The more basic handmade setup has a rotation speed of about 20 rpm. The setup can be seen on Figure 3.9. Before starting the test, a sample probe of the solution is taken to measure the dissolved oxygen partial pressure [17]. After immersion, the samples are cleaned with the use of ethanol and dried. Again, a sample probe is taken in order to measure the dissolved oxygen partial pressure after immersion [18]. The samples microstructure was then analyzed using the SEM and the corrosion products composition were estimated using the EDX. Finally, some

[14]The tests were not totally static as the samples underwent a continuous rotation but this will be explained later.

[15]Buffer was used to avoid too important pH deviations especially for longer periods.

[16]It has been noticed lately that with the IKA Loopster rotor, the samples were stuck at the bottom of the flask and during upwards rotation, they were not totally immersed. This accounted for about one fourth of the rotation time.

[17]The measurements were made using a SERIE ABL90 Radiometer, located in St. Luc Hospital. The probes ranged between 1.5 and 2.5 ml depending on the sample.

[18]The probe is ranging between 1 to 2 ml and has to be taken into account when seeking to find the right sample area to solution volume ratio.

samples were chemically attacked using different HCl concentration (50%, 10%, and 1%) and 3.5g/l of hexamethylenetetramine.

TABLE 3.3: Immersion samples with their immersion time, solution composition and rotor used.

One day immersion		
Sample	**SBF solution**	**Rotor used**
TWIP 1	50mM buffer	VWR Tube Rotator
TWIP 3	50mM buffer	VWR Tube Rotator
TWIP 40%-5	50mM buffer	Handmade setup (3.9)
One week immersion		
Sample	**SBF solution**	**Rotor used**
TWIP 6	50mM buffer	IKA Loopster rotor
TWIP 9	50mM buffer	IKA Loopster rotor
TWIP 10%-1	50mM buffer	IKA Loopster rotor -
TWIP 10%-3	50mM buffer	Handmade setup (3.9)
TWIP 20%-1	50mM buffer	IKA Loopster rotor
TWIP 20%-2	50mM buffer	IKA Loopster rotor
TWIP 40%-1	50mM buffer	IKA Loopster rotor
TWIP 40%-4	50mM buffer	Handmade setup (3.9)
TWIP 8	100mM buffer	Handmade setup (3.9)
TWIP 10%-2	100mM buffer	IKA Loopster rotor
TWIP 30%-1	100mM buffer	IKA Loopster rotor
TWIP 30%-2	100mM buffer	IKA Loopster rotor
TWIP 40%-3	100mM buffer	IKA Loopster rotor
Three weeks immersion		
Sample	**SBF solution**	**Rotor used**
TWIP 4	50mM buffer	IKA Loopster rotor
TWIP 5	50mM buffer	IKA Loopster rotor
TWIP 7	50mM buffer	Experimental setup (3.9)
TWIP 40%-2	50mM buffer	VWR Tube Rotator

The corrosion rates will be calculated according to two different ways:

1. by using the ICP-OES results. Indeed, according to the ASTM G 31-72 standard, the corrosion rate can calculated from the concentrations of matrix elements in the solution and can be compared to the mass loss rate. Nevertheless, when corrosion products adhere on the metal surface, this corrosion rate calculation based on the released ion concentration is not totally correct. The equation used for this purpose is equation 2.55 reminded here:

$$CR = \frac{cV}{ST} \tag{3.5}$$

where c is the released ion concentration in g ml^{-1}, V is the volume in ml, S is the specimen surface area in m^2 and T is the immersion time in days. Thus CR has g/(m^2d) as units.

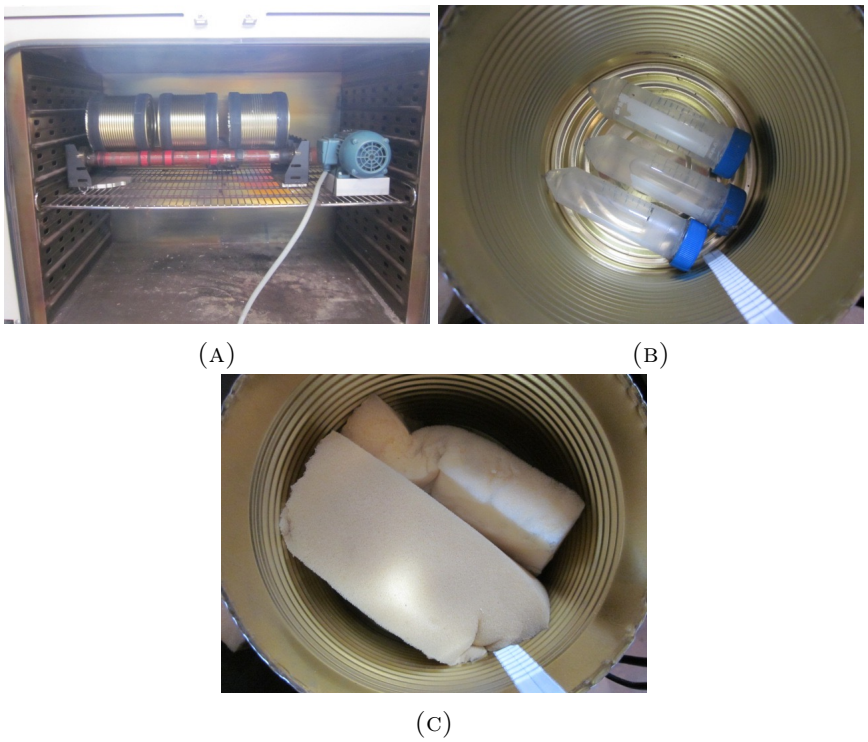

(A) (B)

(C)

FIGURE 3.9: (A) Handmade setup for immersion tests (by Jonathan Lorfèvre), (B) the sample disposition, and (C) the samples are covered by foam to keep them in place.

2. by using the mass loss rate calculated from:

$$CR = \frac{KW}{STρ} \tag{3.6}$$

where W is the mass loss in g, T is the exposure time in hours, S is the surface in cm^2, ρ is the density in g/cm^3, and K is a constant that exists in a variety of units. The units that will be used here, and thus the correspondant constants are:

$K = 8.76 \cdot 10^4$ for mm/year units.
$K = 24 \cdot 10^4 \rho$ for $g/(m^2 d)$ units.

By using the corrosion rate in $g/(m^2 h)$, the results will be more accurate as in this case, no knowledge of the reacting species is needed, which is not the case when using the mm/year unit, where the density of the material is needed, which will be calculated for each sample.

3.4 Corrosion product layer determination

Once the immersion test was performed, the corroded sample contains a certain corrosion products layer and this layer needs to be removed in order to accurately calculate the mass loss and then the released ion concentration. In order to do so, the sample will be chemically attacked using HCl with different concentrations and 3.5g/l of hexamethylenetetramine. Different HCl concentrations were studied in order to find the most accurate concentration that would remove the corrosion products layer without attacking the underneath laying metal. The sample was first immersed in the solution for 2 seconds followed by 10 seconds total (8 additional seconds) then 30 seconds, 1 minute, 2 minutes,

3 minutes, 4 minutes, 5 minutes, 8 minutes, and 10 minutes [19]. Between each cleaning cycle, the specimen was weighed and the solution was analyzed with the use of the ICP instrument. From there, an approximation of the moment when the mass loss is still due to the corrosion products before the bulk starts to get attacked should be made possible. As no ideal HCl concentration could be found, only a few samples were attacked, which means that the corrosion rates of the static immersion tests will be measured including the corrosion products layer [20].

The technique is explicited in the IO 8407:2009 standard: *Corrosion of metal and alloys - Removal of corrosion products from corrosion test specimens* and a desired outcome can be seen on Figure 3.10. Between each cleaning the sample is weighed and the mass loss is plotted. The mass losses being minimal after 21 days and the weighing scale only being precise to the 0.1mg, ICP values after each cleaning have been measured and these were also used to plot the mass loss against the cleaning time. However, if the corrosion products contain oxide or hydroxide, these will not be accounted for with the ICP. Thus, ICP gives a minimal estimation.

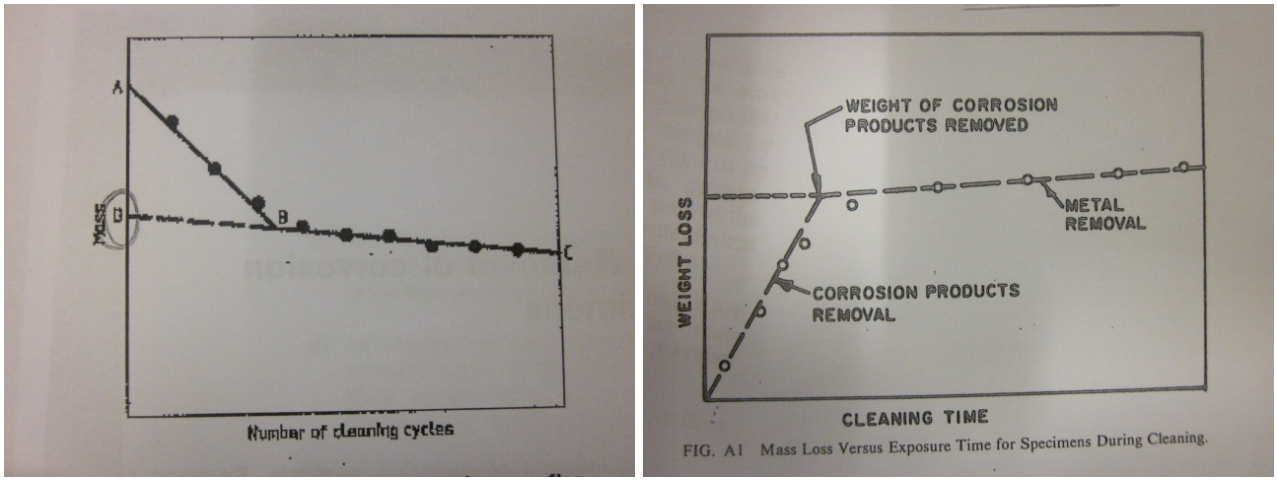

(A) (B)

FIGURE 3.10: (A) mass of corroded sample after repetitive cleaning [75] and (B) mass loss versus expsure time (especially suitable for electrolytic cleaning) [76].

3.5 Inductively coupled plasma (ICP)

The ICP used for this work is an Agilent Technologies 5100 ICP-OES. Inductively coupled plasma (ICP) is a method used to determine the elemental composition of specimens. The samples are ionized by the use of an inductively coupled plasma, which is a type of plasma source where electric currents produced by electromagnetic induction supply the energy. Argon is used for the plasma. [77] The energy provided by the plasma is sufficient enough to break the atomic bonds creating ions. In order to quantify the elements found, ICP can either be coupled to Optical Emission Spectrometry (OES) or mass spectrometry (MS). In the first example, the intensity of the light emitted from the plasma at a particular wavelength is used in order to identify an element as well as its quantity. The nature of the element is determined by the wavelength of the atomic spectral line and the the intensity is proportional to the number of atoms of that element [78]. When ICP is coupled to MS, the ions are

[19]The first two test samples at 50% HCl solution were only immersed up to 1 and 2 minutes. But this will clearly be stated in the result section.

[20]This will not affect mass losses that are already considerable but for very small corrosion rates (typically throughout the time range tested here), this could possibly considerably change the corrosion rate.

sorted according to their mass to charge ratio [79].

In our case, ICP-OES was performed in order to find the composition of the Armco iron and Fe-22Mn-0.6C TWIP steel [21]. It was also performed on all immersion samples flasks in order to determine the elements that were released and their proportions. It was also performed on a blank flask for each immersion time. In order to define the right moment when the whole corrosion product layer was removed, ICP was performed after different times of chemical attack on the immersion samples (more information on that technique can be found in the next section). Finally, ICP was also used to determine the change in solution after potentiodynamic polarisation tests. It has to be kept in mind that SBF contains chlorine but that such element cannot be detected using the ICP (along with oxygen and hydrogen). From the 24^{th} of march on [22], all analyzed solutions were attacked in order to make sure that all possibly formed precipitates would be taken into account. However, this results in a possible errors when measuring the flask volume. As a matter of fact, when the solutions were not attacked, a precise volume of 10 ml was taken, whereas when the solution was attacked, the whole volume is important.

3.6 Scanning electron microscopy (SEM) and Energy Dispersive X-ray Spectroscopy (EDX) for surface and composition analysis

This section is mainly inspired by Laura Höltschi, Pierre-Olivier Colard and myself's report on scanning electron microscopy for the LMPR2011 lecture.

In a scanning electron microscope the sample is scanned on its surface with an electron beam produced by a heated filament and this beam is directed towards the specimen surface thanks to magnetic coils. The SEM used for this work is an Ultra-55 from Zeiss, which uses a field emission electron beam source (FESEM) giving rise to a very high imaging resolution. The primary electron beam is focused on the sample surface and this produces secondary electrons, which will further be emitted by the sample in order to get rid of the surplus of electrons and stabilize. These electrons are less energetic than the primary electrons and the intensity of the electrons will reflect the morphology of the sample surface. Some of the electrons cannot directly leave the sample and are scattered in the sample before reaching the detector. These electrons are called backscattered electrons. These electrons give information on the sample topography but also on the chemistry as the backscattered detector can distinguish light atoms from heavy atoms. These two electron types are not the only possible produced electrons. Indeed, primary electrons can also produce Auger electrons, X-rays, and heat. By analyzing the X-rays, information on the sample surface chemical composition can be obtained when these rays are collected by the specialized X-ray detector, Quantax Bruker in this case. Secondary electrons are mostly used and thus the SEM is a surface analysis technique a their energy is quite low. X-rays are giving information on a depth of maximum 0.8 μm if a 15KV beam is used and 0.1 μm if a 5kV beam is used. The interaction pear is illustrated on Figure 3.11. In order to avoid the electrons to react with air, the microscope is under vacuum. [80]

By using lower accelerating voltages, images with higher resolution can be obtained but with higher voltages, information from a deeper layer can be obtained.

[21] When solid samples are investigated, they need to be a attacked in order to become a liquid solution. For these alloys, acid attack using aqua regia (a mix of HNO_3 and HCl) was used.

[22] This includes all immersion tested samples.

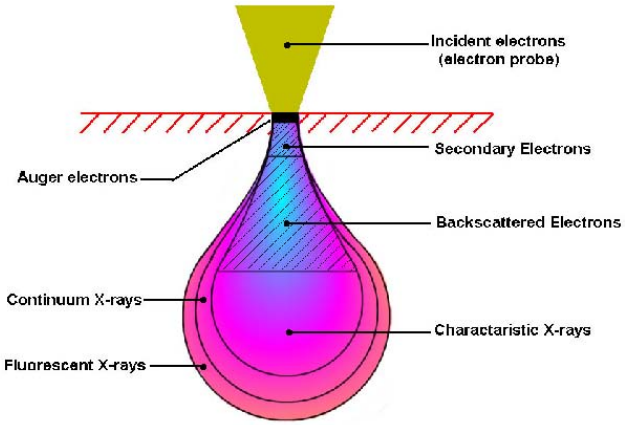

FIGURE 3.11: Electron beam interaction diagram (maximum depth around 1 μm) [81].

3.6.1 Potentiodynamic polarization samples

SEM investigation was undertaken for some potentiodynamic polarisation tests before and after the tests. Before the test, the backscattered mode was used and some of these images have already been shown in the sample preparation section. The aperture used ranges from 30 μm (for SE images) to 120 μm for the most sensible samples (TWIP samples BSD images in order to investigate the twinning presence) and the voltages used were either 5kV or 15kV. It will always be stated which aperture size and accelerating voltage is used.

3.6.2 Immersion samples

Immersion tests were first investigated by SEM and EDX before immersion but this was then replaced by an optical microscope. After immersion, all samples morphologies were determined by SEM and the composition of the surface products was determined by EDX as well as by ICP.

3.7 X-ray diffraction (XRD) for corrosion products analysis

X-ray diffraction is a non-destructive technique that is used to characterize the atoms arrangement inside a crystal. A X-ray emitting tube is used to irradiate the sample and the detector is made in such a way to only be sensitive to the X-ray emitted by the anode (copper in our case). The detector then collects the angles at which an X-ray is diffracted from the sample and measures the ray intensity in that direction and there is a relationship between the diffraction angle and the characteristic crystal network distances. The Bruker D8 advance XRD instrument has 120 LYNXEYE detectors [23]. The resulting graph is a diffractometer that gives the intensity of a diffracted ray as a function of the detector angle (2θ) and these peaks are compared to a database of all possible element peaks. [79, 82]

XRD was performed by analyzing the sample every 0.02° per step and for 4 seconds on each point from 15° to 90° (2θ) on some potentiodynamic polarisation samples in order to analyse which species could be found on the corrosion product layer. This technique could be complementary to the EDX analysis made on these samples if enough information can be obtained from these diffractometers.

[23] This is the XRD instrument available at the IMAP.

3.8 X-Ray Photoelectron Spectroscopy (XPS) for corrosion products analysis

This section will mainly be inspired by a report done on X-Ray Photoelectron Spectroscopy (XPS) by Laura Höltschi and myself for the LMAPR2011 lecture.

In XPS, the X-rays are created thanks to an electron gun (with a tungsten filament). The electrons are then accelerated (10kV) towards an anode (target). The anode is made of a light material such as aluminium. Two situations can take place when the electrons hit the anode: their velocity can either be decreased due to the presence of the electric field of the atoms and this gives rise to the Bremsstrahlung or they can eject a core electron. In the latter case, the state becomes unstable and thus, an electron from an upper shell will go down in order to fill the whole, this will give rise to the emission of a photon (in the range of the X-rays). This photon emission energy Kα of 1486 eV will be used. Other rays are still present, thus the X-rays still need to go through a monochromator crystal. Then, the rays will hit the sample through about 1mm of thickness but only the very upper surface electrons (1-10nm) can get out of the sample and reach the detector, which is why XPS is a surface analysis technique. Once the X-rays hit the sample, they ionize the atom by photoelectric effect and the photoelectron ejected from the surface will have a kinetic energy KE of:

$$KE = h\nu - E_{bind} \tag{3.7}$$

where E_{bind} is the binding energy and hν the photon energy (1486 eV). The photon energy is thus known and the kinetic energy can be measured. This leaves the field clear for a calculation of the binding energy. When these photoelectrons are emitted, again an electron from an upper shell will come down to fill in the whole and in order to conserve the released energy, an Auger electron is emitted. The working principle of XPS is illustrated on Figure 3.12. H and He cannot be detected by XPS as their binding energies are too small.

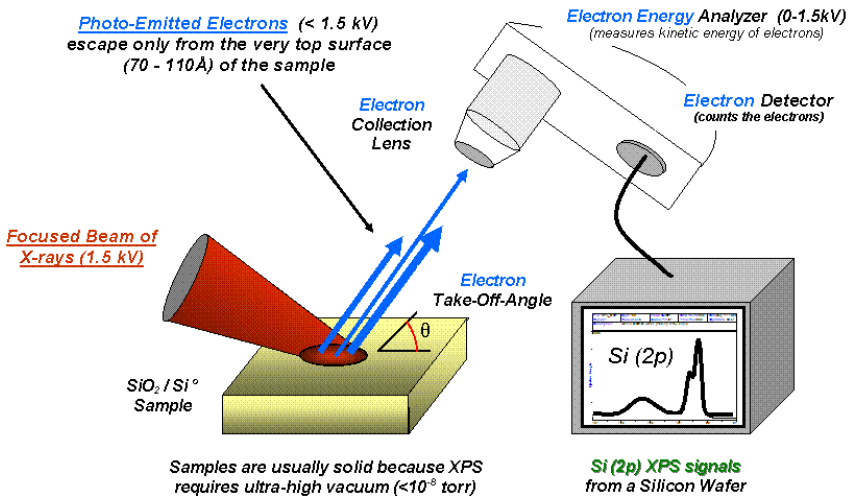

FIGURE 3.12: XPS working principle [83].

XPS was performed on four different immersion samples. One blank sample was used in order to compare the results before and after immersion. The samples investigated are following:

- **TWIP 2**: This is the blank sample, polished and left for one week in the dessicator.

- **TWIP 9**: This sample was immersed for a week in a 50mM Hepes buffer SBF solution [24].
- **TWIP 4**: This sample was immersed for three weeks in a 50mM buffer solution.
- **TWIP 40%-1**: This 40% deformed sample was immersed for one week in a 50mM buffer solution.

3.9 Time-of-Flight Secondary Ion Mass Spectrometry (ToF-SIMS) for corrosion products analysis

Time-of-Flight Secondary Ion Mass Spectrometry (ToF-SIMS) is a technique used for surface analysis. It uses a pulsed beam of primary ion beams (Cs+ in this case) with several keV of energy that ionizes species from he uppermost surface of the sample and the sputtering of material is caused by a collision cascade caused by the energy transferred by the primary ions on target atoms and a small fraction of that sputtered material ends as ions that are accelerated into a mass spectrometer where the mass analysis uses the time of flight of these ions to determine the elements. Mass spectra, chemical images and depth profiles can be determined by ToF-SIMS. It has to be kept in mind that ToF-SIMS is a semi-quantitative method but is can be used for a wide variety of materials, including metals, catalysts, polymers, and many other materials. [84, 85]

ToF-SIMS was performed on one TWIP sample (TWIP 6) using a ToF.SIMS 5 instrument from Ion TOF. This depth profiling will make it possible to have a more precise idea of the different components that are found on the surface of the samples after immersion.

3.10 Optical microscope for surface analysis

The first immersion samples were analyzed using the SEM and EDX before immersion, whereas the last samples were observed using a Olympus Provis A052 optical microscope. Bright field images were taken. Some potentiodynamic polarisation samples were also observed on that microscope before being tested but mostly they were observed on a more basic microscope. The mode used was bright field. In bright-field mode, the sample is illuminated from below and white light as well as contrast in the sample is achieved by the absorbance of some of the transmitted light in dense areas of the sample. The light path is quite simple: a transillumination light source is used and a condenser lens is present to focus the light from the source onto the sample. The image is then collected by the help of an objective lens that collects the light and magnifies the image. [86]

[24] It was supposed to be brought to the XPS at the end of the immersion time in order for the blank sample to be perfectly comparable to this sample. However, due to some technical issues with the XPS instrument, this sample was only analyzed 17 days after the beginning of the immersion time.

CHAPTER 4

RESULTS

4.1 Potentiodynamic polarisation tests

In this section the different results of potentiodynamic polarisation tests will be highlighted. First, the results of the impact of stabilisation, scan rate, scan range, method (CV vs LSV), and electrical contact will be presented. All these impacts will be tested on Armco iron in order to choose an adequate experimental protocol. Then the comparison of Armco iron with the different deformed TWIP samples will be shown. For all these results, the corrosion rate was calculated in mm/year using equation 2.19. Unless specified, no Hepes buffer was used. As the solution is considered quite conductive [1] and the encountered currents being very small, the iR drop will be neglected in the result analysis. The corrosion current densities (and thus corrosion rates) will be calculated using the four methods stated in section 3.2.5. Finally, the potential values shown in this section are all values against SCE.

4.1.1 Impact of OCP stabilization on corrosion (CV 50mV/s)

As stated in the previous chapter, the effect of previously stabilizing the corrosion potential has a certain effect on the corrosion. This is why it has been tested to see if the potential is not previously stabilized, this would result in higher reproducibility. As a matter of fact, by not letting the potential stabilize, no surface changes are allowed to take place. Especially that the method used for this comparison is the fastest method used in this study: CV 50mV/s. As a reminder, the potentiodynamic polarisation tests are performed over a scan range of ±100mV (from OCP for stabilized samples and from the potential value after 3 minutes immersion for the unstabilized samples). A total of five samples were tested in the stabilized category and a total of four samples in the unstabilized category.

Figure 4.1 shows the effect of stabilisation on the corrosion rate. As two values were highly different from the rest of the values, a statistical Dixon's Q-test[2] has been performed to see if this data point could be designated as an outlier and the test was positive. Thus on Figure 4.1b, the corrosion rates for methods 1 to 4 are recalculated. It can be seen that the overall corrosion rate with stabilisation became smaller when excluding the outlier, whereas the corrosion rate of non-stabilizing tests increased. By excluding the outlier in each family, the standard deviation also became less important. Table

[1] 12.75 mS/cm for SBF + 50mM Hepes.

[2] To apply this test, the data must be arranged in increasing order. Q is given by the gap between the value and it's closest neighbour divided by the range (difference between the highest and lowest value of the data set) and if the value of Q found is bigger than the Q_{table} value then the point should be rejected. The Q_{table} values are given values depending on the number of data points and confidence level. This test can only be used once in a data set [87].

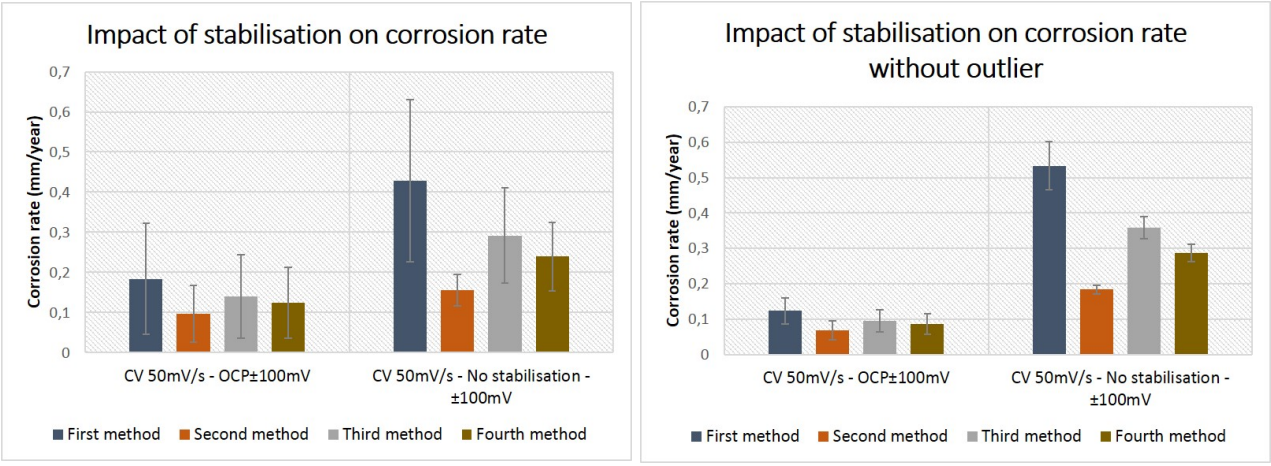

(A) (B)

FIGURE 4.1: Corrosion rates using the four different methods to compare samples with or without OCP stabilisation for CV 50mV/s and ±100mV scan range (A) including outliers of both families and (B) excluding the outlier in both families.

4.1 shows the exact values of the corrosion rates and standard deviations of the stabilized and non-stabilized samples as well as the proportional corrosion current densities. Whether the outlier is taken into account or not, the corrosion rate is higher for the unstabiliized samples. However, the standard deviations of the latter samples are relatively smaller than for the stabilized samples. Statistically, the fourth method is the one giving the smallest relative standard deviation for the stabilized samples with outlier and the first method is the one giving the smallest relative standard deviation for the stabilized samples without outlier. The two unstabilized categories have the smallest relative standard deviation using the second method. The second method results in the smallest corrosion rates for the four categories and the first method is the one resulting in the highest corrosion current. On Figure 4.3, the Evans plot and OCP plots of the different samples can be seen. A second table (Table 4.2) is also present to show the impact of stabilisation on all the other corrosion parameters (Tafel slopes, OCP and E_{corr} observed and measured). The difference between the three corrosion potentials (i.e. OCP, E_{corr} observed and E_{corr} measured) can also be seen on Figure 4.2. Table 4.2 also shows that the observed corrosion potential is closer to the theoretical corrosion potential (open circuit potential) compared to the measured corrosion potential. The Tafel slopes are smaller when not taking the outlier into account except for the cathodic slope of unstabilized samples. As a reminder, the expected anodic Tafel slope for iron is of 58 mV/dec (for a room temperature of 19°C) but can typically range between 30 and 70 mV/dec [88]. The cathodic Tafel slope for oxygen reduction typically lies around 120mV/dec [88].

Therefore, these two methods (first and second) will be plotted on Figure 4.4. On that figure, it is also shown that samples which did not encounter OCP stabilization have higher corrosion current densities and less negative observed corrosion potentials. The two outliers are also clearly seen on that Figure. Thus, for further studies, these data points will not be taken into account.

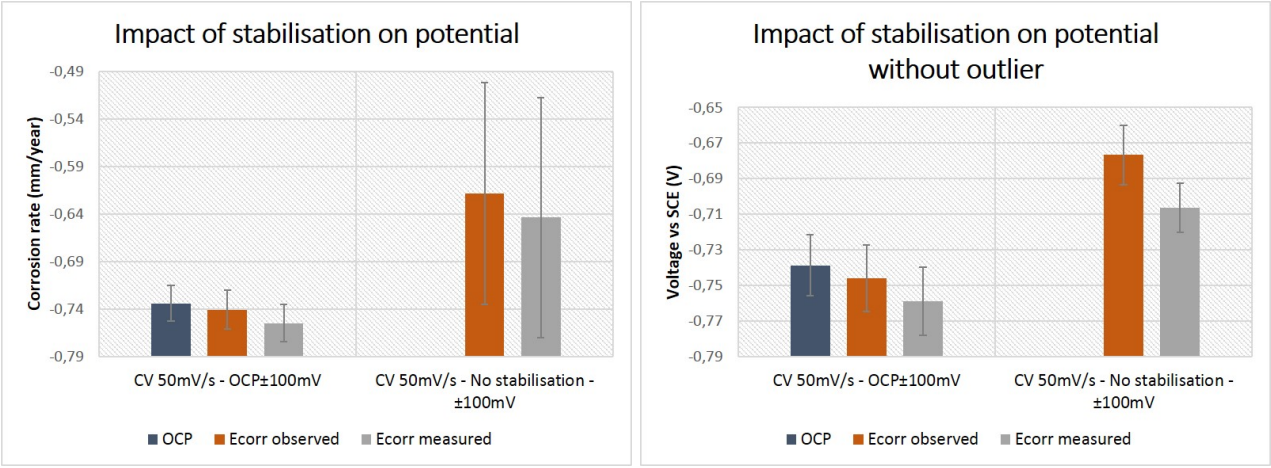

(A) (B)

FIGURE 4.2: Corrosion potentials after steady state achieved (OCP), for a zero measured current (E_{corr} observed) and at the intersection of anodic and cathodic extrapolated values (E_{corr} measured) for samples with or without OCP stabilisation for CV 50mV/s and ±100mV scan range (A) including outlier in each family and (B) excluding an outlier in each family.

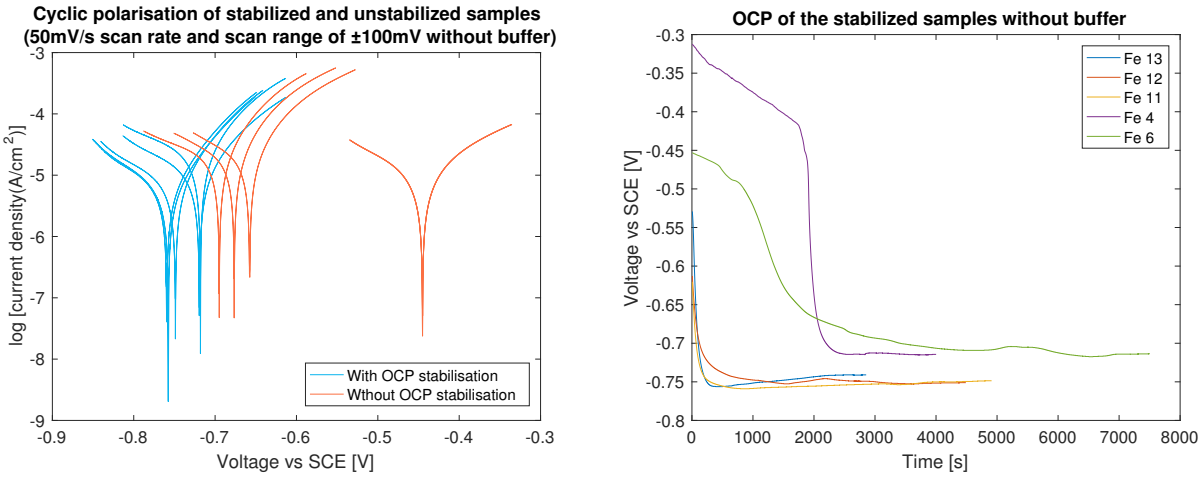

(A) (B)

FIGURE 4.3: (A) CV plot of previously stabilized and unstabilized samples and (B) OCP plot of previously stabilized samples.

It should be noted that all following tests will always be preceded by an OCP stabilization (with no exact time limit). As a matter of fact, stabilization did not occur after an exact amount of time but changes from sample to sample between 3000s and 7200s.

TABLE 4.1: Mean corrosion rates and current densities (with standard deviation) of five stabilized and four unstabilized samples using CV 50mV/s method with scan ranges ±100mV (from OCP for stabilized samples and from the potential value after 3 minutes immersion for the unstabilized samples). The electrolyte used is SBF without buffer

Method	$\mathbf{v}_{corr}$ **(mm/year) method 1**	$\mathbf{v}_{corr}$ **(mm/year) method 2**	$\mathbf{v}_{corr}$ **(mm/year) method 3**	$\mathbf{v}_{corr}$ **(mm/year) method 4**
Stab. with outlier	0.184±0.139	0.097±0.070	0.140±0.104	0.124±0.088
Stab. w/o outlier	0.123±0.037	0.0674±0.0267	0.0954±0.0313	0.0861±0.0294
Unstab. with outlier	0.428±0.202	0.156±0.040	0.292±0.119	0.239±0.086
Unstab. w/o outlier	0.534±0.068	0.183±0.012	0.359±0.031	0.287±0.024
Method	$\mathbf{i}_{corr}$ **(μA/cm^2) method 1**	$\mathbf{i}_{corr}$ **(μA/cm^2) method 2**	$\mathbf{i}_{corr}$ **(μA/cm^2) method 3**	$\mathbf{i}_{corr}$ **(μA/cm^2) method 4**
Stab. with outlier	15.8±11.9	8.34±6.03	12.1±9.0	10.7±7.6
Stab. w/o outlier	10.6±3.2	5.80±2.29	8.21±2.69	7.41±2.53
Unstab. with outlier	36.8±17.4	13.4±3.5	25.1±10.3	20.6±7.4
Unstab. w/o outlier	45.9±5.9	15.8±1.0	30.9±2.7	24.7±2.1

TABLE 4.2: Mean corrosion potentials and Tafel slopes (with standard deviation) of five stabilized and four unstabilized samples using CV 50mV/s method with scan ranges ±100mV (from OCP for stabilized samples and from the potential value after 3 minutes immersion for the unstabilized samples). The electrolyte used is SBF without buffer

Method	**OCP (V)**	$\mathbf{E}_{corr}$ **(V) observed**	$\mathbf{E}_{corr}$ **(V) measured**	β_a **(mV/dec)**	β_c **(mV/dec)**
Stab. with outlier	-0.734±0.018	-0.740±0.020	-0.754±0.019	77.1±27.3	-118±50
Stab. w/o outlier	-0.739±0.017	-0.746±0.019	-0.759±0.019	70.9±27.2	-102±43
Unstab. with outlier	/	-0.619±0.117	-0.644±0.126	118±18	-149±24
Unstab. w/o outlier	/	-0.677±0.017	-0.706±0.014	111± 11	-161±28

4.1.2 Impact of the electrode contact on the corrosion behaviour and the reproducibility of the system

Due to several leaks encountered during the tests, it was needed to improve the electrical contact of the working electrode. For this purpose, it was studied if by taking the Armco iron sample out of its resin and by allowing the electrical contact to take place from behind the sample (with a copper sheet), less

leaks would happen and also more reproducible results would arise[3]. Furthermore, one iron rod sample was manufactured in such a way that the rod would be tall enough to allow direct electrical contact on the piece of metal. Again, the same questions are asked in this case. Besides these tests, it was also tried to allow a better contact by attaching the copper sheet to the metal by means of carbon lacquer or carbon tape but in both cases a high increase in OCP resulted soon after the sample was immersed, characteristic of leakage or of copper being in contact with the solution. These techniques were thus not investigated any further. The scans were performed using 50mV/s cyclic voltammetries with scan ranges of OCP±100mV. A total of four samples are used for the "mounted" category[4], two samples were used for the "unmounted" category [5] and one sample was used for the "Iron rod" category [6].

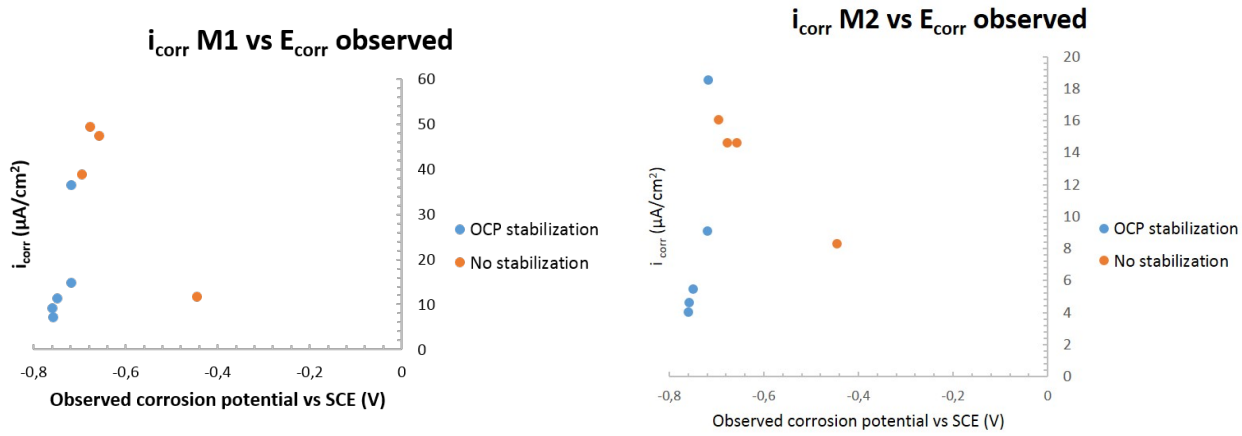

(A) (B)

FIGURE 4.4: Corrosion current densities ((A) first method and (B) second method) versus observed corrosion potential for five iron samples where the OCP was left to stabilize and four iron samples where the OCP was not left to stabilize (CV 50mV/s and ±100mV scan range).

The differences in corrosion rates and corrosion potentials can be seen on Figure 4.5. The values are exposed in Tables 4.3 and 4.4. The Table 4.3 also exposes the corrosion current densities using the different methods. It has to be said that sample Fe SR2 will not be taken into account in the "unmounted" category due to a high increase of the OCP from second 2000 to second 8000, it increased of 30mV without stabilizing at any point. However, it can be interesting to note that the corrosion current densities of that sample were similar to the Fe 13SR sample, bringing the average corrosion rate down as the only other sample studied in that category (Fe SR1) has a relatively much higher corrosion rate than the two previously exposed ones. But even by not taking this sample into account, the unmounted samples still seem to corrode slower than mounted samples according to the results and the iron rod even slower than the two latter categories.

OCP and CV plots can be found on Figure 4.6. The OCP values of the unmounted samples and the iron rod were not well stabilized and would still continue to raise. A graph showing the observed corrosion potential and corrosion current densities determined by the first and second method (best methods statistically for the mounted category and unmounted category respectively) for the different samples of interest can be seen on Figure 4.7. The first method is also the one resulting in the highest

[3]The electrical contact on the classical mounted samples is done by a copper sheet placed on the iron surface that is in contact with the solution but in such a way that the copper sheet does not get into contact with the electrolyte.
[4]i.e. the category where the electrical contact is made by the use of a copper sheet placed on top of the sample.
[5]i.e. the category where the electrical contact was made by the use of a copper sheet placed behind the sample.
[6]where the electrical contact was made directly in the sample.

corrosion rates for all three categories. The second method is the one resulting in the lowest corrosion rates for the mounted samples and the iron rod. The smallest standard deviations are found for the mounted samples compared to the unmounted ones.

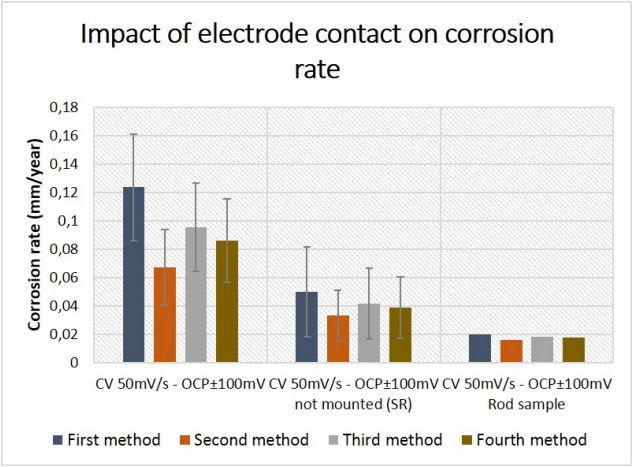

(A)

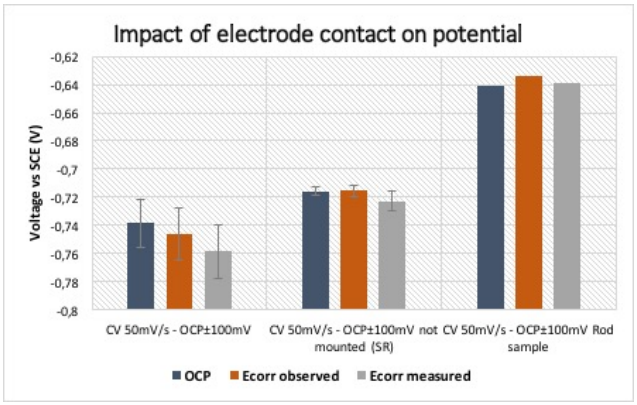

(B)

FIGURE 4.5: (A) Corrosion rates and (B) corrosion potentials using the four different methods for CV 50mV/s scans (OCP±100mV scan range) of samples where the electrical contact was made with a copper sheet in front of the sample (mounted), behind the sample (unmounted) and directly on the sample (Rod sample).

TABLE 4.3: Mean corrosion rates and current densities (with standard deviation) of 4 mounted samples (electrical contact with a copper sheet in front of the sample), 2 unmounted samples (electrical contact with a copper sheet behind the sample), and one iron rod sample (electrical contact directly on the sample). Method used: CV 50mV/s and OCP±100mV scan range. The electrolyte used is SBF without buffer

Sample preparation	$\mathbf{v}_{corr}$ **(mm/year) method 1**	$\mathbf{v}_{corr}$ **(mm/year) method 2**	$\mathbf{v}_{corr}$ **(mm/year) method 3**	$\mathbf{v}_{corr}$ **(mm/year) method 4**
Mounted	0.123±0.037	0.0674±0.0267	0.0954±0.0313	0.0861±0.0294
Unmounted	0.0499±0.0317	0.0334±0.0177	0.0416±0.0247	0.0288±0.0217
Iron rod	0.0202	0.0163	0.0183	0.0176
Sample preparation	$\mathbf{i}_{corr}$ **(μA/cm^2) method 1**	$\mathbf{i}_{corr}$ **(μA/cm^2) method 2**	$\mathbf{i}_{corr}$ **(μA/cm^2) method 3**	$\mathbf{i}_{corr}$ **(μA/cm^2) method 4**
Mounted	10.6±3.2	5.80±2.29	8.21±2.69	7.41±2.53
Unmounted	4.29±2.73	2.87±1.52	3.58±2.13	3.34±1.87
Iron rod	1.74	1.40	1.57	1.51

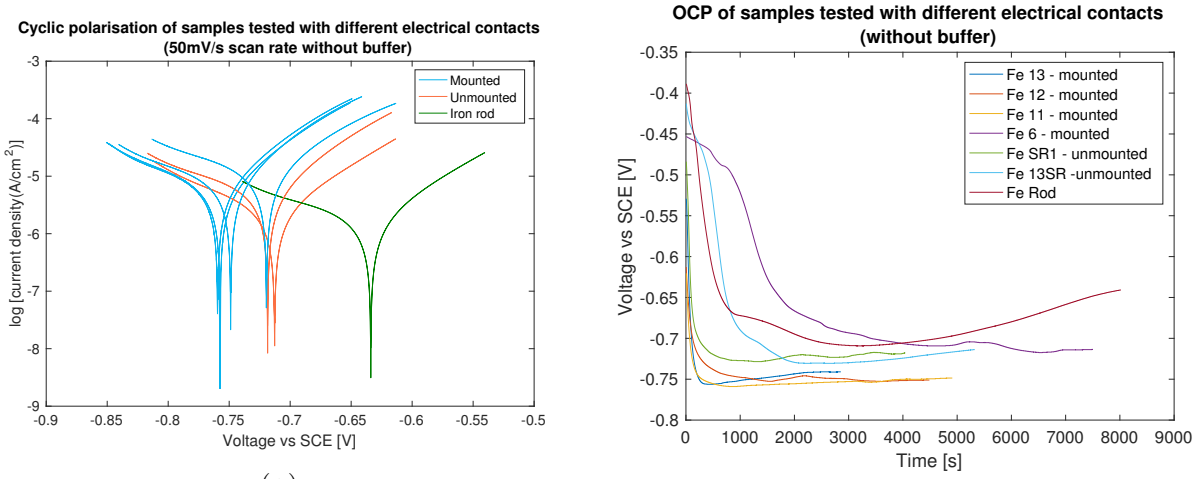

(A) (B)

FIGURE 4.6: (A) CV 50mV/s (OCP±100mV scan range) and (B) OCP plots for samples where the electrical contact was made with a copper sheet in front of the sample (mounted), behind the sample (unmounted) and directly on the sample (Rod sample).

TABLE 4.4: Mean corrosion potentials and Tafel slopes (with standard deviation) of 4 mounted samples (electrical contact with a copper sheet in front of the sample), 2 unmounted samples (electrical contact with a copper sheet behind the sample), and one iron rod sample (electrical contact directly on the sample). Method used: CV 50mV/s and OCP±100mV scan range. The electrolyte used is SBF without buffer

Sample preparation	**OCP (V)**	**E_{corr} (V) observed**	**E_{corr} (V) measured**	**β_a (mV/dec)**	**β_c (mV/dec)**
Mounted	-0.739±0.017	-0.746±0.019	-0.759±0.019	70.9±27.2	-102±43
Unmounted	-0.716±0.003	-0.716±0.004	-0.723±0.007	76.9±0.8	-117±20
Iron rod	-0.641	-0.634	-0.639	79.4	-148

4.1.3 Impact of the method and scan rate on corrosion behaviour and reproducibility of the system

After undergoing tests with rapid cyclic voltammetry, linear sweep volammetry was tested in order to see if the reproducibility would be better. As a reminder, most articles use slow linear sweep voltammetry to study the corrosion mechanisms. Two different scan rates were investigated: 0.33mV/s (2 samples tested) and 1mV/s (2 samples tested). The resulted effects of these changes compared to 50mV/s cyclic voltammetry will be seen in the different figures and tables of this section. The scan range was OCP±100mV to accurately compare these results to the previously obtained CV 50mV/s with OCP±100mV scan range (4 samples).

The corrosion current densities using the four different methods can be seen on Table 4.5, where the corrosion rates are also present. These can also be seen on the comparative diagram on Figure 4.8a. The different corrosion potentials are compared on Figure 4.8b and Table 4.6. In both LSV cases, the different corrosion potentials are quite close to each other. Note that one of the two samples from the LSV 0.33 mV/s category encountered a sudden raise in OCP explaining the higher error bar of these

tests on OCP values. This OCP rise can be seen on Figure 4.9b. On Figure 4.9a, the potentiodynamic polarisation scans of all the tested samples included in this category can be seen.

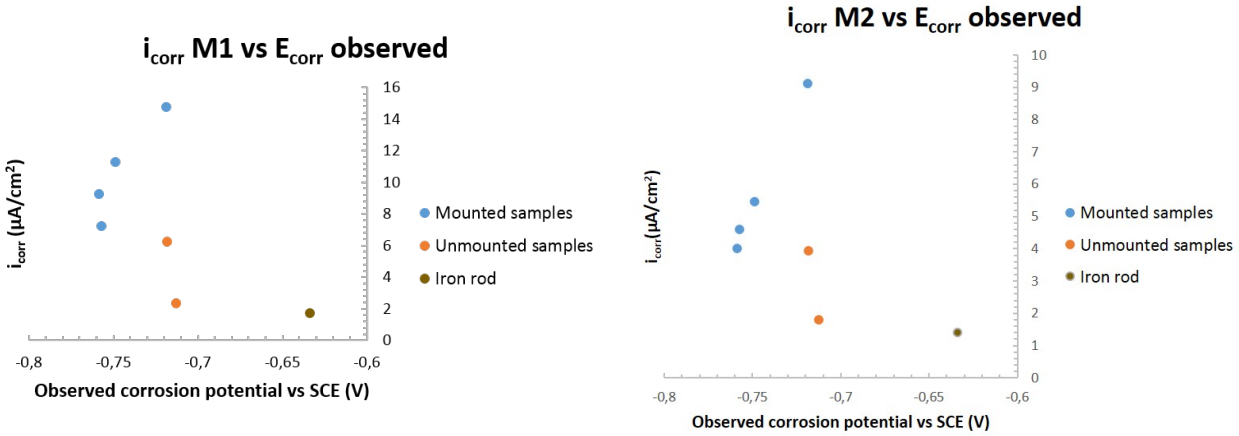

(A) (B)

FIGURE 4.7: Corrosion current densities ((A) first method and (B) second method) versus observed corrosion potential for samples where the electrical contact was made with a copper sheet in front of the sample (mounted), behind the sample (unmounted) and directly on the sample (Rod sample). Method used: CV 50mV/s and OCP±100mV scan range

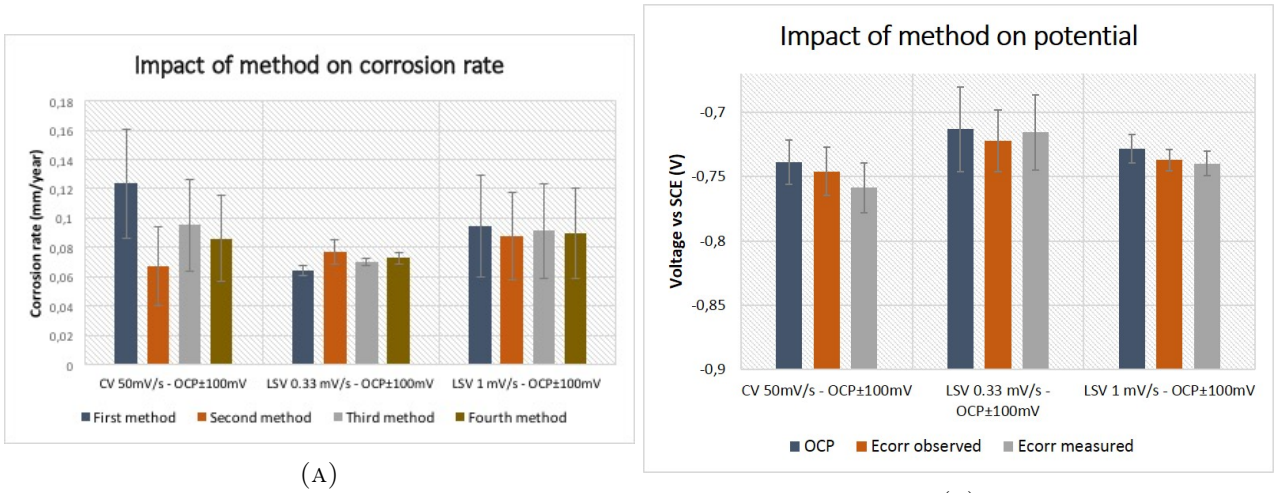

(A) (B)

FIGURE 4.8: (A) Corrosion rates (using the four different methods) and (B) corrosion potentials for polarisation scans of samples that underwent either cyclic (50mV/s: 4 samples) or linear polarisation (0.33mV/s and 1mV/s: 2 samples each) with OCP±100mV scan range.

It can be seen that the LSVs exhibit smaller corrosion rates than CVs and it can even be differentiated between LSV 0.33mV/s and LSV 1mV/s, where the latter has a slightly higher corrosion rate than the former.
As has already been seen, the best statistical method for the 50mV/s CVs is the first one. For the LSV 0.33mV/s category, the smallest relative standard deviation is given by method three and the second method is the one giving the smallest relative standard deviations for the LSV 1mV/s category. LSV 0.33mV/s is the method with the smallest standard deviations compared to the two other categories.

TABLE 4.5: Mean corrosion rates and current densities (with standard deviation) for CV 50mV/s (4 samples), LSV 0.33mV/s (2 samples) and LSV 1mV/s (2 samples). The scan range of these tests was OCP±100mV. The electrolyte used is SBF without buffer

Method	$\mathbf{v}_{corr}$ **(mm/year) method 1**	$\mathbf{v}_{corr}$ **(mm/year) method 2**	$\mathbf{v}_{corr}$ **(mm/year) method 3**	$\mathbf{v}_{corr}$ **(mm/year) method 4**
CV 50 mV/s	0.123±0.037	0.0674±0.0267	0.0954±0.0313	0.0861±0.0294
LSV 0.33mV/s	0.0640±0.0032	0.0768±0.0082	0.0704±0.0025	0.0727±0.0041
LSV 1mV/s	0.0946±0.0345	0.0879±0.0298	0.0913±0.0321	0.0896±0.0306
Sample preparation	$\mathbf{i}_{corr}$ **(μA/cm^2) method 1**	$\mathbf{i}_{corr}$ **(μA/cm^2) method 2**	$\mathbf{i}_{corr}$ **(μA/cm^2) method 3**	$\mathbf{i}_{corr}$ **(μA/cm^2) method 4**
CV 50mV/s	10.6±3.2 2	5.80±2.29	8.21±2.69	7.41±2.53
LSV 0.33mV/s	5.51±0.28	6.61±0.71	6.06±0.22	6.25±0.36
LSV 1mV/s	8.14±2.97	7.57±2.56	7.85±2.76	7.71±2.63

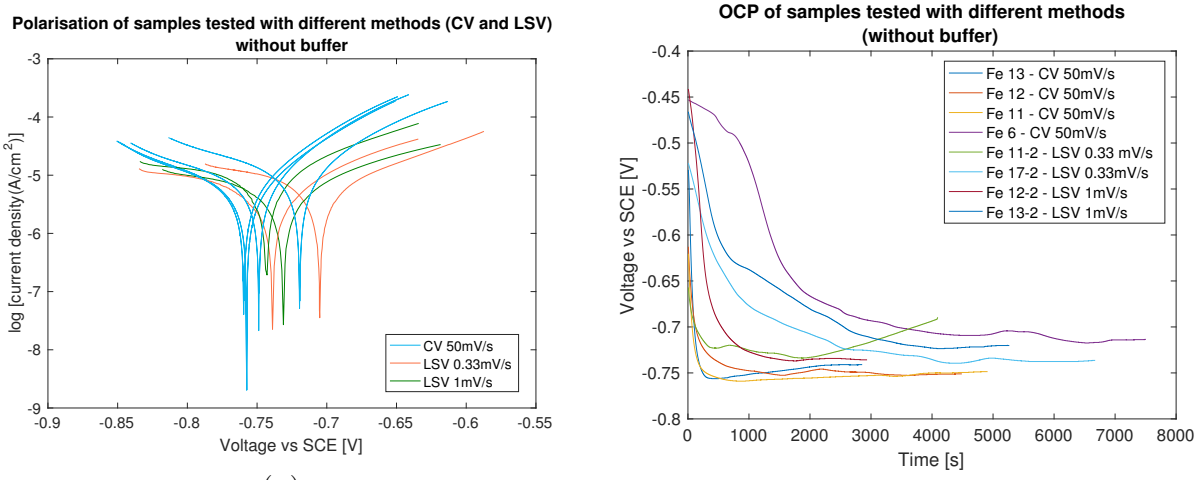

(A) (B)

FIGURE 4.9: (A) Potentiodynamic polarisation and (B) OCP plots for samples tested with different methods: CV 50mV/s (4 samples), LSV 0.33mV/s (2 samples), LSV 1mV/s (2 samples). The scan range of these tests was OCP±100mV.

Figure 4.10 exhibits the observed corrosion potentials with the corrosion current densities found by the first, second and third methods. On Table 4.5, it can also be seen, that method one gives the highest corrosion rates for LSV 1mV/s and CV 50mV/s and the smallest corrosion rate for LSV 0.33mV/s, whereas method two gives the smallest corrosion rates for LSV 1mV/s and CV 50mV/s and the highest corrosion rate for LSV 0.33mV/s.

TABLE 4.6: Mean corrosion potentials and Tafel slopes (with standard deviation) for CV 50mV/s (4 samples), LSV 0.33mV/s (2 samples) and LSV 1mV/s (2 samples). The scan range of these tests was OCP±100mV. The electrolyte used is SBF without buffer

Sample preparation	OCP (V)	E_{corr} (V) observed	E_{corr} (V) measured	β_a (mV/dec)	β_c (mV/dec)
CV 50mV/s	-0.739±0.017	-0.746±0.019	-0.759±0.019	70.9±27.2	-102±43
LSV 0.33mV/s	-0.713±0.033	-0.722±0.024	-0.716±0.029	117±2	-292±45
LSV 1mV/s	-0.728±0.011	-0.737±0.008	-0.740±0.009	135±18	-351±89

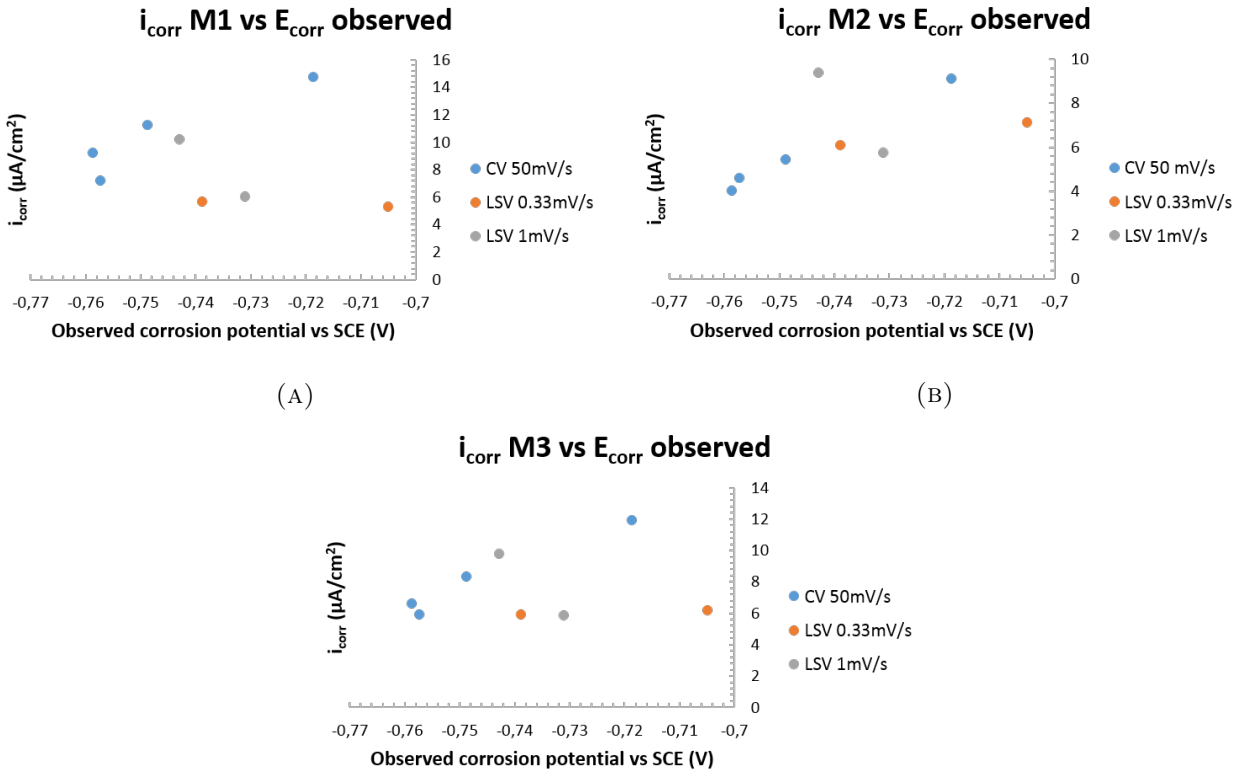

(A) (B)

(C)

FIGURE 4.10: Corrosion current densities determined from (A) first method, (B) second method, and (C) third method versus observed corrosion potential for the samples tested in the "impact of method" category: CV 50mV/s (4 samples), LSV 0.33mV/s (2 samples) and LSV 1mV/s (2 samples). The scan range of these tests was OCP±100mV.

4.1.4 Impact of the scan range on the corrosion behaviour and the reproducibility of the system

A further investigation considered the effect of scan range on the different corrosion parameters. This was investigated as well for cyclic voltammetries than for linear sweep voltammetries.

4.1.4.1 Cyclic voltammetry

The effect of allowing the scan to be performed over a wider range was studied in order to see how this would affect the corrosion parameters. For this purpose, the previously studied CV with scan range OCP±100mV samples (4 in total) are compared to a single sample that underwent a cyclic voltammetry 50mV/s scan rate and OCP±300mV scan range.

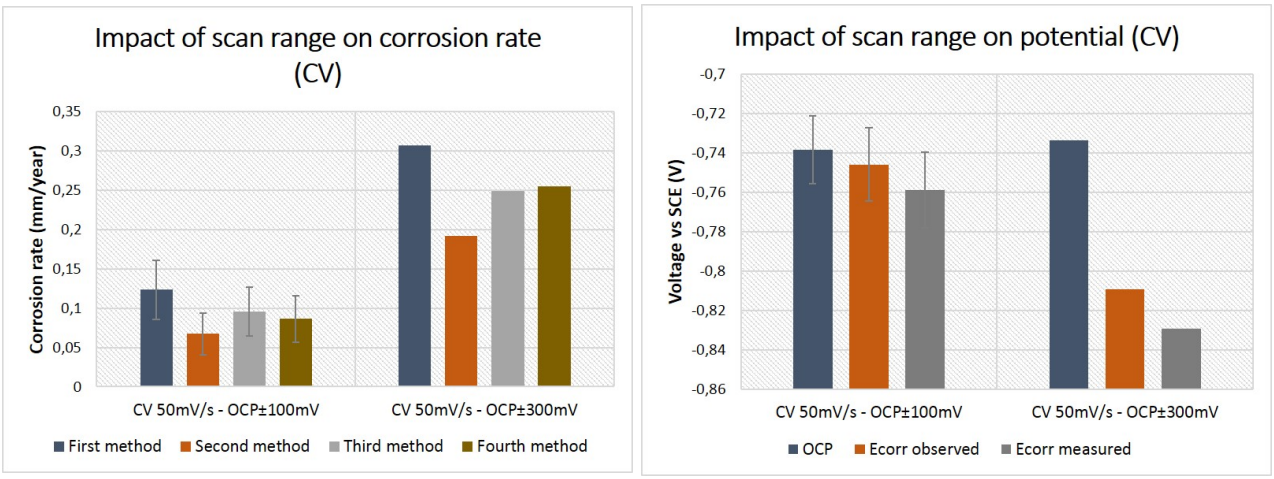

(A) (B)

FIGURE 4.11: (A) Corrosion rates and (B) corrosion potentials using the four different methods for 50mV/s CV scans over different scan ranges around OCP: 100mV (4 samples) and 300mV (1 sample).

TABLE 4.7: Mean corrosion rates and current densities (with standard deviation) of 50mV/s CV scans with different scan ranges around OCP: 100mV (4 samples) and 300mV (1 sample). The electrolyte used is SBF without buffer

Scan range	$\mathbf{v}_{corr}$ **(mm/year) method 1**	$\mathbf{v}_{corr}$ **(mm/year) method 2**	$\mathbf{v}_{corr}$ **(mm/year) method 3**	$\mathbf{v}_{corr}$ **(mm/year) method 4**
OCP±100 mV	0.123±0.0374	0.0674±0.0267	0.0954±0.0313	0.0861±0.0294
OCP±300 mV	0.307	0.192	0.249	0.255
Scan range	$\mathbf{i}_{corr}$ **(μA/cm^2) method 1**	$\mathbf{i}_{corr}$ **(μA/cm^2) method 2**	$\mathbf{i}_{corr}$ **(μA/cm^2) method 3**	$\mathbf{i}_{corr}$ **(μA/cm^2) method 4**
OCP±100 mV	10.6±3.22	5.80±2.29	8.21±2.69	7.41±2.53
OCP±300 mV	26.4	16.5	21.5	21.9

The impact on the corrosion rate and corrosion potentials can be seen on Figure 4.11 and this is also exposed on Tables 4.7 and 4.8. On Table 4.7, the different current densities are also made explicit. No real statistics can be undertaken in this case as only one sample has been tested for an OCP±300mV range. However, it is seen that again, the second method corresponds to the lower limit and the first method to the upper limit of corrosion rate. In either case, letting the scan range be more important increases the corrosion current density and thus the corrosion rate. Considering again, that method one is the best fit (concluding solely on the previously studied OCP±100mV samples), a graph comparing the observed corrosion potentials and corrosion current densities of the different samples can be seen on Figure 4.12. Quite a high negative shift in corrosion potential and increase in corrosion rate is observed for the OCP±300mV sample. The effect on the corrosion potentials can be seen on Figure 4.11b as well as on Table 4.8. A much higher change between the OCP and observed corrosion potential is present when the scan range is increased.

Finally, the CV as well as OCP plots of the samples used for this comparison can be seen on Figure 4.13. For the larger scan range, the observed corrosion potential is more negative. Regarding the slopes, the cathodic slopes of the different scan ranges look more alike (especially with some samples) whereas the anodic slope is much bigger in the case of a larger scan range.

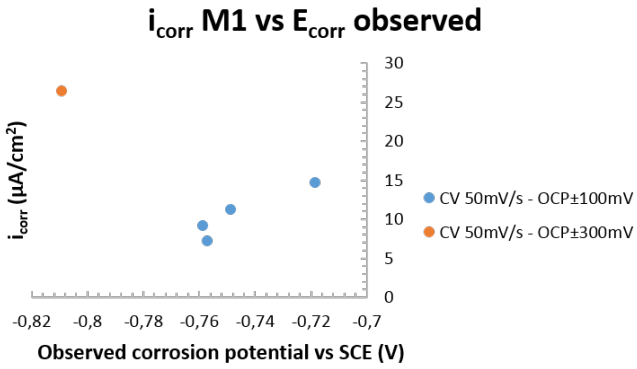

FIGURE 4.12: Corrosion current densities (first method) versus observed corrosion potential for 50mV/s CV scan over different scan ranges around OCP: 100mV (4 samples) and 300mV (1 sample).

TABLE 4.8: Mean corrosion potentials and Tafel slopes (with standard deviation) of 50mV/s CV scans with different scan ranges over OCP: 100mV (4 samples) and 300mV (1 sample). The electrolyte used is SBF without buffer

Scan range	**OCP (V)**	**E_{corr} (V) observed**	**E_{corr} (V) measured**	**β_a (mV/dec)**	**β_c (mV/dec)**
OCP±100 mV	-0.739±0.0172	-0.746±0.0186	-0.759±0.0191	70.9±27.2	-102±42.8
OCP±300 mV	-0.734	-0.809	-0.829	247	-161

4.1.4.2 Linear sweep voltammetry

The same investigation was undertaken for the different linear voltammetries (0.33mV/s and 1mV/s).

LSV 0.33mV/s

The different scan ranges studied for the LSV 0.33mV/s category are OCP±100mV (2 samples) and OCP±150mV (1 sample). The results can be seen on Figure 4.14 and Tables 4.9 and 4.10.

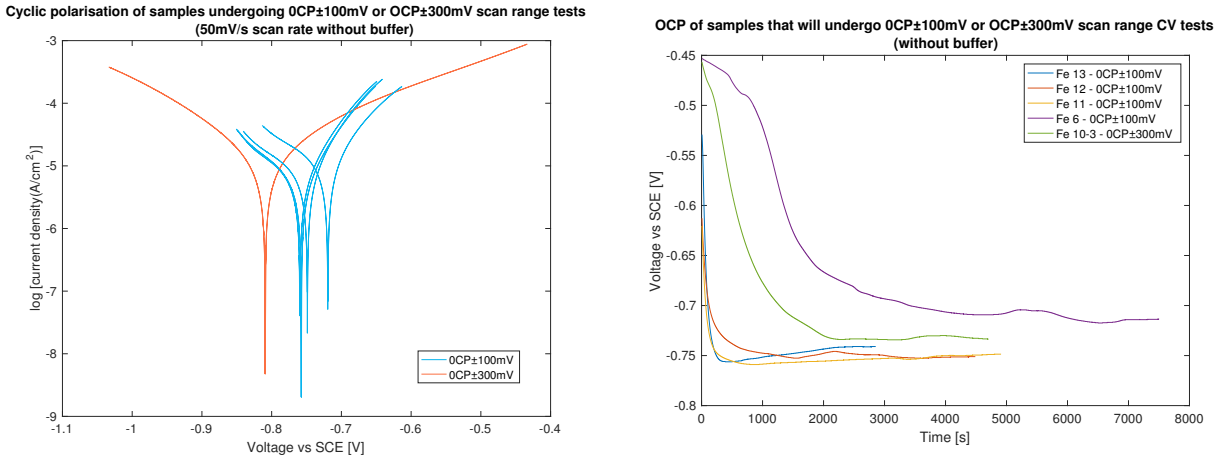

(A) (B)

FIGURE 4.13: (A) 50mV/s CV and (B) OCP plots for samples undergoing scan ranges of OCP±100mV and OCP±300mV.

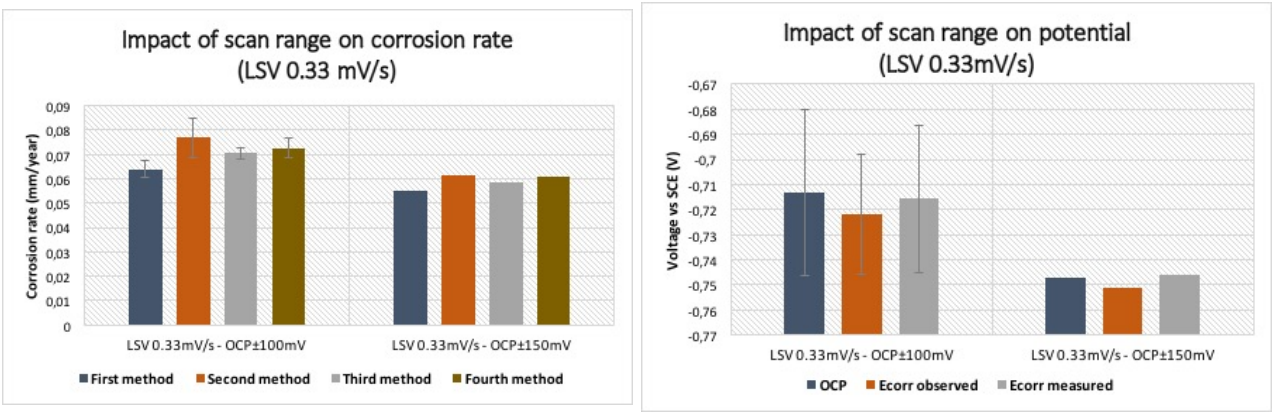

(A) (B)

FIGURE 4.14: (A) Corrosion rates and (B) corrosion potentials using the four different methods for LSV 0.33mV/s scans over different scan ranges.

Only one sample was used for the LSV 0.33mV/s with OCP±150mV scan range category. Thus, the third method is going to be used to graphically illustrate the observed corrosion potential and the corrosion current as this was the statistically best method for the LSV 0.33mV/s with OCP±100mV scan range category. The outcome of this can be seen on Figure 4.17. This method gives the second smallest corrosion current density for both categories. It can be seen that by increasing the scan range, the corrosion current densities (and thus the corrosion rates) are smaller. The corrosion potential

values are close as well in the OCP±100mV family as in the OCP±150mV family. The cathodic Tafel slope for the OCP±150mV sample is much higher than for the other category.

TABLE 4.9: Mean corrosion rates and current densities (with standard deviation) of LSV 0.33 mV/s scans with different scan ranges around OCP: 100mV (2 samples) and 150mV (one samples). The electrolyte used is SBF without buffer

Scan range	$\mathbf{v}_{corr}$ **(mm/year) method 1**	$\mathbf{v}_{corr}$ **(mm/year) method 2**	$\mathbf{v}_{corr}$ **(mm/year) method 3**	$\mathbf{v}_{corr}$ **(mm/year) method 4**
OCP±100 mV	0.0640±0.0032	0.0768±0.0082	0.0704±0.0025	0.0727±0.0041
OCP±150 mV	0.0550	0.0617	0.0584	0.0607
Scan range	$\mathbf{i}_{corr}$ **(μA/cm^2) method 1**	$\mathbf{i}_{corr}$ **(μA/cm^2) method 2**	$\mathbf{i}_{corr}$ **(μA/cm^2) method 3**	$\mathbf{i}_{corr}$ **(μA/cm^2) method 4**
OCP±100 mV	5.51±0.28	6.61±0.709	6.06±0.216	6.25±0.356
OCP±150 mV	4.73	5.31	5.02	5.22

TABLE 4.10: Mean corrosion potentials and Tafel slopes (with standard deviation) of LSV 0.33mV/s scans with different scan ranges around OCP: 100mV (2 samples) and 150mV (one samples). The electrolyte used is SBF without buffer.

Scan range	**OCP (V)**	$\mathbf{E}_{corr}$ **(V) observed**	$\mathbf{E}_{corr}$ **(V) measured**	β_a **(mV/dec)**	β_c **(mV/dec)**
OCP±100 mV	-0.713±0.033	-0.722±0.024	-0.716±0.029	117±2	-292±45
OCP±150 mV	-0.747	-0.751	-0.746	121	-670

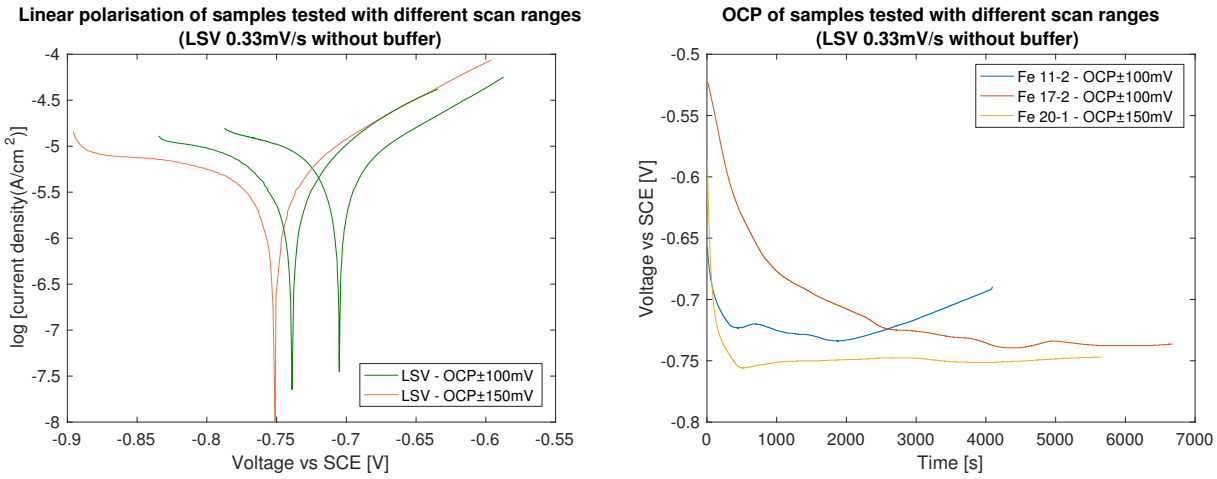

(A) (B)

FIGURE 4.15: (A) LSV 0.33 mV/s and (B) OCP plots for samples undergoing scan ranges of OCP±100mV and OCP±150mV.

LSV 1mV/s

For this category, the different studied scan ranges are OCP±100mV (2 samples), OCP±200mV (1 sample) and OCP±300mV (2 samples). As shown on Figure 4.16, the corrosion rate decreases when the scan range increases. The corrosion potentials are the closest for the OCP±100mV family.

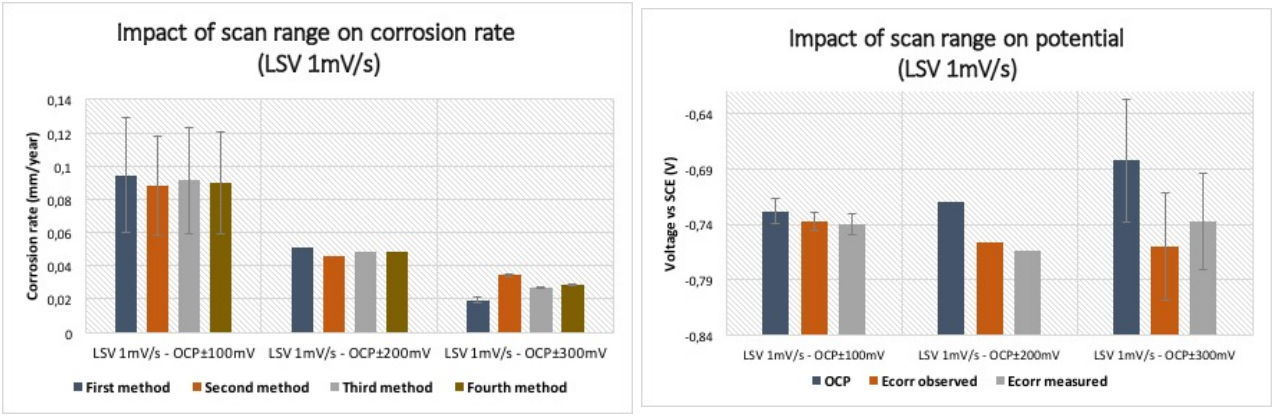

(A) (B)

FIGURE 4.16: (A) Corrosion rates and (B) corrosion potentials using the four different methods for LSV 1mV/s scans over different scan ranges.

Notice the excessive high value of the anodic Tafel slope for the OCP±200mV sample on Table 4.12. Also, the OCP from one of the two OCP±300mV samples had a raise in OCP, still ending towards a common corrosion rate, which is why it got included in the study.

The OCP±200mV family was only composed of one single sample. So, only the two other categories will be considered to see which of the four different methods is the most suitable. By looking at the standard deviations, in both of these categories, it can be seen that the second methods is the best for the 200mV scan range family and the fourth mehod is the best for the 300mV method. This is why these corrosion current densities along with the observed corrosion potential and measured corrosion potential can be seen on Figure 4.19. Note that the second method brings to the highest corrosion

rate for the OCP±300mV category and the smallest for the two other categories.

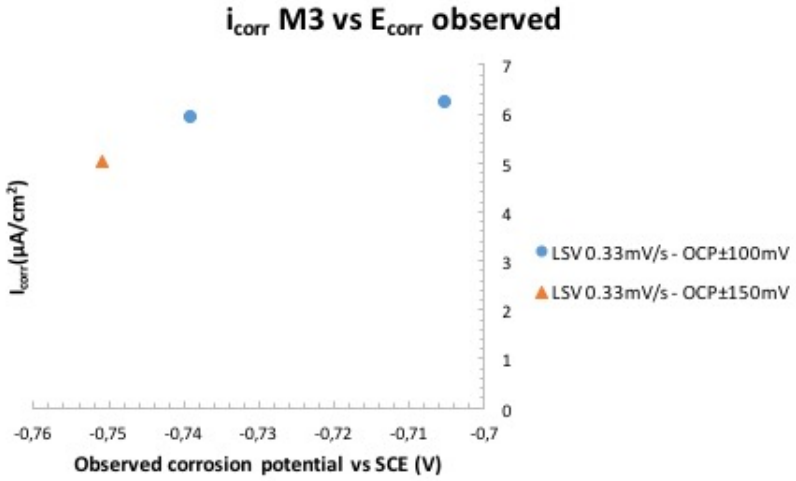

FIGURE 4.17: Corrosion current densities (third method) versus observed corrosion potential for the different scan ranges (LSV 0.33mV/s).

TABLE 4.11: Mean corrosion rates and current densities (with standard deviation) of LSV 1mV/s scans with different scan ranges around OCP: 100mV (2 samples), 200mV (1 sample), 300mV (2 samples). The electrolyte used is SBF without buffer.

Scan range	$\mathbf{v}_{corr}$ **(mm/year) method 1**	$\mathbf{v}_{corr}$ **(mm/year) method 2**	$\mathbf{v}_{corr}$ **(mm/year) method 3**	$\mathbf{v}_{corr}$ **(mm/year) method 4**
OCP±100 mV	0.0946±0.0345	0.0879±0.0298	0.0913±0.0321	0.0896±0.0306
OCP±200 mV	0.0514	0.0456	0.0485	0.0485
OCP±300 mV	0.0193±0.0018	0.0343±0.0008	0.0268±0.0005	0.0285±0.0003
Scan range	$\mathbf{i}_{corr}$ **(µA/cm²) method 1**	$\mathbf{i}_{corr}$ **(µA/cm²) method 2**	$\mathbf{i}_{corr}$ **(µA/cm²) method 3**	$\mathbf{i}_{corr}$ **(µA/cm²) method 4**
OCP±100 mV	8.14±2.97	7.57±2.56	7.85±2.76	7.71±2.63
OCP±200 mV	4.43	3.93	4.18	4.18
OCP±300 mV	1.66±0.15	2.95±0.07	2.30±0.04	2.45±0.03

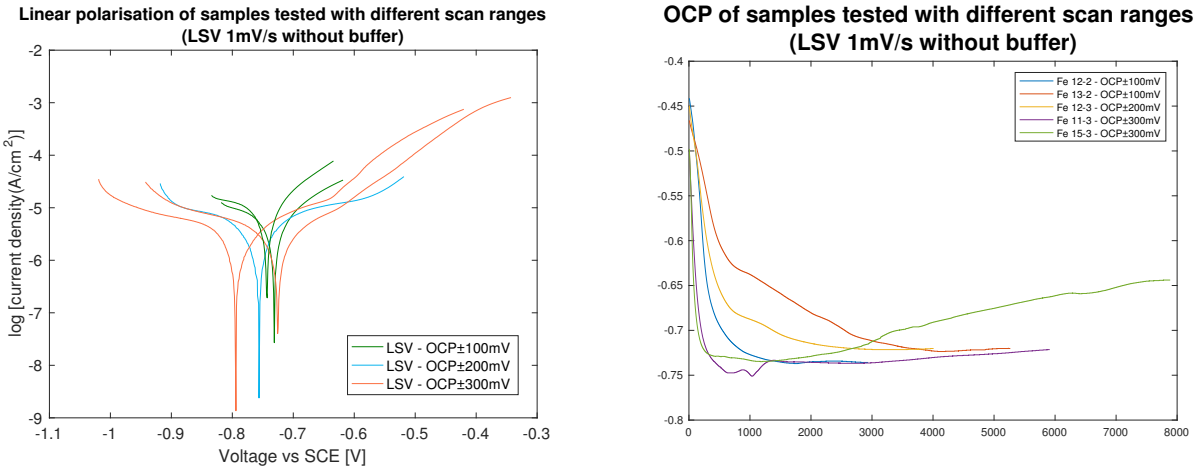

(A) (B)

FIGURE 4.18: (A) LSV 1mV/s and (B) OCP plots for samples undergoing scan ranges of OCP±100mV, OCP±200mV, and OCP±300mV.

TABLE 4.12: Mean corrosion potentials and Tafel slopes (with standard deviation) of LSV 1mV/s scans with different scan ranges around OCP: 100mV (2 samples), 200mV (1 sample), 300mV (2 samples). The electrolyte used is SBF without buffer.

Scan range	**OCP (V)**	**E_{corr} (V) observed**	**E_{corr} (V) measured**	**β_a (mV/dec)**	**β_c (mV/dec)**
OCP±100 mV	-0.728±0.011	-0.737±0.008	-0.740±0.009	135±18	-351±89
OCP±200 mV	-0.720	-0.756	-0.764	292	-283
OCP±300 mV	-0.683±0.055	-0.760±0.048	-0.737±0.043	131±5	-278±17

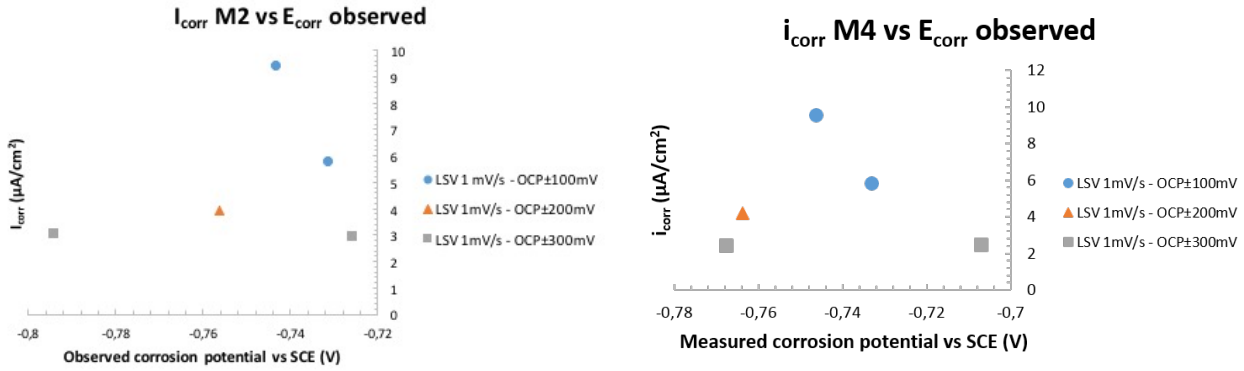

(A) (B)

FIGURE 4.19: Corrosion current densities (A) second versus observed corrosion potential and (B) fourth method versus measured corrosion potential for the different scan ranges (LSV 1mV/s).

4.1.5 Effect of buffer and pH on corrosion parameters

It was then further investigated if by adding Hepes buffer, the corrosion parameters would be affected. This investigation was undertaken because the immersion tests that started to get carried out needed a pH stabilizer for the longer immersion times. Two effect will be studied: the effect of the buffer itself and its concentration and the effect of the change in pH due to the addition of buffer[7].

4.1.5.1 Impact of pH

Samples with an electrolyte not containing any buffer started the test with a pH around 7.4 and ended the test with a pH around 7.56, which could possibly result in a $Fe(OH)_3$ passivity layer when looking at a Pourbaix diagram (see Figure 2.20). Thus, one sample with 50mM Hepes and starting pH of 7.53 was tested. No HCl was needed to be added for this sample in order to regulate the starting pH and the test ended with a pH of 7.54. This sample is then compared to one other sample immersed in an electrolyte with no buffer. This particular sample had an end pH of 7.6. Both samples were tested using LSV 0.33mV/s and a scan range of OCP±150mV. Table 4.13 compares the corrosion rates and corrosion current densities of the two samples. Figure 4.20 shows the difference in corrosion rate and corrosion potentials for these two samples. The difference in corrosion potentials and Tafel slopes can also be seen on Table 4.14. The overall corrosion potentials are less negative for the sample immersed in 50mM buffer. The corrosion rates follow different routes depending on which method is used. If the first method is considered, the sample with an electrolyte without buffer exhibits the highest corrosion rate. If method two and four are considered, the sample immersed in a 50mM buffer containing electrolyte exhibits the highest corrosion rate. Finally, if the third method is considered, the corrosion rate are similar. The four methods bring about the same corrosion rate for sample immersed in a solution without buffer, whereas the corrosion rates calculated with the four methods differ a lot for the other sample.

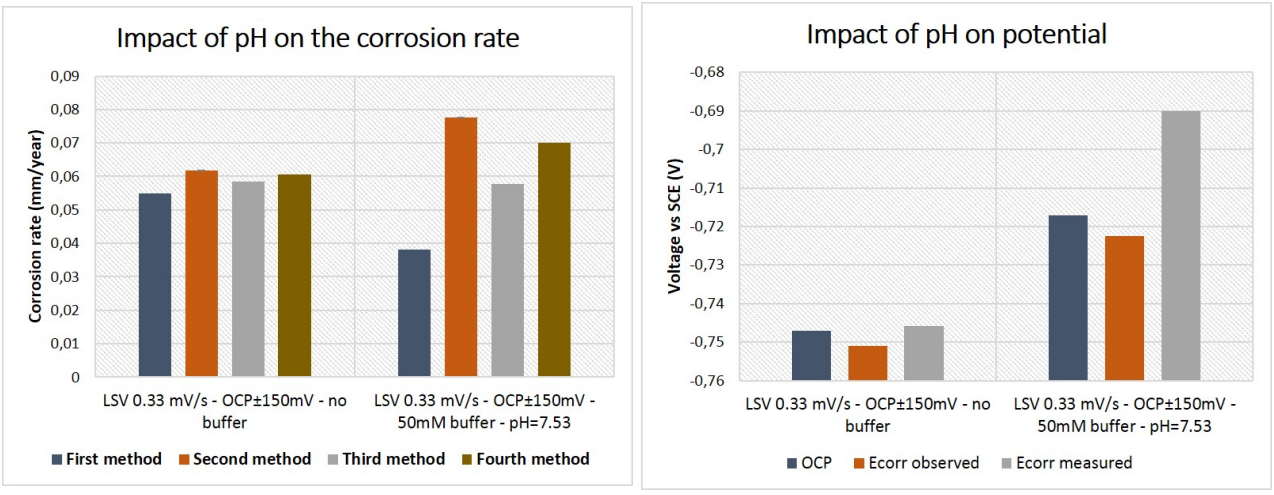

(A) (B)

FIGURE 4.20: (A) Corrosion rates and (B) corrosion potentials using solutions with or without Hepes buffer and end pH around 7.55.

Figure 4.21 shows the LSV plots as well as the open circuit potential of the two samples. When looking at the polarisation scans, it is seen that both scans look very similar with a shift towards higher current

[7]It has to be noted that for samples immersed in a solution not containing any buffer, the pH increased from 7.4 to around 7.56. For samples immersed in a 25mM buffer solution, the pH increased from 7.4 to about 7.46. For samples immersed in 50mM buffer solution, the pH increased from 7.4 to approximately 7.43.

density values for the cathodic branch of the 50mM sample and a shift towards lower current density values for the anodic branch of that sam sample. This sample also encounters a shift towards a more positive observed corrosion potential. When looking at Table 4.14, it can also be seen that the Tafel slopes are close to each other in both samples.

TABLE 4.13: Mean corrosion rates and current densities (with standard deviation) of samples immersed in solutions with or without Hepes buffer and end pH around 7.55.

Sample	$\mathbf{v}_{corr}$ **(mm/year) method 1**	$\mathbf{v}_{corr}$ **(mm/year) method 2**	$\mathbf{v}_{corr}$ **(mm/year) method 3**	$\mathbf{v}_{corr}$ **(mm/year) method 4**
0mM buffer	0.0550	0.0617	0.0584	0.0607
50mM buffer	0.0381	0.0775	0.0578	0.0699
Buffer concentration	$\mathbf{i}_{corr}$ $(\mu\mathbf{A/cm}^2)$ **method 1**	$\mathbf{i}_{corr}$ $(\mu\mathbf{A/cm}^2)$ **method 2**	$\mathbf{i}_{corr}$ $(\mu\mathbf{A/cm}^2)$ **method 3**	$\mathbf{i}_{corr}$ $(\mu\mathbf{A/cm}^2)$ **method 4**
0mM buffer	7.45	10.0	8.74	9.50
50mM buffer	3.28	6.67	4.97	6.02

Only one sample of each was tested, thus no decision can be made on which method brings the best corrosion current density. Therefore, the choice will be made regarding which method gives the lowest corrosion rate, which is the first method in both cases. Therefore, this method is illustrated on Figure 4.22.

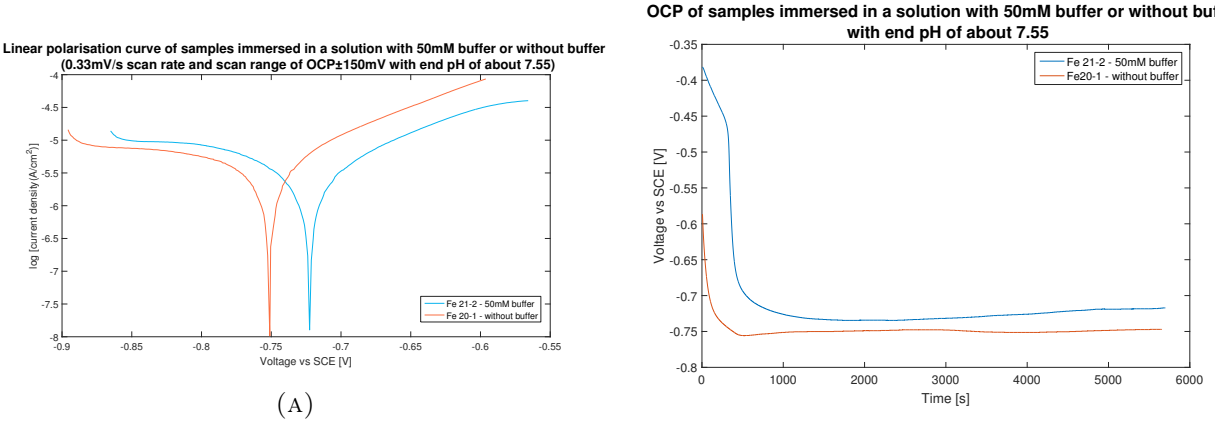

(A) (B)

FIGURE 4.21: (A) LSV and (B) OCP plots for of samples immersed in solutions with or without Hepes buffer and end pH around 7.55.

4.1.5.2 Impact of buffer concentration

In this section three different Hepes concentrations will be studied: 0mM, 25mM, and 50mM. The method used for comparison is LSV 0.33mV/s and OCP±150mV. Four samples were tested in a solution exempt of buffer. However, three samples three samples had a raise in OCP of more than 50mV,

which is why they will not be taken into account in here. Thus, the samples studied are composed of one sample immersed in an electrolyte without buffer, two samples immersed in a solution containing 25mM buffer and five samples immersed in a solution with 50mM buffer. All samples were started with a pH close to 7.4.

TABLE 4.14: Mean corrosion potentials and Tafel slopes (with standard deviation) for samples immersed in solutions with or without Hepes buffer and end pH around 7.55.

Sample	**OCP (V)**	**E_{corr} (V) observed**	**E_{corr} (V) measured**	**β_a (mV/dec)**	**β_c (mV/dec)**
0mM buffer	-0.747	-0.751	-0.746	121	-670
50mM buffer	-0.717	-0.723	-0.690	123	-723

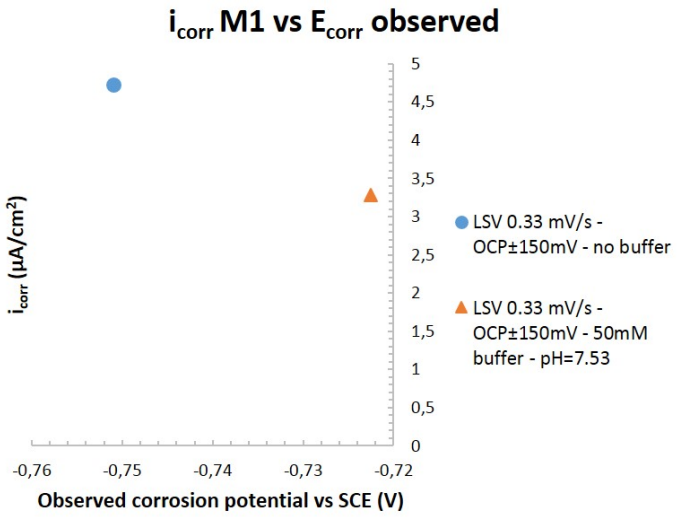

FIGURE 4.22: Corrosion current densities (first method) versus observed corrosion potential for samples being immersed in solutions not containing any buffer or a solution containing 50mM Hepes buffer but with starting pH of 7.53 (and end pH of 7.54).

Figure 4.23a and Table 4.15 show that by adding 25mM Hepes buffer, the corrosion current densities (thus corrosion rate) seem to increase compared to a solution prepared without any buffer. However, by adding 50mM Hepes buffer the corrosion rate decreases compared to the samples immersed in a 25mM buffer solution, still exhibiting a slightly higher corrosion rate than for the samples immersed in solutions containing no buffer at all. Figure 4.23b and Table 4.16 show that the corrosion potentials (OCP and E_{corr}) are higher for the samples in presence of higher buffer concentrations. The measured corrosion potential exhibits a quite high standard deviation and is higher for the samples immersed in 25mM buffer solution than for the ones immersed in 50mM buffer solution. Regarding the observed corrosion potentials, they are very close between each category. On the same table, it is seen that the cathodic Tafel slope are differing a lot between the two samples immersed in 25mM buffer solution, with one being much more limiting than for the two other categories.

The LSV scans as well as the OCP plots for the families with different buffer concentrations can be seen on Figure 4.24. The LSV plots show that the curves are very close to each other with the 25mM

sample being the highest in the current range. The OCP plots agree with this closeness.

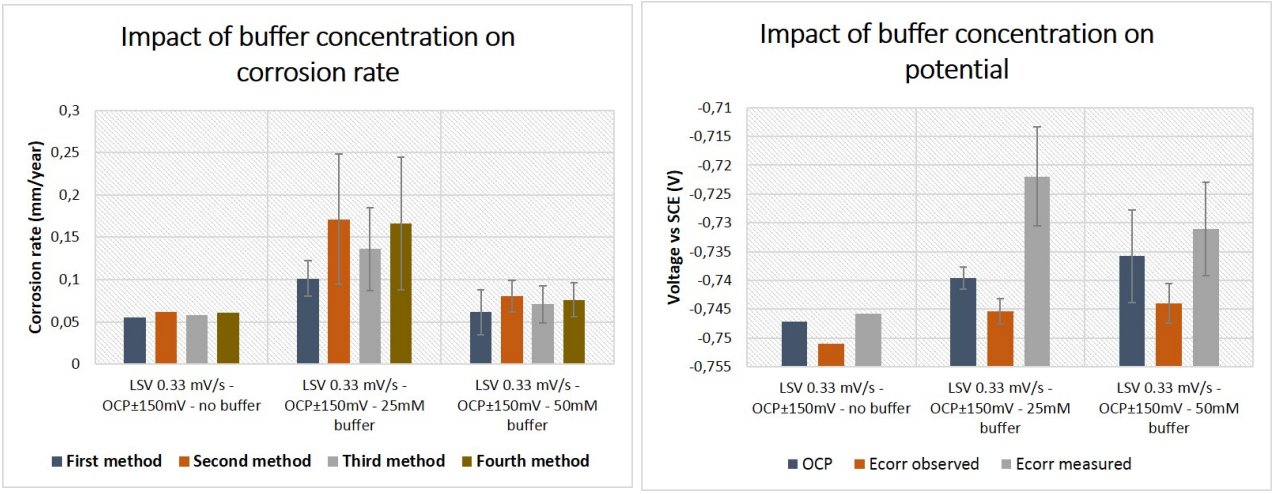

(A) (B)

FIGURE 4.23: (A) Corrosion rates and (B) corrosion potentials using solutions with different Hepes buffer concentrations.

TABLE 4.15: Mean corrosion rates and current densities (with standard deviation) of samples immersed in solutions with different Hepes buffer concentrations.

Buffer concentration	**v_{corr} (mm/year) method 1**	**v_{corr} (mm/year) method 2**	**v_{corr} (mm/year) method 3**	**v_{corr} (mm/year) method 4**
0mM buffer	0.0550	0.0617	0.0584	0.0607
25mM buffer	0.101±0.021	0.171±0.077	0.136±0.049	0.166±0.078
50mM buffer	0.0615±0.0265	0.0802±0.0185	0.0708±0.0221	0.0761±0.0203
Buffer concentration	**i_{corr} (μA/cm^2) method 1**	**i_{corr} (μA/cm^2) method 2**	**i_{corr} (μA/cm^2) method 3**	**i_{corr} (μA/cm^2) method 4**
0mM buffer	4.73	5.31	5.02	5.22
25mM buffer	8.71±1.79	14.7±6.6	11.7±4.2	14.3±6.7
50mM buffer	5.29±2.28	6.90±1.59	6.09±1.90	6.55±1.75

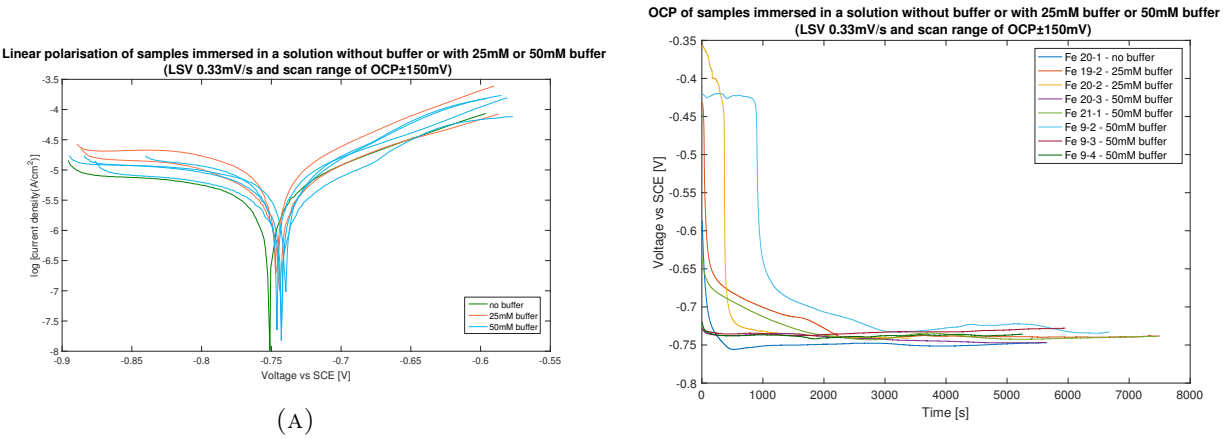

(A) (B)

FIGURE 4.24: (A) LSV and (B) OCP plots for tests using solutions with different Hepes buffer concentrations.

Statistically, the first method is by far the best statistical one for the 25mM buffer concentration samples, also resulting in the lowest corrosion rate. The second method result in the highest corrosion rate. On the other hand, the samples immersed in 50mM buffer solution exhibit the best statistical behaviour with the second method and the worst statistical behaviour with the first method. Here again, the first method exhibits the lowest corrosion rate and the second method exhibits the highest corrosion rate. This is also true for the samples immersed in a solution without buffer. Thus, both methods will be plotted and this will lead to a graphical illustration of the methods leading to the highest and lowest corrosion rates. These plots can be seen on Figure 4.25. Figure 4.25b shows that the data points are closer to each other when using the second method, regarding the 50mM buffer samples.

TABLE 4.16: Mean corrosion potentials and Tafel slopes (with standard deviation) for samples immersed in solutions with different Hepes buffer concentrations.

Buffer concentration	**OCP (V)**	**E_{corr} (V) observed**	**E_{corr} (V) measured**	**β_a (mV/dec)**	**β_c (mV/dec)**
0mM buffer	-0.747	-0.751	-0.746	121	-670
25mM buffer	-0.740±0.002	-0.745±0.002	-0.722±0.009	130±27	-2150±2063
50mM buffer	-0.736±0.008	-0.744±0.003	-0.731±0.008	116±31	-474±97

4.1.6 Impact of re-polishing a sample on the corrosion behaviour and the reproducibility of the system

The effect of re-polishing the sample has been investigated on "Fe-19" sample. The results can be seen throughout the figures and tables of this section 4.1.6.

The samples were tested using a solution with added buffer (25mM Hepes) and the tests were performed using LSV 0.33mV/s scans with a scan range of OCP±150mV in one case (Fe 19-2: first sample) and [OCP-150mV; OCP+200mV] in the other case (Fe 19-3: re-polished sample). In Figure 4.26a and

Table 4.17, the resulted corrosion rates and corrosion current densities are shown to be slightly higher for the re-polished sample and each method gives a close value compared to the other methods. Figure 4.26b and Table 4.18 show the difference in corrosion potentials between those two samples and it is shown that the re-polished sample has a higher OCP and observed corrosion potential but a lower measured corrosion potential.

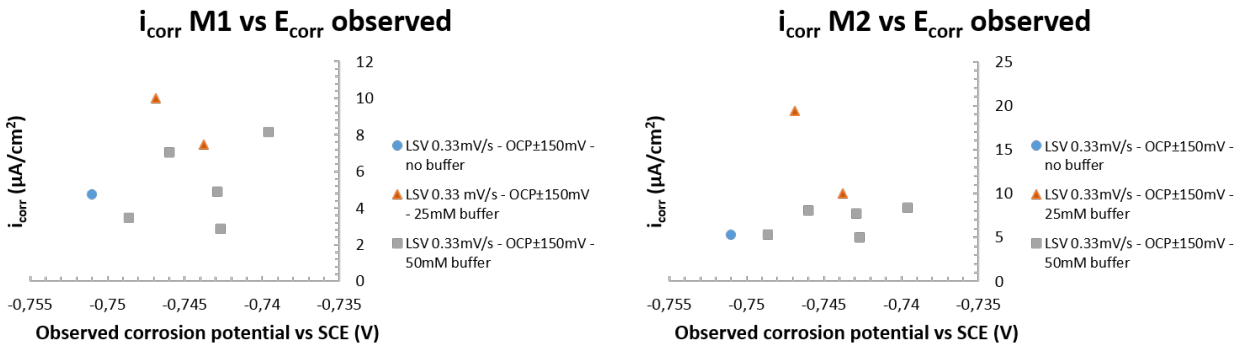

(A) (B)

FIGURE 4.25: Corrosion current densities (A) first method and (B) second method versus observed corrosion potential for samples being immersed in solutions containing different Hepes buffer concentrations.

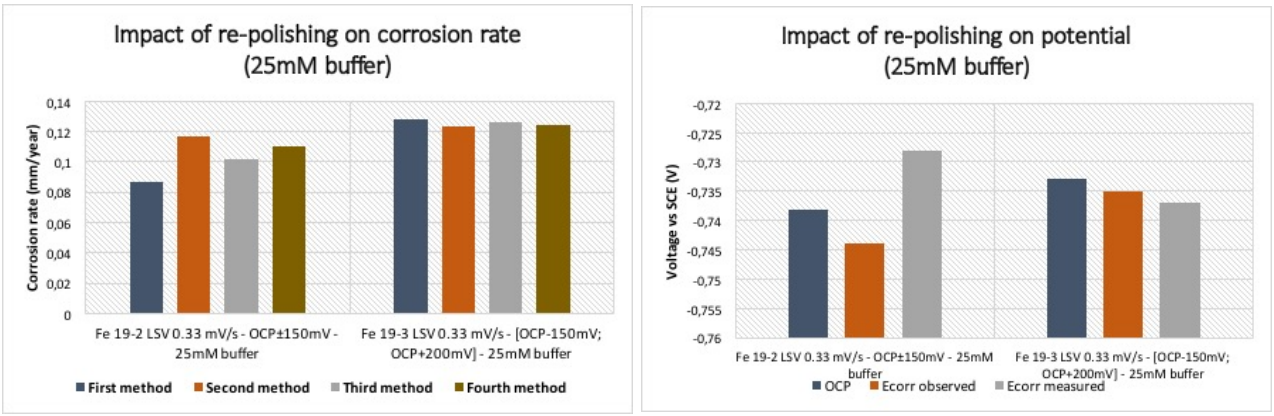

(A) (B)

FIGURE 4.26: (A) Corrosion rates and (B) corrosion potentials for samples that got re-polished.

The LSV scans as well as the open circuit potentials of the two samples can be seen on Figure 4.27. Both OCPs stabilized very well around the same value and the two LSV scans have a very similar cathodic behaviour with however different anodic slopes.

4.1.7 Impact of the deformation on the corrosion bevahiour of Fe-22Mn-0.6C compared to Armco iron

To allow a better comparison with the static immersion tests that were performed in SBF + 50mM buffer, the rest of the potentiodynamic polarisation tests were undergone using 50mM Hepes buffer as well. However, the surface polishing of the static immersion samples was not identical: the samples were polished up to OP-S for the polarisation tested samples and up to MD-Piano 1200 disc for the

static immersion samples.

TABLE 4.17: Mean corrosion rates and current densities (with standard deviation) of two samples that got re-polished: LSV 0.33mV/s (with 25mM buffer).

Sample	v_{corr} (mm/year) method 1	v_{corr} (mm/year) method 2	v_{corr} (mm/year) method 3	v_{corr} (mm/year) method 4
Fe 19-2	0.0866	0.117	0.102	0.110
Fe 19-3	0.128	0.123	0.126	0.124
Sample	i_{corr} (μA/cm^2) method 1	i_{corr} (μA/cm^2) method 2	i_{corr} (μA/cm^2) method 3	i_{corr} (μA/cm^2) method 4
Fe 19-2	7.45	10.0	8.74	9.50
Fe 19-3	11.0	10.6	10.8	10.7

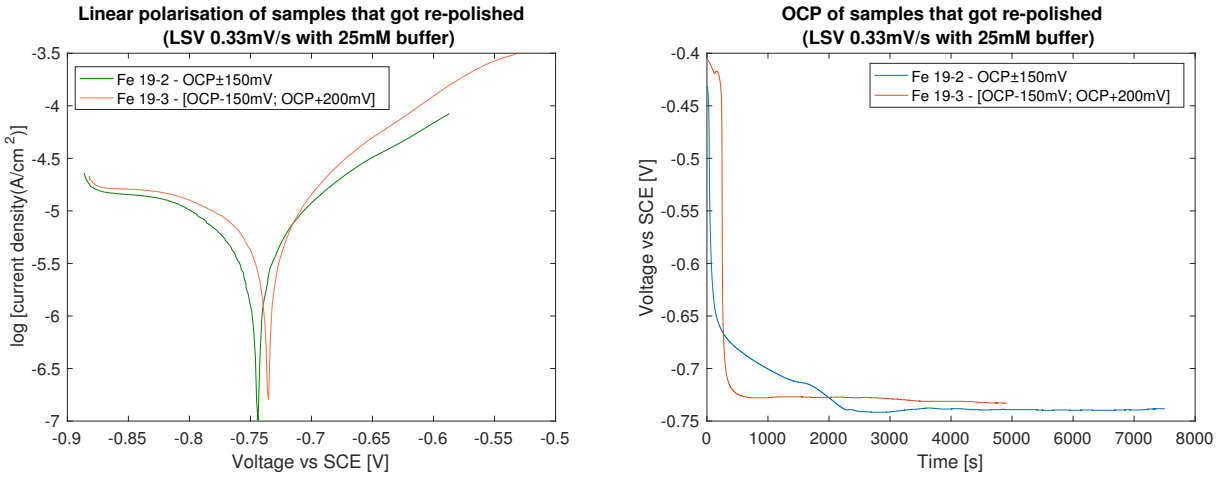

(A) (B)

FIGURE 4.27: (A) LSV and (B) OCP plots for samples that got re-polished.

TABLE 4.18: Mean corrosion potentials and Tafel slopes (with standard deviation) for samples that got re-polished: LSV 0.33mV/s (with 25mM buffer).

Sample	OCP (V)	E_{corr} (V) observed	E_{corr} (V) measured	β_a (mV/dec)	β_c (mV/dec)
Fe 19-2	-0.738	-0.744	-0.728	149	-692
Fe 19-3	-0.733	-0.735	-0.737	132	-643

As no statistic can be made directly on these two unique samples, the choice made in the previous section (section 4.1.5.2), i.e. the first method, will be used and this corrosion current density along

with the observed corrosion potential for the two investigated samples are shown on Figure 4.28.

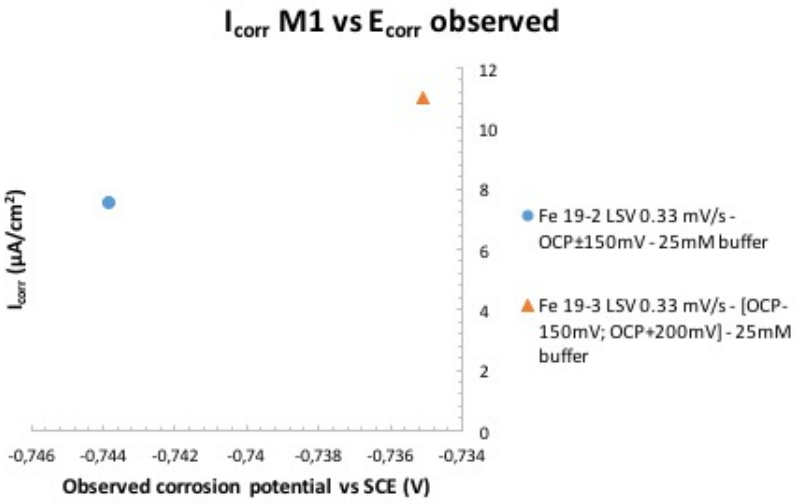

FIGURE 4.28: Corrosion current densities (first method) versus observed corrosion potential for samples that got re-polished.

Additionally, the method used for the following steps was the LSV 0.33mV/s with a scan range of OCP±150mV. The reason why this procedure was chosen is discussed in section 5.1.1.

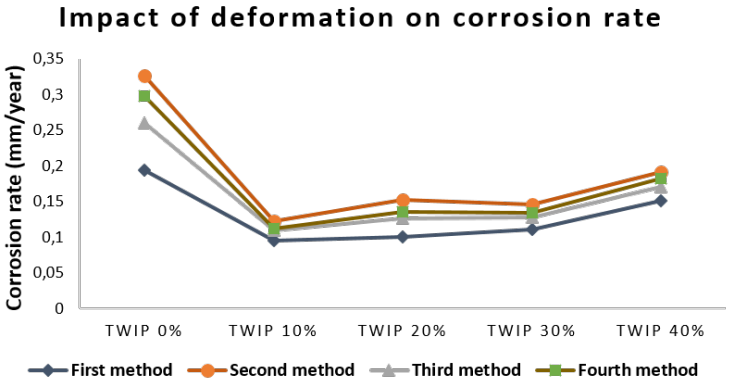

FIGURE 4.29: Corrosion rate evolution with respect to deformation level for Fe-22Mn-0.6C TWIP samples in a 50mM buffer solution. The outcome is similar to a fourth order polynomial.

The impact of deformation on the corrosion rate can be seen on Figure 4.29. The corrosion rate is maximal for a non deformed sample and minimal for a 10% deformed sample. The corrosion rate between 10% and 40% deformation tends to increase. The values of the corrosion rates and current densities can be seen on Table 4.19, where the values found for Armco iron samples in the same conditions are presented. Whatever method is used, the tendency is kept the same.

Figures 4.30a and 4.30b show the corrosion rates and corrosion potentials for the different samples compared to Armco iron. On these figures, it can be seen that the standard deviation is important. This is due to the fact that there were two families within each category: one family with a smaller corrosion

rate and another one with much higher corrosion rates (often being twice the value of the other family).

It has to be noted that in this category, some samples will be excluded from the analysis. Indeed, for these 8 samples, a swab of 5ml was taken after each OCP. However, as the setup was left in place in order to allow the LSV to take place afterwards, the swabs were not always taking homogeneous parts of the solution, hence the solution after OCP and before LSV could possibly have changed. This is the reason why these samples will be removed from this study.

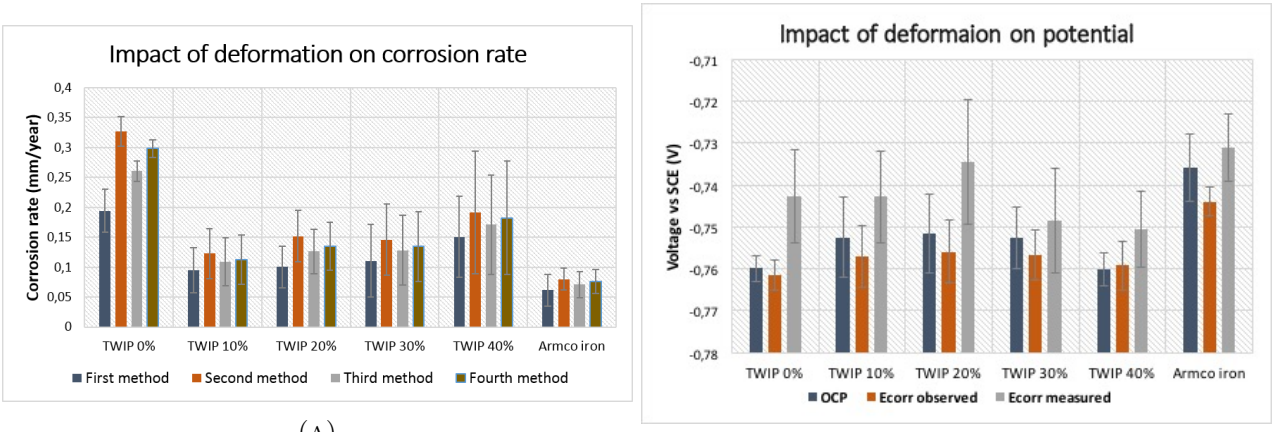

(A) (B)

FIGURE 4.30: (A) Corrosion rates and (B) corrosion potentials for TWIP samples that underwent different deformations. The LSV scans were performed using a 0.33mV/s scan rate throughout an OCP±150mV range in a 50mM buffer solution.

Table 4.20 as well as Figure 4.30b show the closeness between the observed corrosion potentials and the open circuit potentials. The family with the highest corrosion rate (non deformed TWIP) is also the one exhibiting the most negative OCP and observed corrosion potential. The Armco Iron family, with the smallest corrosion rate is the one exhibiting the highest OCP and observed corrosion potential. This relationship is also followed for the other intermediary families. Table 4.20 clearly shows how small the standard deviations are. This is especially true for the OCP and observed corrosion potential.

The OCP and LSV scans of the different tested samples for this comparison will also be illustrated. In order to avoid overloading one graph, the family with the highest corrosion rate (i.e. the non deformed TWIP samples) and the one resulting in the lowest corrosion rate (TWIP 10% samples) will be plotted against each other and can be found on Figures 4.31a and 4.31b. The three other families will be plotted separately on Figures 4.31c and 4.31d. Finally, as the Armco iron starts with a potential much higher than the TWIP samples, these samples will also be plotted individually in order to allow more clarity on Figures 4.31e and 4.31f.

When looking at Table 4.19, it can be seen that the fourth method brings the lowest standard deviation for the non deformed TWIP samples. The first method brings the best results for the TWIP 40% family. Finally, the second method brings the best results for the Armco iron family as well as the TWIP 30%, TWIP 20% and TWIP 40% families. Therefore, the three different corrosion current densities (method one, method two, and method four) will be plotted against their respective corrosion potentials (observed for first and second methods and measured for the fourth method). This can be seen on Figure 4.32.

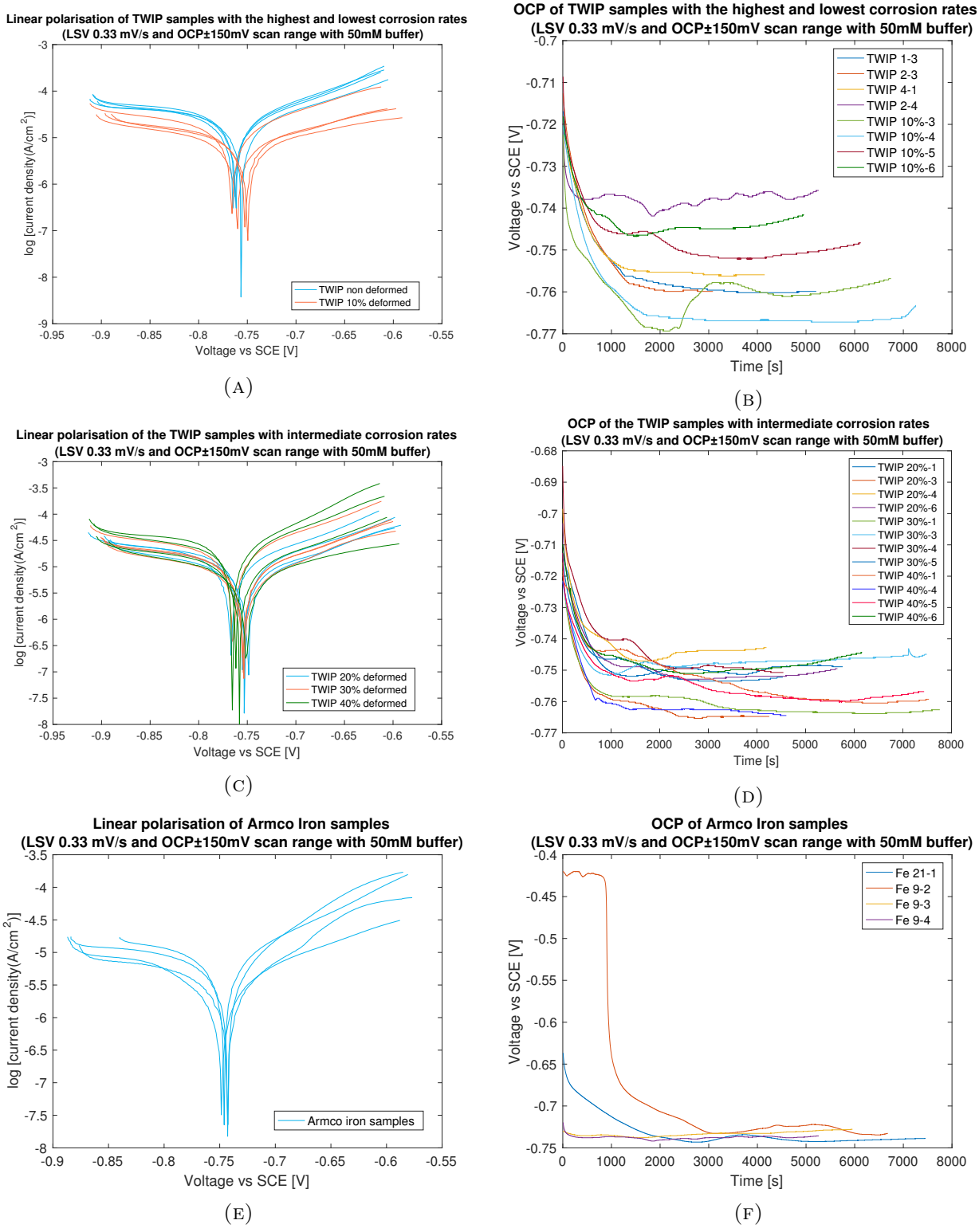

FIGURE 4.31: LSV plots of (A) non deformed against 10% deformed TWIP samples which exhibited the highest and lowest corrosion rates respectively, (C) 20%, 30%, and 40% deformed TWIP samples which exhibited intermediary corrosion rates, (E) Armco iron samples. OCP plots of (B) non deformed against 10% deformed TWIP samples which exhibited the highest and lowest corrosion rates respectively, (D) 20%, 30%, and 40% deformed TWIP samples which exhibited intermediary corrosion rates, (F) Armco iron samples.

TABLE 4.19: Mean corrosion rates and current densities (with standard deviation) of TWIP samples with different deformations compared to Armco iron samples (immersed in 50mM buffer solution).

Sample	$\mathbf{v}_{corr}$ **(mm/year) method 1**	$\mathbf{v}_{corr}$ **(mm/year) method 2**	$\mathbf{v}_{corr}$ **(mm/year) method 3**	$\mathbf{v}_{corr}$ **(mm/year) method 4**
Armco Iron	0.0615±0.0265	0.0802±0.0185	0.0708±0.0221	0.0761±0.0203
TWIP 0%	0.194±0.036	0.327±0.025	0.260±0.017	0.298±0.0144
TWIP 10%	0.0950±0.0377	0.123±0.042	0.109±0.040	0.112±0.042
TWIP 20%	0.100±0.034	0.152±0.043	0.126±0.038	0.135±0.040
TWIP 30%	0.110±0.061	0.146±0.059	0.128±0.058	0.135±0.058
TWIP 40%	0.151±0.068	0.191± 0.103	0.171±0.083	0.182±0.095
Sample	$\mathbf{i}_{corr}$ **(μA/cm^2) method 1**	$\mathbf{i}_{corr}$ **(μA/cm^2) method 2**	$\mathbf{i}_{corr}$ **(μA/cm^2) method 3**	$\mathbf{i}_{corr}$ **(μA/cm^2) method 4**
Armco Iron	5.29±2.28	6.90±1.59	6.09±1.90	6.55±1.75
TWIP 0%	16.4±3.0	27.7±2.1	22.0±1.4	25.2±1.2
TWIP 10%	8.04±3.19	10.4±3.5	9.23±3.35	9.51±3.51
TWIP 20%	8.49±2.91	12.9±3.6	10.7±3.2	11.4±3.4
TWIP 30%	9.34±5.13	12.3±5.0	10.8±4.9	11.4±4.9
TWIP 40%	12.8±5.7	16.2±8.7	14.5±7.0	15.4±8.0

On Figure 4.32a, it is clearly seen that the zero deformation samples exhibit the highest corrosion rate, whereas the Armco Iron standard samples exhibit the lowest corrosion current densities. The TWIP 40% family is split in two groups, with highly different corrosion rates (especially seen for method one and four). The three other deformation families (10%, 20%, and 30%) seem to exhibit a smaller corrosion rate than the 40% deformation family, with however one outlier. When using the fourth method, as seen on Figure 4.32c, the outliers are less pronounced, when talking about the current density. The measured corrosion potential of one TWIP30% sample is however very negative and differs a lot from its OCP and observed corrosion potentials (-0.745V and -0.752V respectively, whereas the measured corrosion potential lies at -0.784V).

TABLE 4.20: Mean corrosion potentials and Tafel slopes (with standard deviation) of TWIP samples with different deformations compared to Armco iron samples (immersed in 50mM buffer solution).

Sample	OCP (V)	E_{corr} (V) observed	E_{corr} (V) measured	β_a (mV/dec)	β_c (mV/dec)
Armco Iron	-0.736±0.008	-0.744±0.003	-0.731±0.008	116±31	-474±97
TWIP 0%	-0.760±0.003	-0.761±0.004	-0.743±0.011	131±12	-553±128
TWIP 10%	-0.752±0.009	-0.757±0.007	-0.743± 0.011	187±36	-283±83
TWIP 20%	-0.752±0.009	-0.756±0.008	-0.735±0.015	164±13	-399±58
TWIP 30%	-0.753±0.007	-0.757±0.006	-0.749±0.012	170±30	-332±121
TWIP 40%	-0.760±0.004	-0.759±0.006	-0.751±0.009	169±74	-413±113

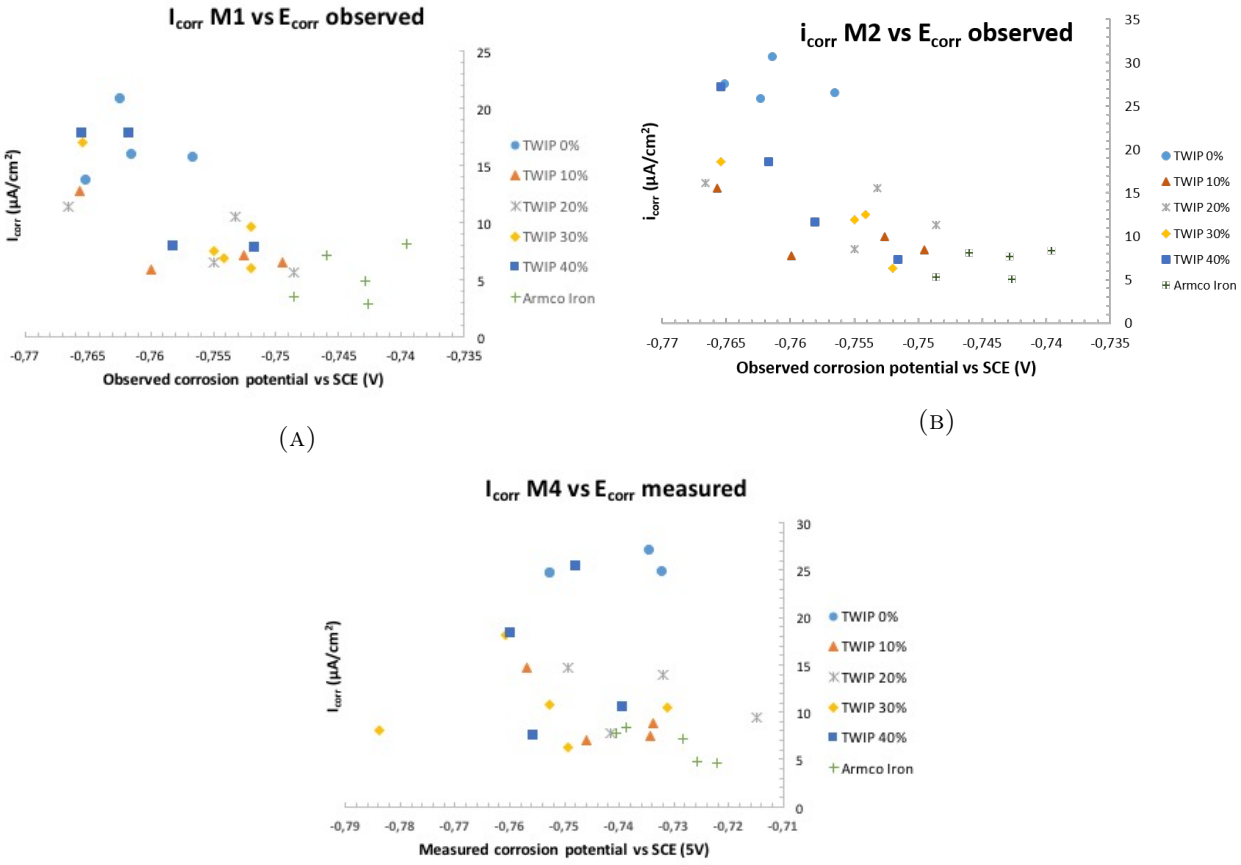

(A) (B)

(C)

FIGURE 4.32: Corrosion current densities ((A) first method, (B) second method, and (C) fourth method) versus observed/measured corrosion potential for TWIP samples with different deformations and the Armco iron standards.

4.1.8 XRD for potentiodynamic polarisation samples

XRD analysis has been performed on three Armo iron samples and two TWIP samples after potentiodynamic polarisation tests in order to investigate if any element of the corroded surface could be detected. Three iron samples and one non deformed TWIP sample as well as a 40% deformed one were studied.

The results can be seen on Figure 4.33. On Figure 4.33a, the peaks correspond to the αFe (ferrite) phase and on Figure 4.33b, the peaks correspond to γFe (austenite) phase. For the iron samples (Figure 4.33), there seem to be some small peaks around 31°, 40° and 73° but these are too small to make sure that they are not just due to the noise. These peaks are more clearly seen on Figure 4.33c, where the background signal has not been removed. Except for the crystalline structure of the ion and TWIP samples, nothing could be concluded.

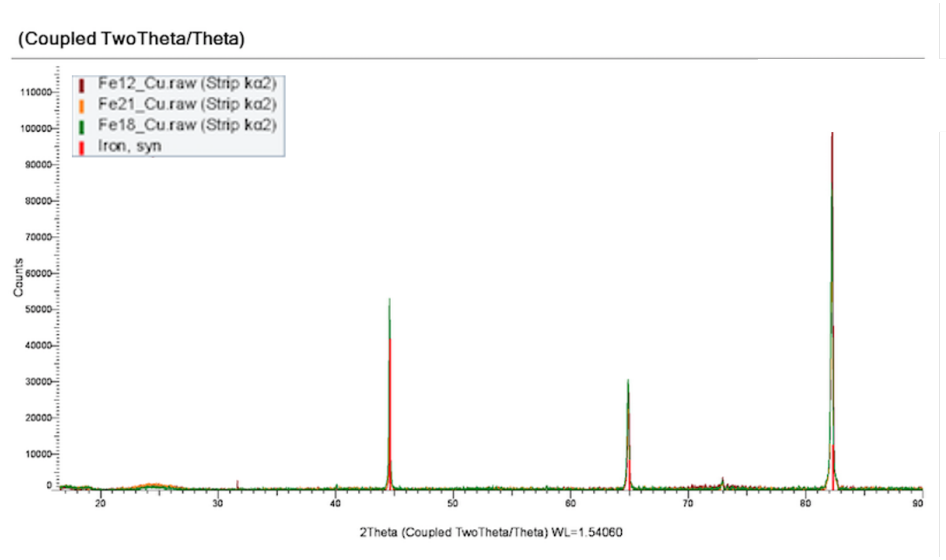

(A)

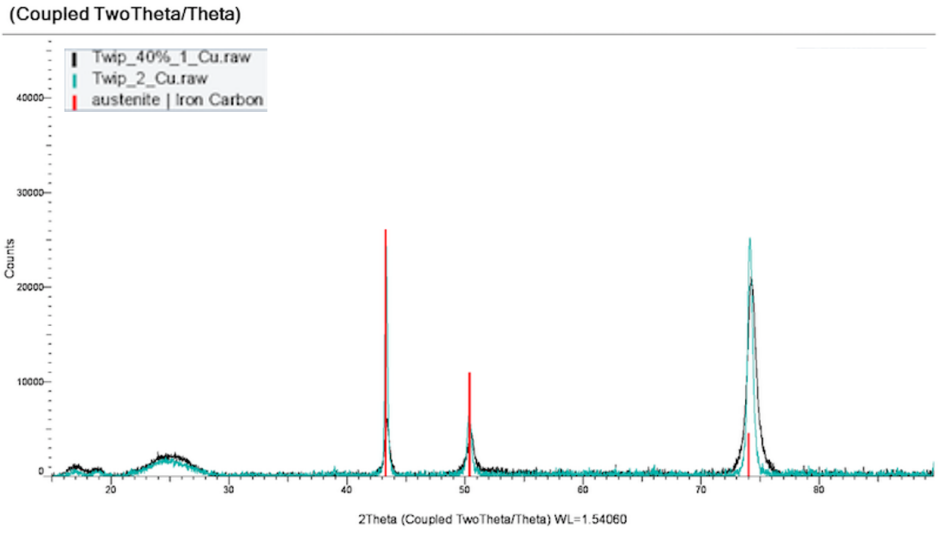

(B)

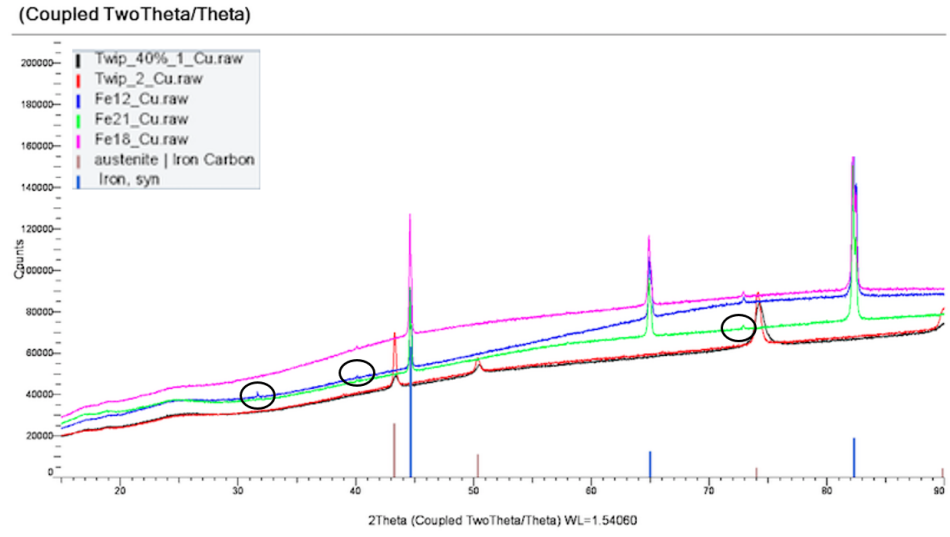

(C)

FIGURE 4.33: XRD spectra for (A) iron samples after polarisation test, (B) TWIP samples after polarisation test, and (C) raw spectra with background signal.

4.1.9 SEM and EDX for potentiodynamic polarisation samples

The microstructure of both, Armco iron and Fe-22Mn-0.6C samples have been studied.

The Armco iron samples microstructure has already been shown on Figure 3.2, where the grain size is of about 20μm. A similar sample, polished up to one minute OP-S is seen on Figure 4.34, where inclusions can be seen. The microstructure of the TWIP samples with different deformation rates can be seen on Figure 4.35, where the average grain size is about 2-5 μm.The TWIP non deformed, 10%, and 20% samples were polished up to three minutes OP-S as opposed to one minute OP-S when immersed in the electrolyte. The OP-S time was increased in order to get images with less scratches. The other samples were polished up to one minute OP-S. On that figure 4.35, it can be seen that the more the sample is deformed, the more twins are present. A few twins can already be pointed out in the non deformed sample. This sample also presents porosities around some grain boundaries.

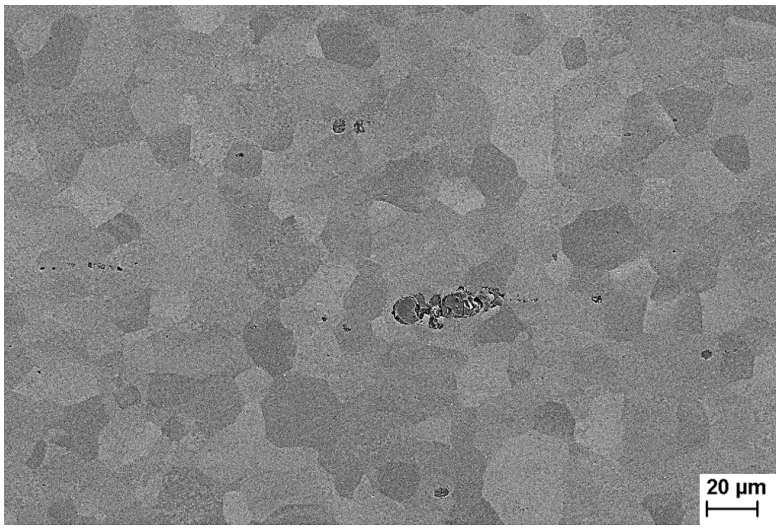

FIGURE 4.34: SE image of the microstructure of an Armco iron sample with the presence of an inclusion.

Figure 4.37, shows EDX spectra of the inclusions and the matrix of the sample shown on Figure 4.34. It is seen that the matrix is made exclusively of iron, whereas the inclusions contain manganese, aluminum, silicon, a little bit of chromium and sulfur.

Some samples were also observed after the potentiodynamic polarisation test was performed. Figures 4.36 and 4.40 show some images of the corroded surface after the polarisation tests on Armco iron and TWIP samples respectively. Some spots have also been investigated in a composition point of view.

Figure 4.36a shows a general image of the corroded surface where the delimitation with the non corroded part of the sample can be seen on the top left part of the figure. The Figures 4.36b, 4.36c, and 4.36d show images of that surface with higher magnification and they clearly illustrate the presence of a layer that was deposited on the metal surface, which got broken at some places. An EDX investigation of such layer has been done using a 5kV EHT beam. Such accelerating voltages are not enough in order to quantify the layer. Additionally, the layer seems to make less than one micron, which would mean that the studied volume would be greater than the layer and some metal would be accounted in. This is why only a qualitative study was undertaken and this can be seen on Figure 4.39. It can be seen that the metal layer beneath the corrosion product layer is indeed mostly composed of Fe, which is consistent with the SEM images, where the microstructure can be seen at these spots (especially in Figure

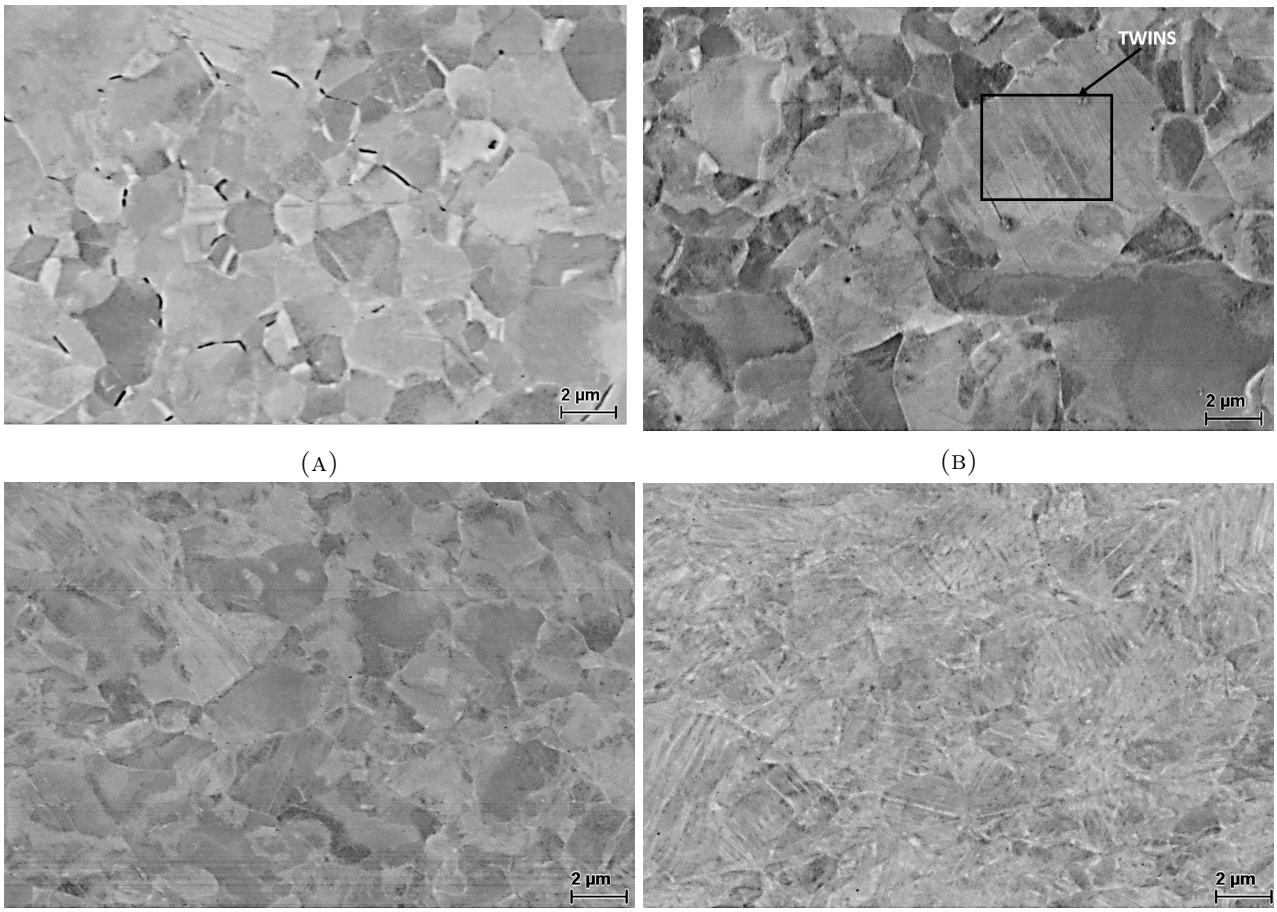

(A) (B)

(C) (D)

FIGURE 4.35: BSD images of the microstructure of (A) a non deformed TWIP sample, (B) a 10% deformed TWIP sample with twins highlighted, (C) a 20% deformed TWIP sample, and (D) a 40% deformed TWIP sample. The images were taken using a 120μm aperture and 15kV gun. Due to a defect in the BSD detector, no better quality images could be obtained.

4.36c). The deposited layer is composed of Mg, Na, Ca, and P and the oxygen peak is very large, illustrating the presence of oxides or phosphates on that layer. These spectra can be seen on Figure 4.39.

Another investigation consisted in looking if there seemed to be any change in morphology and composition regarding different areas of the corroded surface of a TWIP 30% sample. As a matter of fact, after polarisation test, the sample exhibits two colored regions: a blue one and a brown one [8]. These are not always identical from sample to sample. Thus, it was thought interesting to study the difference in morphology and composition of these two areas to possibly explain the high standard deviations found on the samples (described above). Figure 4.40 shows the different resulting SEM images of the brown and blue parts from Figure 4.38. EDX analysis [9] showed that in both cases the corrosion products seemed to be made of Na, P, Cl, and Mg. However, no cracked layer has been observed, compared to the iron sample (see Figure 4.36). The matrix beneath the localized corrosion products differs between the brown region and the blue region. The matrix in the blue region is mainly composed of Fe and Mn (with the other elements present in the steel, i.e. V, Cr,V, and Si) but it also contains elements of the SBF solution and especially Mg and Ca. Some Al as contamination is also

[8] This is valid for most samples (iron and TWIP).

[9] Only qualitative analysis will be undertaken due to the corrosion products thickness being very small. Here the EDX analysis used a 15kV beam

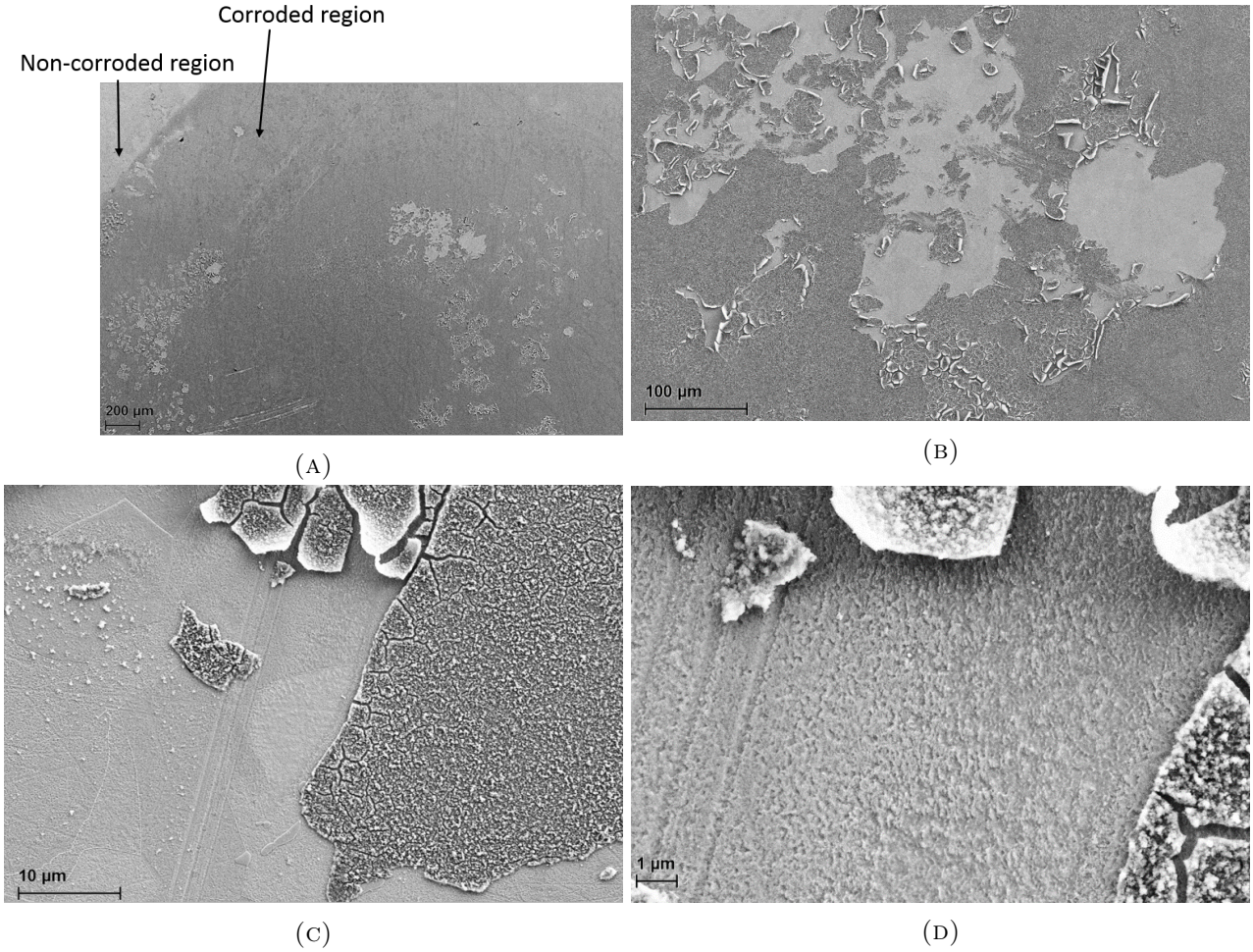

(A) (B) (C) (D)

FIGURE 4.36: Illustration of SE images of the corroded layer of an Armco iron sample that underwent a cyclic polarisation test: (A) a general image, (B) an enlargement of Figure (A), (C) an enlargement of Figure (B), and (D) an enlargement of Figure (C)

present as well as traces of Zr. The matrix of the brown part also mostly contains the alloy elements but it also contains some Ca, K, and very few P. Aluminium as contaminant is again present. Thus, it seems that not the same SBF elements get deposited at the same places on the alloy surface.
When looking at the deposits on both parts, the following behaviour is seen on EDX analysis. Some blue spots contain considerable amounts of Mg and Cl and fewer amounts of P, Ca, and Na. These spots also contain considerable amounts of Si and Al, more than the usual amounts found in the metal piece, thus coming from a contamination source. Other spots contain more Na, Ca, and P and less, even no traces of Mg and Cl. These spots contain fewer amounts of Al and Si. For the brown part, the elements that are the most deposited are Na, P, and Cl with acceptable amounts of Si and slightly higher amounts of Al. It must also be considered in mind that the piece of metal also contains small traces of phosphorus.

4.1.10 ICP analysis of the potentiodynamic polarisation tests

ICP has been performed on most samples after the polarisation test was performed. For one Armco iron sample, no polarisation was performed and the sample was only left to stabilize its OCP before taking a sample for ICP analysis.

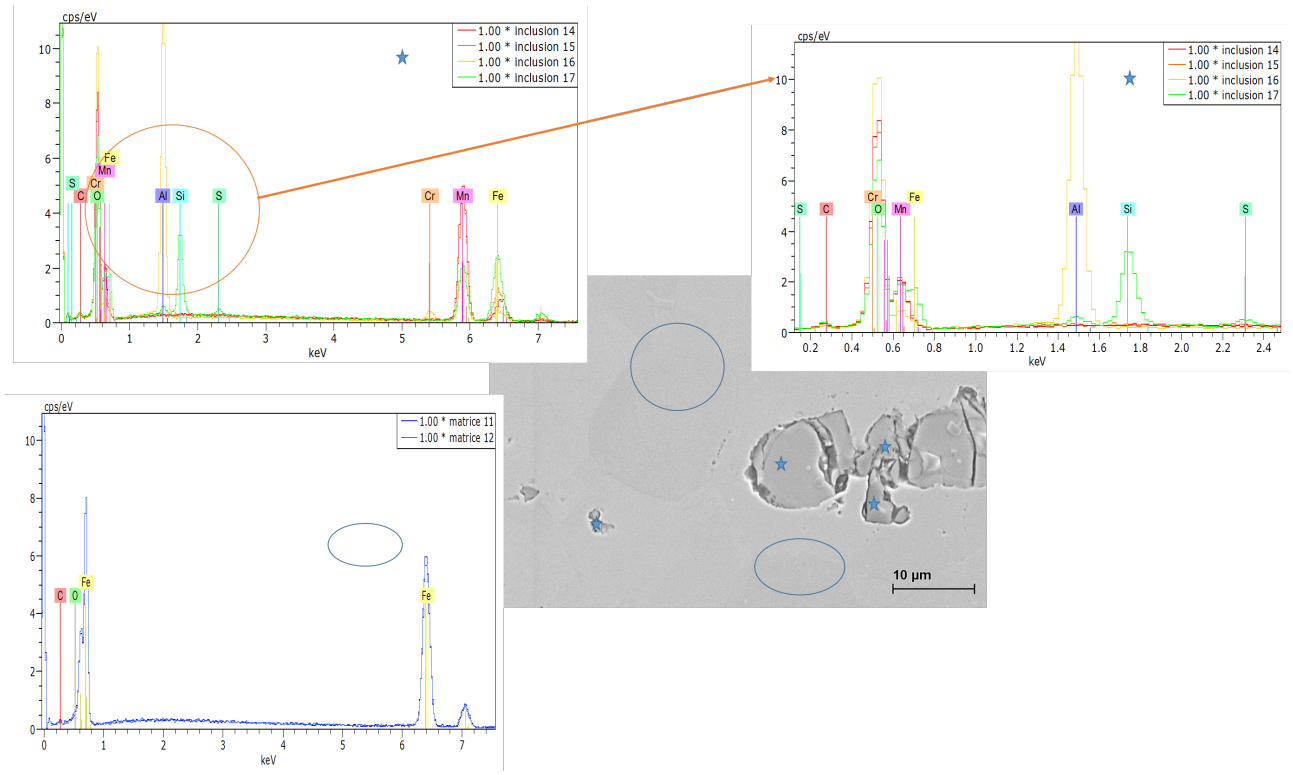

FIGURE 4.37: EDX spectra of the inclusion found on Figure 4.34 on Armco iron compared to the matrix.

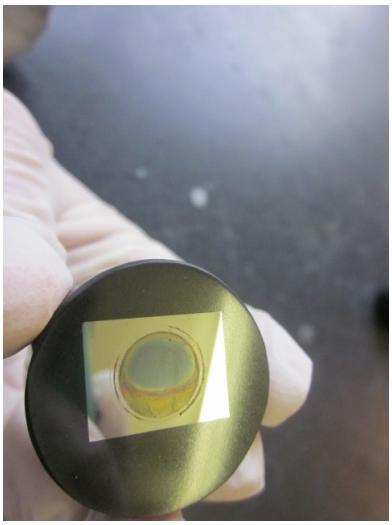

FIGURE 4.38: Picture illustrating the presence of two coloured regions: a brown one and a blue one.

Armco iron samples

The results of the ICP analysis are that after polarisation tests, the amount of iron that is released in the solution is about 0.06 to 0.08 mg/l and no significant changes in the SBF compounds can be concluded. The sample that did not undergo any polarisation scan, released 0.03 mg/l iron in solution after OCP stabilisation, which is thus the amount of iron released in order to reach the system equilibrium.

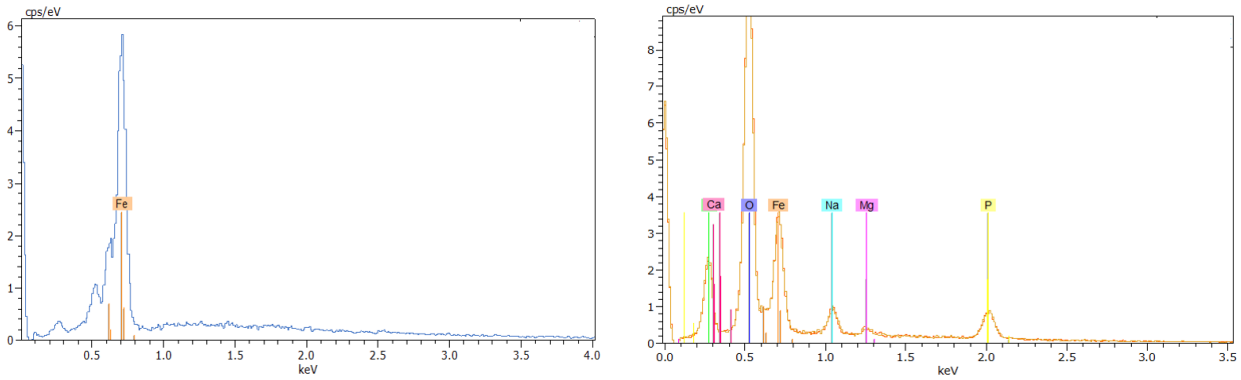

(A) (B)

FIGURE 4.39: EDX spectra for (A) the metal surface underneath the deposited layer and (B) the deposited layer (cfr. Figure 4.36 for the SEM images of these two regions). The images were taken using a 5kV beam and 30μm aperture.

TWIP samples

The results of the ICP analysis for these samples illustrate that the non deformed samples released an average iron concentration of 0.09 mg/l and 0.02 mg/l of manganese (note that the manganese concentration stays the same and only the iron concentration differs from sample to sample). The TWIP 10% family releases on average 0.07 mg/l iron (with quite different values from sample to sample) and 0.02 mg/l manganese for each sample. The TWIP 20% family releases 0.06 mg/l iron on average and 0.02 mg/l manganese for each sample. The TWIP 30% family releases on average 0.07 mg/l iron and 0.02 mg/l manganese for each sample. Finally, the TWIP 40% family releases 0.09 mg/l iron on average (with high standard deviation) and 0.03 mg/l manganese for each sample.

It will now be seen if there is a relationship between the amount of ions released in solution and the corrosion rate, as would be expected. Table 4.21 summarizes some samples with their corrosion rate and released ion concentrations. The corrosion rates displayed will be the ones calculated with the first method (one of the three best statistically for these samples, see section 4.1.7). By looking at the TWIP 40% family, the lowest corrosion rate corresponds to the lowest amount of iron released in solution and the two highest corrosion rate release 0.02 and 0.04 mg/l iron more than the previous sample. For the TWIP 30% family, the lowest corrosion rates and highest corrosion rate correspond to the smallest amount of iron released and highest amount of iron released respectively. This is also the case in the TWIP10% family. The non deformed TWIP family exhibits the opposite behaviour, with more iron released for a sample that corroded slower than the other sample. It can be noted that the manganese concentration does not change from sample to sample and is equal to 0.02 mg/l for each family except the TWIP 40% family, where this concentration is equal to 0.03 mg/l.

4.2 Static immersion tests of Fe-22Mn-0.6C samples

In this section, the outcomes of the static immersion tests will be detailed. The changes in surface morphology of the samples will be investigated and the different components that get deposited on the sample will be pointed out. Mass loss rates will also be calculated after immersion, including corrosion products and deposits (some samples will undergo HCl attack with 3.5 g/l hexamethylenetetramine as already detailed in the materials and methodology section 3.4 in order to evaluate the corrosion product after attack).

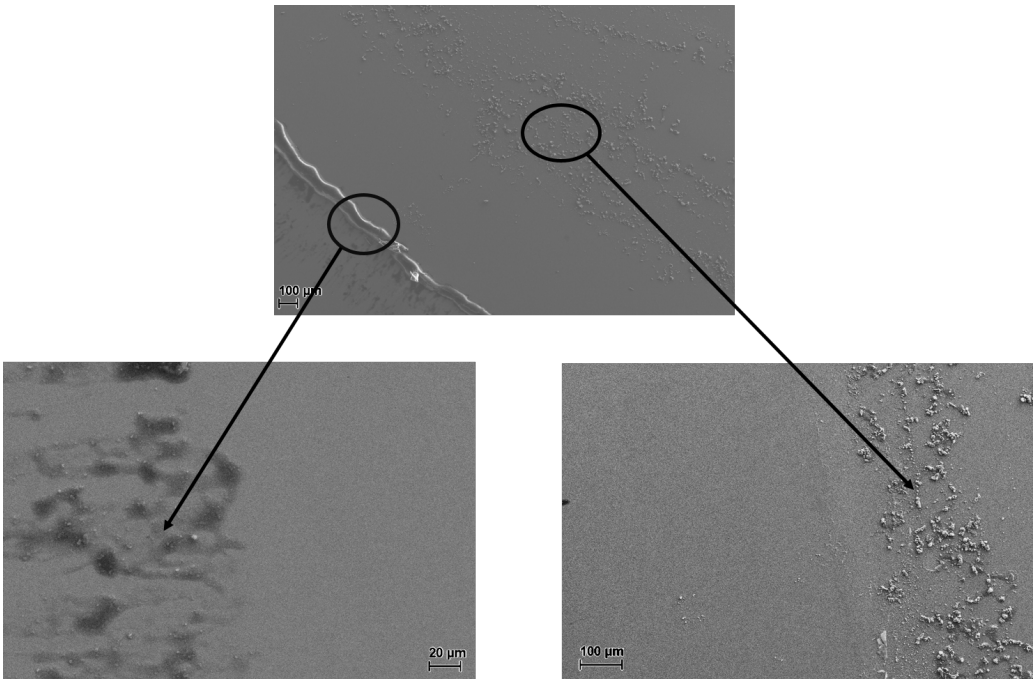

(A)

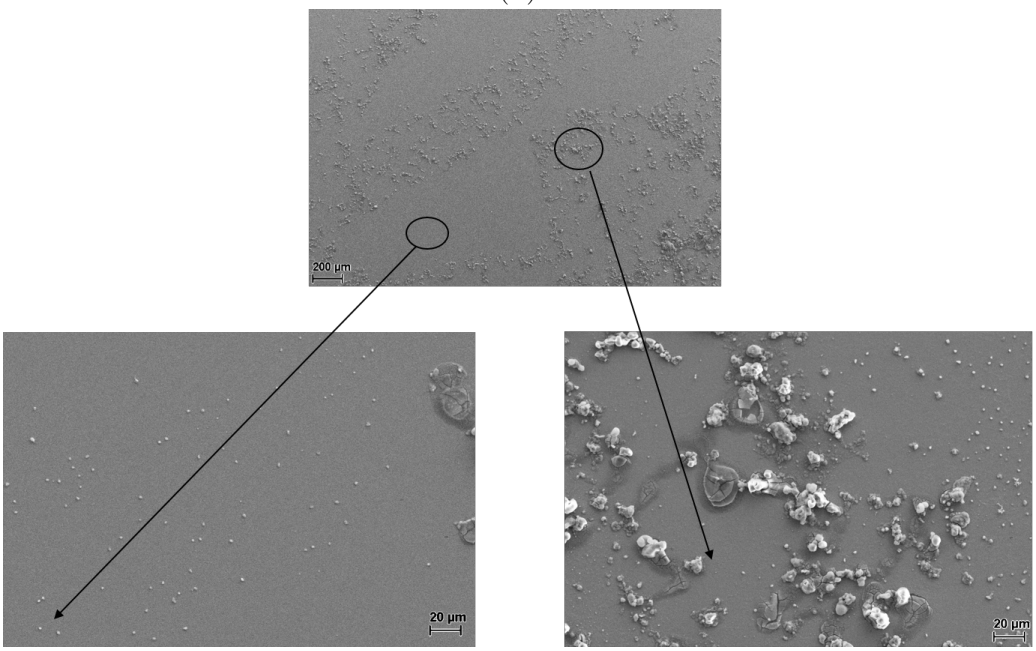

(B)

FIGURE 4.40: SE images of the corroded layer of a 30% TWIP sample that underwent a polarisation test. (A) represents the brown looking part of Figure 4.38 and (B) represents the larger blue looking part. The images were taken using a 5kV beam and 30μm aperture.

The samples will be immersed in a SBF solution containing 50mM Hepes buffer with a pH around 7.4 and 37°C. The dissolved oxygen pressure will be measured before and after immersion of most samples. The immersion times were 1, 7, and 21 days.

The first samples were analyzed using the SEM and EDX to study the starting morphology and composition of the samples. Later on, the samples were only analyzed using the optical microscope. When

TABLE 4.21: Mean corrosion rates and current densities (with standard deviation) and released iron and manganese concentrations for different TWIP samples. As a reminder, the polarisation tests are performed in a cell containing 315 ml solution.

Family	Sample	v_{corr} (mm/year) method 1	Fe released (mg/l)	Mn released (mg/l)
TWIP 40%	40%-1	0.194	0.11	0.03
	40%-4	0.195	0.09	0.03
	40%-5	0.0863	0.07	0.03
TWIP 30%	30%-3	0.0661	0.06	0.02
	30%-4	0.0824	0.08	0.02
	30%-5	0.0750	0.06	0.02
TWIP 10%	10%-4	0.140	0.09	0.02
	10%-5	0.0774	0.08	0.02
TWIP 0%	1-3	0.227	0.08	0.02
	2-3	0.174	0.07	0.02
	2-4	0.149	0.10	0.02

SEM images have been taken before immersion, these will be presented next to the SEM images after immersion. When the surface investigation was made using the optical microscope, the images won't be shown. An example of an optical microscope image of the center of a sample before immersion can be seen on Figure 4.41.

4.2.1 One day immersion tests

Three samples have been immersed during one day: two non deformed samples (TWIP 1 and TWIP 3) and one 40% deformed sample (TWIP 40%-5) [10]. The non deformed samples were both immersed the same day.

4.2.1.1 Surface morphology changes

Figure 4.43 illustrates changes in morphology due to immersion for one sample: The TWIP 3 sample. No significant changes can be seen for the TWIP 1 sample, except that the polishing scratches are not all well directed in one direction (see Figure 4.42 for an illustration of the worst spot of that sample). On hat Figure it can be seen that the center of the corroded sample presents holes. The corners are worn out and corrosion products/deposits are also illustrated.

[10] It is reminded that this 40% deformed sample used another setup for the immersion (Table 3.3)

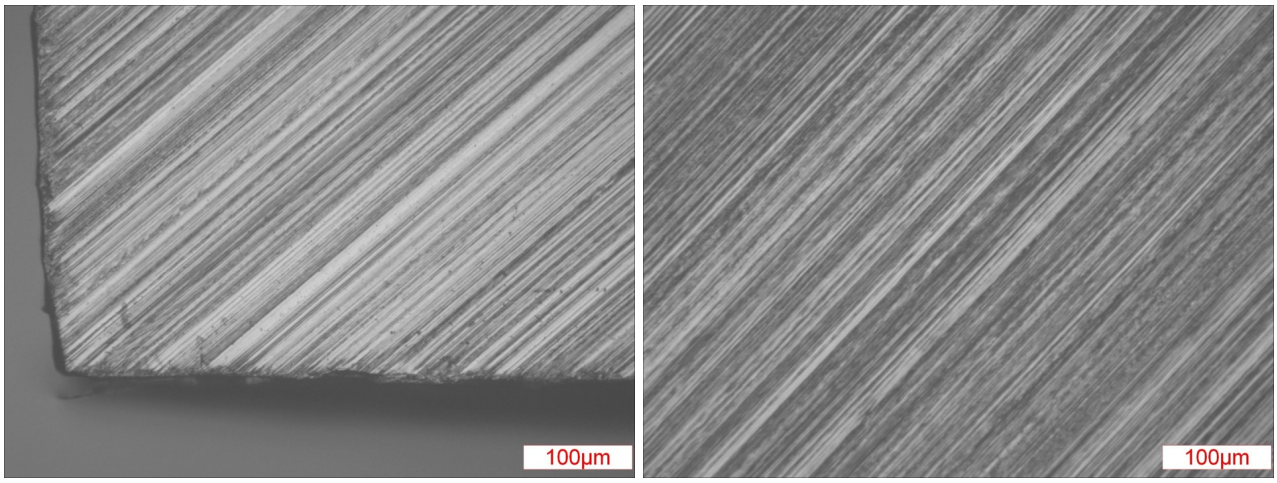

(A) (B)

FIGURE 4.41: Optical microscope images of the corners and center of sample TWIP 7 before immersion using Bright field mode.

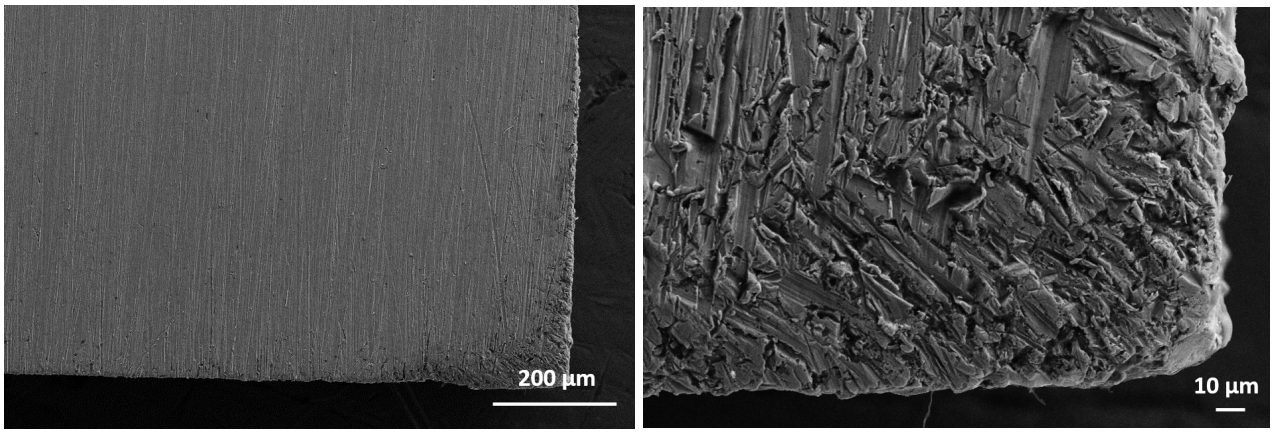

(A) (B)

FIGURE 4.42: SE images of TWIP 1 sample illustrating the edges with scratches in various directions.

A description of the corrosion behaviour for each sample is following:

- **TWIP 1**: In general, the TWIP 1 seemed to have occurred light attacked with some corrosion on the edges, and few corrosion pits in the centre of the samples. However, two corners were eaten away.
- **TWIP 3**: To the naked eye, it looks more or less like the TWIP 1 sample. However, when looking at SEM images, there are more elements that got deposited at certain spots as can be seen on Figure 4.43. Some corners are also eaten away and corrosion products were deposited on some edges. It is also clearly visible that at the corners, a certain layer is coming off the sample, exposing the metal surface beneath. The composition of this layer will be addressed later in this document.
- **TWIP 40%-5**: Upon initial inspection, only one corner seemed attacked and this was confirmed on SEM images. The deposited layer seems to stay in place even at the corners except at one

corner, where it got eaten away. Some spots are full of corrosion products [11], especially at one corner that can be seen on Figure 4.44 and some holes are visible in the center of the sample as is also the case for the TWIP 1 and TWIP 3 samples.

Besides the TWIP 40%-5 sample corner covered with corrosion scale, Figure 4.44 also shows some corrosion pits that were found on the TWIP 3 sample.

EDX analysis was performed on each sample for various spots. As was already the case for the polarisation samples, no quantitative analysis can be made due to the very thin corrosion layers [12]. The results will be presented following the different spots already highlighted above: the deposited layer analyzed in the corners, the metal surface underneath, the cracked regions of that layer, pits as well as spots where a build up of corrosion products is formed and the center of the specimen:

1. Deposited layer (corners): It presents considerable amounts of phosphorus, followed by calcium, and sodium and in lower amounts magnesium and potassium were found and at some particular spots, chlorine was also found as well as sulfur.
2. Cracked region: The same elements with similar amounts as for the deposited layer are found.
3. Pits with build-up of corrosion products: The same elements with similar amounts as for the deposited layer and cracked region are found.
4. Metal surface underneath the deposited layer: very small concentrations of the elements found in the deposited layer, cracked region, and pits.
5. Center: Very similar to the metal surface underneath the deposited layer.

It has to be noted that at the corner, there seemed to be a lot of aluminum contamination and a tiny bit of coper was also found on the deposited layer. The differences between the non-deformed samples and the 40% deformed one are minimal, with possibly slightly higher concentrations of the deposited elements on the 40% deformed sample.

4.2.1.2 Corrosion rate

The corrosion rates of the different samples can be seen in Table 4.22 along with the initial mass and mass after immersion[13]. It is shown that the two non deformed samples have very similar corrosion rates and the 40% deformed sample has results in a higher corrosion rate than the non deformed samples.

A graph encompassing these samples along with the one week and three weeks immersed samples (non deformed and 40% in 50mM buffer solution) can also be seen on Figure 4.54.

On Table 4.23, the initial and final pH as well as temperatures can be seen along with the sample immersed surface. Only small variations are present.

[11] When "corrosion products" is used it encompasses everything that could compose the agglomerates found on the sample: as well oxides as salts.

[12] As a reminder, by using a 15KV beam, the volume analyzed is 1 μm^3

[13] The corrosion rates are calculated following the methods detailed in section 3.3.

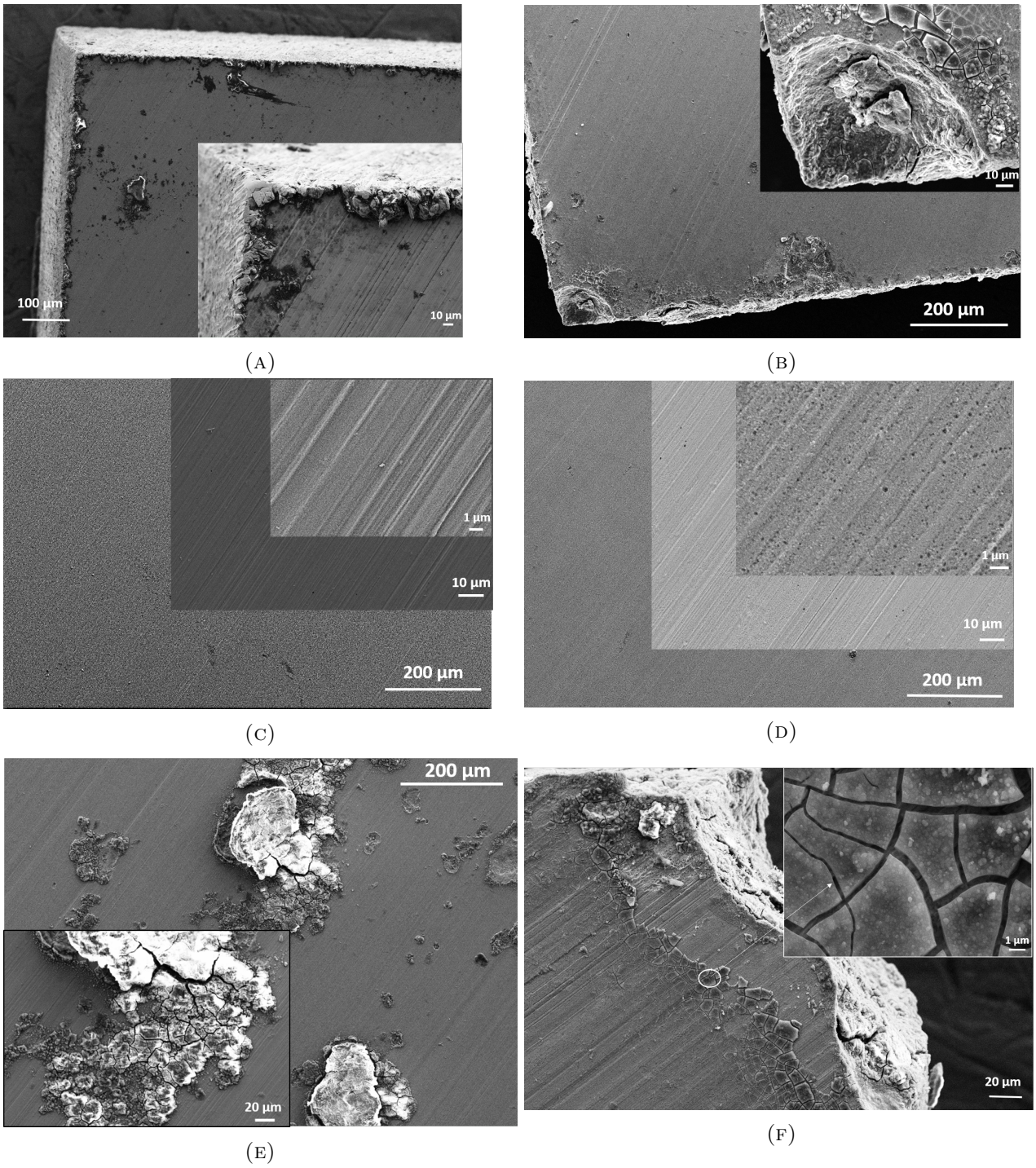

FIGURE 4.43: SE images of TWIP 3 sample before and after one day immersion: (A) and (C) images of non immersed corners and center of the sample respectively, (B) and (D) immersed images of a corner that got eaten away and of the center of the sample, (E) an image of corrosion scale, and (F) an image of the cracking deposited layer. The images were taken using a 15kV beam and 30μm aperture.

4.2.2 One week immersion tests

The one week immersion tests will be divided into two parts. Some samples were immersed in a SBF solution containing 100mM Hepes buffer, whereas the majority of the one week immersed samples used a solution containing 50mM buffer.

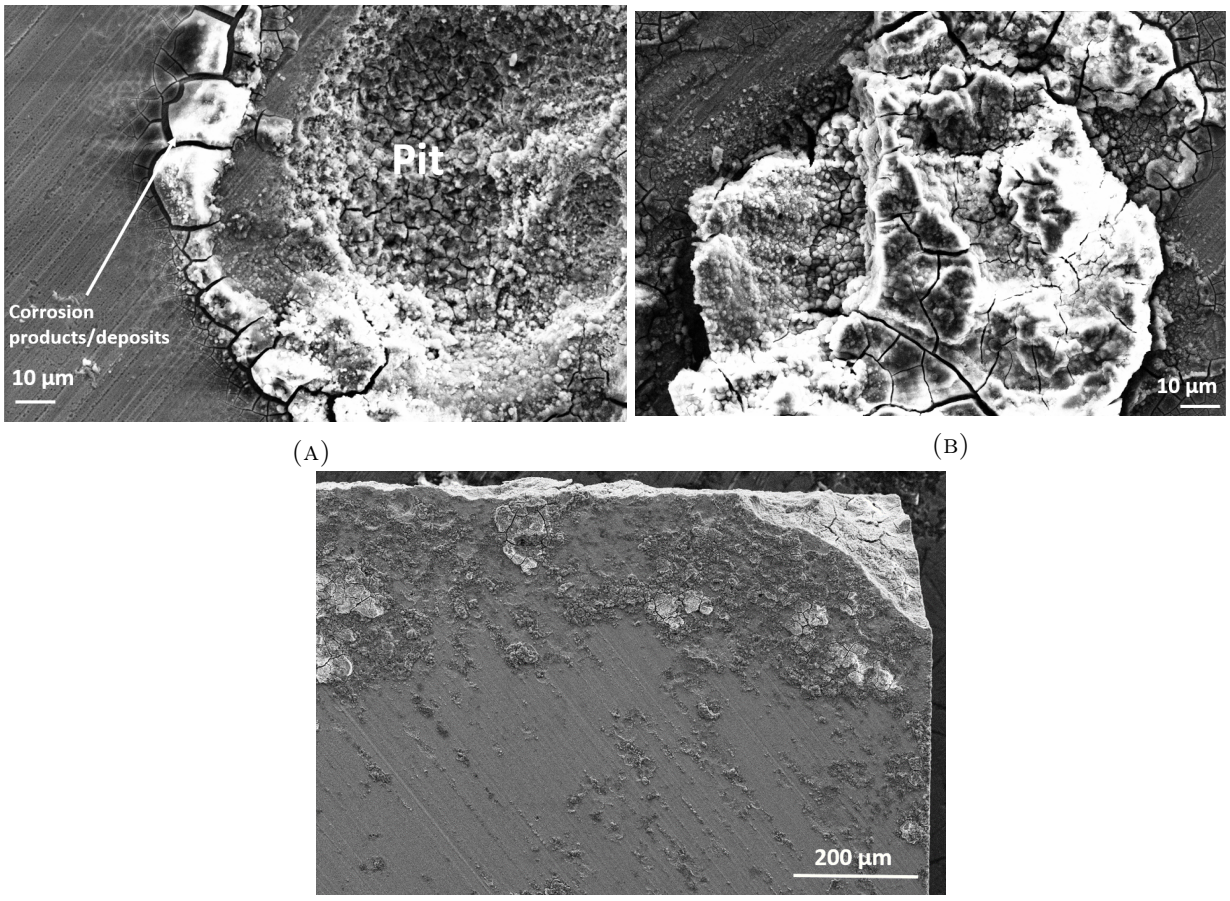

(A) (B)

(C)

FIGURE 4.44: SE images of (A) and (B) corrosion pits on TWIP 3 sample and (C) corrosion scale on TWIP 40%-5 sample corner. The images were taken using a 15kV beam and 30μm aperture.

TABLE 4.22: Corrosion rates of the different samples immersed for one day in an SBF solution containing 50mM Hepes buffer.

Sample	$\mathbf{m}_i$ **(mg)**	$\mathbf{m}_f$ **(mg)**	$\mathbf{v}_{corr}$ **(g/(m^{2}d)) mass loss**	$\mathbf{v}_{corr}$ **(mm/year) mass loss**	$\mathbf{v}_{corr}$ **(g/(m^{2}d)) released [ion]**
TWIP 1	586.5	586.3	0.888	0.0419	1.21
TWIP 3	603.8	603.6	0.889	0.0419	1.62
MEAN			**0.888±0.0003**	**0.0419±0**	**1.41±0.30**
TWIP 40%-5	568.8	568.6	0.915	0.0435	1.27

4.2.2.1 Samples immersed in SBF containing 50mM Hepes buffer

This category encompasses a total of nine samples: three non deformed, two samples that underwent a 10% deformation, two samples that underwent a 20% deformation, and two samples that underwent

a 40% deformation. The TWIP 6, 20%-1, and 40%-1 samples were immersed the same day. Same goes for the TWIP 12, and 20%-2 samples. TWIP 12, 10%-3, and 40%-4 were also immersed the same day. These three samples were immersed in the hand made setup and they showed presence of a few magnetic products in the solution that were attracted by the pH meter probe for example. These product were shown to be volatile and containing iron, aluminium, phosphorus, magnesium, and zirconium as well as titanium.

TABLE 4.23: Main parameters of samples immersed for one day in an SBF solution containing 50mM Hepes buffer.

Sample	Surface (cm^2)	pH_i	pH_f	T_i (°C)	T_f (°C)
TWIP 1	2.25	7.29	7.35	36.7	37.5
TWIP 3	2.25	7.3	7.35	37	37.3
TWIP 40%-5	2.19	7.3	7.37	36.1	35.4

Surface morphology changes

As was done for the one day immersion samples, a typical sample will be chosen in order to show the changes in morphology on the corners and center and can be seen on Figure 4.45. The other samples will be illustrated when showing particularities.

A description of the corrosion behaviour for each sample can be found in Appendix B. Upon first inspection, the corrosion seems uniform except at the corners that are much more attacked and the presence of some pits (more or less depending on the sample). A general description is found hereunder:

- **Corners**: The corners are eaten away for most samples and present a cracked layer that reveals the metal underneath it.
- **Center**: No layer or corrosion products can be seen in the center. However, the presence of holes is made visible in Figure 4.45.
- **Spherical-like agglomerates**: TWIP 12 and TWIP 10%-3 presented spherical-like agglomerates that can be seen on Figure 4.48c.
- **Pits**: TWIP 12 exhibited a lot of pits/corrosion products compared to the other samples. This is shown on Figure 4.46. The other samples also presented agglomeratees of corrosion products and pits but in fewer extent.

The 40%-1 sample exhibited an important brown area, that can be seen on Figure 4.47.

EDX analysis

EDX analysis was also performed on these samples. Again, no quantitative analysis can be made due to the very thin corrosion layers. The samples will be compared to each other regarding the different important spots: the deposited layer analysed in the corners, the metal surface underneath, the cracked regions of that deposited layer, pits as well as spots where a build up of corrosion products is formed

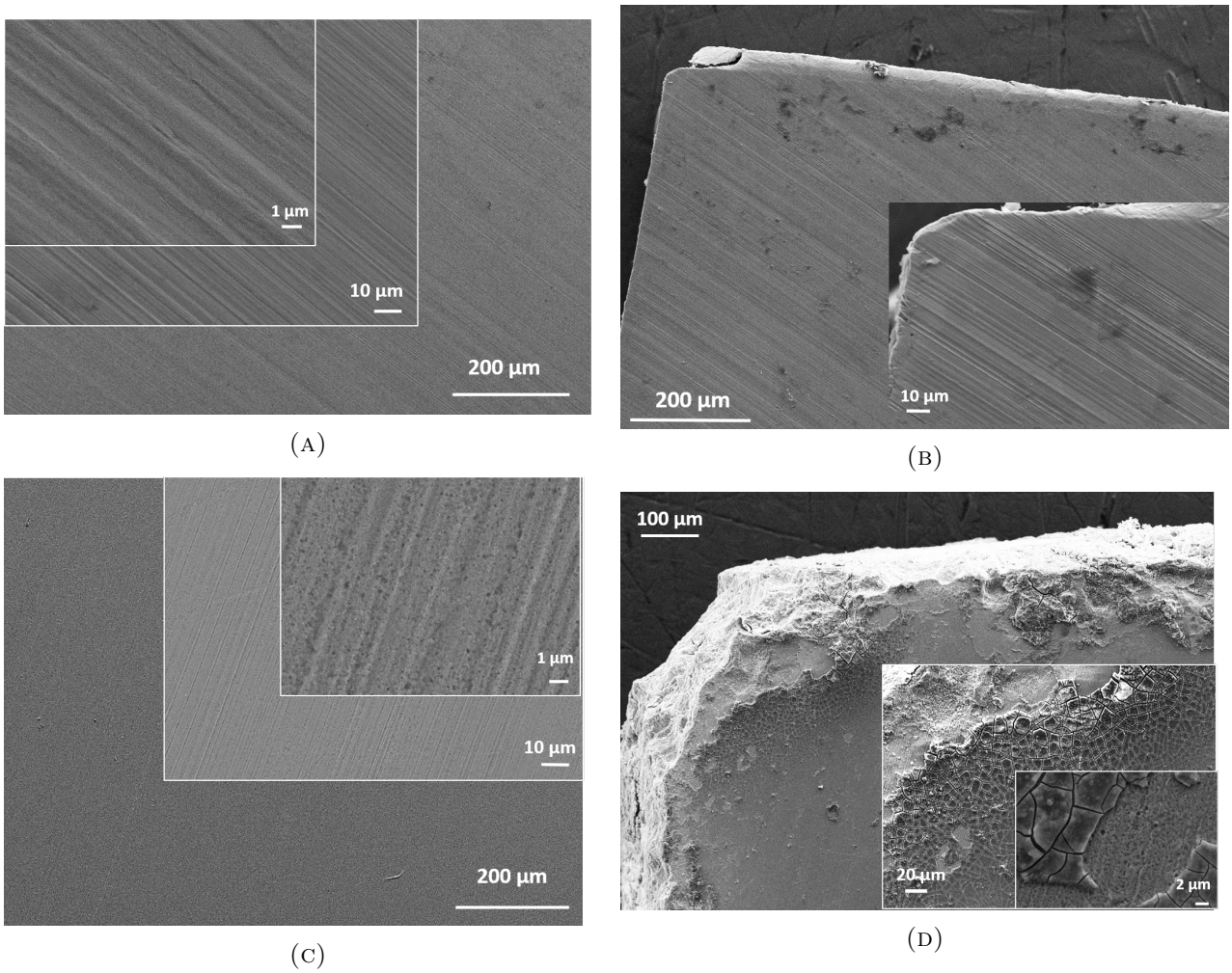

(A) (B) (C) (D)

FIGURE 4.45: SE images of TWIP 6 sample before and after one week immersion: (A) and (B) images of center and corner of the non immersed sample respectively, (C) and (D) immersed images of the center of the sample and a corner that got eaten away respectively. The images were taken using a 15kV beam and 30μm aperture.

and the center of the specimen. A detailed analysis of each sample can be found in Appendix B. But first, the EDX analysis of a few samples before immersion will be highlighted. No quantitative analysis will be undertaken. As the specimens before immersion do not contain corrosion products it could be possible to undertake a quantitative analysis. However, these analyses will be used for comparison with the samples after immersion.

Before immersion:

- **TWIP 6**: An EDX analysis on the corners and the centre of the specimen was undertaken and it was found that there was clear aluminum contamination on the corners (3.5 at.% at the corners against 0.05 at.% at the centre). No other elements than the alloy elements were found and these were present in acceptable amounts compared to the ICP analyses detailed in section 3.1.
- **TWIP 40%-1**: This sample not only showed considerable amounts of aluminum on the corners but also some copper, sodium, and magnesium and sodium and magnesium contamination on the centre of the sample was also visible.

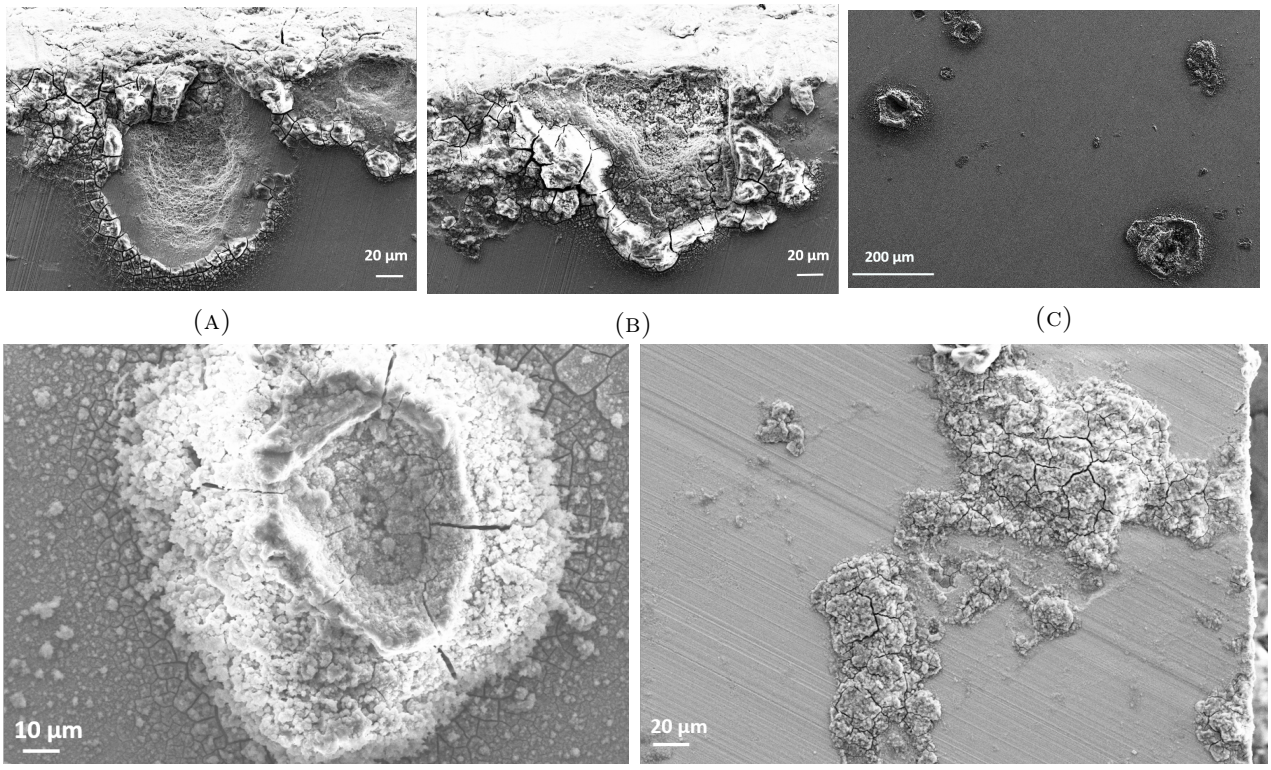

FIGURE 4.46: SE images of (A) and (B)TWIP 6 edge pits, (C) agglomeration of pits in the centre of TWIP 20%-1 sample, (D) a pit covered by corrosion products on TWIP 40%-1 sample, and (E) agglomeration of corrosion products on TWIP 40%-4 sample. The images were taken using a 15kV beam and 30μm aperture.

- **TWIP 20%-1**: The sample was analyzed in the centre but not in the corners and the centre showed a similar, not contaminated composition as for the TWIP 6 sample.

After immersion:

The important spots of the samples immersed for one week in SBF + 50mM Hepes buffer will be compared regarding the deformation rate of the sample. These spots are: the (cracked) deposited layer on the corners, the underneath laying surface, and the centre. An emphasis will be made on the three most important elements: phosphorus, calcium and chlorine.

1. Cracked deposited layer (corners): The 10% and 40% deformed samples exhibited quite different behaviours regarding the two samples included in each family with one sample having on average twice as much phosphorus and calcium deposited on the corners. For the non deformed samples, the TWIP 9 and 12 exhibit a similar behaviour but the TWIP 6 sample has a much thicker layer of phosphorous and calcium with no visible chlorine. The 40% samples contain the highest amount of phosphorus, calcium and chlorine compared to the three other families. Follows the 20% and 10% Families with similar amounts and finally the non deformed family with much smaller proportions.

2. Metal surface underneath the deposited layer: No significant changes between the samples are found. Small amounts of the salts are still present, but mostly the metal is detected.

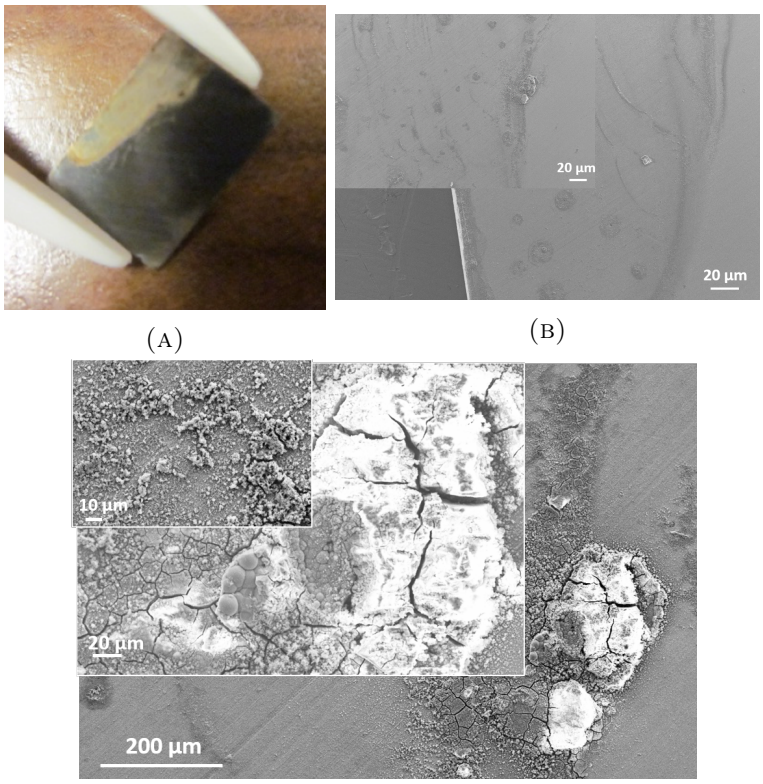

(A) (B)

(C)

FIGURE 4.47: (A) a photograph of the brown stain found on the TWIP 40%-1 sample and (B) and (C) SE images of that same brown spot with different magnifications. The images were taken using a 15kV beam and 30μm aperture.

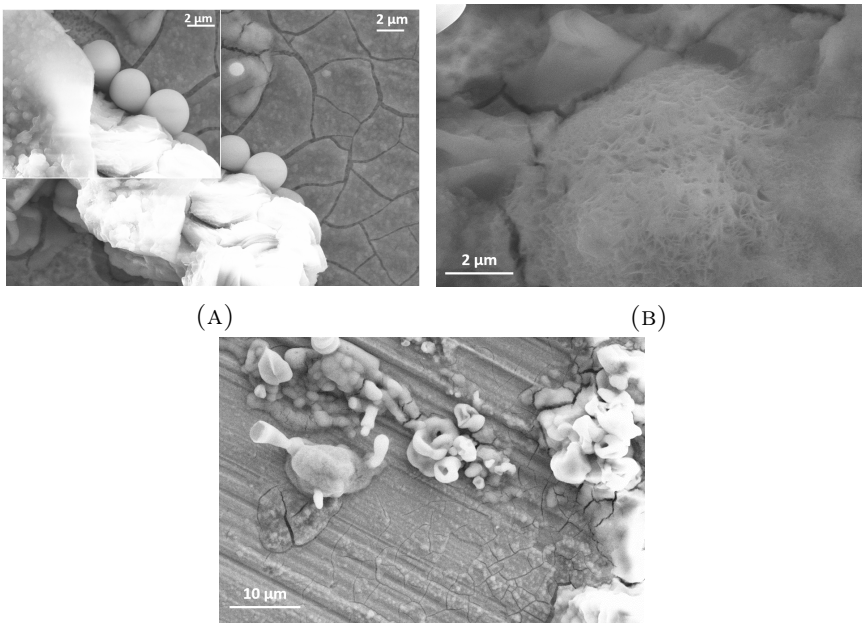

(A) (B)

(C)

FIGURE 4.48: SE images of (A) and (B) TWIP 10%-3 sample and (C) TWIP12 sample sphere-like agglomerates. The images were taken using a 15kV beam and 30μm aperture.

3. Center: The differences between the two 10% samples are high, with the 10%-3 sample having

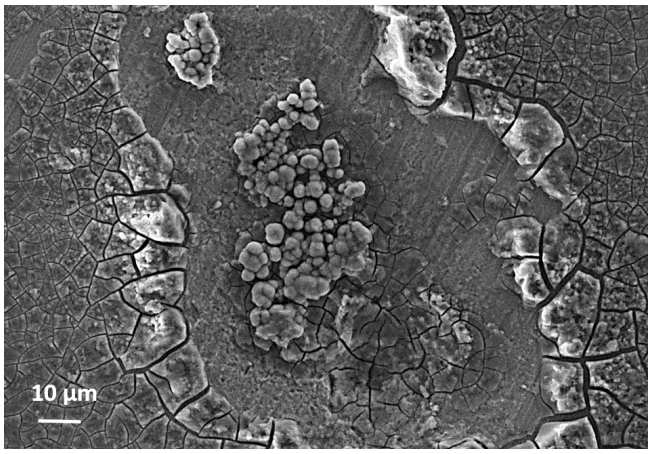

FIGURE 4.49: SE images of TWIP 10%-1 sample illustrating an agglomeration of corrosion products over a pit. The image was taken using a 15kV beam and 30μm aperture.

a thinner salt deposited layer[14]. The other categories also contain differences between their two samples but the differences are not as pronounced as for the 10% family. On average, the proportions are comparable between the four different families.

When material has been eaten away (result of pitting), there seems to be more chlorine in the close vicinity. Some zirconium was found on most analyzed spots, but the zirconium rays being close to the phosphorus rays, this statement could be faulty.

The TWIP 6 sample was also analyzed by ToF-SIMS. This will bee detailed later and 40%-1 was also investigated with XPS, which will also be detailed later. These analysis were undertaken to get an idea of the depth of the corrosion layer and to qualitatively know where the different corrosion compounds were found on the corrosion layer.

Corrosion rate

The corrosion rates of the different samples immersed for one week in a SBF solution containing 50mM Hepes buffer can be seen in Table 4.24 along with the initial mass and mass after immersion. It is shown that the 10% samples have the highest mean corrosion rate followed by the 20% samples, the non deformed samples and finally the 40% samples have the lowest corrosion rates. However, when considering the corrosion rate calculated from the released ion concentration, the 40% samples exhibit a higher corrosion rate than the 20% deformed samples.

A graph encompassing these samples along with the one day and three weeks immersed samples (non deformed and 40% in 50mM buffer solution) can also be seen on Figure 4.54.

On Table 4.25, the initial and final pH as well as temperatures can be seen along with the sample surface. Finally, when measured, the dissolved oxygen partial pressure is presented.

[14]The salt deposited layer is mainly composed of phosphorus and calcium followed by intermediary amounts of sodium and magnesium and small amounts of potassium.

TABLE 4.24: Corrosion rates of the different samples immersed for one week in an SBF solution containing 50mM Hepes buffer.

Sample	$\mathbf{m}_i$ **(mg)**	$\mathbf{m}_f$ **(mg)**	$\mathbf{v}_{corr}$ **(g/(m^{2}d)) mass loss**	$\mathbf{v}_{corr}$ **(mm/year) mass loss**	$\mathbf{v}_{corr}$ **(g/(m^{2}d)) released [ion]**
TWIP 6	787.5	786.0	0.916	0.0427	0.748
TWIP 9	519.2	518.9	0.218	0.0104	0.203
TWIP 12	560.2	559.7	0.340	0.0163	0.356
MEAN			**0.492±0.373**	**0.0231±0.0172**	**0.436±0.281**
TWIP 10%-1	665.1	663.4	0.997	0.0472	0.973
TWIP 10%-3	622	621.5	0.328	0.0156	0.449
MEAN			**0.662±0.473**	**0.0314±0.0224**	**0.711±0.371**
TWIP 20%-1	510.6	509.8	0.498	0.0244	0.358
TWIP 20%-2	281.2	280.4	0.528	0.0250	0.464
MEAN			**0.513±0.0213**	**0.0247±0.0004**	**0.411±0.075**
TWIP 40%-1	343.1	342.4	0.445	0.0261	0.467
TWIP 40%-4	496.3	496.1	0.132	0.00633	0.378
MEAN			**0.288±0.0003**	**0.0162±0.0140**	**0.422±0.0.063**

4.2.2.2 Samples immersed in SBF containing 100mM Hepes buffer

Five samples were investigated in this category: one non deformed sample (TWIP 8), one sample that underwent a 10% deformation, one sample that underwent a 40% deformation and two samples that underwent a 30% deformation. All samples were immersed the same day.

Surface morphology changes

The corrosion behaviour is very similar compared to samples exposed previously (one day immersion and one week with 50mM Hepes buffer added) except that potassium is mostly not present on the different samples and spots. Thus, no detailed description of each sample will be made again. Nevertheless, the main spots will be compared to the samples immersed in a 50mM solution:

1. Cracked deposited layer (corners): No significant changes between the samples of that category are found and the proportions correspond to the average of the 50mM category.
2. Metal surface underneath the deposited layer: The 40% sample does not contain any phosphorus or chlorine and only minimal amounts of calcium on that surface. Same goes with one of the 30% deformed sample (with minimal amounts of phosphorus however). The other samples present a similar composition to the 50mM sample, i.e. slightly higher amounts of phosphorus, calcium, sodium, magnesium, potassium, and chlorine.

TABLE 4.25: Main parameters of samples immersed for one week in an SBF solution containing 50mM Hepes buffer.

Sample	Surface (cm^2)	pH_i	pH_f	T_i (°C)	T_f (°C)	$p_{O_2 i}$ (mmHg)	$p_{O_2 f}$ (mmHg)
TWIP 6	2.34	7.4	7.42	35.8	35.6	158	163
TWIP 9	1.97	7.37	7.46	36.6	35.9	162	165
TWIP 12	2.10	7.32	7.40	35	36.1	/	/
TWIP 10%-1	2.44	7.31	7.43	36	36.4	168	140
TWIP 10%-3	2.18	7.33	7.39	34.4	35.9	/	/
TWIP 20%-1	2.30	7.4	7.44	36.5	35.2	155	159
TWIP 20%-2	2.17	7.37	7.45	36.8	36.5	152	158
TWIP 40%-1	2.25	7.44	7.52	35.8	35.4	157	163
TWIP 40%-4	2.17	7.31	7.42	35.3	35.6	/	/

3. Centre: The centre of the samples look similar to the 50mM samples, with only minimal amounts of phosphorous, and calcium but no chlorine detected.

Some aluminum contamination on the two 30% samples corners and slightly on the 40% sample corners is spotted.

Typical morphologies are shown on Figure 4.50, where the corners that were eaten away can be seen, along with the cracked deposited layer and the centre of the samples and finally some pits.

Corrosion rate

The corrosion rates of the different samples immersed for one week in a SBF solution containing 100mM Hepes buffer can be seen in Table 4.26 along with the initial mass and mass after immersion. It is shown that the 10% deformed sample have the highest corrosion rates and the 40% the lowest. The 30% deformed samples and the non deformed one have similar intermediate corrosion rates. This behaviour is similar to the previous category: the samples immersed in a SBF solution containing 50mM Hepes buffer for one week.

On Table 4.27, the initial and final pH as well as temperatures can be seen along with the sample surface. The dissolved oxygen partial pressure is also presented.

It has to be noted that one of the control flask used for these samples[15] contained a significant amount of iron (0.18 mg/l) and manganese (0.06 mg/l). However, the other control flasks did not show any traces of iron and manganese.

[15] As a reminder, these samples were immersed the same day.

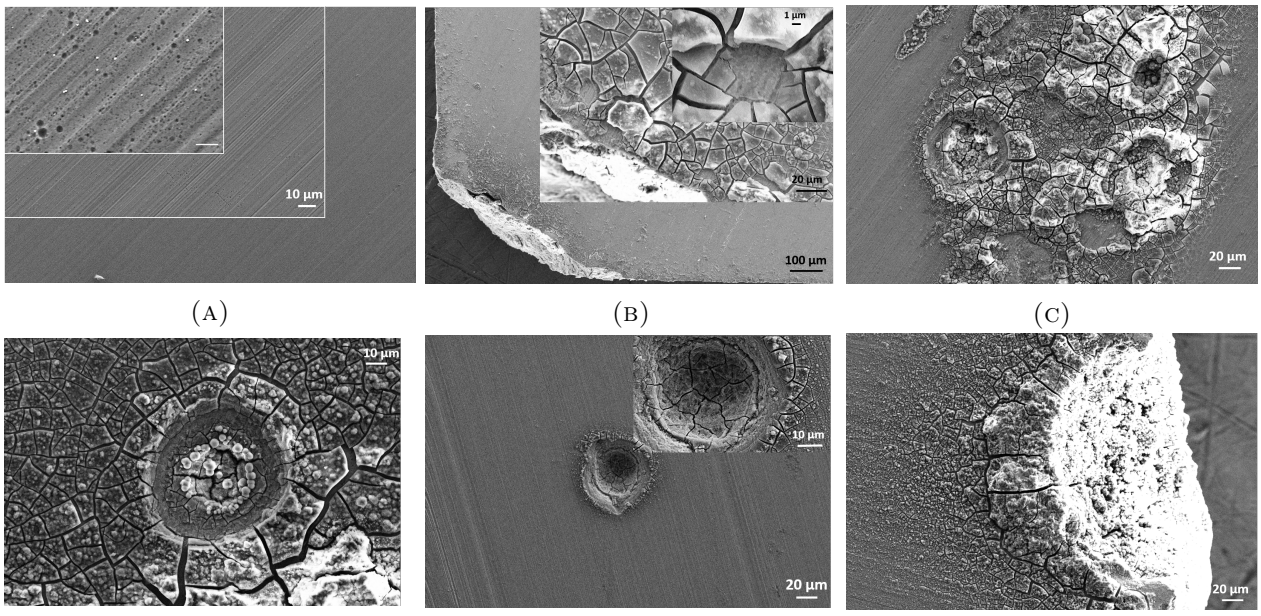

(A) (B) (C)

(D) (E) (F)

FIGURE 4.50: SE images of (A) a TWIP 8 corroded centre (where the holes inside the surface are clearly visible), (B) a TWIP 10%-2 corroded corner, (C) and (D) pits as well as corrosion products on TWIP 10%-2 sample, (E) a pit in the middle of sample TWIP 30%-2 and (F) a TWIP 40%-3 edge that got eaten away. The images were taken using a 15kV beam and 30μm aperture. The samples were immersed for one week with 100mM buffer.

TABLE 4.26: Corrosion rates of the different samples immersed for one week in an SBF solution containing 100mM Hepes buffer.

Sample	$\mathbf{m}_i$ **(mg)**	$\mathbf{m}_f$ **(mg)**	$\mathbf{v}_{corr}$ **(g/(m^{2}d)) mass loss**	$\mathbf{v}_{corr}$ **(mm/year) mass loss**	$\mathbf{v}_{corr}$ **(g/(m^{2}d)) released [ion]**
TWIP 8	712.8	711.1	1.03	0.0492	1.13
TWIP 10%-2	504.5	502.2	1.51	0.0716	1.45
TWIP 30%-1	642.7	640.9	1.12	0.0524	1.20
TWIP 30%-2	665.4	663.7	1.04	0.0494	1.11
MEAN			**1.08±0.06**	**0.0509±0.0021**	**1.16±0.06**
TWIP 40%-3	493.4	492.7	0.491	0.0235	0.612

Figure 4.51 illustrates the effect of deformation on the two previous categories: samples immersed for one week in a SBF solution with 50mM or 100mM Hepes buffer. It is seen that the 100mM category exhibits higher corrosion rates than the 50mM samples. The 10% samples seem to exhibit slightly higher corrosion rates but the standard deviations of the different categories are too important to conclude that.

TABLE 4.27: Main parameters of samples immersed for one week in an SBF solution containing 100mM Hepes buffer.

Sample	Surface (cm^2)	pH_i	pH_f	T_i (°C)	T_f (°C)	$p_{O_2 i}$ (mmHg)	$p_{O_2 f}$ (mmHg)
TWIP 8	2.35	7.32	7.36	36.7	36.8	146	160
TWIP 10%-2	2.18	7.3	7.37	36.7	36.4	160	164
TWIP 30%-1	2.30	7.31	7.37	36.8	36.9	159	162
TWIP 30%-2	2.34	7.32	7.38	35.9	36.7	155	158
TWIP 40%-3	2.04	7.3	7.35	35.7	36.5	161	160

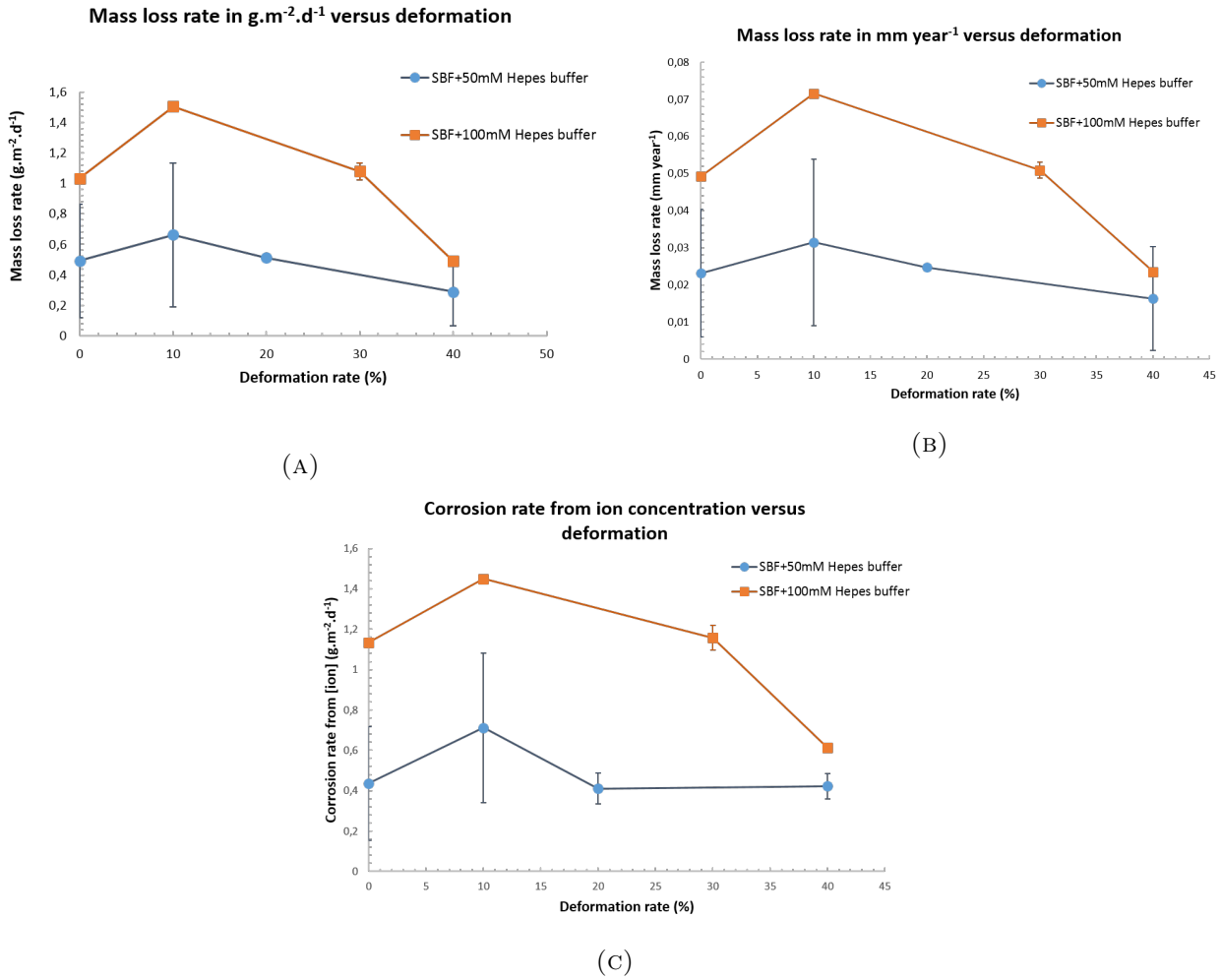

(A) (B)

(C)

FIGURE 4.51: Effect of deformation on mass loss rate (A) in g m^{-2} d^{-1}, (B) in mm $year^{-1}$, (C) calculated using the ion released concentration.

4.2.3 Three weeks immersion tests

Four samples have been tested in this category: three non deformed samples (TWIP 4, 5, and 7) and one 40% deformed one in a SBF solution containing 50mM Hepes buffer. TWIP 4, 7, and 40%-2 were immersed the same day. All these samples presented the a

4.2.3.1 Surface morphology changes

Here again, the surface morphology looks similar to the previous samples on SEM images. This is why only a comparative study with the one week samples immersed in a 50mM buffer solution will be undertaken.

1. Cracked deposited layer (corners): The 40% contains high amounts of phosphorus and calcium on that layer and one non deformed sample contains lower amounts. In both cases, calcium and phosphorus are present in similar amounts whereas for the most previous samples, the phosphorus was always more present than calcium. The 40% sample presents the same amounts as the one week 40% sample. Same goes for the non deformed sample investigated in this case and the previously non deformed samples.
2. Metal surface underneath the deposited layer: The 40% sample is similar to the non deformed samples and the elements are present in more significant amounts than the one week immersed samples.
3. Centre: The non deformed samples contains chlorine in the centre but not the 40% sample. For the rest, the proportions are similar to the equivalent one week samples.

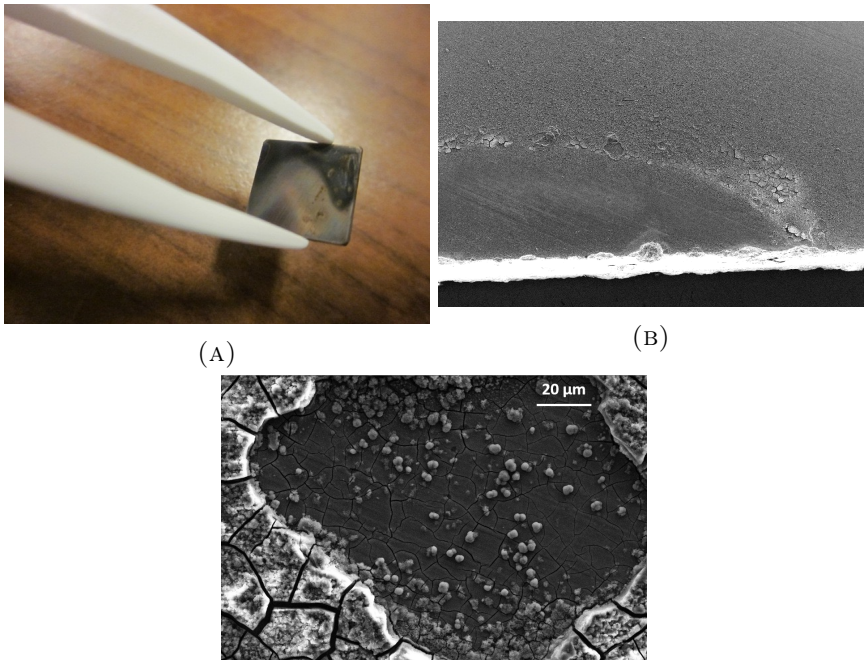

(A) (B)

(C)

FIGURE 4.52: (A) a photograph of the black stain seen on sample TWIP 7, (B) and (C) SE images of that same region, where spherical-like deposited products can be seen. The images were taken using a 15kV beam and 30μm aperture. This sample was immersed in a SBF solution containing 50mM buffer during three weeks.

The TWIP 7 sample presented black spots (on one side) that can be seen on Figure 4.52. No significant changes could be seen on EDX analysis.

No images of corners and centre will be shown as they do not differ from the previous shown examples, except that more material were eaten away on the corners. A few pits are shown on Figure 4.53 along with cracked regions.

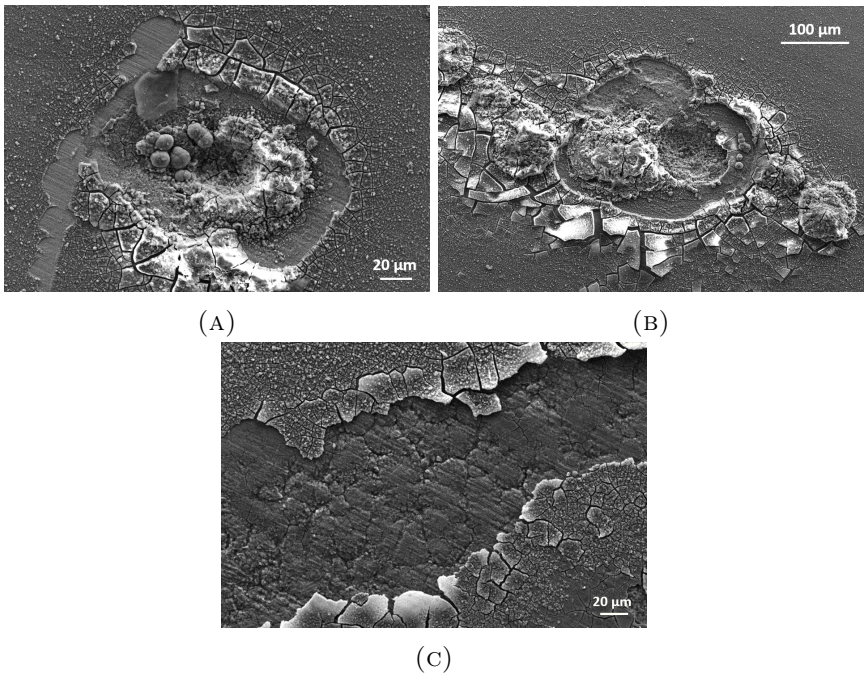

(A) (B)

(C)

FIGURE 4.53: SE images of (A) and (B) pits and corrosion products on TWIP 7, and (C) cracked region in the middle of the sample. The images were taken using a 15kV beam and 30μm aperture. This sample was immersed in a SBF solution containing 50mM buffer during three weeks.

4.2.3.2 Corrosion rate

The corrosion rates of the different samples immersed for three week in a SBF solution containing 50mM Hepes buffer can be seen in Table 4.28 along with the initial mass and mass after immersion. It has to be noted that it has been omitted to measure the dimensions and mass of the TWIP 7 sample before immersion. Thus, it will not be shown on that Table. However, an approximate corrosion rate has been calculated using the released ion concentration and the sample dimensions after immersion. Table 4.28 shows that on average the 40% deformed sample corrodes faster than the non deformed samples even if sample TWIP 5 has a slightly higher corrosion rate than the 40%-2 sample. If the TWIP 7 sample is taken into account it has an approximate corrosion rate, measured by released ion concentration, of 0.371 g m^{-2} d^{-1} is obtained, raising the average value to a value slightly higher than the 40% sample (0.244 g m^{-2} d^{-1}).

On Table 4.29, the starting and end pH as well as temperatures can be seen along with the sample surface. The dissolved oxygen partial pressure is also presented.

4.2.4 Corrosion rate over time

Figure 4.54 illustrates the effect of immersion time on the corrosion rates and mass losses. The samples compared are the one day immersion samples, the one week immerion samples in a 50mM buffer containing solution and the three weeks samples (without the TWIP 7 sample) The deformation does not seem to have an impact on the corrosion. The corrosion rate decreases over time: a high decrease

TABLE 4.28: Corrosion rates of the different samples immersed for three weeks in an SBF solution containing 50mM Hepes buffer.

Sample	m_i (mg)	m_f (mg)	v_{corr} (g/(m^{2}d)) mass loss	v_{corr} (mm/year) mass loss	v_{corr} (g/(m^{2}d)) released [ion]
TWIP 4	770.9	770.4	0.103	0.00490	0.124
TWIP 5	731.8	730.5	0.264	0.0126	0.236
MEAN			0.184±0.080	0.00877±0.00387	0.180±0.056
TWIP 40%-2	569.2	569.2	0.215	0.0102	0.231

TABLE 4.29: Main parameters of samples immersed for three weeks in an SBF solution containing 50mM Hepes buffer.

Sample	Surface (cm^2)	pH_i	pH_f	T_i (°C)	T_f (°C)	$p_{O_2 i}$ (mmHg)	$p_{O_2 f}$ (mmHg)
TWIP 4	2.30	7.54	7.71	36.1	36.1	149	163
TWIP 5	2.35	7.4	7.58	36.4	35.7	158	153
TWIP 7	≈ 2.21	7.35	7.57	33.6	34.4	/	/
TWIP 40%-2	2.22	7.43	7.64	37.2	35.6	155	158

is present between 1 and 7 days immersion and a slower decrease is observed between 7 and 21 days immersion.

4.2.5 XPS analysis on one week and three weeks immersed samples

It was seen during SEM sessions that the deposited layer is very thin. Thus, a more sensitive analysis needs to be undertaken: XPS that gives information on a depth between 1 and 10 nm.

XPS analysis was therefore performed on the following samples: TWIP 40%-1 and TWIP 9 that were immersed for one week in a SBF solution containing 50mM buffer and the TWIP 4 sample that was immersed for three weeks. As a reminder, the TWIP 40%-1 sample was covered by a brown stain on one of its sides. This spot was also analyzed using the XPS. Finally, a pitting area on the TWIP 4 sample was also analyzed. For the one week non deformed sample, a control sample (i.e. polished and stored in a desiccator for one week) was also analyzed to compare the corroded state to the non-corroded state [16].

First, the manganese and iron states will be presented:

[16] It should be noted that due to some instrument failure, the tests were undergone a few weeks after the immersion test was finished. However, the control sample was repolished a week before the actual analysis.

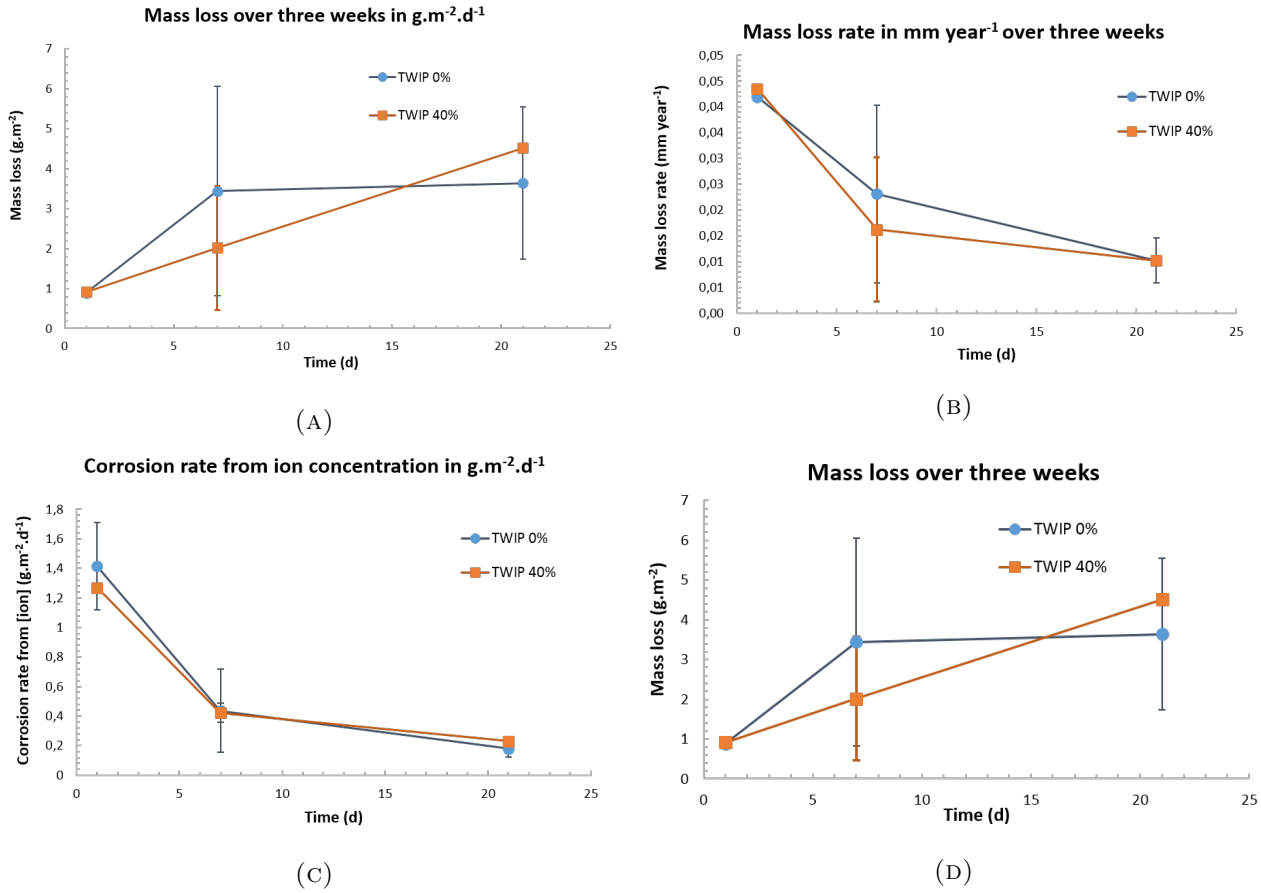

FIGURE 4.54: Effect of deformation on mass loss rate over three weeks (A) in g m^{-2} d^{-1}, (B) in mm $year^{-1}$, (C) calculated using the ion released concentration and (D) illustrates the mass loss over time.

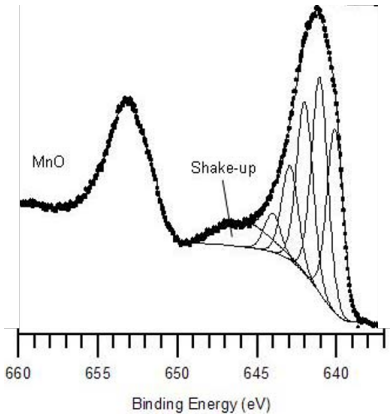

FIGURE 4.55: Representation of a Shake-up satellite peak.

- Manganese: The literature states that from all the Mn possible states, when a Shake-up satellite is present, it is a clear sign of MnO presence. This Shake-up satellite can be seen on Figure 4.55. This Shake-up is significant on the control sample and slightly visible on the other samples. However, the MnO is the principal form of manganese present, Mn_2O_3 and MnOOH could also be present in smaller amounts as their theoretical peaks are close to the MnO one.
- Iron: The different iron chemical oxide states are difficult to differentiate but three indications can be used to determine which state is the most probable to be present:

  1. The FeOOH peak is located at slightly higher energies than the Fe_2O_3 one (around 711 eV against 710 eV). All immersed samples presented a peak at higher energies, whereas the non-immersed control has its peak at exactly 710 eV. Thus it can be concluded from this indication method that the control sample principally contains an iron oxide layer, whereas the immersed samples present a higher amount of iron hydroxide.
  2. If the satellite peak is more important, a presence of FeOOH is likely. This is the case for all immersed samples.
  3. By performing a mass balance study on the oxygen bound to C, P, and Mn the rest of oxygen that is left will undergo a stoechiometric analysis to define if there is presence of FeOOH or Fe_2O_3 [17]. The value expected for FeOOH is 2 and the value expected for Fe_2O_3 is 1.5. For the 3 weeks immersed sample, the value found is lower than the expected value for FeOOH possibly due to the presence of more complex compounds such a Fe-O-P or Fe-O-C. The one week immersed TWIP 9 sample results in a close value to the one expected for FeOOH, possibly showing a smaller presence of complex compounds. This is also the case for the 40% deformed sample immersed for one week. The control sample results in a higher value than expected for Fe_2O_3, possibly due to the presence of manganese species more oxidized than MnO or by a presence of manganese or iron hydroxide on the upper surface.

To summarize, the control sample presents Fe_2O_3, whereas the immersed samples are more likely to contain hydroxides (FeOOH) instead of oxides.

It should be noted that some samples present a slight shouldered peak representative of a metallic presence (valid for manganese and iron).

Quantitatively, following can be said (see Table 4.30 for the exact values[18]):

[17] It should be noted that this method is more reliable when there are less elements that can bind with oxygen.
[18] When a and b are denoted, it means that two spots have been analyzed on the centre of the sample.

TABLE 4.30: XPS values (in at%) of the different elements found on the extreme surface layer (5-10nm).

Sample	Na^+	Fe ox	Fe°	MnO	Mn°	O	N	Ca^{2+}	C	P in Phosphat
TWIP 4	0.8	1.5	0	1.3	0.026	41.2	0.4	7.2	41.2	6.5
TWIP 4 pits	0.6	1.6	0.011	1.1	0	42.8	0.7	7.2	39.7	6.3
TWIP 9a	2.6	3.2	0.1	0.8	0.031	45	0	5.3	37.5	5.6
TWIP 9b	1.6	3.3	0	0.6	0.1	44.5	0	5.7	38	6.1
TWIP 2a (control)	0	6.8	0.4	4.5	0.2	37.5	0	0	50.7	0
TWIP 2b (control)	0	5.9	0.1	4.2	0.2	32	0	0	57.6	0
TWIP 40% a	0.6	2.6	0.012	1.2	0.044	42.3	0.5	5.8	41.2	5.8
TWIP 40% b	0.6	2.6	0	1.1	0.041	41.3	0.6	5.7	42.6	5.5
TWIP 40% brown spot	0.5	2.8	0.006	0.9	0	46.7	0.4	6.6	35.4	6.8

- $\underline{Na^+}$: The non deformed sample immersed for one week (TWIP 9) presents the highest percentage of Na^+.The two other samples present similar amounts (slightly higher for the three weeks immersed one (TWIP 4)) and in both cases, the pit or brown spot present a slightly lower amount. No sodium is found on the control sample.
- $\underline{Fe_{tot}}$: The control sample presents significantly the highest percentage of total amount of iron, with also the highest proportion of metallic iron (it should be noted that the metallic iron percentage differs quite a lot between the two analyzed spots). For the immersed samples, the highest iron presence is found in the TWIP 9 sample,, followed by the 40%-1 sample and finally by the TWIP 4 sample. Metallic iron is found in the TWIP 9 sample.
- $\underline{Mn_{tot}}$: Again, the control sample contains the most manganese. However, this time the immersed sample presenting the highest amount of manganese is the TWIP 4 followed by the 40%-1 sample and then TWIP 9. Metallic manganese in found in the control sample and in minimal amounts in TWIP 40%-1 and TWIP 9.
- $\underline{O}$: The control sample presents the least amount of oxygen on the upper surface. For the immersed samples, the TWIP 40% brown spot has the highest oxygen content, followed by TWIP 9, the pitting region on the TWIP 4 sample, then the other spots on the 40%-1 sample and finally the non pitted region from TWIP 4 sample.
- $\underline{N}$: The nitrogen present on some samples resembles to organic nitrogen and can is found on the TWIP 4 and TWIP 40%-1 samples.
- $\underline{Ca^{2+}}$: TWIP 4 contains the highest amount of Ca^{2+} as well on the pitting area as on the non-pitted area. TWIP 40%-1 follows leaving TWIP 9 with the lowest amount. No calcium is found on the control sample.

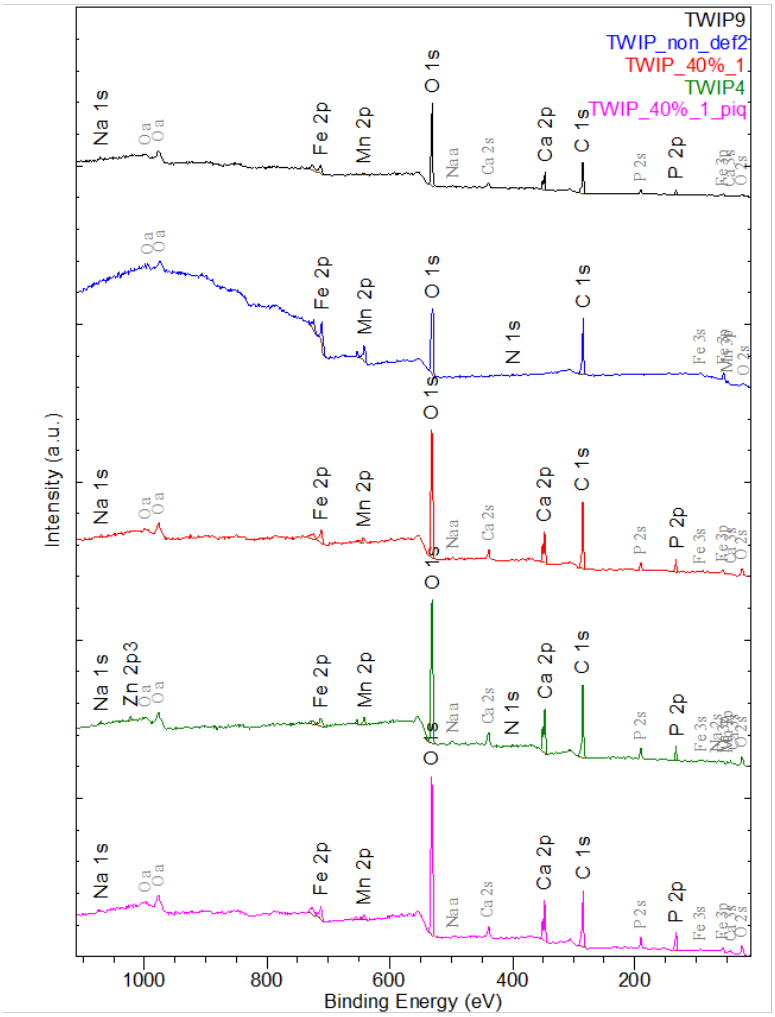

FIGURE 4.56: General XPS plot for TWIP 9, TWIP 4, TWIP 40%-1 and control TWIP 2 sample. The general plot for the brown spot on the TWIP 40%-1 sample is also shown.

- C: The control sample is the one presenting the highest carbon contain. TWIP 9 has the lowest carbon content. Intermediary amounts are found for the other two samples. These carbon contents are due to "normal" contamination.
- P in Phosphate: The brown region on TWIP 40%-1 presents the highest phosphate content, followed closely by the TWIP 4 sample, then by the TWIP 9 and finally by the other 40%-1 spots.

A general plot of the four analysed samples as well as the brown area on the 40%-1 sample are shown on Figure 4.56.

4.2.6 ToF-SIMS analysis on TWIP 6 sample immersed for one week

Now that the corrosion layer elements have been identified by the use of XPS analysis, it is interesting to see where these compounds are found spatially and a ToF-SIMS depth profile has been undertaken. Figure 4.57 shows the obtained profile while collecting either the negative or positive ions for the analyzed TWIP 6 sample. The negative ions depth profile shows a carbon contamination at the very top of the layer. PO^- is increasing up to a certain depth where is decreases again until reaching a constant value. Iron oxides increase until reaching a constant value; The manganese oxides behave

similarly but at lower intensity. Same goes for the iron hydroxides. When zooming into the lower intensities and by keeping the species showing a similar behaviour, Figure 4.58a is obtained, where it is also seen that some Fe^- is starting to grow. When doing the same for the elements behaving like PO^-, Figure 4.58b is obtained, where it can be seen that P^-, C^-, Cl^-, S^-, and F^- exhibit the same behaviour. No real information can be obtained from the positive ion plot, when wanting to "locate" the species. However, the presence of magnesium, potassium, sodium, and calcium is highlighted.

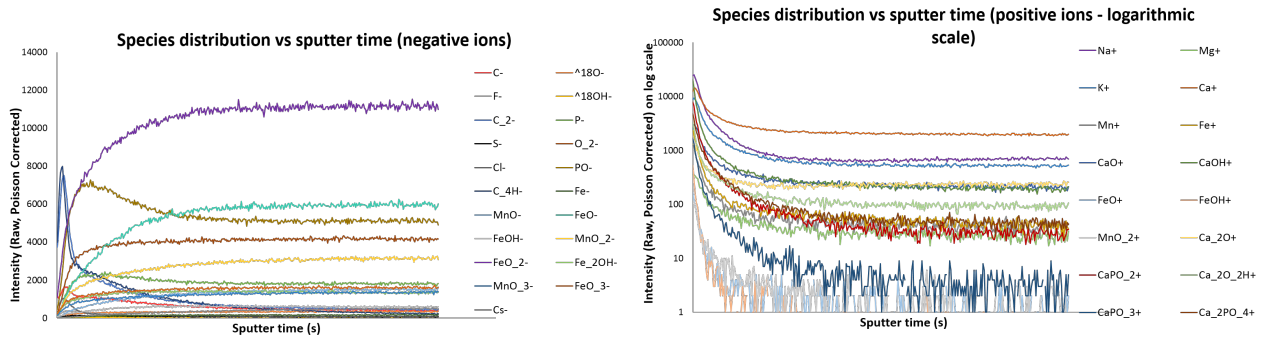

(A) (B)

FIGURE 4.57: ToF-SIMS depth profile for sample TWIP 6 by collecting positive ions (on log scale) and negative ions.

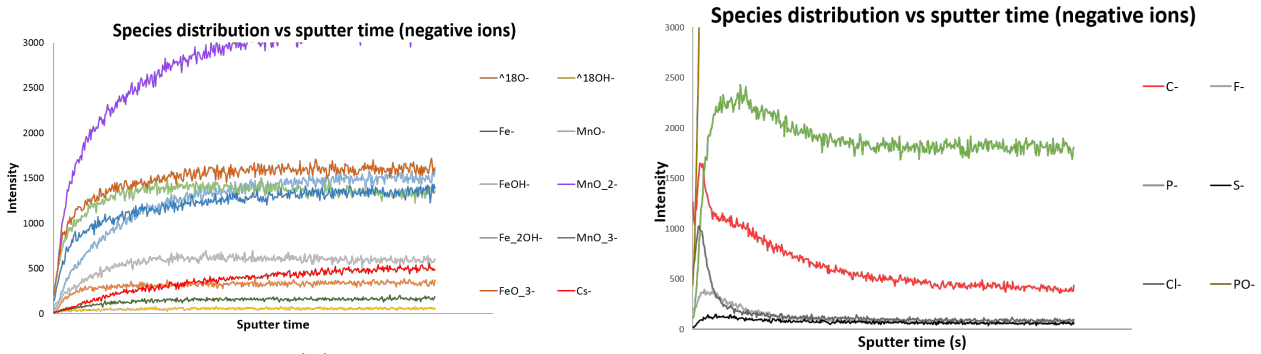

(A) (B)

FIGURE 4.58: ToF-SIMS depth profile (the sputter time can be thought of as the depth) for sample TWIP 6 by collecting positive and negative ions at different magnifications: (A) negative ions general plot, (B) positive ions general plot, (C) negative ions magnified plot highlighting the hydroxides and oxides, and (D) negative ions magnified plot highlighting the compounds issued from the SBF compounds.

4.2.7 Corrosion products removal by chemical attack

During immersion, corrosion products (hydroxides and oxides) as well as SBF elements get deposited on the surface and these need to get rid off in order to measure an accurate mass loss. In the IO 8407:2009 standard: *Corrosion of metal and alloys - Removal of corrosion products from corrosion test specimens*, different methods are proposed to remove these corrosion products. The most popular one in the literature is following: a chemical attack using 500ml HCl and 3.5g hexamethylenetetramine and adding distilled water to make one liter. The hexamethylenetetramine is supposed to protect the sample matrix from being attacked. Indeed, what is wanted is for the corrosion products to get removed

but not the metal matrix underneath as this would result in faulty corrosion rate determination. The outcome of this repeated procedure should look similar to the images on Figure 4.59 (see section 3.4 for more details on the procedure).

A 50% HCl solution was thought to possibly be already too concentrated for the small mass losses obtained in this present work. Thus, different concentrations of HCl have been tested.

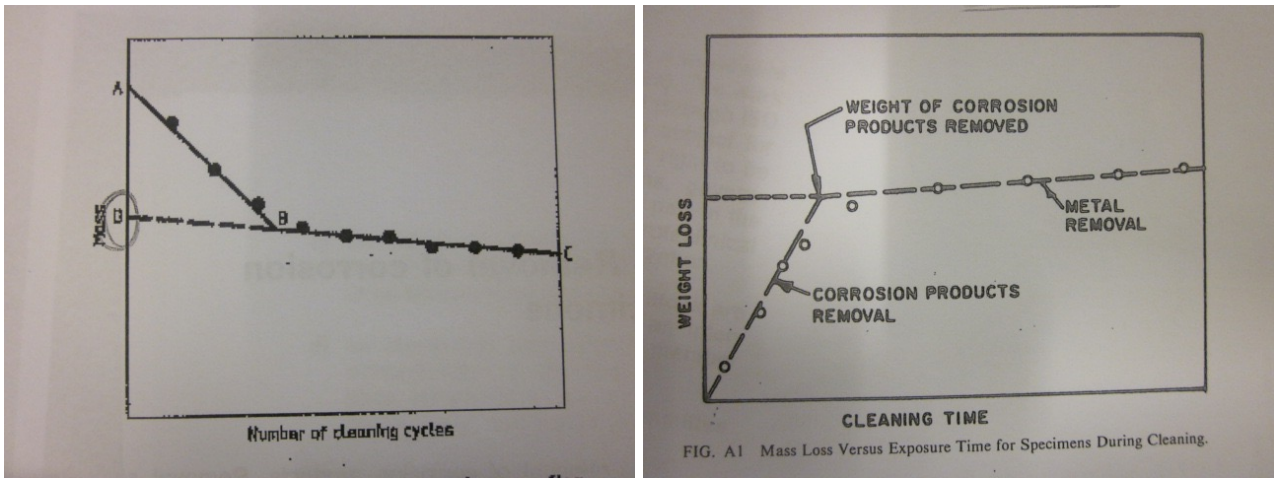

(A) (B)

FIGURE 4.59: (A) mass of corroded sample after repetitive cleaning [75] and (B) mass loss versus expsure time (especially suitable for electrolytic cleaning) [76].

50% HCl

Figure 4.60 illustrates the effect of 50% HCl attack on a sample that underwent a one week immersion. Two graphs are shown, one mass loss is measured by weighing, the other by ICP analysis. The sample was cleaned in different cycles: 2 seconds, 10 seconds, 30 second, 1 minute, and 2 minutes. It can be seen that a similar behaviour than shown on Figure 4.62a is found when using the mass losses weighed. However, if the extrapolation is made, a mass loss rate of 1.49 g/(m^2.d) against 0.997 (g/(m^2.d) before cleaning. It should be noted that after only two seconds already approximately 32nm have been removed when using ICP iron and manganese concentration:

$$thickness \quad lost = \frac{c(Fe, Mn)V}{\rho} \cdot \frac{1}{S} \tag{4.1}$$

where c is the ion concentration in mg/l, V is the volume is l, ρ is the density and S is the surface of one side.

10% HCl

This procedure was tested on the TWIP5 sample that underwent a three weeks immersion with the cleaning times being: 2 seconds, 10 seconds, 30 seconds, 1 minute, 2 minutes, 3 minutes, 4 minutes, 5 minutes, 8 minutes, and 10 minutes.

Figure 4.61 shows the obtained curve when cleaning with a 10% HCl solution. No rigorous lines can be drawn but after 2 seconds, it can be calculated from ICP, using equation 4.1, that the removed layer corresponds to approximately 42nm. It should be reminded that this sample underwent three weeks

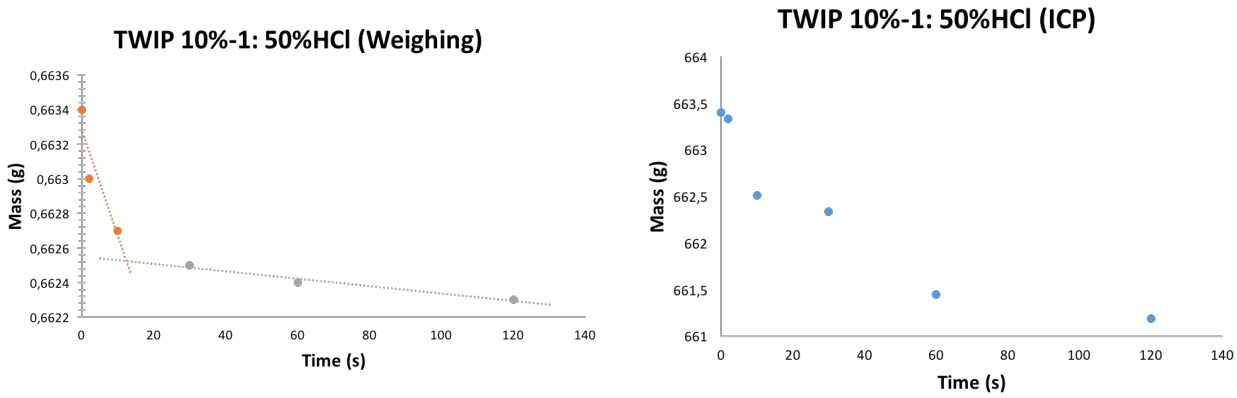

(A) (B)

FIGURE 4.60: Mass of corroded sample after repetitive cleaning by (A) weighing, and (B) ICP determination: 50% HCl.

immersion.

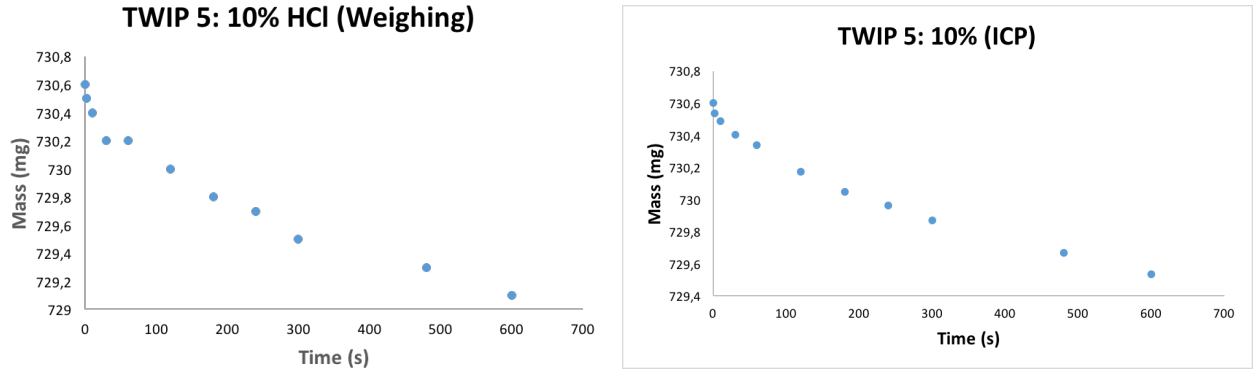

(A) (B)

FIGURE 4.61: Mass of corroded sample after repetitive cleaning by (A) weighing, and (B) ICP determination: 10% HCl.

1% HCl

The procedure was tested on TWIP 30%-1 sample that underwent a one week immersion with the same cleaning times as for the 10% procedure. The same as for the 10% test can be said here, no real extrapolation[19] can be undertaken (see Figure 4.62). However, after 2 seconds exposition, the removed layer corresponds to approximately 11nm.

4.3 Summary of the different experiments

From the polarisation tests it was found that the corrosion rates were ranked as follows:

[19] in the sense of Figure 4.59).

$$0\% > 40\% > 30\% \approx 20\% > 10\%$$

After one week immersion in SBF+50mM Hepes, the impact of deformation on the corrosion rate measured by mass loss was found to be as follows:

$$10\% > 0\% > 20\% > 40\%$$

And the impact on the corrosion rate measured by released ion concentration was following:

$$10\% > 0\% > 40\% > 20\%$$

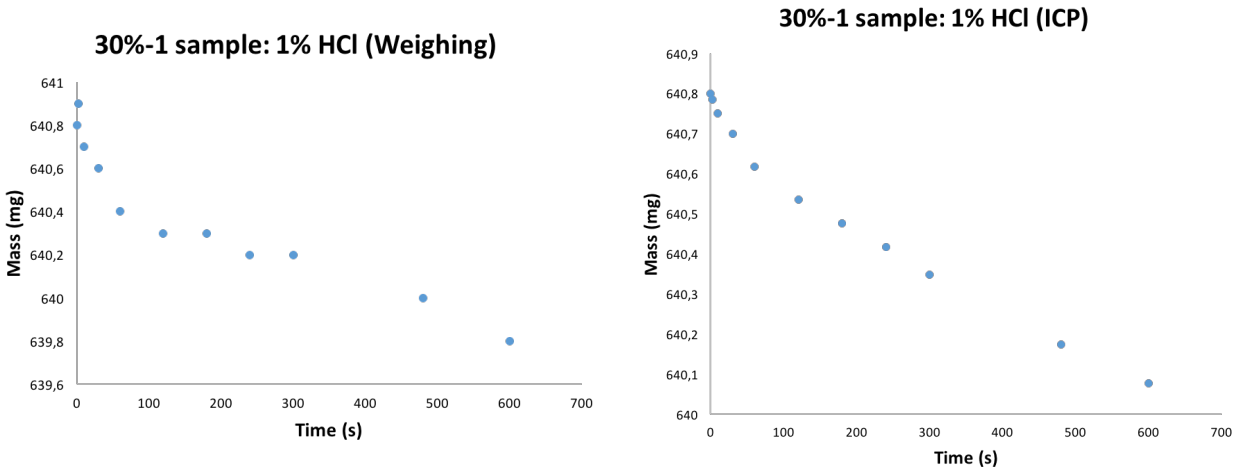

(A) (B)

FIGURE 4.62: Mass of corroded sample after repetitive cleaning by (A) weighing, and (B) ICP determination: 1% HCl.

By comparing the corrosion rates in SBF + 50mM Hepes buffer after one week immersion[20] to the ones found in the polarisation tests using the first method (being the one resulting with the lowest corrosion rates), Table 4.31 is obtained, showing the clear differences between the corrosion rates found by polarisation tests and the ones found by immersion tests.

Morphology analysis shows that during the corrosion process, SBF elements get deposited on the metal surface, especially P, Ca, and Na. No chlorine has been detected by XPS, however ToF-SIMS revealed some presence of chlorine at the upper part of the layer and disappearing afterwards.

Finally, for the corrosion products removal, all three tested methods (50%, 10%, and 1% HCl) showed that the removed layer, even after 2 seconds exposition is already significant.

[20]Without removing the corrosion products.

TABLE 4.31: Corrosion rates in mm/year comparing polarisation tests to immersion tests.

Family	$\mathbf{v}_{corr}$ **(mm/year) polarisation**	$\mathbf{v}_{corr}$ **(mm/year) immersion**
TWIP 0%	0.18	0.0231
TWIP 10%	0.088	0.0314
TWIP 20%	0.093	0.0247
TWIP 40%	0.14	0.0162

CHAPTER 5

DISCUSSION OF THE EXPERIMENTAL RESULTS

5.1 Polarisation tests

In this section, the different results of potentiodynamic polarization tests are discussed. First, a reproducible protocol had to be put in place. Once this was done, the chosen protocol was used to compare different deformation rates of Fe-22Mn-0.6C TWIP samples.

5.1.1 Choice of protocol

As has already been exposed, the first thing that needed to be done was to find the most suitable experimental protocol. Different parameters have been tested. The different steps will now be discussed.

5.1.1.1 Impact of OCP stabilisation on corrosion parameters

By not letting the sample reach its stabilized potential value but directly start the potentiodynamic scan after exactly 3 minutes immersion, higher corrosion rates (with however smaller standard deviations) were obtained (see Table 4.1). The observed corrosion potential are less negative than the samples that underwent previous OCP stabilisation (Table 4.2). The fact that the observed corrosion potential is less negative for the non stabilized samples compared to the previously stabilized samples can be explained by the fact that the system did not have the time to reach a steady state and as can be seen on a typical OCP plot (see Figure 4.13b for example), the voltage tends to get lower over time (due to metal dissolution). It is often thought that when a corrosion potential is more negative, the corrosion current density is more important as the material at lower voltages is supposed to be less noble. Here, the opposite is observed. An explanation could be that due to the very small immersion times for these samples, the metal surface did not have the time to change and get covered by any kind of protective layer compared to stabilized samples, exposing more active sites to the electrolyte and thus, resulting in higher corrosion rates.

Another statement can be made when looking at the differences between the open circuit potentials and observed corrosion potentials in the stabilized category. The observed corrosion potential was found to be more negative than the OCP (Table 4.2), illustrating a certain breakdown of passive film during the polarisation process. [69, 63]

Even if the samples that did not undergo previous OCP stabilization are the samples presenting the smallest standard deviation, the future samples will always be left to reach a steady state. This is decided in order to avoid obtaining corrosion rates way

higher than in reality, due to the fact that the material is not in its natural steady state while undergoing the polarisation scan.

5.1.1.2 Electrode contact's impact on corrosion behaviour

As already mentioned, a considerable amount of failures due to leakage were encountered. Therefore, substitutes to the electrical contact made by front contact of the sample with a copper sheet have been investigated in section 4.1.2. It has been seen that for the samples that got taken out of the mounted resin, the corrosion rate diminished and it became even smaller for the Rod sample. Nevertheless, it should be kept in mind that the Rod sample was the only one of its family.

The OCP of the Rod sample and some of the unmounted samples started raising after some time. This is unexpected, as increases in voltage throughout time were typical of leakage systems, were copper could have possibly taken part in the reactions. This is, however, not the case for the two new categories. The presence of passivation can explain a small raise in open circuit potential. The corrosion potential depends on the oxidant and reducing agent concentrations, and thus to their respective surfaces. Over time these ratio change, changing the corrosion potential. Until a steady state is achieved. For example, the formation of products can lower the anodic active area and the adsorption of species from the solution could cover cathodic sites [89]. A drop in potential means the dissolution of the metal, whereas an increase in potential can be due to the formation of passive films. Small increases in OCP have been observed for a few samples, but here the Rod sample encounters a much higher increase, that could possibly be explained by a certain resistance inside the metal or resistances due to contact. See Figure 4.6b for illustration of OCP drops at the beginning of the measurement and OCP raise later during the measurement for some samples. These tests did not show any improvement to the previous problems and even added new ones. Carbon tape and carbon lacquer were also tried (to allow an optimal contact between the copper sheet and the metal surface). This also resulted in increased OCP, probably because the carbon tape or lacquer added a certain thickness to the whole setup, leading to possibly more impermeability issues between the setup and the test whole (see Figure 3.3).

In these categories, only the mounted samples present a decrease in potential between the open circuit potential and the observed corrosion potential (see Figure 4.5b). The samples, which resin got removed before testing do not present any change in corrosion potentials during the potentiodynamic polarisation test. The Rod sample on the contrary presents an increase in potential during the polarisation test. This could notify on a passivation during the scan. As a reminder, this sample presented an increase in potential during the OCP stabilization, even if no leakage could be inspected. This strengthen the possibility of a film that got deposited during the stabilisation and continued to be formed during the forced cathodic reaction along with possible resistance effects. The other category (samples taken out of their mounted resin), illustrate a constant behaviour: this could mean that a film that got deposited during the OCP did not break down or got reinforced or if so, only in insignificant amounts.

The sample will continue to be mounted, polished, and tested the same way as before, i.e. with the use of physical contact between the front iron surface and a copper sheet (see Figure 3.1). Indeed, the new methods tried do not seem to bring solutions to the present problems, even bringing more complications.

It should be noted that from the 24^{th} of March, portholes started to be used to allow a better adherence between the sample and the copper sheet and avoid leakage. Portholes are also supposed to delimit an

area in such a way that the electrolyte does not get concentrated on the corners of the opening between the sample and the electrolyte. However, the cell opening used for the polarisation tests undertaken in the present work was smaller than the porthole diameter, loosing this feature. As a reminder, see Figure 3.3b.

5.1.1.3 Differences between cyclic and linear polarisation on corrosion behaviour

The previous impacts of stabilization and electrode contact were tested using a cyclic voltammetry with 50mV/s scan rate. In Declerck's Master's thesis [67] it was thought that by using a faster method than the one usually used in the literature, it would prevent the surface to change during polarisation and it was thought that this could improve the reproducibility issues. The most common method used in the literature is a slow rate linear sweep voltammetry (scan rate between 0.17 and 1mV/s). The changes observed were that the corrosion rates were smaller for LSV and even smaller when the scan rate is reduced in that category (see Table 4.5 for the detailed results). The corrosion potentials are also following this conclusion (the highest being for the LSV 0.33mV/s followed by LSV 1mV/s and CV 50mV/s). In terms of statistics, the LSV 0.33mV/s have the lowest standard deviations and the LSV 1mV/s and CV 50mV/s have similar standard deviations.

The observed corrosion potentials of each family are smaller than the OCP values, with the LSV methods having slightly higher differences between the two values, illustrating a more significant breakdown of passive film. Nevertheless, the corrosion rates are lower for these families. Thus these smaller corrosion rates cannot be explained by this potential shift. A possible explanation could be that during the anodic reaction the passive film has enough time to rebuild itself and to protect the sample for more severe corrosion. Additionally, SBF elements could have the time to deposit on the metal surface and protect it.

No definite choice can be made based on the results found in that section. The effect of scan ranges on the corrosion will be helpful for when making a decision. However it should already be noted that when using high scan rates, the system is not left enough time to stabilize at each potential [90].

5.1.1.4 Impact of scan range changes on corrosion behaviour

As has already been detailed throughout the report, a certain scan range needs to be present for Tafel extrapolation (the extrapolation should not start before 50-100mV [1]). For the first tests, a scan range of OCP±100mV was used, as well on CVs than on LSVs (see section 4.1.4 for the detailed results).

The fact that the corrosion rate decreases when the scan range increases for the LSVs is explained by a longer polarisation time, leaving more time for protective layers to deposit. The opposite is found for the CVs, where the OCP±300mV scan range results in a much higher corrosion rate than the OCP±100mV. This could be explained by the fact that the observed corrosion potential encountered a significant decrease compared to the OCP (for the 300mV scan range), which could be a sign of a weak film breakdown[2], allowing more active sites to be present for the anodic reaction. And, as the scan rate is fast, the oxide film does not have enough time to be rebuilt or even that localized corrosion occurs after film breakdown. Some LSV samples were also tested over a OCP±300mV range

[1] It should be kept in mind that some papers also advised to have a linear behaviour over at least one decade of current, which was not the case for all samples.

[2] When aggressive ions are present, the passive film that got formed on the metal can break down at a certain potential, which can either trigger localized corrosion (pitting) or repassivate [74].

and as it is the same material and the same electrolyte, there are chances that, if the previous sample (CV 50mV/s) went beyond the breakdown potential, these samples would do too. The explanation to the decreased corrosion potential could then be due to the metal repassivating and not creating localized corrosion. However if strong passivation and break-down are present, these should clearly be seen on the anodic part of the Tafel plots with a sudden drop in current density due to passivaion and an increase at higher potentials if pitting occurs after breakdown. The unstable pits around the breakdown potential are of low intensity. All that is seen on Figure 5.1. By looking at Figure 4.18, it can be seen that at the of the anodic scan of the LSV 1mV/s and OCP±300mV, the current increases rapidly (a sign of pitting corrosion). However, as the Tafel slope used for the corrosion rate calculation was excluding this sudden raise, this could explain the smaller corrosion rate, where just the reinforced passive layer is taken into account. It is to be reminded that the electrolyte also takes part in the corrosion mechanism and it can thus affect the Tafel slopes. The question is now if this could shadow the passivation and breakdown behaviours and should be further investigated, for example by testing the specimen in an inert electrolyte (the ASTM G61 standard could be helpful for highlighting localized corrosion). The other LSV 1mV/s investigated sample (OCP±200mV) exhibited an intermediary corrosion rate between the OCP±100mV samples and the OCP±300mV samples (see Table 4.11).

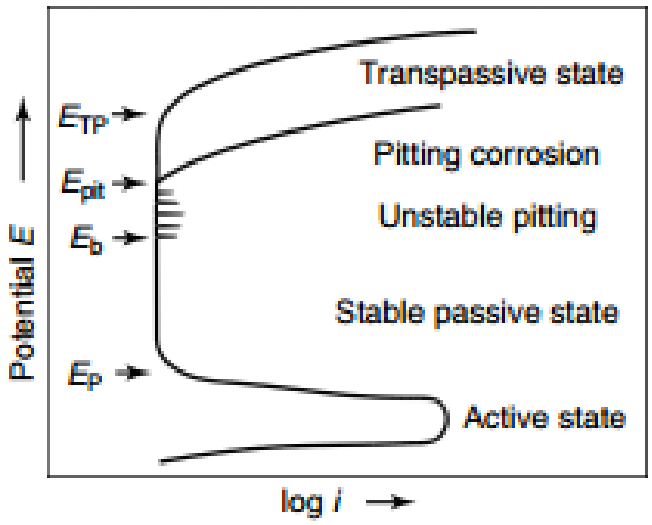

FIGURE 5.1: Passivation, breakdown and pitting potentials [74].

The corrosion rates in the LSV 0.33mV/s are slightly smaller for the OCP±150mV compared to the OCP±100mV family. The minimal variations are due to the small changes in scan ranges.

It is desired to study the corrosion behaviours the closest possible to the "in field" conditions, i.e. where no current is added and no electrochemical reactions forced. Therefore, the smallest shift between OCP and observed corrosion potential is desired. However, an accurate study of corrosion rates is wanted and thus OCP±100mV might be too low for Tafel extrapolation and it was shown that no significant changes in corrosion rate between LSV 0.33mV/s OCP±100mV and OCP±150mV was seen.

Therefore, the method that will be used is LSV 0.33mV/s with OCP±150mV scan range. This scan rate is quite often used in the literature but the scan ranges found there are more important in the range of OCP±300mV.

5.1.1.5 Impact of repolishing on corrosion parameters

By repolishing a sample, increased corrosion rates are obtained (Table 4.17). These changes are a sign of the statistical and experimental errors as a repolished sample should not show any differences with the results of the previous polishing of that sample.

Samples will continue to be repolished between tests as the changes are due to statistical and experimental errors and cannot be caused by polishing.

5.1.1.6 Impact of buffer and pH on the corrosion behaviour

The immersion tests lasting for a longer period than the polarisation tests, buffer was added in order to regulate the pH around physiological values (7.3 to 7.5) throughout the test for comparison reasons. It was then investigated if by adding buffer, and thus keeping the buffer closer to neutral pH, this would have an impact on the corrosion. By having a look at Pourbaix diagram (Figure 2.20, it could possibly thought that a passive hydroxide film would get deposited. The tests undergone without pH ended with a pH around 7.56 against 7.43 for 50mM buffer and 7.46 for 25mM buffer. Thus, one 50mM sample was tested with starting pH of 7.54. No conclusion could be drawn from this test, as the changes in corrosion rates ranking were differing depending on the calculation method used. Nevertheless, no changes should be due to the pH value within a pH range of 4 to 10, where the only factor theoretically influencing the corrosion rate is the rate of oxygen diffusion on the metal surface [91, 92]. Indeed, the change in pH is only supposed to change the hydrogen evolution reaction but not the oxygen reduction reaction or iron dissolution one (only the hydrogen evolution reaction depends on the H^+ concentration, thus the pH). Their reversible potentials are expressed here follow:

Fe^{2+}/Fe:

$$E_{Fe^{2+}/Fe} = E^{\circ}_{Fe^{2+}/Fe} + \frac{RT}{2F} \ln \left(a_{Fe^{2+}} \right).$$

with $E^{\circ}_{Fe^{2+}/Fe} = -0.44$ vs SHE

H^+/H_2:

$$E_{H^+/H_2} = E^{\circ}_{H^+/H_2} - \frac{RT}{F} \ln \left(\frac{p_{H2}^{0.5}}{a_{H^+}} \right)$$

with $E^{\circ}_{H^+/H_2} = 0V$ vs SHE

O_2/OH^-:

$$E_{O_2/OH^-} = E^{\circ}_{O_2/OH^-} - \frac{RT}{4F} \ln \left(\frac{a_{OH^-}^4}{p_{O_2}} \right)$$

$with E^{\circ}_{O_2/OH^-} = +0.4V$ vs SHE

More detailed discussion on corrosion affected by oxygen parameters can be found in section 5.1.3. Nevertheless, depending on the pH of the electrolyte some passive layers can form on the metal surface as is dealt with in Pourbaix diagrams (the data are thermodynamical data and the kinetics can greatly affect this diagram). By ICP it was shown that the iron concentration found in the solution before the potentiodynamic polarisation test starts is about 5.10^{-7} mol/l, so the Pourbaix diagram at these concentrations (seen one on Figure 2.20), shows that thermodynamically, a passive layer has only small changes to differ between pH values of 7.43 and 7.56.

The change in pH induced by the presence of buffer does not seem to be responsible for any changes. The effect of buffer and buffer concentration will now be related. As is detailed in section 4.1.5.2, the

immersion tests were taking place using 50mM Hepes buffer, 25mM still presenting high pH changes over longer immersion times. In this section, it was shown that by adding 50mM buffer, the corrosion rate seemed to be intermediary between no buffer and 25mM buffer, with slightly smaller standard deviations than for the 25mM tested samples (see Table 4.15). Some contradictions are for example that the most negative open circuit potential is found for the sample immersed in an electrolyte exempt of buffer. The fact that this sample is the one presenting the slowest corrosion rate can be explained by the Hepes taking place in the electrochemical reactions at certain forced potentials and thus, altering the ranking. The decreased corrosion rate between samples immersed in a 25mM and 50mM buffer electrolyte is unexpected. One reason could be experimental errors, possibly due to the experimental setup (please see section 6.2 for more details on the experimental setup errors). Therefore, the effect of buffer is still unclear for the moment and should be further investigated, once a better experimental setup is put in place.

Despite the fact that the buffer might have a certain impact on the corrosion behaviour, the classification in terms of deformation rate on the TWIP samples will be made using a 50mM buffer solution, to more accurately compare these results to the static immersion tests. However, it should be tried for future tests to avoid the presence of buffers that alter the electrolyte composition that needs to be the closest possible to human blood. Regulating the pH by the help of gaseous CO_2 could be investigated. This has already been used by *Schinhammer at al.* [3] as detailed in section 2.6.

5.1.2 Impact of deformation on corrosion parameters

Summarizing all the previous points, the following method was used for comparing the impact of deformation of TWIP samples on corrosion: first, the samples will be mounted and polished and the electrical contact will be made by a copper sheet placed on the metal surface and a porthole will help maintain the copper sheet and metal surface in close vicinity, avoiding contact failures. Then, OCP stabilization will be followed by a polarisation test performed using LSV method with 0.33mV/s scan rate and OCP±150mV scan range. The SBF electrolyte will contain a 50mM Hepes buffer.

The results from section 4.1.7, showed a corrosion rate ranking as follows (see Table 4.19):

$$0\% > 40\% > 30\% \approx 20\% > 10\% > Armcoiron$$

It should however be noted that the standard deviations are important, especially for the 40 % sample, where two families are present (see Figure 4.32): the maximal values are close to the values found for the non deformed samples and the minimal values are close to the other deformation categories. Thus, due to the statistical errors there is no certainty in that statement. However, it was shown by *Schinhammer* [3] among others that twins are favourable sites for corrosion. In the study, it was however shown that except for the special TWIP-1Pd samples, the corrosion would be concentrated around the twin boundaries but otherwise the corrosion would be homogeneous. *Ghayad et al.* also showed that annealing twins formed due to deformation would cause faster dissolution and consequently higher corrosion rates. All these reasons could explain the slight behaviour from the 10% sample to the 40% sample. But especially between the TWIP samples and the Armco iron. The maximal corrosion rate for the non deformed samples compared to the deformed categories cannot be explained by these factors.

5.1.3 Tafel interpretation and setup changes

The results discussed above were all using four different methods to determine the corrosion current density and thus the corrosion rate (section 3.2.5 details these four methods). To make it simpler, only three methods will be discussed: the first method, where the extrapolated anodic current intersects the observed corrosion potential, the second method, where the extrapolated cathodic current intersects the observed corrosion potential, and the fourth method, where the extrapolated cathodic and anodic values intersect. **The first method** is supposed to be the most accurate method when the oxygen reduction reaction is limited by diffusion processes. **The second method** is supposed to be the most accurate method when the oxygen reduction reaction is not limited by diffusion processes and the anodic reaction is altered due to surface changes. **The fourth method** is supposed to be the most accurate method when the oxygen reduction reaction is not limited by diffusion processes and the anodic reaction is only due to the metal dissolution. Please see section 3.2.5 for more information on the different methods. As already said above (section 5.1.1.6), at neutral pH, the dominant cathodic reaction is the oxygen reduction reaction and only depends on the oxygen diffusion rates and concentrations. Thus, no differences should be expected due to metallurgical changes if the electrolyte contains the exact same oxygen concentration [92].

Changes in oxygen behaviour

The different polarisation tests were performed in the lab, where the temperature could change by 7 degrees depending on the time of the year. The dissolved oxygen concentration is temperature dependant, highest for cold temperatures as the solubility of oxygen decreases with temperature [93]. The dissolved oxygen of the **immersion tests** at 37° was measured around 150-160 mmHg (equivalent to 8.8-9.4 mg/l) and did not seem to change between the different solutions prepared. However, during the polarisation tests, the electrolyte was in contact with air, which can alter the dissolved oxygen concentration from test to test, possibly explaining that the cathodic slopes are sometimes found to be limiting and sometimes not. Also, the differences due to the buffer could be due to a diffusion coefficient altered by the presence of Hepes. As a matter of fact, the electrolyte is changed by adding buffer. The fact that the corrosion rates increase when adding buffer would suppose a higher diffusion coefficient when buffer is present. Equation 2.62 recalls the limiting current for oxygen reduction reaction.

$$i_L = \frac{zFDc_{O_2}}{d} \tag{5.1}$$

where F is Farady constant, D is the diffusion coefficent, z the number of electrons transferred, and d is the thickness of the stagnant layer.
Therefore, only the concentration should be responsible for any changes in limiting current. Along with the number of cathodic sites present on the metal surface, on a microstructural point of view.

Up to now, it has been thought that oxygen reduction was the only cathodic reaction taking place. However, other reactions could be present with current considerable enough to alter the oxygen reduction reaction. Water could reduce into OH^- ions and hydrogen following:

$$2H_2O + 2e^- \longrightarrow H_2 + 2OH^-$$

This reaction is not known for being diffusion limiting [88] and could thus alter the cathodic Tafel slope. Also, as hydrogen is produced, hydrogen bubbles could cover a more or less extended metal surface, changing the effective surface present during the polarisation test. In order to avoid these changes, the sample should be rotated continuously to allow a constant hydrogen "layer" around it

and thus allow the same surfaces present for corrosion[3].

Tafel slopes

Section 4.1.1 showed that the actual Tafel slopes values were not that far away from the expected values from the literature (70mV/dec for iron dissolution and 120mV/dec for oxygen reduction reaction [88]). The samples that did not encounter OCP stabilisation have higher slopes than the samples that underwent previous OCP stabilization, especially the anodic slopes (see Table 4.2). This could be due to the more important impact of the iR drop (section 2.5.2.3 already exposed the effect of the uncompensated resistance). As a matter of fact, the iR drop was neglected in the calculations. The corrosion rates were found higher for the samples that did not encounter OCP stabilization, which means that the scanned currents were more important, leading to a bigger importance of the iR drop (V=iR). The uncompensated cell resistance has been measured using electrochemical impedance spectroscopy (EIS) was found to be somewhere between 65 Ω and 78 Ω [4,5]. It has been measured for an electrolyte containing 50mM Hepes buffer only.

The impact of the iR drop has been tested on one of the samples that did not undergo OCP stabilisation (with a resistance of 65 Ω) and the anodic Tafel slope underwent a high change: from 97 mV without iR compensation and 66 with iR compensation). The cathodic slope underwent a smaller change: from -185 mV without iR compensation to -180 mV with iR compensation.

For future tests, it would be recommended to measure the uncompensated resistance once for each system. The polarisation tests can then take this iR drop into account by asking the software using the iR drop compensation command, where the resistance value needs to be added by the user.

- **OCP stabilization**
  To go back to the Tafel slopes presented above (see Tabel 4.2), the samples, which OCP was stabilized before undergoing the polarisation scan do not show limitation in the cathodic slope. Therefore, an interesting question would be to see if the corrosion current density found using the method typical of reduction reaction not limited by the by diffusion control (i.e. fourth method: it is supposed hat no surface alteration takes place in high scan rate polarisations) would be extremely different from the corrosion current density found using the extreme opposite method, typical of oxygen diffusion control (i.e. first method). If the outlier is included in the calculation, the corrosion current densities differ from 15.8 μA/cm^2 for method one to 10.7 μA/cm^2 for method four. The corrosion current densities are 10.6 (first method) against 7.41 (fourth method) if the outlier is not taken into account. The changes are significant. An explanation could be that the first method, by not taking into account the oxygen reduction reaction, is supposing that the metal dissolution is the limiting reaction. Yet, the fact that the equilibrium potential of the system is close to the reversible potential of the Fe^{2+}/Fe system [6], shows that

[3] Please note, that no sign of hydrogen evolution could be detected during the polarisation tests.

[4] Other methods have been used to determine the cell resistance, using the positive feedback method or the i-interrupt method but the results found ranged from 70 Ω to 1400 Ω. The EIS method is the most accurate method. The uncompensated resistance is given by the resistance value (on a Nyquist plot) at high frequencies where the imaginary resistance is zero. Please see [94] for more detailed information on the different methods to measure the iR drop.

[5] The 78 Ω value was obtained on a system that already underwent positive feedback and i-interrupt, which bring the cell potential to 0V and this has possibly altered the surface before the EIS measurement was taken. As a matter of fact, the iron is heavily corroded at potentials such as 0V. The second value, 65 Ω was obtained another day, with the same solution, directly after immersion, making it more reliable.

[6] $-0.41 + \frac{8.3145*293}{2*96500} \ln(0.0096) = -0.469$ vs SHE for Fe^{2+}/Fe with an initial iron concentration (after OCP) of 0.03 mg/l and the corrosion system has an OCP of about -0.498 vs SHE.

the corrosion is limited by the cathodic reaction and not the anodic reaction. This would make the fourth method more accurate.

- **Electrical contact**
  For the different electrode contacts, section 4.1.2 showed a more limiting cathodic Tafel slope for the Rod sample (Tabel 4.4), also presenting the lowest corrosion rate, which is in agreement with the fact that if the diffusion of oxygen is more limited, less oxygen can reach the cathodic sites and be responsible for corrosion.

- **LSV methods**
  The LSV methods had more limitations as well for the cathodic slope as for the anodic slope (Table 4.6). The limitation in the anodic slope could be explained by a thin protection layers that gets deposited and also plays a role in the iR drop [7]. An example of the increasing effect of resistance on the Tafel slopes can be found on Figure 5.2, where a cathodic scan from 0.16V to -0.9V vs SCE was undertaken on a given TWIP sample. The plateau in the anodic region is a sign of high ohmic drop due to high currents. On that Figure, it can also be seen that the observed corrosion potential is less negative than the measured OCP of that sample (-0.746 V). An explanation is that the sample, by undergoing a cathodic scan, underwent heavy corrosion from the beginning, not allowing any protective layer to deposit. The effect of the iR drop shows that the Tafel line has a more pronounced linear behaviour up to a point where the solution resistance compensation is not enough anymore to account for the whole system resistance and the anodic branch reached its limiting current (see section 2.5.2.2 for a reminder on limiting currents). This can be seen on Figure 5.2. No changes in the cathodic slope are visible. In that Figure it is visible that at low current values, taking the solution resistance into account does not affect the results.

- **CV method**
  By increasing the scan range for CV polarisation tests, the cathodic slope increased slightly, whereas the anodic slope shows clear signs of limitation (see Table 4.8). The corrosion rate of this sample was found to be much higher than the samples with smaller scan ranges. The explanation of a higher contribution of the iR drop at these currents can also be used. Figure 5.4 shows the slight increase in cathodic and anodic Tafel slopes: 202 mV/dec against 247 mV/dec without iR compensation for the anodic slope and -140 mV/dec against -161 mV/dec without iR compensation for the cathodic slope. The anodic slope is still important and is thus affected by other unknown effects (possible film resistance).

- **LSV 0.33mV/s**
  When the scan range is increased in a 0.33 mV/s LSV scan, the cathodic slope is greatly more limiting (see Table 4.10). The changes show an oxygen reduction that seems to be diffusion controlled. In this case, it would be interesting to see if the extreme value, i.e the method where the cathodic reaction is supposed to be not limited by diffusion processes: the fourth method (indeed, it was supposed that for slow scans, passivation layers would form on the metal surface) is far away from the value found with the method considering that the oxygen reduction reaction is diffusion controlled, i.e the first method (even if passivation layers get deposited on the metal

[7] The iR drop measured above was instantaneous to avoid the effect of a surface layer adding its contribution. As a matter of fact, the surface changes throughout the test, and thus the uncompensated resistance due to this surface changes are never the same, making it more accurate to only account for the iR drop due to the solution resistivity and contact resistances. However, the iR drop used in these cases will always be less important than the actual resistance throughout the test.

surface). The changes are less important than for the previous example, when the OCP stabilization did not take place (4.7 μA/cm^2 for the first method against 5.2 μA/cm^2 for the fourth method).

- **Effect of buffer**
  Two samples were tested to see the effect of adding 25mM Hepes buffer to the electrolyte. The cathodic slopes were both limiting: one being -692 mV/dec close to the slope of the sample tested in these conditions with an electrolyte exempt of buffer. The other sample has -3609 mV/dec. The latter sample is also the one that presented the highest corrosion rate. An explanation could be that as the currents scanned were higher, the limiting current from the oxygen reduction reaction was attained, whereas it still was not the case for the first sample, which would have needed the scan to start at more negative potentials to allow higher currents in the system.

- **TWIP samples**
  The final point that will be discussed here is the Tafel slopes of the TWIP samples (see Table 4.20). The mean cathodic Tafel slopes are more negative for the most rapidly corroding family and get less negative (i.e. less limiting) for the TWIP family with exhibiting the lowest corrosion rate (i.e. the 10% family). An explanation could again be that the the limiting current is reached as the scanned currents are higher. The fact that the scanned currents are higher, is possibly a consequence of more cathodic sites presents. The effect of taking into account the iR drop has been evaluated for one 30% deformed sample: 140 against 145 without iR compensation and no changes for the cathodic slope. Thus, the changes are minimal in these cases.

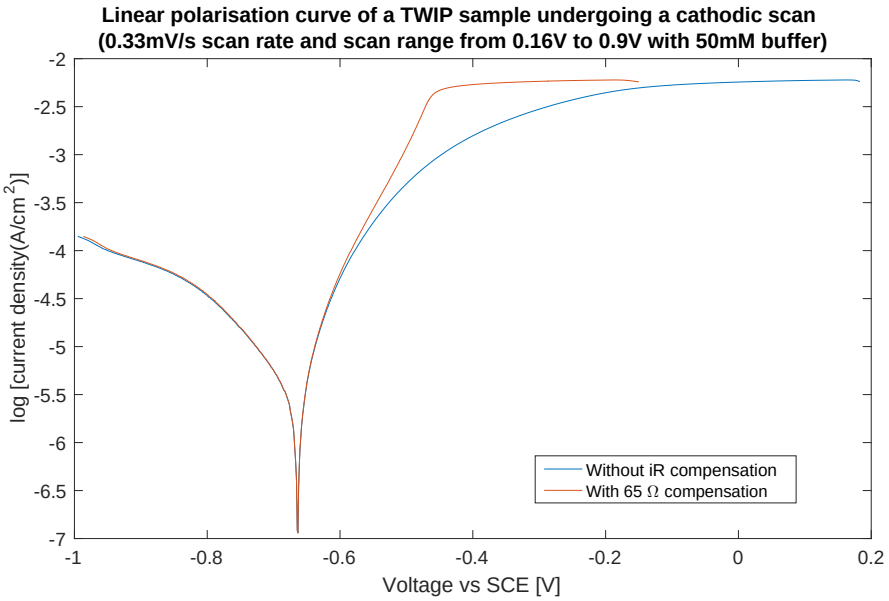

FIGURE 5.2: A cathodic scan (LSV 0.33 mV/s) from 0.16 to -0.9 V vs SCE

FIGURE 5.3: Outcome of a cathodic scan with or without iR compensation

5.1.4 Morphology changes due to corrosion

XRD analysis only showed the iron crystalline phases: ferrite in the case of Armco iron and austenite in the case of Fe-22Mn-0.6C. EDX analysis showed that the principal elements that get deposited on the

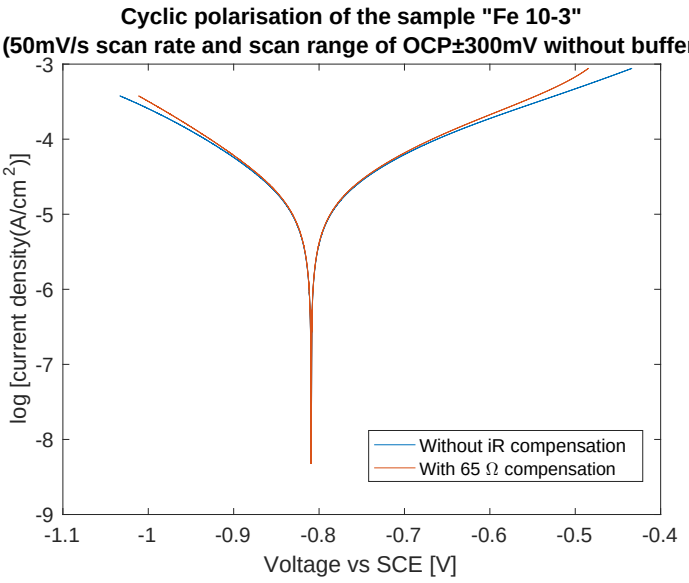

FIGURE 5.4: Outcome of a CV 50mV/s scan rate and OCP±300mV scan range with or without iR compensation

metal surface are phosphorus and calcium. Some magnesium and sodium are also detected. Sodium is the most present element in SBF but not the one that is the easiest deposited on the metal surface. Hereunder (Table 5.1), an ICP average composition of SBF solution with 50mM Hepes buffer before undergoing any test (H, O, and Cl are not detected by ICP):

TABLE 5.1: SBF content in P, Ca, Mg, Na, and S

Na (g/l)	**S (g/l)**	**K (mg/l)**	**Ca (mg/l)**	**P (mg/l)**	**Mg (mg/l)**
3	1.5	230	90	30	23

Actually, the two elements that are the most present on the deposited layer are only the fourth and fifth most present elements in the solution. This could be explained by a higher affinity of these elements to combine and precipitate on the metal surface. Zhang et al. [4] highlighted the fact that increases in pH during immersion tests promoted phosphates to precipitate and deposit on the metal surface. This theory is based on immersion tests but can also be used in this section to explain the higher calcium and phosphorous contents. As a matter of fact, the formation of ferrous hydroxide ($Fe(OH)_2$) increases the pH locally to 9.3 without considerably affecting the bulk solution pH [95, 92].

SEM images showed that the deposited layer is homogeneous (see Figure 4.39 but that at some spots, this layer breaks down. Spots with agglomerates of corrosion products/deposits could also be seen on Figure 4.40 for one TWIP sample. The corrosion products agglomerates were not seen on the two iron samples analysed at the SEM. Maybe, this could be a consequence of the concentrated corrosion at twin boundaries, bringing about more localized corrosion than for iron.

ICP analysis showed that a sample stopped after OCP stabilization released less iron in solution compared to a sample that underwent a polarisation test, which is logical as the sample is forced to corrode when undergoing a polarisation scan. However, these values are very small (0.03 and 0.07 mg/l). The SBF elements changes in concentration before and after polarisation test cannot be concluded from ICP analysis. This shows that the deposited layer is extremely thin. The TWIP samples released

slightly more iron than for Armco iron samples. However, the amount of iron and manganese released did not always coincide with the highest corrosion rate between the TWIP samples. An explanation could be that not all solution samples underwent acid attack before ICP analysis (see section 3.5) and with small values as the ones found after polarisation tests this could result in significant changes. Also, for ICP, 50ml were taken from the 315ml. It could lead to a non homogeneous probe, especially with small values, this could change the outcome. The best would have been to attack the whole solution to have the most accurate value. It had been tested to take probes (for five samples) between the OCP and polarisation test to differentiate the iron concentrations for each test (see section 4.1.7) but ICP showed that the SBF elements and iron concentrations were greatly different from sample to sample. As examples, iron concentrations ranged from 0.07 to 0.42 mg/l , manganese from 0.03 to 0.04, and phosphorus from 30 to 65 mg/l. Manganese did not change a lot through all the samples but it also did not change between each deformation sample as seen on Table 4.21. These changes could only be due to non homogeneous sample taking as this was done through the filling whole at different spots and with no stirring to make the solution homogeneous[8]. The same day a blank solution was tested and presented some Zr at the ICP, which could explain the Zr found on some samples after immersion[9].

Finally, α ferrite is known to be less corrosive than γ austenite [5]. This explains why TWIP samples corrode faster than Armco iron samples.

5.1.5 Corrosion rates measured in the present work compared to previous papers

The average corrosion rates for iron and iron based alloys (not deformed) are compared in Table 5.2. Please note that most articles do not relate in detail their experimental procedures omitting sometimes important information, such as the scan range, the volume of solution, previous OCP stabilization, the method used, the temperature, the pH,...

TABLE 5.2: Comparison of iron and iron based alloys corrosion current densities in $\mu A/cm^2$

Material	**Present work**	**Harjanto et al [6]**	**Liu et al. [51]**	**Moravej et al. [22]**
Armco/pure iron	5.3 - 6.6	/	8.96	16.3
Fe-22Mn-0.6C	16.4-27.7			
Fe-25Mn-1C		53.7		
Fe-35Mn-1C		95.5		
Material	**Zhang et al.[4]**	**Sherif et al. [96]**	**Liu et al. [5]**	**Hermawan et al. [25]**
Armco iron	16.8	18-28	9	14
Fe-30Mn-6Si			24.7	
Fe-30Mn			10.7	
Fe-35Mn				up to 105.6

The values for iron in the present work are smaller than the ones found in the literature but are the closest to the ones found by Liu et al. [5]. An explanation could be that the tests were performed using the same scan rate and same method with OCP stabilization up to 7200s. The differences must arise from other parameters when comparing to Liu et al. [5], possibly the difference in electrolyte (Hank's solution for Liu et al.) or working temperature (37° C agains room temperature for the present

[8]No stirring was undertaken to avoid changing the electrical contacts and changing the reference electrode spot
[9]No Zr was checked for in the polarisation sample EDX spectra.

work) The most important difference is found with Zhang et al. [4]. The differences could be due to the different temperatures[10] (37° for Zhang et al.), volumes (350 ml against 315 ml in the present work), the OCP stabilization (3600s for Zhang, whereas OCP was left to stabilize to a certain value and not for a certain time), the actual polarisation tests: it seems as if the working electrode, after OCP stabilization, is removed from the electrolyte and placed in a new cell, where it immerses for 20 minutes before undergoing the polarisation scan. This alters the electrolyte composition before the scan starts. No details about the scan range are given, but it looks approximately to be [-900mV -500mV]. The second highest change is with Hermawan et al. [7], who used Hank solution as well but with OCP±250mV scan range and 0.166 mV/s. The investigation of LSV scan range and scan rate in this study showed that the corrosion rate is highered when the scan range is increased or the scan rate decreased. Thus, the results of Hermawan are hard to explain as not enough details are given on the procedure: nothing is said about previous OCP stabilization, electrolyte volume or working temperature.

These papers do not give any detail on the way they measure their corrosion current or the values of their Tafel slopes. But it can be approximated that for Liu et al. [51], the anodic Tafel slopes are about 120 mV/dec, i.e. also higher than the expected theoretical values. The cathodic slopes are also limiting.

5.2 Static immersion tests

To go directly to the most important aspect of the immersion tests, the morphological aspect will be briefly discussed, followed by the corrosion rates as well as the impact of buffer concentration on this corrosion rate.

5.2.1 Morphology and corrosion rates of immersed samples

For each sample, the corners were always more attacked than the rest of the sample. An explanation is that the corners are encompassed by more solution than the center of one side. Samples with more or less pits were also present. The differences in pit concentrations can be due to metallurgical changes, such as a higher twinning percentage (by considering twinning boundaries being favourable sites), the grain size (much smaller for TWIP samples) but also to the metal/electrolyte contact. Concentration cells of oxygen can be formed at some spots, resulting in localized corrosion. The samples underwent rotation to avoid this concentration cell forming, which is often caused by stagnant electrolyte. Some samples, especially TWIP 40%-1 (one week immersed) and TWIP 7 (three weeks immersed) showed concentrated brown or black layers.
The black spots are typical of FeO presence [5] and the brown spots are typical of rust. Follows how rust is formed. Ferrous hydroxide $Fe(OH)_2$ is formed from the combination of Fe^{2+} ions and OH^- ions. Saturated $Fe(OH)_2$ has a pH of 9.5 making the metal surface alkaline. It then reacts with oxygen to form $Fe_2O_3.2H_2O$, which is the outer rust layer when atmospheric corrosion takes place. Rust does not totally protect the metal as it is permeable to air and water [92]. FeOOH is the main component of rust when water is present. This is consistent with the XPS findings, stating that the blank sample that was not immersed was composed of an oxide layer, whereas the immersed samples detected essentially FeOOH (see section 4.2.5).
EDX analysis showed that when pits were present, chlorine was detected in the vicinity of these pits. Chlorine is known to have devastating effects on corrosion and Schinhammer et al. [3] showed that the corrosion layers were divided in three sublayers: the closest to the metal surface contained significant amounts of chlorine, the second and third had increased concentrations of calcium and phosphorous. The fact that chlorine is detected in the vicinity of pits, could be explained by a deeper surface made

[10] It was shown in section 2.4.6

available for EDX analysis and exposing the first sublayer. Chlorine ions react with iron to form $FeCl_2$, which wears material away [49, 51].
EDX analysis also showed that the main components of the deposited layer is phosphorus and calcium. This was also the case for polarisation samples. Some samples presented more calcium and phosphorus than other samples. For example, TWIP 6 showed a more important calcium and phosphate layer than TWIP 9 and TWIP 12 (all immersed in SBF for one week). The corrosion rate of that sample was much higher than for the two other samples. It could be thought that if a thicker deposited layer is present, this would protect the sample in a higher extent. This does not seem to be the case in first approach. An explanation could be that if the sample underwent more severe corrosion, it would present spots with different roughness, making it more favorable for the calcium and phosphorus to deposit there. *Liu et al.* [51] obtained the same result, i.e . a more rapidly increasing Ca/P layer on already corroded surfaces. As the centre seems less covered by salt deposits, it seems like the corrosion is not homogeneous throughout the sample, with favourable sites of corrosion near the edges. No difference in layer composition could be made for the one day immersion samples. and the corrosion rates of these two families were indeed quite close. For the one week immersion tests in 50mM buffer (section 4.2.2.1), the 40% samples presented the highest proportion in phosphorus and calcium, followed by the 20 % and 10% families and finally the non deformed family. The corrosion rates were more important for the 10% family and smallest for the 40% one. This could be explained by a possible more important impact of localized corrosion. Indeed, measuring the corrosion rates this way is to be done with precaution. As a matter of fact, if pitting is present in important amounts, the corrosion rates can be greatly increased because of one spot. Not that many pits could be seen on the 10% samples. However, these pits could be more important and not covered by corrosion products/deposits. Indeed, some pits get deactivated by corrosion products/deposits that build up on these pits, whereas other pits continue to grow further deeper.
The fact that the 40% samples have the lowest corrosion rate can be explained by the fact that the second sample was performed using the handmade setup and resulting in a corrosion rate three times lower. Nevertheless, the TWIP 40%-1 sample still have a lower corrosion rate than the other categories.

The high phosphorus and calcium contents of the deposited layer can be explained by Zhang et al.'s theory that the increase of pH during immersion is favourable for phosphate precipitation and deposition. This was already highlighted in the polarisation section.

The impact of buffer on the immersion corrosion rates can be seen on Figures 4.51. The corrosion rates doubled when immersed in an electrolyte containing 100mM Hepes buffer. However, the standard deviations of the samples immersed in a SBF solution with 50mM buffer are important. Still, the samples immersed in 100mM Hepes buffer are corroding slightly higher than the upper value, considering the standard deviation. The corrosion rates in mm/year result in the a 40% sample immersed in 100mM buffer having a smaller value that the maximal value for the 50mM samples, considering standard deviations. The changes are due to the density being considered in the mass loss rate in mm/year but not in $g/(m^2.d)$. The densities were measured for each sample, from their initial mass and dimensions. The samples being very small and light, errors are easily made. For the one week samples tested using the handmade setup instead of the IKA Loopster rotor, the corrosion rate was lower. An explanation could be that the samples were covered by foam to avoid that these fall out of the container (see Figure 3.9) and this could act as a temperature barrier (see section 2.4.6 for detail on the impact of temperature on corrosion rate). Indeed, the measured temperatures were always around 34-36°C before and after immersion. Also, the setup being different, the samples can be in different contacts with the electrolyte. For the three weeks immersion, the opposite was found where the TWIP 7 samples (immersed using the handmade setup) presented a higher corrosion rate (when considering the released ion concentration)[11]. This could be explained by the black FeO presence, possibly formed

[11] Only an approximation could be made for this sample as it was omitted to be weighed and measured before testing.

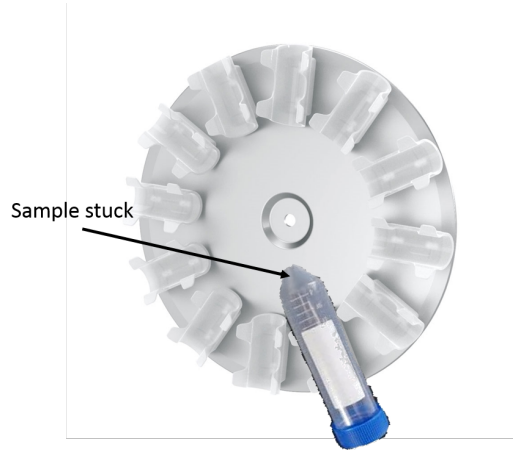

FIGURE 5.5: Illustration of the moment when the sample can be stuck and not in contact with the electrolyte.

because of concentrated corrosion at these spots.

A certainty is that the corrosion depends on a lot of different factors and also on some randomness that can make the corrosion rates significantly different from sample to sample. The corrosion rates being very small, it is difficult to be 100% sure that the classification found (10%>O%>20%>40%). However the same light tendency has been obtained for different electrolyte concentrations, which strengthen the validity of this classification.

For the the corrosion behaviour over three weeks (see Figure 4.54), it is shown that the corrosion rate is maximum after one day and greatly decreases after one week, where a certain plateau is attained for the 40% deformed samples. The mass losses increase linearly for the 40% samples throughout the three weeks, whereas they stagnate after one week for the non deformed samples. The latter observation can be explained by the formation of the insoluble precipitates found in the three weeks samples. But these were also present in the 40% sample, which does not suffer stagnant weight losses. It could be that the precipitates do not cover the whole surface in such a way that cathodic sites are still available for oxygen reduction.

It should be noted that lately it has been noticed that during immersion using the IKA Loopster rotor, the samples would get stuck when situated at the bottom of the rotor and thus, they are not in contact with the solution anymore (see Figure 5.5 for a visual representation of that issue). Thus, the actual corrosion rate could be up to $\frac{4}{3}$ higher than calculated [12]. It can not be said that all samples were stuck the same way. Also, the fact that the sample gets stuck and does not move around can also explain the presence of localized corrosion on one side and not both. As a matter of fact, this was often observed.

The three weeks samples as well as the one week samples tested using the handmade setup presented white magnetic precipitates. The three week tubes were full of these precipitates, whereas the one week samples were only containing a few of these precipitates. When the pH was measured these precipitates would climb around the pH probe. They were also stuck on the sample itself. When attacking the solution with acids as is done for the ICP analysis, they would not dissolve. They were thus collected and melted. It was found that they were made of mainly silicon and sulphur. Iron, aluminium, phosphorus,

[12]The sample would not be in contact with the solution for about a fourth of a turn.

magnesium, and zirconium as well as titanium on some samples was also contained [13,14]. The TWIP 4 (3 weeks immersion) contained much more iron in the insoluble precipitates than the other samples and it presents a much lower corrosion rate than TWIP 5 (also 3 weeks). These precipitates could thus be responsible for a decrease in corrosion rate, which would explain the differences between the one week immersion tests undertaken using the handmade setup and the IKA Loopster rotor. However, the fact that these precipitates were present in the former samples and not in the latter is surprising. An explanation is that the precipitates could appear when either the immersion time is increased or when the actual contact between the sample and the electrolyte are improved, by better mixing and less localized corrosion.

The corrosion rates measured using the ICP values were higher than the corrosion rates measured by mass loss. An explanation would be that the weighing scale is only precise to the 0.1 mg and as the samples tested were light and the mass losses very low, this 0.1 mg precision is not enough to accurately measure the corrosion rates. The ICP can detect most elements for concentrations as small as 0.01 mg/l, making it more precise. ICP does not detect oxygen or hydrogen, but if hydroxide layers are deposited on the metal surface, there is little chance that these would dissolve and be present in the solution after immersion. The corrosion rates measured by ICP are thus more accurate than the ones measured by mass loss.
As has already been detailed in section 3.4, the corrosion products need to be removed from the metal surface to accurately calculate the corrosion rate. The mass loss encountered in the present work are very small and the removal of this layer could greatly change the values obtained. However, the three HCl concentrations used did not bring conclusive results (see section 4.2.7). The 50% HCl concentration as suggested in the literature allow the best interpolations but the removed layers are important and the corrosion rate can also be greatly increased by using this method. The two other concentrations (10% and 1%) did not give a good enough plot to allow two interpolations. The layers removed after two seconds were still important. Therefore, an accurate idea of the corrosion thickness should be known (possibly obtainable by SEM examination of the surface layer thickness or by ToF-SIMS depth-profile over a deeper layer) before attacking the sample. The time when the closest value to the measured layer thickness is obtained, this mass loss will also be the one chose for the corrosion rate measurements. Another approach would be to attack the sample by the use of NaOH at 90°C. This method should be tried to see if a better interpretation can be made. As the last resort, electrolytic cleaning could be tested instead. In the previous paragraph it was stated the the ICP method gave a more accurate corrosion rate. This is not totally true when calculating the corrosion rate after HCL attack (with 3.5g/l hewamethylenetetramine). Indeed, the corrosion products/deposits contain oxides and hydroxides, which the ICP cannot detect. Thus, the loss due to the corrosion products/deposits will be more accurate using the weighing scale.

XPS showed that the immersed samples presented hydroxides compared to oxides for a non-immersed sample (see section 4.2.5. Phosphate and calcium are present in similar atomic percentages. The TWIP 4 sample, that was immersed for three weeks is the sample presenting the most manganese on the top layer. This is consistent with Schinhammer et al.'s model (Figure 2.42) stating that manganese diffuses away from the metal interface to react with dissolved oxygen. The brown rust layer of sample TWIP 40%-1 is the spot that has the highest presence of oxygen, which is logical. The three weeks immersed sample also presents the highest calcium concentration, illustrating the growth of the protection layer over time. For the phosphate ions, the brown spot on the TWIP 40%-1 sample also contains a high amount of phosphates, showing a build-up of rust with phosphate layer.
ToF-SIMS showed that P^-, S^- , Cl^-, and PO^- were present in higher concentration at the upper

[13]Only the three weeks samples were analysed. Also it has to be kept in mind that the values found are minimal values as losses due to the filtering as well as the precipitates that climbed on the pH probe and were stuck on the sample and the tube walls.

[14]The iron content could illustrate the presence of magnetite in these precipitates.

surface and still present with lower content in the intermediate surface. This is also consistent with Schinhammer et al. ' model. PO^- is the most present component, also in consistence with the values found in EDX analysis. The iron oxide and hydroxide are starting to be present at a slightly deeper thickness compared to the salts and increase until they reach a plateau. Some metallic iron is also detected after a certain depth, but in very low extents. The profile depth was not going deep enough into the sample and new tests, that would go further down, up to the point where only the metallic compounds are present should be undertaken.

5.2.2 Comparison with corrosion rates found in the literature

Zhang et al. [4] observed different corrosion rates relationships over time compared to this study. These were obtained for pure iron. They observe an increasing mass loss throughout time until day 21, which is similar to the behaviour of TWIP 40%.

Schinhammer et al. [3] investigated Fe-21Mn-0.7C alloys with or without 1Pd addition. They obtained a similar relationship over time than the present study regarding the degradation rates. However, their mass losses increased throughout the time and did not reach a plateau as has been observed here for the non deformed samples. Also between day 14 and 28 they find a corrosion rate of 2.86 g/(m^2.d), whereas it is found here a corrosion rate of 0.178 g/(m^2.d), which is more than 10 times smaller. The differences could arise from the fact that the volume used in the present work was 50 ml, i.e. about 20ml/cm^2, whereas the volume to surface ratio used by Schinhammer is of 160 ml/cm^2, possibly reflecting an early saturation of the present system. Despite these differences, they obtained corrosion rates of $\approx$ 0.10mm/year for pure iron samples, which is smaller to the values obtained by Zhu et al. [97] (0.23 mm/year; measured in SBF). The Fe-21Mn-0.7C corrosion rates between this period were also lower than the corrosion rates present in the literature when Mn is added to the alloy: Liu et al. [5] observed a corrosion rate of 0.3 mm/year for Fe-30Mn-6Si, and Hermawan et al. [2] obtained scan ranges of 0.44mm/year for Fe-35Mn and 0.52 mm/year for Fe-25Mn. Schinhammer et al. explained their smaller corrosion rates by the fact that they did not use any buffer to regulate the pH throughout immersion tests. Zhu et al had [97] an average corrosion rate of 4.9 g/(m^2.d) during the 28 days. However, they performed their test in dynamic conditions. As has been seen in section 2.4.4, a flowing electrolyte increases the corrosion rate due to different factors: the oxygen is continuously replenished as well as other components that can be damaging, and finally the corrosion products are scoured away leaving more active surface available for corrosion. Thus, this value is supposed to be higher than the ones measured in the present study. It was a mistake of Schinhammer et al. to compare their results to these. Also, no values are given in Liu et al. [5], only an increasing graph of the released ion concentration in solution after immersion test (in μg/ml). They measured their corrosion rates by released ion concentration, making them not totally comparable to the Schinhammer et al. results. Additionally, Hermawan et al. performed their tests in dynamic conditions. Therefore these results cannot be used for comparison. For pure iron, Cheng et al. [52] showed that after 30 days the released ion concentration of W was 20 mg/l, which has a higher corrosion rate. These values are already closer to the values found in the present work for non deformed samples after 21 days immersion in a 50mM buffer solution (14mg/l on average). Schinhammer et al. [3] also noted that the corners were the first to suffer corrosion.

Liu et al. [5] also showed that iron corrodes faster than the different Fe-Mn alloys tested, whereas the inverse was found for electrochemical tests. This was explained by a higher importance of the corrosion product layer for immersion tests. After 6 month it was shown that the whole iron surface was covered by corrosion products, whereas the Fe-30Mn and Fe-30Mn-6Si alloys still presented some shiny spots. This build-up of corrosion products on the metal surface is a negative aspect. This can cause material limitation [3]. In the present study, it was also shown that the corrosion rates ranking are different in

terms of polarisation tests or static immersion tests:

Polarisation tests: 0%>40%>30%≈20%>10%>Armco Iron
Immersion tests: Armco Iron[15] >10%>0%>20%40%

The high phosphorus and calcium contents of the deposited layer can be explained by Zhang et al.'s theory that the increase of pH during immersion is favourable for phosphate precipitation and deposition. This was already highlighted in the polarisation section.

Schinhammer et al. [3] emitted the hypothesis that the differences in corrosion rates are due to the changes in composition and structure of the deposited layer between each family (Pure iron, TWIP, TWIP-1Pd). This hypothesis is based on the fact that if oxygen reduction is the main cathodic reaction, there shouldn't be any differences between the families, as the cathodic reaction would be the determining one. This would explain the small differences between the different deformations tested in the present study. However, as said by Liu et al. [5], the ferrite and austenite do not behave the same way in corrosion resistance, which is more acceptable reason of the increased corrosion rates for TWIP and TWIP-1Pd families compared to pure iron.

Aude Thomas and Eleonora Scarcello performed immersion tests on Armco iron. They found that for one week immersion tests in SBF solution with 50mM Hepes buffer, the average corrosion rate was of 3.24 g/(m^2.d). However, they discovered that the Armco iron used presented traces of copper and niobium on three of the four samples, highering the corrosion rate. The only sample without this presence had a corrosion rate of 0.57 (g/m^2.d), which is still higher than the corrosion rate of the TWIP samples investigated in the present work, with the exception of the 10% samples that had a slightly higher corrosion rate (0.66 mg/(m^2.d). This higher corrosion rate for iron compared to Fe-Mn has also been determined by Liu et al. [5], who explained the differences to be due to the higher corrosion products importance on iron samples, as detailed previously. Aude Thomas and Eleonora Scarcello also investigated the effect of previous sample oxidation [16] and a corrosion rate of 4.95 g/(m^2.d) was found, not quite different from the other samples also containing Cu and Nb. They also investigated the effect of phosphate on the corrosion, by preparing an electrolyte with no phosphate present. The corrosion rate was found to be 6.95 g/(m^2.d), showing an increase compared to the other samples also containing Cu and Nb, and strengthening the theory of phosphate protection layer.

5.3 Conclusion

5.3.1 Polarisation tests

It has been shown that the main features in corrosion rate determination are oxide film formation, breakdown and possible localized corrosion. During OCP stabilization, a weak passive film can be formed and depending on the method used this one can be broken down during the cathodic reaction scan (especially when the scan range is larger). When using the fast method (CV 50mV/s) the system is not left the time to fully stabilize between each potential. The LSV 1mV/s and OCP±300mV scan range samples exhibited sudden raises in current during the polarisation scan at the end of the anodic branch (see Figure 4.27a). This is possibly highlighting the presence of pitting due to localized oxide layer breakdown. Adding buffer to the solution could either have an effect by reacting during the polarisation scan or by changing the diffusion coefficient of the solution. The cathodic reaction being mainly oxygen reduction into OH^- ions, the pH range value should not affect the corrosion (true for pH 4 to pH 10). TWIP samples corrode faster than Armco iron samples but the impact of the

[15] This is based on the results found by A. Thomas and E. Scarcello.
[16] Indeed, the stent will undergo sterilization before being placed in the artery, which will oxidize the material.

deformation is not well detected. If the oxygen reduction is diffusion controlled, no significant changes are expected between these samples. However, a higher amount of twins present could also present a higher amount of cathodic sites, thus higher corrosion rates. Generally, the trend seen is the non deformed samples having the highest corrosion rates followed by the deformed samples with similar corrosion rates[17]. The iR drop effect has also be studied and it was found that most of the time, it has been a good assumption to neglect it. Localized corrosion was spotted on one TWIP samples but not on the two Armco iron samples analysed.

Finally, the corrosion rates calculated are lower than the corrosion rates found in the literature. Unfortunately, the articles do not state clearly how they proceed.

5.3.2 Immersion tests

It has been seen that samples exhibiting higher corrosion rates are also the ones containing the thickest corrosion/deposited layer, which is explained by a surface first undergoing corrosion forming hydroxides and chlorides and finally a Ca/P layer that gets deposited on top of that corrosion layer. The centre of the samples seemed to have undergone attack (presence of holes) but only minimal amounts of SBF got deposited on the centre. The buffer affect the corrosion rate by increasing it. The corrosion rates found are lower than the ones found in the literature and also lower than the ones found during polarisation tests. The latter can be explained by the fact that during immersion, the corrosion products are taken into account, whereas the polarisation tests only lasting a few hours does not take this aspect into account. Here again, the effect of deformation is not pronounced with a slight ranking following 10%>0%>20%≈40%. The corrosion rate measured by released ion concentration exhibited higher corrosion rates than the corrosion rates measured by sample weighing. This is explained by a lower precision of the weighing scale. Other sources of errors are present: the fact that 1.5-2.5ml was retrieved from the tube after immersion for the dissolved oxygen concentration measurement could possibly change the corrosion rates and the tendency. Also, if localized corrosion takes place, no "real" corrosion rate can be calculated.

It has also been proved that the solution after immersion only contained Fe^{3+} ions and no sign of Fe^{2+} was detected by spectrophotometry [18]. As stated by Moravej et al. [22], iron can easily change from ferrous (Fe^{2+}) to ferric (Fe^{3+}) ions by accepting and donating electrons. These easy changes are useful for many biological components, such as oxygen-binding molecules (hemoglobin and myoglobin). This transformation from ferrous to ferric ions is obtained from a reaction between ferric ions, oxygen, and hydroxyl ions [4]

$$Fe^{2+}+O_2+3OH^- \longrightarrow Fe(OH)_3 \downarrow + {O_2}^-$$

Indeed iron has a standard electrode potential of -0.44V vs SHE, the reduction of oxygen into hydroxyl ions has a standard electrode potential of +0.4V, and the Fe^{2+}/Fe^{3+} system has a standard electrode potential of +0.77V. Thus, when corrosion takes place, a potential of $0.4-(-0.44)=0.84V$ is supplied to the system and for ferrous ions to convert into ferric ions a voltage of $0.77-0.4=0.37V$ needs to be supplied to the system for this reaction to take place and if complexes can be formed from these ferric ions, by Le Châtelier, this ferrous transformation into ferric ions will be favoured throughout the process.

[17] Please note that the 40% category exhibited two families of corrosion rates, one close to the non deformed samples and one close to the other deformed samples.

[18] The intensity of colours is detected with this method. Ferric ions and ferrous ions have different colours that can be distinguished by this method.

Finally, the corrosion rates measured by immersion tests are significantly slower than the ones measured by electrochemical tests, even after only one day immersion. This is explained by the more important surface contributions to the corrosion and the changes of ranking between immersion tests and polarisation tests can be due to the different surface effects. Nevertheless, the changes in corrosion rates, on an absolute scale, are not that significant, the individual corrosion rates being small. Another aspect is that the dissolved oxygen pressure present in the electrolyte are more important than the actual pressures present in arterial blood (about 150mmHg for the electrolyte against 75-100mmHg in arterial blood). As the corrosion in neutral pH is limited by the oxygen reduction, the values found in vitro could possibly be significanly higher than the actual corrosion rates in an artery.

CHAPTER 6
CONCLUSION AND FUTURE RECOMMENDATIONS

6.1 Conclusion

The subject of this Master's thesis was to determine the corrosion behaviour of iron-based alloys for coronary stent applications. Bioresorbable stents are a developing technology. The mechanical support of a stent is needed for about 6 months, after which they are obsolete foreign bodies that can cause medical complications such as late-thrombosis, positive remodelling of the arterial vessel, avoid stenting "sandwiches" in case of restenosis. This late-thrombosis can be avoided if the stent is degraded after fulfilling its task. However, restenosis can still occur with biodegradable stents. Re-endothelialization should not be obstructed by the stent presence but excessive re-endothelialization can lead to restenosis, which re-narrows the stented area. These are features that need to be optimised in the design of stents. Another possibly negative feature of resorbable stents is a possible inflammatory response due to the degradation process [98]. Another important factor is the radial strength. The stent should be able to withdraw the arterial wall pressure in order to avoid mechanical failure. TWIP alloys have impressive work-hardening properties making them very suitable for withstanding external load without shrinking and thus avoid a gap formation between the arterial wall and the stent, which could lead to complication. This impressive work-hardening is explained by twins that are straining induced and become planar obstacles to the dislocation glide [28]. Iron is an element needed by the human body to a certain extent. A typical stent weighs around 41 mg, which corresponds to a monthly iron oral intake and much less than the amount of iron transfused with one unit blood (200-250 mg) [20].

These are the reasons why this thesis focused on the degradation behaviour of Fe-22Mn-0.6C TWIP samples. Another aspect is that the stent is undergoing deformations from the fabrication process to the stent placement inside the artery. The stent is first shrunk around a balloon before implantation. Once the stent has reached the injured area, a radial pressure is applied on the stent by the use of a balloon to expand it to the diameter size of the injured artery. Thus, the stent undergoes compression followed by expansion. Due to buckling, no compression behaviour can be studied. Therefore, tensile tests were performed on TWIP samples to obtain the following deformations: 10%, 20%, 30%, and 40% deformation.

In order to study the corrosion behaviour of these materials, potentiodynamic polarisation tests have been performed to give a first idea of the corrosion rates in more rapid tests. Afterwards, immersion tests were performed to study the effect of time on corrosion, the presence of protection layer and localized corrosion.

The first investigation made was the setting up of a reproducible experimental setup for the electrochemical polarisation tests. The setup tested that gave the best results was an LSV scan with a scan rate of 0.33 mV/s and a scan range of OCP±150mV. The 315 ml electrolyte contains 50mM Hepes buffer. The tests were performed at room temperature. The results measured by this method for the different deformed TWIP samples compared to Armco iron had following ranking:

$$\text{TWIP } 0\% > \text{TWIP } 40\% > \text{TWIP } 30\% \approx \text{TWIP } 20\% > \text{TWIP } 10\% > \text{Armco iron}$$

The difference in corrosion rate between the non deformed samples and iron samples is clear. However, the slight difference between the differences deformations are too low to draw a real conclusion out of it.

Theoretically, the anodic and cathodic extrapolated Tafel slopes intersect at the observed corrosion potential. However, this was rarely the case in practice, due to experimental disturbances and effects other than electron transfer, being of less or more importance from time to time (especially diffusion limitation). Therefore, the corrosion rates were measured using four different methods: one method where the anodic Tafel extrapolated corrosion current value intersects the observed corrosion potential, one method where the cathodic extrapolated current value intersects the observed corrosion potential, a third method using the average between the two latter values, and finally a fourth method evaluating the corrosion current density as the intersection between the cathodic and anodic extrapolated lines. The corrosion rates ranking is maintained whatever method is used [1]. The Hepes buffer was seen to increase the corrosion rates of the systems suing Hepes (Schinhammer et al. [3] pointed that out as well as Cuculic et al. [99] on Copper(II)-Salicylaldoxime Complex). Indeed it contains SO_2, H^+, and OH^-, which can alter the corrosion rates.

Hermawan et al. [2], Schinhammer et al. [3], as well as Zhang et al. [4] presented a possible corrosion mechanism in simulated body fluids. Hermawan et al. described the first hydroxide layer to be composed of black (FeO and Fe_3P_4) and brownish spots (Fe_2O_3). Due to the non homogeneous layer, chlorine would compensate by forming metal chlorides, which lowers the pH inside the pits but the bulk solution still remains neutral. This process is auto-catalytic. After these steps, a calcium/phosphorus agglomerate layer is formed on top of the degradation layer. The composition is interesting as it could form hydroxyapatite, which is biocompatible. A similar mechanism was described by Schinhammer et al. [3]. Zhang et al [4] concentrated their mechanism on the compounds formed from ferrous hydroxide and chlorine ion combination. They supposed a final step of iron phosphate precipitates (combined from Fe^{3+} and ${PO_4}^{3-}$ ions). Other precipitates are shown to be magnesium phosphate, calcium phosphate, and ferric hydroxide. The switching from ferrous ions to ferric ions is illustrated by Zhang et al. as being done following:

$$Fe^{2+} + O_2 + 3OH^- \longrightarrow Fe(OH)_3 \downarrow + {O_2}^-$$

A similar corrosion mechanism has been investigated in the present study immersion tests. The attacked metal regions were the regions containing the highest chlorine concentration and the most attacked regions were also found to be covered by a calcium/phosphorus layer. XPS analysis did not detect chlorine but the hydroxide and Ca/P layer were well detected and ToF-SIMS analysis showed the higher presence in salts at the upper surface and an increase in hydroxide and oxide presence in slightly deeper layers where the salts presence diminishes. Some irons started to be detected. XPS also showed that for longer immersion times, three weeks, a smaller Fe/Mn ratio than expected is found, concording with Shinhammer et al.'s theory that manganese diffuses to the surface to combine with hydroxyl ions. Finally, the iron found after immersion test was solely composed of Fe^{3+} ions, which is

[1] The second method changes the ranking of the 20 % and 30% families but these were approximated as equal. Therefore, this change does not alter the overall ranking.

consistent with Zhang et al.'s mechanism.

The corrosion rates throughout time for non deformed and 40% deformed TWIP samples decreased between day 1 and day 7 immersion and continued to decrease from day 7 to day 21, but with a smaller pronounced decrease. The corrosion rates were measured without removing the corrosion products and thus, they can be very underestimated. The impact of the deformation on the quasi static immersion tests for 7 days immersion, presented only small differences. The standard deviations being too important to conclude a real impact of deformation on corrosion. However, the average values conclude in a ranking as follows:

$$\text{TWIP } 10\% > \text{TWIP non deformed} > \text{TWIP } 20\% \approx \text{TWIP } 40\%$$

The samples immersed in higher buffer concentration (100mM) showed an increase in corrosion rate compared to the samples immersed in 50mM buffer, making the use of Hepes buffer undesirable for the corrosion determination.

6.2 Future recommendations

6.2.1 Polarisation tests

One future recommendation would be to change the test cell (see Figure 3.3 for the current test cell). The hole where the reference potential is placed is about 5mm wide. The iR drop depends on the distance between the working electrode and the reference electrode but not in a linear relationship (see Figure 2.29). Therefore, depending on the test the electrode could be placed at a different spot between these 5mm, possibly changing the value of the uncompensated resistance. It can also be noted that the distance between the working electrode and the reference electrode is of about 2.5cm, which also affects the resistance value (as explained in section 2.5.2.4). The fact that the distance between the working electrode and the reference electrode is already important can possibly have as consequence that the resistance differences inside the 5mm hole are not as significant as described previously. Also, depending on how deep the reference electrode is lowered in the hole, the iR drop could differ[2]. The electrical contact for the working electrode should be improved. Instead of a copper sheet, an electrical contact should be set in place from behind the sample before mounting (by welding conducting wires on the sample back). Another possibility would be to use a rotating disk electrode[3], which would allow a better reproducibility of the effective surface present throughout the test by "creating " a constant diffusion layer around the sample. Moreover, the system should either be changed to seal it from the atmosphere to avoid the atmospheric oxygen to alter the dissolved oxygen concentration during the test or, once that a better system has been set up, it can be tried to better regulate the dissolved oxygen pressure by bubbling the system with either oxygen or nitrogen [4].

The samples could also be tested with a previous anodic pre-polarisation to start the polarisation tests with a more reproducible surface. However, if this is done, small changes due to previous deformation of the sample for example, will be distorted. As a matter of fact, by pre-polarising the samples, they start the test with a common surface. Another negative aspect of this pre-treatment is that the polarisation tests should correspond to "field" behaviours and the stent won't undergo this kind of surface treatment before placement into the artery. Additionally, *Zhang et al.* [69] recommend to undergo a

[2]The contact with the electrolyte is made through a small hole at the bottom of the cylindrical hole containing the reference electrode.

[3]This method is also highlighted in [34], where they state that measurement undergone using rotating disk electrodes result in more accurate results.

[4]This has already been tried in Olivier Declerck's Master's thesis [67] but it did not bring conclusive results. This is why, if a better system is put in place and the oxygen problems are still present it could be tried again.

reverse scan in addition to the forward scan to reduce the disturbances of charging current (averaging the two scans), which should diminish the differences between the "anodic corrosion current density" and the "cathodic corrosion current density". However, in this study salts get deposited on the metal surface, which means that the electrolyte will be slightly altered before the reverse scan starts and same goes for the metal surface. It can still be interesting to see if indeed smaller changes in corrosion values for anodic and cathodic extrapolated values are obtained. Another possibility is to perform the cathodic and anodic scans separately on identical samples. By doing so, the anodic scan will not be dependant on the previously performed scan on the cathodic region. One possible problem of such method is that the samples seem to have experimental errors between each polarisation test, which means that a reconstruction of an Evans plot from the two different scan could be difficult to obtain. However, it is worth trying. This technique is also proposed by [73] for example, where it is said that this method results in more accurate corrosion current densities.

The impact of buffer concentration is still unclear. Once the new set-up is ready to use, this effect should be re evaluated, and decisions on either keeping the buffer or not should be made.

Also, the OCP stabilization should be optimised. Each sample was left to stabilize for different times. The best would be to determine one time when all the samples are certain to stabilize and start the polarisation test at that time, to avoid longer or shorter immersion times from sample to sample which could affect the importance of deposited/passivating layers.

It was also tried to stir the electrolyte to avoid the oxygen reduction to be diffusion limited. The results were not conclusive. This is due to the fact that the manufactured stirrer was not tall enough and disturbed the right functioning of the reference electrode. A new stirrer could manufactured and the effect of stirring on the oxygen limitation could be investigated.

The pitting tendency of the tested materials could also be investigated basing the tests on the ASTM G61 Standard: *Standard Test Method for Conducting Cyclic Potentiodynamic Polarization Measurements for Localized Corrosion Susceptibility of Iron-, Nickel-, or Cobalt-Based Alloys*. The best way of studying pitting, breakdown, and passivation of the material is to first use an inert electrolyte that could not alter the intrinsic behaviour of the material and then compare it to the same tests undergone in SBF to possibly better understand the effect of the deposited elements.

The tests should be undertaken at 37°C by the use of a oven keeping its temperature around 37°C.

6.2.2 Immersion tests

The immersion tests showed a decrease in corrosion rate for longer immersion periods. This is of particular interest for the wanted application. Indeed, the corrosion rate should be as slow as possible at the beginning to avoid mechanical failure while the stent is the most needed. The slow corrosion rate should be maintained for about 6-12 months, after which the mechanical support is not needed anymore. After that period, the material should corrode as fast as possible to degrade in a short period of time without overcharging the blood system by corrosion products in a too short time range. Therefore, it should be investigated up to when this low corrosion rate is maintained, by undergoing longer immersion tests. Still it should be kept in mind that "in vivo" the stent will be covered by cells and the contact with blood decreases, thus the corrosion rates will not be able to fully mimic the "in vivo" mechanisms.

The immersion tests should also be performed under dynamic conditions to allow a better study of what actually happens in the artery. The wall shear stress should be chosen to mimic the best the artery wall shear stress. The corrosion rates are expected to increase in such tests as newer electrolyte

is continuously provided. Indeed, for the static immersion tests it should be tested up to which time period, the solution is not oversaturated with corrosion products. As a matter of fact, the more the solution contains corrosion products, the less the metal will be subject to corrosion. A replenishment of solution after a certain time could be considered. Additionally, for dynamic immersion tests, the flow will limit the deposition of corrosion products/deposits. Also, the sample preparation should be improved:

- **Polishing**: A polishing up to 1 μm should be performed on the samples to allow better surface analysis after immersion test. As a matter of fact, the samples for static immersion samples are polished up toMD-Piano 1200 discs but this makes it more difficult to analyse using surface analysis such as ToF-SIMS or even SEM. If the sample would undergo a mirror-like polishing, as is the case for the polarisation samples, it could be possible to see where the localized corrosion is concentrated, if this is near twin/grain boundaries or other particular spots. For ToF-SIMS depth profile, a mirror like polishing is favoured for a better depth determination.

- **Shape**: The sample shape should be improved to avoid the sample to be stuck during a fourth of the immersion time. This could be done by preparing round specimens or by putting in place a system that would hold the specimen while being inert to the solution[5]. A sketch of such a system can be seen on Figure 6.1.

- **Rotation**: If no better system to prepare the sample can be put in place, the rotation should be stopped to avoid this quarter of time when the sample is not in contact with the solution.

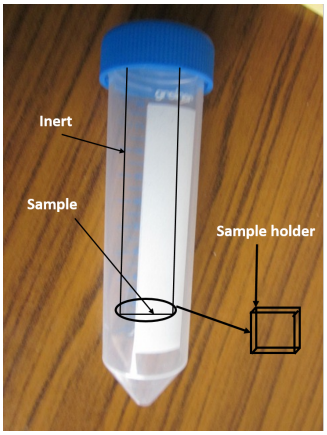

FIGURE 6.1: An illustration of a possible sample holder for static immersion tests. The sample would be stuck inside a sample holder leaving the two main surfaces at the open air. This way, the sample will always be in contact with the solution and homogeneously.

Corrosion under stagnant electrolyte is slower than flow induced corrosion but stagnant corrosion should be avoided because it brings about localized corrosion [100]. Figure 6.2 shows the effect of increased flow rate on corrosion rate. First, the flow rate increases the corrosion rate but once there is enough oxygen that reached the metal surface, this oxygen can form a protective surface with ferrous hydroxyde over the entire metal surface, lowering the corrosion rate[6] [100].

[5] At the same time, the recipient could be changed and not present this tip at the bottom of the tube.

[6] This passive layer might not form on pure iron or other materials compared to stainless steel that has a high tendency to passivate.

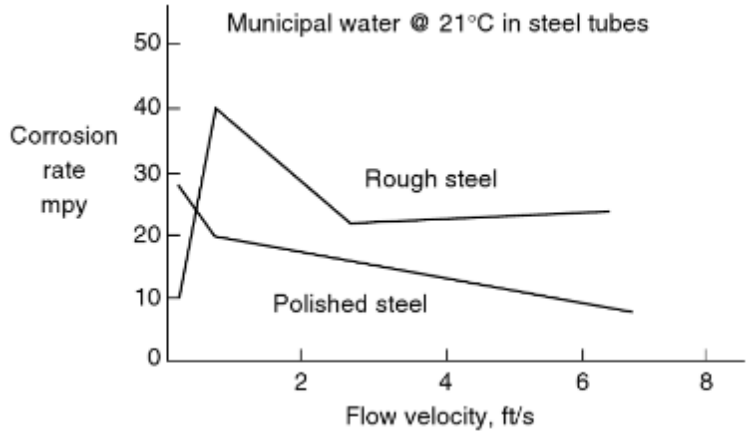

FIGURE 6.2: Effect of water flow on steel corrosion [100].

For the time periods investigated, the corrosion rates were too slow to make a mechanical properties study on the samples before and after immersion. However, for the longer periods, this should be undertaken by preparing small tensile test specimens, which will undergo tensile tests after immersion.

The dissolved oxygen concentration should be measured by another method, that does not need to take in any solution. Indeed, each probe was different and this could possibly affect the corrosion rate, especially at such low corrosion rates.

6.2.3 Future materials of interest

The electrochemical study showed promising results on TWIP alloys, exhibiting higher corrosion rates than Armco iron as this is the wanted feature. The immersion tests also show that the evolution over time for short periods is promising. Thus, these alloys seem to have a future in the stent industry on a corrosion point of view. However, more rapid rates would be favourable and this could be obtained by adding a fourth element to the alloy (like *Schinhammer et al.* did [3]). Laurine Choisez investigated the Fe-Mn-Zn alloys and the preliminary results (considering the crystalline phases formed) are quite promising, which is why this path should also be investigated along with Fe-Mn-C-Zn alloys to see if the corrosion properties of these alloys are as good as their mechanical properties seem to be.

Another interesting path could be to study the corrosion rate of alloys fabricated by powder metallurgy. Indeed, *Hermawan et al.* Hermawan already highlighted the fact, that the corrosion rates can be almost quadrupled by fabricating the stent with powder metallurgy. However, this technique also leaves porosities behind, which are negative for the mechanical properties. Thus, a good compromise between fast corrosion rate and good mechanical properties should be sought.

6.3 Last word

The amendment of one or a multiple of the factors outlined in this section may be a subject of key benefit. In particular, I believe that further study into the issue of TWIP alloys corrosion behaviour during long-term trials may contribute to the field and address many key questions that remain unanswered in this report, such as wether or not the low corrosion rate will be maintained for long enough and if a wanted sudden increase in corrosion rate will happen after 6 months immersion. This thesis

shed the light on various experimental parameters that need to be improved in future studies, in order to make sure that the corrosion rates measured (along other factors) are accurate. While this study has a number of merits, such as the explicit examination of the corrosion behaviour of TWIP samples compared to Armco iron, I believe that there is hope in making bioresorbable stents a more suitable implant option for people suffering from heart disease.

APPENDIX A
MATLAB CODES FOR TAFEL AND OCP DETERMINATION

A.1 OCP determination

```
%% OCP determination

% Author: Sarah Reuter
% Description: This script enables the user to plot a CV plot wher the mean
% value of the last five seconds is calculated.


close all;


a = TempsTwip30P5OCP(2:end);
b =VoltageTwip30P5OCP(2:end);
Twip30P5=mean(b(end-5:end)) % mean value for the last five seconds


plot(a,b);
hold on;


%% General Figure
 title ( sprintf ( 'OCP of TWIP 30%%-5 sample' , i ) , 'FontSize' , 20 );
 set(gca,'fontsize',15);
 ylabel('Voltage vs SCE [V]');
 xlabel('Time [s]');
```

A.2 Tafel determination for CV scan

```
%% Cycic polriation Tafel determination

% Author: Sarah Reuter
% (inspired from Olivire Declerck's code for the first part,
% where the average is plotted).
% Description: This script enables the user to plot a LSV plot with
% Tafel lines. The corrosion potential is also diplayed on the graph.
% From the graph, anodic and cathodic corrosion current densities can be
% determined. The measured corrosion current density and potential are
% returned by the script (in X).

close all;

```

```
index = ScanFe171; %gives the cycle

nCycle = ScanFe171(end-2);




a = VoltageFe171(1:end); % gives the potential

b = CourantFe171(1:end); % gives the current

A = cell ( 1 , nCycle ) ;

B = cell ( 1 , nCycle ) ;

C = cell ( 1 , nCycle ) ;


figure ( );
for i = 5 : 5

X = a(index == i);

Y = b(index == i);


 A{i} = tempa ;
 B{i} = tempb ;


p = polyfit ( X , Y , 6 );

y = polyval( p , X ) ;

y = abs (y/0.894);

C{ i } = y ;

y=1/log(10)*log(y); %make the y-axis logarithmic

plot ( X , y ) ;
hold on;



end


%% TAFEL DETERMINATION
%% PLOT ECORR

indice1=find(y==min(y));
indice1=indice1(1);
Ecorr=X(indice1)
plot([Ecorr Ecorr], [-4 -7.7]);
hold on;
%% Anode

%inferior index
essai1=X(indice1)+0.048; % finds the first value located between 48mV
essai2=X(indice1)+0.052; % and 52 mV from OCP

essai3=zeros(length(X),1);
```

```
for i=1:length(X)
    if X(i)>=essai1 && X(i)<=essai2
        essai3(i,1)=X(i);
    end
end


index=find(essai3~=0);
index2=index(1);
indexGood=find(X==essai3(index2))

%%superior index
essaiX=zeros(length(X),1);
essai1=X(find(X==max(X)));
essai2=X(find(X==max(X)));
for i=1:length(X)
    if X(i)>=essai2 && X(i)<=essai1
        essaiX(i,1)=X(i);
    end
end
indexX=find(essaiX~=0);
indexX2=indexX(1);
indexGoodmax=find(X==essaiX(indexX2));

tafelA=polyfit(X(indexGood:indexGoodmax),y(indexGood:indexGoodmax),1);
Anode=polyval(tafelA,X(indexGood:indexGoodmax));

deltaY=Anode(end)-Anode(1);
deltaX=X(indexGoodmax)-X(indexGood);

a=deltaY/deltaX; % gives the slope in decade/V
a=a(1);  % The first value is considered if more than one values found
b = - a(1) * X(indexGoodmax) + Anode(end); % gives the intersection with the y axis
b=b(1); % The first value is considered if more than one values found
yX=a(1)*X+b(1); % equation of the anodic Tafel line
plot(X,yX);

hold on;



%% Cathode

% first index
essai4=zeros(length(X),1);
essai1=X(indice1)-0.048; % finds the first value located between 48mV
essai2=X(indice1)-0.052; % and 52 mV from OCP
for i=1:length(X)
    if X(i)>=essai2 && X(i)<=essai1
        essai4(i,1)=X(i);
    end
end

index2=find(essai4~=0);
index22=index2(1);
indexGoodmax=find(X==essai4(index22));
indexGoodmax=indexGoodmax(1);

% Inferior index
essai5=zeros(length(X),1);
essai1=X(1)+0.01; % Does not take into account the curvy end of the
essai2=X(1)+0.012; %cathodic branch
for i=1:length(X)
```

```
    if X(i)>=essai1 && X(i)<=essai2
        essai5(i,1)=X(i);
    end
end

index3=find(essai5~=0);
index32=index3(1);
indexGoodmin=find(X==essai5(index32));

tafelB=polyfit(X(indexGoodmin:indexGoodmax),y(indexGoodmin:indexGoodmax),1);
Cathode=polyval(tafelB,X(indexGoodmin:indexGoodmax));

deltaY=Cathode(end)-Cathode(1);
deltaX=X(indexGoodmax(1))-X(indexGoodmin(1));

a2=deltaY(1)/deltaX(1); % gives the slope in decade/V

b2 = - a2 * X(indexGoodmax(1)) + Cathode(end); % gives the intersection
                                               % with the y axis

y=a2(1)*X+b2(1);% equation of the cathodic Tafel line
plot(X,y);

%% Determination of measurd corrosion potential
 % and current density (intersection)
syms x y

eqn1 = a(1)*x - y  == -b(1);
eqn2 = a2(1)*x - y == -b2(1);

[A,B] = equationsToMatrix([eqn1, eqn2], [x, y])
X = linsolve(A,B)


hold on;


%% General figure
 title ( sprintf ( 'Cyclic polarisation of the sample "Fer 17-1" \n '
 '(50mV/s scan rate and scan range of 100mV without OCP stabilization '
 'and without buffer)' , i ) , 'FontSize' , 20 );
 hleg1=legend('Polarisation curve','E_{corr} observed', 'Tafel anode',
 'Tafel cathode');
 set(gca,'fontsize',15);
 ylabel('log [current density(A/cm^2)]');
 xlabel('Voltage vs SCE [V]');
```

A.3 Tafel determination for LSV scan

```
%% Linear Polarisation Tafel deteremination

% Author: Sarah Reuter
% (inspired from Olivire Declerck's code for the first part,
% where the average is plotted).
% Description: This script enables the user to plot a LSV plot with
% Tafel lines. The corrosion potential is also diplayed on the graph.
% From the graph, anodic and cathodic corrosion current densities can be
% determined. The measured corrosion current density and potential are
% returned by the script (in X).

close all;

```

```
a = VoltageTwip30P5(2:end); % gives the potential
tempa=a;

b = CourantTwip30P5(2:end); % gives the current
tempb=b;

y = abs (tempb/0.894);



y=1/log(10)*log(y);

plot ( tempa , y ) ;
hold on;


%% Tafel determination
figure;
plot ( tempa , y ) ;
hold on;

%% ECORR
indice1=find(y==min(y));
Ecorr=tempa(indice1)
plot([Ecorr Ecorr], [-4.2 -7]);
hold on;




%% Anode
essai1=tempa(indice1)+0.048; % finds the first value located between 48mV
essai2=tempa(indice1)+0.052; % and 52 mV from OCP

essai3=zeros(length(tempa),1);
for i=1:length(tempa)
    if tempa(i)>=essai1 && tempa(i)<=essai2
        essai3(i,1)=tempa(i);
    end
end


index=find(essai3~=0);
index2=index(1);
indexGood=find(tempa==essai3(index2))



%%superior index
essaiX=zeros(length(tempa),1);
essai1=tempa(end);
essai2=tempa(end);
for i=1:length(tempa)
    if tempa(i)>=essai2 && tempa(i)<=essai1
        essaiX(i,1)=tempa(i);
%     else
%         new(i,1)=0;
    end
end
indexX=find(essaiX~=0);
indexX2=indexX(1);
indexGoodmax=find(tempa==essaiX(indexX2));

```

```
77 tafelA=polyfit(tempa(indexGood:indexGoodmax),y(indexGood:indexGoodmax),1);
78 Anode=polyval(tafelA,tempa(indexGood:indexGoodmax));
79
80 deltaY=Anode(end)-Anode(1);
81 deltaX=tempa(indexGoodmax)-tempa(indexGood);
82
83
84 a=deltaY/deltaX; % gives the slope in decade/V
85 a=a(1);  % The first value is considered if more than one values found
86 b = - a(1) * X(indexGoodmax) + Anode(end); % gives the intersection with the y axis
87 b=b(1); % The first value is considered if more than one values found
88 yX=a(1)*X+b(1); % equation of the anodic Tafel line
89 plot(X,yX);
90
91 plot(tempa,yX);
92
93 hold on;
94
95
96
97 %% Cathode
98
99 % First index
100 essai4=zeros(length(tempa),1);
101 essai1=tempa(indice1)-0.048; % finds the first value located between 48mV
102 essai2=tempa(indice1)-0.052; % and 52 mV from OCP
103 for i=1:length(tempa)
104     if tempa(i)>=essai2 && tempa(i)<=essai1
105         essai4(i,1)=tempa(i);
106     end
107 end
108
109 index2=find(essai4~=0);
110 index22=index2(1);
111 indexGoodmax=find(tempa==essai4(index22));
112
113 % Inferior index
114 essai5=zeros(length(tempa),1);
115 essai1=tempa(1)+0.02;  % Does not take into account the curvy end of the
116 essai2=tempa(1)+0.022; % cathodic branch
117 for i=1:length(tempa)
118     if tempa(i)>=essai1 && tempa(i)<=essai2
119         essai5(i,1)=tempa(i);
120 %     else
121 %         new(i,1)=0;
122     end
123 end
124
125 index3=find(essai5~=0);
126 index32=index3(1);
127 indexGoodmin=find(tempa==essai5(index32));
128
129 tafelB=polyfit(tempa(indexGoodmin:indexGoodmax),y(indexGoodmin:indexGoodmax),1);
130 Cathode=polyval(tafelB,tempa(indexGoodmin:indexGoodmax));
131
132 deltaY=Cathode(end)-Cathode(1);
133 deltaX=tempa(indexGoodmax)-tempa(indexGoodmin);
134
135 a2=deltaY(1)/deltaX(1); % gives the slope in decade/V
136
137 b2 = - a2 * X(indexGoodmax(1)) + Cathode(end); % gives the intersection
138                                                % with the y axis
139
```

```
140 y3=a2(1)*X+b2(1);% equation of the cathodic Tafel line
141 plot(X,y3);
142
143 %% Determination of measurd corrosion potential
144  % and current density (intersection)
145 syms x y
146
147 eqn1 = a(1)*x - y  == -b(1);
148 eqn2 = a2(1)*x - y == -b2(1);
149
150 [A,B] = equationsToMatrix([eqn1, eqn2], [x, y])
151 X = linsolve(A,B)
152 plot(tempa,y3);
153
154 hold on;
155
156
157
158
159
160
161 %% Gneral figure
162  title ( sprintf ( 'Linear polarisation curve of the sample "Twip 30%%-5" '
163  '\n (0.33mV/s scan rate and scan range of OCP150mV with 50mM buffer)' ,
164  'i ) , 'FontSize' , 20 );
165  hleg1=legend('Polarisation curve','E_{corr} observed', 'Tafel anode',
166  'Tafel cathode');
167  set(gca,'fontsize',15);
168  ylabel('log [current density(A/cm^2)]');
169  xlabel('Voltage vs SCE [V]');
```

APPENDIX B

SEM AND EDX DESCRIPTION OF ONE WEEK IMMERSION SAMPLES (50MM BUFFER)

B.1 SEM description

- **TWIP 6**: One pitting spot is visible on one side of the piece of metal to the naked eye. The corners highlight the presence of a deposited layer that starts to crack at the corners, which started to get worn away. Some edges also showed pitting; this can be seen on Figures 4.46a and 4.46b. The center did not show any significant presence of pitting or corrosion products.

- **TWIP 9**: To the naked eye, this sample corroded in a more homogeneous way. Brown glimmer can be observed, especially on one side. When analyzing the SEM image, the same is observed. Only very few spots differ from the whole sample, with a bit of pitting. The corners also start to get worn out.

- **TWIP 12**: To the naked eye, this sample looks similar to the TWIP 9 sample. However, the SEM images highlight the presence of spherical-like compounds, as can be seen on Figure 4.48c, where a similar behaviour is shown for the TWIP 10%-3 sample. The edges also got worn out and a few spots where either corrosion products got deposited or where pits got formed are also found.

- **TWIP 10%-1**: Upon first inspection, only one corner seemed attacked and this was confirmed on SEM images. Small pits got formed, especially at the sample corners, that got worn out as well. An example of a pit covered with corrosion products is seen on Figure 4.46. The center did not encounter the presence of deposition of corrosion products.

- **TWIP 10%-3**: Upon first inspection, this sample presented brown parts concentrated o the edges and corners of one side of the sample, leaving the center in a blue shiny state. The other side presented these brown parts on a smaller area and two pits located at the edges were visible. Spherical-like agglomerates of corrosion products around pits were observed and are illustrated on Figures 4.48a and 4.48b. The edges and corners seem to have suffered more severe attack than the center, where the surface layer only consists of a few small holes, compared to a more concentrated amount of holes in the edges and corners surfaces.

- **TWIP 20%-1**: About fourteen pits are visible to the naked eye on one side of the sample with eight pits concentrated in the centre and two in the edges with the other pits dispatched throughout the rest of the surface. The other side presents less pits (around four) and one edge is also attacked. The corners show clear signs of attack. The SEM images show that the corners were worn out but not as much as could be supposed by the simple look at the sample as was

detailed previously. The pits are effectively seen on the SEM and shown on Figure 4.46. Except for the pits found in the centre of the sample, the behaviour is the same as for the above for that region.

- **TWIP 20%-2**: The corners look attacked to the naked eye and one important pit is observed on one side. On the other side, two corners look more attacked than the other two and four important pits are observed, located two by two at the long edges of the sample. This is validated by SEM investigation and the cracked layer is also present as was for all previous samples.

- **TWIP 40%-1**: That sample presents an important brown area. A photograph of the stain can be seen on Figure 4.47. The other side looks normal with only the presence of one or two small pits on the edges and worn out corners. The brown stain looks like an agglomerate of corrosion products over a large surface and can be seen on Figure 4.47. The corners present a starting wear out of material and the centre looks similar to the other samples. Pits covered by corrosion products can be seen on Figure 4.46d. Holes are visible in the center of the sample as is also the case for the TWIP 1 and TWIP 3 samples.

- **TWIP 40%-4**: Only the corners seem attacked to the naked eye for one side of that specimen. The other side is not much more different with only the presence of two or three pits along the edges and one small pit in the centre of the sample. A bit more corrosion products deposits are visible on the SEM with some forming agglomerates as can be seen on Figure 4.46e. As for the other samples, the deposited layer cracks on the corners and the centre presents a few holes from material wear out.

B.2 EDX analysis

- **TWIP 6**: The worn out corners present the expected aluminum contamination. They also show a considerable amount of phosphorus and calcium presence. Sodium, magnesium, and chlorine are also present with insignificant sulfur presence. The cracked layer presents a much higher presence of sodium, phosphorus and calcium than the worn out corners. No sign of chlorine was found on that layer. However, potassium in small amounts is found whereas no potassium could be found on the worn out corners. Aluminum contamination is still present on the cracked layer. The same layer further inside the sample, not presenting any cracks did not present any aluminum contamination and phosphorus, calcium, sodium and magnesium were found in smaller but still close amounts than at the worn out corners. No signs of potassium and chlorine were found. The layer found underneath the cracked layer presented very few presence of phosphorous, sodium, calcium and magnesium compared to the previous spots. No chlorine is found, and potassium is present in small proportions. However, some quite significant presence of sulfur was found and significant aluminum contamination is also seen. An edge pit was also analyzed and at the spot were material is eaten away, there is presence of chlorine and potassium. Phosphorus, calcium, sodium and magnesium are present in comparable proportions than on the non-cracked deposited layer described before. Aluminum contamination is still present. Finally, the centre consists of mostly the metal components with amount of phosphorus, calcium, and sodium equivalent to the ones found on the surface underlaying the cracked corrosion layer. Same goes for chlorine and potassium. No aluminum contamination is present at the centre.

- **TWIP 9**: The cracked deposited layer on top of the metal is found to be mainly composed of phosphorous and calcium with smaller amounts of sodium and magnesium. Even smaller amounts of chlorine and potassium are present. The layer found underneath contains insignificant amounts of phosphorus and calcium. Chlorine and potassium in more significant amounts are present. The centre is made of very few amount of potassium and calcium, slightly more than

the surface underneath the cracked layer. No chlorine is found and potassium is found in very small amounts. No aluminum contamination is found at the corners.

- **TWIP 12**: The uncracked deposited layer seems to be made of phosphorus and calcium with smaller amounts of sodium, magnesium and tiny amounts of chlorine and potassium. The layer underneath consists of smaller amounts of phosphorus, calcium, and magnesium but bigger amounts of chlorine. No sodium is detected. The centre is made of even smaller amounts of phosphorus, calcium and magnesium. Sodium is present in minimal amounts, as well as chlorine and potassium. No aluminum contamination was seen either on the corners or in the centre. No aluminum contamination is found at the corners.

- **TWIP 10%-1**: The cracked layer is made of high amounts of phosphorus and calcium. Quite significant amounts of sodium and magnesium are present. And small amounts of potassium and chlorine are also present. The surface underneath that cracked layer contains much smaller amounts of these elements than on the cracked layer. However, there is one exception, the chlorine content increased. The deposited layer further inside is made of smaller amounts of phosphorus, calcium, magnesium, potassium and chlorine than on the cracked layer. The center is made of even smaller amounts of all the above described elements. Figure B.1 shows that the spherical-like agglomerates are made of phosphorus, calcium, sodium and magnesium in comparable amounts than the sublayer next to it. Unlike the sublayer, chlorine and potassium is present in higher rates. As already detailed, holes are present in the metal surface after immersion. These were investigated in this sample at the centre and the only difference with the rest of the centre is a slight increase in chlorine and potassium concentration and lower concentrations of the other elements. Aluminum contamination on the corners has to be noted.

- **TWIP 10%-3**: High amounts of phosphorus and calcium were detected on the cracked layer. The other usual elements are also present in smaller amounts. Chlorine is present in quite high amounts compared to the other samples. Theses elements affect the manganese composition more than the iron composition. The surface found underneath is made of the same elements stated above in much smaller proportion with no chlorine. The centre is made of the same elements in similar amounts. Aluminum contamination on the corners is visible.

- **TWIP 20%-1**: High amounts of phosphorus and calcium are found on the cracked layer. as well as small amounts of sulfur and potassium. Sodium and magnesium are also present in intermediate amounts. The underlaying layer is made of comparable amounts of sodium and magnesium. However, phosphorus and calcium are resent in much smaller amounts. Chlorine that was not present on the cracked layer is present underneath and potassium in higher concentration is found and sulfur in smaller amounts is still present. The centre of the sample is made of all the above in smaller quantities or comparable to the underlaying surface. No aluminum contamination is found at the corners.

- **TWIP 20%-2**: The same behaviour as previously is detected.

- **TWIP 40%-1**: Same behaviour but with much higher amounts of phosphorus and calcium bringing the amount of manganese down. High amounts of chlorine are also present. The underlaying surface is made of insignificant amounts of all the above elements. The pits present significant amounts of chlorine, phosphorous and calcium. The centre is made of equivalent amounts of the previous elements than the underlaying layer stated above. Small aluminum contamination is detected at the corners.

- **TWIP 40%-4**: The morphology study of this sample showed the presence of a brown spot. This one is made of less salt elements but more iron and oxygen than the cracked and worn out regions, which are made of lesser amounts than the cracked layer. The centre is composed of very few amounts of the salty elements, even smaller than the brown region.

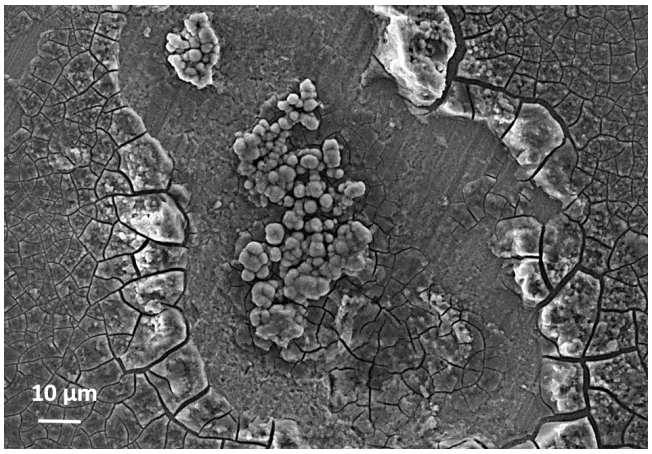

FIGURE B.1: SE images of TWIP 10%-1 sample illustrating an agglomeration of corrosion products over a pit. The images were taken using a 15kV beam and 30μm aperture.

BIBLIOGRAPHY

[1] Bureau fèdèral du Plan. *Maladies cardio-vasculaires: décès dus aux maladies cérébro-vasculaires.* `http://www.indicators.be/fr/indicator/maladies-cardio-vasculaires-deces-dus-aux-maladies-cerebro-vasculaires?detail=`. accessed on the 18^{th} of June 2016.

[2] Hendra Hermawan et al. "Fe–Mn alloys for metallic biodegradable stents: degradation and cell viability studies". In: *Acta biomaterialia* 6.5 (2010), pp. 1852–1860.

[3] Michael Schinhammer et al. "Degradation performance of biodegradable Fe Mn C (Pd) alloys". In: *Materials Science and Engineering: C* 33.4 (2013), pp. 1882–1893.

[4] Erlin Zhang, Haiyan Chen, and Feng Shen. "Biocorrosion properties and blood and cell compatibility of pure iron as a biodegradable biomaterial". In: *Journal of Materials Science: Materials in Medicine* 21.7 (2010), pp. 2151–2163.

[5] B Liu, YF Zheng, and Liquan Ruan. "In vitro investigation of Fe30Mn6Si shape memory alloy as potential biodegradable metallic material". In: *Materials letters* 65.3 (2011), pp. 540–543.

[6] Sri Harjanto et al. "Corrosion behavior of Fe-Mn-C alloy as degradable materials candidate fabricated via powder metallurgy process". In: *Advanced Materials Research*. Vol. 576. 2012, pp. 386–389.

[7] Hendra Hermawan. *Biodegradable metals: From concept to applications*. Springer Science & Business Media, 2012.

[8] NIH. *Who Is at Risk for Coronary Heart Disease?* `http://www.nhlbi.nih.gov/health/health-topics/topics/cad/atrisk`. accessed on the 2^{nd} of April 2016.

[9] NIH. *What is a Stent*. `http://www.nhlbi.nih.gov/health/health-topics/topics/stents`. accessed on the 2^{nd} of April 2016.

[10] Buddy D Ratner et al. *Biomaterials science: an introduction to materials in medicine*. 2^{nd} Edition. Elsevier Academic press, 2004.

[11] Preop.com. *Stent Implantation Coronary Angioplasty*. `http://preop.com/freetvwp/Stent_Implantation_Coronary_Angioplasty.html`. accessed on the 2^{nd} of April 2016.

[12] TW Duerig and M Wholey. "A comparison of balloon-and self-expanding stents". In: *Minimally Invasive Therapy & Allied Technologies* 11.4 (2002), pp. 173–178.

[13] Wikipedia. *Hyperplasia*. `https://en.wikipedia.org/wiki/Hyperplasia`. accessed on the 17^{th} of June 2016.

[14] B Thierry et al. "Blood compatibility of nitinol compared to stainless steel". In: *Proceedings of the Shape Memory and Superelastic Technologies Meeting*. 2000, pp. 285–290.

[15] Thamarasee M Jeewandara, Steven G Wise, and Martin KC Ng. "Biocompatibility of coronary stents". In: *Materials* 7.2 (2014), pp. 769–786.

[16] Bong Gun Song. *Multidector CT Imaging of Coronary Artery Stent and Coronary Artery Bypass Graft*. INTECH Open Access Publisher, 2013.

[17] WebMD. *Cardiac Stents Overview. Heart Disease Health Center*. `http://www.webmd.com/heart-disease/guide/stents-types-and-uses`. accessed on the 2^{nd} of April 2016.

[18] John A Ormiston and Patrick WS Serruys. "Bioabsorbable coronary stents". In: *Circulation: Cardiovascular Interventions* 2.3 (2009), pp. 255–260.

[19] John Wiley & Sons, Inc. `http://www.wiley.com/college/callister/1118061608/sae//ch08.html`. accessed on the 19^{th} of June 2016.

[20] M Peuster et al. "A novelapproach to temporary stenting: Degradable cardiovascular stents produced from corrodible metal-results 6-18 months after implanation into New Zealand white rabbits". In: *Heart* 86 (2001), pp. 563–569.

[21] M Peuster et al. "Long term biocompatibility of a corodible peripheral iron stent in the porcine descending aorta". In: *Biomaterials* 27 (2006), pp. 4955–4962.

[22] Maryam Moravej and Diego Mantovani. "Biodegradable Metals for Cardiovascular Stent Application: Interests and New Opportunities". In: *International Journal of Molecular Sciences* 12 (2011), pp. 4250–4270.

[23] Wikipedia. *Hemolysis*. `https://en.wikipedia.org/wiki/Hemolysis`. accessed on the 17^{th} of June 2016.

[24] FL Nie et al. "In vitro corrosion, cytotoxicity and hemocompatibility of bulk nanocrystalline pure iron". In: *Biomedical Materials* 5.6 (2010), p. 065015.

[25] H Hermawan et al. "Iron-manganese: new class of metallic degradable biomaterials prepared by powder metallurgy". In: *Powder Metallurgy* 51.1 (2008), pp. 38–45.

[26] Wikipedia. *Titanium alloy*. `https://en.wikipedia.org/wiki/Titanium_alloy`. accessed on the 20^{th} of May 2016.

[27] O Bouaziz et al. "High manganese austenitic twinning induced plasticity steels: A review of the microstructure properties relationships". In: *Current opinion in solid state and materials science* 15.4 (2011), pp. 141–168.

[28] H Idrissi et al. "On the relationship between the twin internal structure and the work-hardening rate of TWIP steels". In: *Scripta Materialia* 63.10 (2010), pp. 961–964.

[29] Wikipedia. *TWIP steel — Wikipedia, The Free Encyclopedia*. `https://en.wikipedia.org/w/index.php?title=TWIP_steel&oldid=714689953`. accessed on the 16^{th} of May 2016. 2016.

[30] Dierk Raabe. *Twip steels (Twinning Induced Plasticity Steels)*. `http://www.dierk-raabe.com/twip-steels/`. accessed on the 15^{th} of May 2016.

[31] Pascal Jacques. *LMAPR2013: Physical chemistry of metals and ceramics*. SICI, 2011.

[32] C. Phaniraj. *What is the difference between TRIP and TWIP steel?* `https://www.researchgate.net/post/What_is_the_difference_between_TRIP_and_TWIP_steel2`. accessed on the 16^{th} of May 2016.

[33] Michael Schinhammer et al. "Recrystallization behavior, microstructure evolution and mechanical properties of biodegradable Fe–Mn–C (–Pd) TWIP alloys". In: *Acta Materialia* 60.6 (2012), pp. 2746–2756.

[34] K R Trethewey and J Chamberlain. *Corrosion for Science and Engineering*. 2^{nd} Edition. Longman Scientific & Technical, 1995.

[35] Metrohm AG. *Corrosion part 1- Basic concepts.* `http://www.ecochemie.nl/download/Applicationnotes/Autolab_Application_Note_COR01.pdf`. accessed on the 9^{th} of May 2016.

[36] WebCorr the Corrosion Clinic. *Different Types of Corrosion - Recognition, Mechanisms & Prevention: Pitting Corrosions.* `http://www.corrosionclinic.com/types_of_corrosion/pitting_corrosion.htm`. accessed on the 15^{th} of May 2016.

[37] Thomas Woods. *Degradation and Surface Engineering: Portfolio Task 1 - Anodes and Cathodes.* `https://tomwoods91.wordpress.com/2014/11/`. accessed on the 2^{nd} of April 2016.

[38] RN Parkins. "Stress corrosion spectrum". In: *British Corrosion Journal* 7.1 (1972), pp. 15–28.

[39] R. Winston Revie and Herbert H. Uhlig. *Corrosion and corrosion control - An Introduction to Corrosion Science and Engineering.* Fourth. John Wiley and Sons, 2008.

[40] MA Deyab and ST Keera. "Cyclic voltammetric studies of carbon steel corrosion in chloride-formation water solution and effect of some inorganic salts". In: *Egyptian Journal of Petroleum* 21.1 (2012), pp. 31–36.

[41] The McGraw-Hill Companies. *Chapter 19: Electrochemistry - ELECTROCHEMICAL CELLS AND STANDARD REDUCTION POTENTIALS.* `http://www.mhhe.com/physsci/chemistry/chang7/ssg/chap19_2sg.html`. accessed on the 30^{th} of April 2016.

[42] Carl H Hamann, A Hamnett, and W Vielstich. *Electrochemistry.* 2^{nd} Edition. Wiley-VCH, 1998.

[43] Leonard MacEachern. *ELEC 4907: A description of Dr. MacEachern's Capstone engineering projects.* `http://elec4907-maceachern.blogspot.be/`. accessed on the 30^{th} of April 2016. 2011.

[44] Wikipedia. *Électrode au calomel saturée en KCl — Wikipedia, The Free Encyclopedia.* `http://fr.wikipedia.org/w/index.php?title=Electrode_au_calomel_saturee_en_KCl`. accessed on the 30^{th} of April 2016. 2015.

[45] Kingston Technical Software. *Iron E-pH (Pourbaix) Diagram.* `http://www.corrosion-doctors.org/Corrosion-Thermodynamics/Potential-pH-diagram-iron.htm`. accessed on the 3^{rd} of June 2016s.

[46] NPTEL. *Electrochemistry: Lecture 25 (Corrosion).* `http://nptel.ac.in/courses/122101001/Slide/lect25/25_5.htm`. accessed on the 26^{th} of May 2016.

[47] *Pourbaix diagram (stability diagram).* `http://www.uobabylon.edu.iq/eprints/publication_12_18276_228.pdf`. accessed on the 8^{th} of May 2016.

[48] Gamry Instruments. *Getting Started with Electrochemical Corrosion Measurement.* `http://www.gamry.com/assets/Application-Notes/Getting-Started-with-Electrochemical-Corrosion-Measurement.pdf`. accessed on the 30^{th} of April 2016. 2010.

[49] Joris Proost. *Compléments de chimie inorganique.* SICI, 2012.

[50] Metrohm AG. *Ohmic Drop: Part 1 - Basic Principles.* `http://www.ecochemie.nl/download/Applicationnotes/Autolab_Application_Note_EC03.pdf`. accessed on the 9^{th} of May 2016.

[51] B LIU and YF Zheng. "Effects of alloying elements (Mn, Co, Al, W, Sn, B, C and S) on biodegradability and in vitro biocompatibility of pure iron". In: *Acta Biomaterialia* 7 (2011), pp. 1407–1420.

[52] J Cheng et al. "Comparative in vitro study on pure metals (Fe, Mn, Mg, Zn and W) as biodegradable metals". In: *Journal of Materials Science & Technology* 29.7 (2013), pp. 619–627.

[53] Julie Lévesque et al. "Design of a pseudo-physiological test bench specific to the development of biodegradable metallic biomaterials". In: *Acta biomaterialia* 4.2 (2008), pp. 284–295.

[54] Wikipedia. *Fibroblast.* `https://en.wikipedia.org/wiki/Fibroblast`. accessed on the 17^{th} of June 2016.

[55] Wikipedia. *Blood vessel*. https://en.wikipedia.org/wiki/Blood_vessel. accessed on the 17^{th} of June 2016.

[56] Bernard Dery. *Human body: blood vessels*. http://www.infovisual.info/03/061_en.html. accessed on the 17^{th} of June 2016.

[57] Naing Naing Aung and Wei Zhou. "Effect of grain size and twins on corrosion behaviour of AZ31B magnesium alloy". In: *Corrosion Science* 52.2 (2010), pp. 589–594.

[58] Adam Grajcar. "Corrosion Resistance of High-Mn Austenitic Steels for the Automotive Industry". In: *Corrosion Resistance* (2012), pp. 353–376.

[59] IM Ghayad et al. "Effect of cold working on the aging and corrosion behaviour of Fe-Mn-Al stainless steel". In: *Steel Grips* 4.2 (2006), pp. 133–137.

[60] Eva MAZANCOVÁ, P Kozelsky, and Ivo SCHINDLER. "The TWIP alloys resistance in some corrosion reagents". In: *METAL'2010* (2010), pp. 1–6.

[61] Muhammed Musaher Muhammed Khalissi. "Stress corrosion cracking of twinning induced plasticity (TWIP) steel". PhD thesis. Monash University. Faculty of Engineering. Dept. of Mechanical and Aerospace Engineering, 2012.

[62] AS Toloei, V Stoilov, and DO Northwood. "The effect of different surface topographies on the corrosion behaviour of nickel". In: *WIT Transactions on Engineering Science* 77 (2013), pp. 193–204.

[63] L Abosrra et al. "Corrosion of Mild Steel and 316 L Austenitic Stainless Steel with Different Surface Roughness in Sodium Chloride Saline Solutions". In: *WIT Trans. Eng. Sci* 65 (2009), pp. 161–172.

[64] Dieter Landolt. *Corrosion and surface chemistry of metals*. CRC Press, 2007.

[65] Struers. *Active Oxide Polishing Suspensions*. http://ipaper.ipapercms.dk/StruersAS/ActiveOxidePolishingEnglish/.

[66] Metrohm AGt. *NOVA iR compensation tutorial*. http://www.ecochemie.nl/download/NovaTutorials/iR_compensation_tutorial.pdf. accessed on the 3^{rd} of June 2016.

[67] Olivier Declerck. "Caractérisation électrochimique d'aciers à haute résistance pour stents biorésorbables". MA thesis. Université catholique de Louvain - Ecole Polytechnique de Louvain, 2015.

[68] GE Badea et al. "Polarisation Measurements Used for Corrosion Rates Determination". In: *Journal of Sustainable Energy* 1.1 (2010), pp. 140–144.

[69] XL Zhang et al. "Effects of scan rate on the potentiodynamic polarization curve obtained to determine the Tafel slopes and corrosion current density". In: *Corrosion science* 51.3 (2009), pp. 581–587.

[70] D Paul Schweinsberg and Harvey J Flitt. "Reproducibility of corrosion parameters for the acidic dissolution of pure iron: potentiostatic polarisation". In: *Corrosion science* 47.6 (2005), pp. 1520–1533.

[71] K. A. Natarajan. *Advances in Corrosion Engineering - Lecture 10*. http://nptel.ac.in/courses/113108051/module2/lecture10.pdf. accessed on the 4^{th} of June 2016.

[72] Princeton Applied Research. *Application Note CORR-1: Basics of Corrosion Measurements*.

[73] Princeton Applied Research. *Application Note CORR-4: Electrochemistry and Corrosion: Overview and Techniques*.

[74] Norio Sato. "Basics of corrosion chemistry". In: *Green Corrosion Chemistry and Engineering: Opportunities and Challenges* (2011), pp. 1–32.

[75] ISO 8407. *Corrosion of metals and alloys-Removal of corrosion products from corrosion test specimens*. 1991.

[76] ASTM Standard et al. *Standard practice for preparing, cleaning, and evaluating corrosion test specimens*.

[77] Wikipedia. *Inductively coupled plasma*. https://en.wikipedia.org/wiki/Inductively_coupled_plasma. accessed on the 3^{rd} of June 2016s.

[78] Wikipedia. *Atomic emission spectroscopy*. https://en.wikipedia.org/wiki/Atomic_emission_spectroscopy. accessed on the 3^{rd} of June 2016.

[79] A. Delcorte and J. Devaux. *Methods of Physical and Chemical Analysis - Chapter 7,11*.

[80] J.S. Temenoff and A.G. Mikos. *Biomaterials: The Intersection of Biology and Materials Science*. New Jersey: Pearson Education, 2008, pp. 263–267.

[81] DeviantArt. *Electronic Microscopy*. http://www.deviantart.com/journal/Electronic-Microscopy-462654632. accessed on the 3^{rd} of June 2016.

[82] UCL, Earth and Life Institute. *Outiils d'analyse*. https://www.uclouvain.be/72706.html/Diffraction_de_rayons_X_DRX. accessed on the 4^{th} of June 2016.

[83] Wikipedia. *X-ray photoelectron spectroscopy*. https://en.wikipedia.org/wiki/X-ray_photoelectron_spectroscopy. accessed on the 3^{rd} of June 2016.

[84] UCL, IMCN. *ToF-SIMS*. https://www.uclouvain.be/en-357051.html. accessed on the 4^{th} of June 2016.

[85] ION-TOF Gmbh. *TOF-SIMS*. https://www.iontof.com/tof-sims-secondary-ion-mass-spectrometry.html. accessed on the 4^{th} of June 2016.

[86] Wikipedia. *Bright-field microscopy*. https://en.wikipedia.org/w/index.php?title=Bright-field_microscopy&oldid=719806931. accessed on the 26^{th} of May 2016. 2016.

[87] Wikipedia. *Test Q*. https://fr.wikipedia.org/wiki/Test_Q. accessed on the 16^{th} of May 2016.

[88] J G N Thomas. *The electrochemistry of corrosion*. http://www.npl.co.uk/upload/pdf/the_electrochemistry_of_corrosion_with_figures.pdf. accessed on the 5^{th} of June 2016.

[89] VS Muralidharan. "An insight into the origin of corrosion potential-A critical review". In: *Bulletin of electrochemistry* 18.4 (2002), pp. 179–186.

[90] David G. Enos and Louie L Scribner. *The potentiodynamic polarization scan: Technical Report 33*. Tech. rep. Solartron Instruments, 1997.

[91] Lester H Gabriel. *Service life of drainage pipe*. Vol. 254. Transportation Research Board, 1998.

[92] Jayanta Kumar Saha. *Corrosion of Constructional Steels in Marine and Industrial Environment: Frontier Work in Atmospheric Corrosion*. Springer Science & Business Media, 2012.

[93] Fondriest Environmental, Inc. *Dissolved Oxygen*. http://www.fondriest.com/environmental-measurements/parameters/water-quality/dissolved-oxygen/. accessed on the 15^{th} of June 2016. 2013.

[94] NOVA. *The uncompensated resistance: NOVA iR compensation tutorial*. http://www.ecochemie.nl/download/NovaTutorials/iR_compensation_tutorial.pdf. accessed on the 1^{st} of June 2016.

[95] M.C. Bloom and Somers H. Jr. Smith. *The corrosion products of iron and their relation to corrosion in steam-generating equipment*. 1969.

[96] El-Sayed M Sherif. "A comparative study on the electrochemical corrosion behavior of iron and X-65 steel in 4.0 wt% sodium chloride solution after different exposure intervals". In: *Molecules* 19.7 (2014), pp. 9962–9974.

[97] Shengfa Zhu et al. “Biocompatibility of pure iron: in vitro assessment of degradation kinetics and cytotoxicity on endothelial cells”. In: *Materials Science and Engineering: C* 29.5 (2009), pp. 1589–1592.

[98] Philip Urban. “Les stents résorbables”. In: *Forum Med Suisse* (2008), pp. 341–342.

[99] Vlado Cuculic, Marina Mlakar, and Marko Branica. “Influence of the HEPES Buffer on Electrochemical Reaction of the Copper (II)-Salicylaldoxime Complex”. In: *Electroanalysis* 10.12 (1998), pp. 852–856.

[100] Philip A Schweitzer et al. *Fundamentals of metallic corrosion: atmospheric and media corrosion of metals*. CRC press, 2006.

Rue Archimède, 1 bte L6.11.01, 1348 Louvain-la-Neuve **www.uclouvain.be/epl**